Unveiling the Early Stages of Star and Planet Formation:

Observational Insights From Studying Class 0 and I Protostars

Rajeeb Sharma

Dissertation submitted for the degree of

PHILOSOPHIÆ DOCTOR

Niels Bohr Institute
Faculty of Science
University of Copenhagen

November 2024

Supervisor: Jes K Jørgensen

This thesis has been submitted to the PhD School of The Faculty of Science,
University of Copenhagen

Title	Unveiling the Early Stages of Star and Planet Formation: Observational Insights From Studying Class 0 and I Protostars
Author	Rajeeb Sharma
Department	Niels Bohr Institute, Faculty of Science, University of Copenhagen
Academic Advisor	Prof. Jes K. Jørgensen
Assessment Committee	Dr. Troels Haugbølle (chair) Dr. Michiel Hogerheijde Dr. Audrey Coutens

This thesis was typeset using LaTeX and the `memoir` documentclass. Typography inspired by Friedrich Wiemer's thesis using the class `classicthesis` developed by André Miede. Layout adapted from Giulia Perotti's thesis.

To my family,

Abstract

It is now well established that the formation of low-mass stars, like our Sun, begins with the gravitational collapse of cold, dense cores within large interstellar clouds of cold dust and gas. This collapse initiates the birth of a protostar, which gradually grows in mass by accreting gas and dust from its surroundings. To achieve a comprehensive understanding of the star formation process, it is necessary to observe and study the various physical and chemical processes that govern the protostellar systems at each stage of their evolution. Especially in the earliest stages (the so-called Class 0 and I stages), this is challenging, as the young stars are so deeply enveloped in the surrounding dust that they can only be observed at infrared radio wavelengths.

Due to these challenges, previous observations have left many questions unanswered about the physical evolution of such young stars. With the introduction of modern instruments and interferometers like the Atacama Large Millimeter/Submillimeter Array (ALMA), it is now possible to observe the dust and gas around such young stars with high resolution and study, for example, their planet-forming disks or the material falling towards them. This provides a unique opportunity to finally illuminate the processes occurring around young stars in their earliest stages. The purpose of this thesis is to utilize these opportunities to observe and characterize the physical and chemical properties of young protostars and thereby contribute to our understanding of formation of stars and planets.

The foundation for this thesis is ALMA observations at high-resolution ($\sim$0.″04 – 0.″1; $\sim$6 – 15 au) of continuum and molecular lines towards 19 young protostars from nearby star-forming regions ($d < 200$ pc). These observations were carried out as part of a large ALMA program, "Early Planet Formation in Embedded Disks (eDisk)", which primarily aims to investigate whether rotating disks around very young protostars have substructures similar to those seen in more evolved systems.

Chapter 4 presents a comprehensive analysis of the Class 0 protostar R CrA IRS5N from the eDisk program. The continuum emission from the dust shows a smooth, flattened, disk-like structure without obvious substructures. An analysis of the velocity field in the disk reveals the presence of Keplerian rotation around a central star with a mass of $\sim$0.3 $M_\odot$. In addition to IRS5N itself, the observations also show emission from the nearby binary system IRS5a/b. This binary system is considerably smaller than IRS5N and the line emission from it shows that material from IRS5b streams into a disk-like structure around IRS5a.

Chapter 5 presents a systematic investigation of the spatial distribution of the various molecules observed towards all 19 protostars from the eDisk program. While some molecular lines clearly show the presence of extended emission from winds and jets, others are systematically concentrated towards the inner regions around the protostars and show clear signs of rotation. Some molecules are only seen towards the younger protostars which are

typically more deeply embedded in dust and gas. Finally, there are a number of molecules that show very large variation from source to source. This suggests that multiple formation and excitation mechanisms are active in these protostars, which further emphasizes the importance of our understanding of the chemistry during the star formation process so that molecules can be used to study different parts of it.

In chapter 6, I present an analysis of infrared measurements from the Stratospheric Observatory for Infrared Astronomy (SOFIA) of highly excited CO lines for the protostars SVS13-A and SVS13-C as well as the Herbig-Haro object HH-7 in the NGC 1333 cluster. These CO lines are sensitive to the warm part of the gas in these sources, which provides insight into the mechanisms which contributes to the overall cooling budget in these systems.

Dansk Resumé

Det er nu veletableret, at dannelsen af stjerner med lav masse, som vores egen Sol, begynder med gravitationelt kollaps af kolde, tætte kerner i store interstellare skyer af kold støv og gas. Dette kollaps initierer fødslen af en protostjerne, som gradvist vokser i masse ved at akkumulere gas og støv fra sine omgivelser. For at opnå en komplet forståelse af stjernedannelsesprocessen er det nødvendigt at observere og studere de forskellige fysiske og kemiske processer, der styrer protostjernersystemerne i hver fase af deres udvikling. Specielt i de tidligste stadier (de såkaldte Klasse 0 og I stadier) er dette udfordrende, da de unge stjerner er så dybt indhyldede i de omkringlæggende støv at de kun kan observeres ved ved infrarøde eller radio bølgelængder.

På grund af disse udfordringer har tidligere observationer efterladt mange spørgsmål om den fysiske udviking af sådanne unge stjerner. Med introduktionen af moderne instrumenter og interferometre som Atacama Large Millimeter/Submillimeter Array (ALMA) er det nu muligt at observere støvet og gassen omkring sådanne unge stjerner med høj opløsning og studere f.eks. deres planet-dannende skiver eller materialet der falder ind mod dem. Dette giver en unik mulighed for endelig at belyse processerne der foregå om unge stjerner i deres tidligste stadier. Formålet med denne afhandling er at udnytte disse muligheder til at observere og karakterisere de fysiske og kemiske egenskaber af unge protostjerner og dermed bidrage til vores forståelse af dannelsen af stjerner og planeter.

Fundamentet for denne afhandling er ALMA observationer ved høj opløsning ($\sim$0.″04 – 0.″1; $\sim$6 – 15 au) af kontinuum og molekylære linjer mod 19 unge protostjerner fra nære stjernedannende områder ($d < 200$ pc). Disse observatiober er udført som en del af et stort ALMA store program, “Early Planet Formation in Embedded Disks (eDisk)”, der primært har til formål at undersøge om roterende skiver omkring ganske unge protostjerner har substrukturer ligesom det ses i mere udviklede systemer.

Kapitel 4 præsenterer en omfattende analyse af Klasse 0 protostjernen R CrA IRS5N fra eDisk programmet. Kontinuumstrålingen fra støvet viser en jævn, fladtrykt, skive-lignende struktur uden åbenlyse substrukturer. En analyse hastighedsfeltet i skiven afslører tilstedeværelsen af Kepler rotation omkring en central stjerne med en masse på $\sim$0,3 $M_\odot$. Ud over IRS5N selv viser observationerne også emission fra det nærliggende binære system IRS5a/b. Dette binære system er betydeligt mindre end IRS5N og linjeemissionen fra det viser at materiale fra IRS5b strømmer ind i en disklignende struktur omkring IRS5a.

Kapitel 5 præsenterer en systematisk undersøgelse af den rumlige fordeling af de forskellige molekyler observeret mod samtlige 19 protostjerner fra eDisk programmet. Hvor nogle molekylære linjer klart viser tilstedeværelsen af udstrakt emission fra vinde og jets er andre systematisk koncentreret mod de indre områder omkring protostjernerne og viser klare tegn på rotation. Nogle molekyler er kun set mod de yngre protostjerner der typisk er mere

dybt indhyldede i stø og gas. Endelig er der en række molekyler der viser meget stor variation fra kilde til kilde. Dette antyder, at flere dannelses- og excitationsmekanismer er aktive i disse protostjerner, hvilket yderligere understreger vigtigheden af vores forståelse af kemien under stjernedannelsesprocessen for molekyler kan bruges til at studere forskellige dele af den.

I kapitel 6 præsenterer jeg en analyse af infrarøde målinger fra Stratospheric Observatory for Infrared Astronomy (SOFIA) af højt exciterede CO linjer for protostjernerne SVS13-A og SVS13-C samt Herbig-Haro-objektet HH-7 i NGC 1333 hoben. Disse CO linjer er følsomme over for den varme del af gassen i disse kilder, hvilket giver indblik i de mekanismer der bidrager til det samlede kølingsbudget i disse systemer.

Acknowledgements

This PhD has been an incredible journey, both academically and personally, none of which would have been possible without the tremendous help and support I received from a lot of people who pushed and kept me motivated.

First and foremost, I would like to express my deepest and sincerest gratitude to my supervisor, Jes K. Jørgensen. Thank you for your excellent guidance, constant encouragement, and endless patience and support throughout these years. I am incredibly grateful for the many hours you dedicated to discussing ideas with me, revising my work, and helping me shape my research into a more cohesive project. Thank you for always being available when I needed advice and also advocating for me. I remember how you recommended me to the steering committee of the eDisk program to allow me to lead the various projects that now form the core of this thesis. Working alongside you has been a pleasure and has helped me grow as a scientist. I hope to continue working with you in the future. Also, I am deeply appreciative for the excellent advice you gave early in my PhD journey, where you told me, "It is important to also take breaks". This advice made my PhD journey much smoother and enjoyable over the years.

A big thanks goes to my collaborator and officemate of three years, Sacha Gavino. Thank you for always being available to answer my questions (some of which might have been annoying, for which I apologize) and spending a considerable portion of your valuable time to assist me in both my scientific work as well as personal life. When I first arrived in Denmark, I barely knew anything, and you shared your own experience and showed me the ropes, making my transition much easier.

Another huge thank you is owed to John J. Tobin, who first introduced me to the field of embedded protostars and radio astronomy. You also introduced me to Jes K. Jørgensen, for which I am eternally grateful. You have advised and mentored me ever since the beginnings of my scientific career and have sort of served as an unofficial co-supervisor. Thank you especially for always being available to answer my question on working with ALMA data reduction. Without your support and guidance, I would definitely not have been here.

I would also like to thank the ALMA eDisk team, with whom I had the privilege of collaborating during this research. Through this collaboration, I got to work with many incredible individuals whose insights and comments have tremendously helped in improving this thesis work. I am particularly grateful to Nagayoshi Ohashi, Merel van' t Hoff, and Jeong-Eun Lee, for their invaluable discussions and guidance. The many insightful talks I had with you all have significantly improved me as a researcher.

I also want to acknowledge all the past and present members of the sub-mm and the starformation groups, especially Lars Kristensen, Rebecca Pitts, Manar el Akel, Katarzyna Dutkowska, Michael Küffemier, Giulia Perotti, Thomas Berlok, Ida Holk, Krisha Shah, Majid Uzbak, and Martine Lützen. Thank you all for the stimulating weekly discussions and for providing a fresh

new perspective on my research. A special thanks go to Troels Haugbølle, who was always willing to help me resolve any issues I encountered with the HPC systems.

To the colleagues from Starplan (sorry for not individually naming you all), thank you for all the great moments over the years. Starplan has sort of become my second family, and I will greatly miss the lunch talks, the coffee breaks, the weekly badminton sessions, the games, the BBQ sessions, and so on. I will especially miss Jean Bollard's cake sessions. You all made the whole process a lot more fun!

Sundar *dai*, Suraj *dai*, Shova *bhauju*, and Sheeva *bhauju*, thank you for sharing your own PhD experiences with me and helping me navigate and make sense of the logistics of the Danish administration. To my Nepali friends here in Denmark, thank you all for the incredible memories. Because of you guys, I do not feel more homesick!

Last but not least, I would like to thank my incredible family for their continued love, support, and encouragement. Thank you, Mom and Dad, for allowing me to move so far from home in order to pursue my dream of studying astronomy. Thank you for buying all those science books and encyclopedias with pretty pictures of planets and stars when I was little. Thank you for understanding when I didn't respond or call back for weeks during the final stretch. Thank you to my sister, who always supported me. Despite our childhood squabbles, I know I can always count on you for anything. To my wife, Deepika, thank you for taking this incredible journey with me. Thank you for always being there for me and for believing in me. You have always been there to support and motivate me, and saying thank you is not enough to express my gratitude for you. I am lucky to have you in my life and will forever be grateful for your love.

Thank you very much.
Mange tak.
मुरी मुरी धन्यवाद।

Contents

1

Introduction

"Equipped with his five senses, man explores the universe around him and calls the adventure Science."
—Edwin Hubble

For millennia, human beings have been fascinated by the night sky. Looking at the moon and the countless bright dots scattered all over the dark sky, it is only natural that one begins to wonder more about these objects. This curiosity led our ancestors to observe and chart the positions of these objects. Eventually, they discovered that these observations could serve as an excellent tool for navigation and keeping track of time, thus making astronomy one of the oldest sciences. In fact, recent archaeological evidence suggests that the oldest calendar, created by tracing the phases of the Sun, Moon, and constellations, was probably made over 13000 years ago (Sweatman, 2024).

Fast forward to the present, the field of astronomy has grown tremendously from its humble beginnings of bookkeeping the position of celestial objects. We now know that the countless bright dots seen across the sky are stars (although some are planets or galaxies), and our Sun is also a star like them. Likewise, it is now also known that our Earth is a planet, and along with at least seven other planets, it orbits around the Sun. Collectively, the Sun and the planets make up the Solar System, which is a tiny part of the Milky Way galaxy, our home in the universe.

Despite making these incredible discoveries, there are many questions whose answers are still unknown to us. *How did the Sun and Earth form? Why and how did life start on Earth? Is there life elsewhere in the universe?* These are some of the questions for which we are still searching for answers. Answering these questions is incredibly challenging and likely requires the combined efforts of the various disciplines of science. One thing that is abundantly clear is that life on Earth is sustained by the Sun and without it, life as we know it would simply cease to exist. It is therefore safe to assume that the beginnings of life on Earth are closely tied to the formation of the Sun. Thus, by understanding how the Sun and Earth formed, we can get incredible insights into the beginnings of life.

Understanding how the Sun and Earth formed in the past is a daunting task, especially since we cannot directly observe the process as it happened billions of years ago. However, as an excellent alternative, we can study the star-formation process currently taking place in other nearby Sun-like stars. The Sun falls into the category of low-mass stars, which are the most common type of stars, accounting for up to ∼80% of all the stars in the universe. Thus, plenty of low-mass stars of all stages are available nearby that can

be observed. Thanks to the help of modern telescopes and instruments, scientists are now able to routinely observe these systems and slowly unravel the mysteries of the star formation process.

Shu et al. (1987) put forth a seminal theory of low-mass star formation by combining the results of theoretical and observational studies available at that time. Subsequent studies in this field have revealed that star formation is a much more complicated process with multiple physical and chemical processes governing it. Understanding these processes is essential to form a complete picture of star and planet formation.

This thesis utilizes observational data from nearby low-mass protostars with the aim of contributing to our knowledge of the star and planet formation processes in low-mass protostars. Specifically, this work focuses on embedded protostars, which represent the youngest phase of protostellar evolution. By observing these youngest sources in millimeter and submillimeter wavelengths, this thesis seeks to constrain the physical and chemical processes that govern the process of star and planet formation in these sources.

This thesis is structured as follows. Chapter 1 provides the necessary background on the current understanding of low-mass star formation. It begins by explaining where and how star formation begins, defines the different stages of evolution of a protostar, and the observational characteristics of these stages. It then describes the major components of an embedded protostar that are necessary to understand to form a picture of star formation. The remainder of the chapter describes the astrochemistry that governs the process of star formation in these protostars.

Chapter 2 describes the methods used in this thesis. It begins by describing infrared and radio astronomy, explaining the concept of interferometry, and also introduces the instruments used to collect the observational data. It then proceeds to explain how the interferometric data are calibrated, reduced, and imaged for analysis and also explains the concept of moment maps that are frequently used for the analysis of the observational results in this thesis.

Chapter 3 provides a short overview of the research conducted in this thesis, beginning with an introduction to the *Early Planet Formation in Embedded Disks* (eDisk) program and some of the key results from the overall program. This eDisk program forms the basis for the majority of the research conducted in this thesis. The chapter then summarizes the papers that are central to this thesis, discussing their roles in advancing the field of star and planet formation. Finally, the chapter provides an outlook on some of the ongoing and planned projects that directly follow the results of this thesis.

The papers themselves are presented in Chapters 4 and 5 and 6.

1.1 THE FORMATION OF LOW-MASS STARS

The space between the stars is not a perfect vacuum but is rather sparsely populated by gas and dust collectively known as the interstellar medium (ISM). The ISM is extremely diffused with an average particle density of $\sim$1 cm^{-3} and is composed of approximately 99% gas – mainly hydrogen and helium – while the remaining 1% is composed of dust particles (refer to Snow & McCall, 2006; Draine, 2011, for more details).

The ISM is not entirely homogeneous and contains regions where lower temperatures aid in the concentration of material. These cold and dense regions gradually grow larger, becoming huge structures of masses $\sim 10^{5-6}$ M$_\odot$ and sizes $\sim$100 pc called Giant Molecular Clouds (GMCs; Williams & McKee 1997; Herbst & van Dishoeck 2009). Today, GMCs are well known to be the primary sites of star formation. However, the existence of these GMCs was relatively unknown until about fifty years ago due to their higher levels of dust extinction, making them opaque to visible and ultraviolet wavelengths. They were finally revealed in CO emissions at millimeter wavelengths using radio telescopes that were sensitive enough to detect the emissions from these clouds (see Chevance et al., 2023, and references therein).

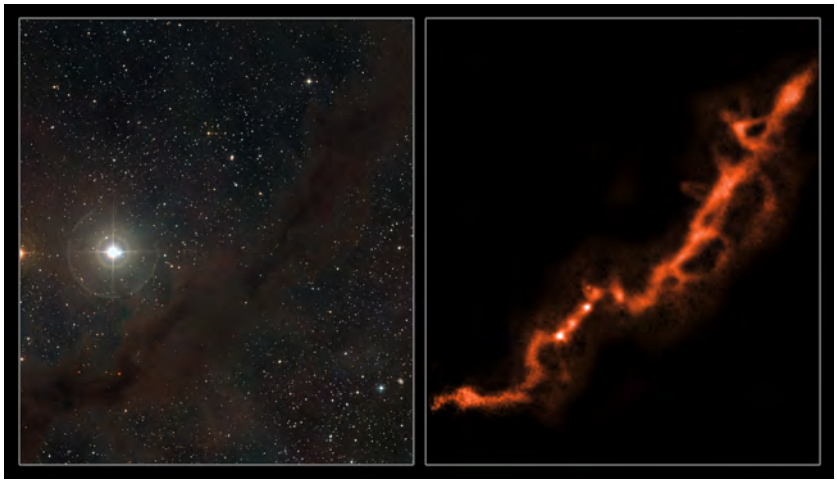

FIGURE 1.1 The Taurus molecular cloud observed at optical wavelength (*left*), and the same region observed in the radio wavelength observed with the LABOCA camera on the APEX telescope (*right*). Credit: ESO/APEX (MPIfR/ESO/OSO)/A. Hacar et al./Digitized Sky Survey 2.

GMCs are gravitationally bound structures and have average densities of $\sim$100 cm^{-3}. Larson (1981) found that turbulences in GMCs are highly supersonic, which results in velocity dispersions in emissions that follow a size-linewidth relation of:

$$\sigma = C\sqrt{R} \tag{1.1}$$

where σ is the 1D velocity dispersion, R is the radius in pc, and $C \approx 0.7$ km s^{-1} pc$^{0.5}$ (Solomon et al., 1987). On larger scales, turbulence in GMCs prevents the cloud from collapsing under its own gravity, whereas on smaller scales, it leads to strong density perturbations within the cloud. These density perturbations lead to the formation of filaments within the molecular clouds

that harbor regions of high densities called dense cores (e.g., Myers, 2009; André et al., 2010, 2014).

There is a delicate balance between the different physical processes such as turbulence, gravity, magnetic fields, and pressures in the cores. When either the mass or the radius of the core exceeds the Jeans instability limit (Jeans, 1902), gravity overcomes the pressure leading to free-fall collapse of the core. Eventually, the collapsing core is thought to reach a stage in which the increasing thermal pressure balances out the gravity, reaching a phase called the first hydrostatic core (FHSC; Larson 1969). This stage is short-lived, lasts only a few thousand years, and is characterized by the fact that the collapsing gas is still molecular. Due to this short timescale, observation of the FHSC stage has proved rather difficult, and to this day only a few potential FHSC candidates have been discovered (e.g., Schnee et al., 2012; Gerin et al., 2015; Young et al., 2018; Friesen et al., 2018). Once the temperatures in the cores reach ∼2000 K, H_2 begins to dissociate, which resumes the collapse and eventually leads to the formation of a protostar. This marks the transition from the prestellar stage to the protostellar stage.

According to the classical picture put forth by Shu (1977), the collapse of a core originates at the center of an isothermal sphere and radially extends outward at the sound speed, a process commonly known as "inside-out collapse." This model shows a simplified version of the protostar formation in which the accretion rate of the protostar remains constant, described by $\dot{M} = 0.975 c_s^3/G$ where c_s is the sound speed, and the density profile of the free-falling cloud follows the power law $\rho(r) \propto r^{-3/2}$. In reality, observations and simulations have shown that neither the core is entirely isothermal and spherical (e.g., Lin et al., 2017; Kuffmeier et al., 2017; Bate, 2018; Zhang et al., 2020) nor the accretion is always constant (e.g., Safron et al., 2015; Fischer et al., 2012, 2019). Despite these limitations, the inside-out collapse model remains an important tool for studying the physics that govern the star formation process.

1.2 CLASSIFICATION OF PROTOSTARS

Once the system enters the protostellar stage, the protostar continues to collapse and evolve as it accretes more material from the surrounding envelope. During this stage, several key components of a protostellar system, such as disk and outflow, begin to appear as well (Section 1.3). These components also evolve together with the protostar. As the evolution of a protostar is a highly dynamic process, its observational characteristics can be quite different depending on the stage the protostar has reached. Lada (1987) and André et al. (1993) proposed to divide the protostars into four "Classes" based on their observational parameters. These classes are thought to correspond to the evolutionary stage of the protostar, where Class 0 is the youngest protostar and Class III is the oldest. This classification is now widely accepted and is the standard approach to recognizing a protostar.

1.2.1 *Spectral energy distribution of a protostar*

The light emitted by a protostar provides valuable information about its evolutionary stage. The spectral energy distribution (SED) of a protostar shows the energy emitted by the source as a function of wavelength. SED is a key tool in the study of a protostar as it forms the basis of protostellar classification. In addition, the SED also allows for the calculation of the bolometric luminosity ($L_{\rm bol}$) and bolometric temperature ($T_{\rm bol}$) of a protostar. Traditionally, protostars have been classified according to their infrared spectral index (α) given by:

$$\alpha = \frac{d\ \log(\lambda F_\lambda)}{d\ \log(\lambda)}, \tag{1.2}$$

which represents the slope of the SED where $\lambda = 2 - 20\ \mu$m. Based on the value of α, the protostars were initially grouped into three classes, Class I – III (Lada & Wilking, 1984; Lada, 1987). André et al. (1993) updated this classification by adding a Class 0 following the discovery of a new kind of embedded source that was undetected at $< 10\ \mu$m by the instruments of that time but had significant luminosity at submillimeter wavelengths. Class 0 sources have similar α values as Class I sources, and the two can be distinguished by calculating the ratios of $L_{\rm submm}/L_{\rm bol}$, where $L_{\rm submm}$ is the luminosity at submillimeter wavelengths ($\lambda > 350\mu$m, Dunham et al. 2014). Figure 1.2 provides an overview of the typical SED profiles for each class.

An alternative classification of protostars was proposed by Myers & Ladd (1993) and Chen et al. (1995) based on the $T_{\rm bol}$ values calculated from the SED of the source. The $T_{\rm bol}$ is defined as the temperature of a blackbody that has the same flux-weighted mean frequency as the observed SED. This method clearly separates all four classes, but the $T_{\rm bol}$ of a protostar is highly dependent on its inclination. The classification criteria and the features of each class are described below.

Class 0

Class 0 sources have $\alpha > 0.3$ and $L_{\rm submm}/L_{\rm bol} > 0.5\%$. In addition, they have $T_{\rm bol} \leq 70$ K. Initially, these sources were characterized by their lack of near- to mid-infrared emissions (André et al., 1993; Barsony, 1994). However, with the launch of more sensitive instruments such as the *Spitzer Space Telescope*, they were finally detected at these wavelengths (e.g., Jørgensen et al., 2005, 2006, 2007; Tobin et al., 2007). The emission of Class 0 sources typically peaks at far-infrared wavelengths, indicative of the emissions being dominated by the infalling cold envelope.

Physically, Class 0 sources are the youngest protostars that are still deeply embedded in a thick envelope of infalling material. At this stage, the envelope accounts for most of the mass of the system–typically 80% or more (Jørgensen et al., 2009). At this stage, the accretion rates are the highest, and these sources thus drive powerful jets and outflows that transfer excess angular momentum from the protostellar system back into the molecular cloud. Emissions towards these outflows have been found to contain clumps and knots, which, along with the discovery of accretion outbursts, suggest that the accretion rates are highly variable during the

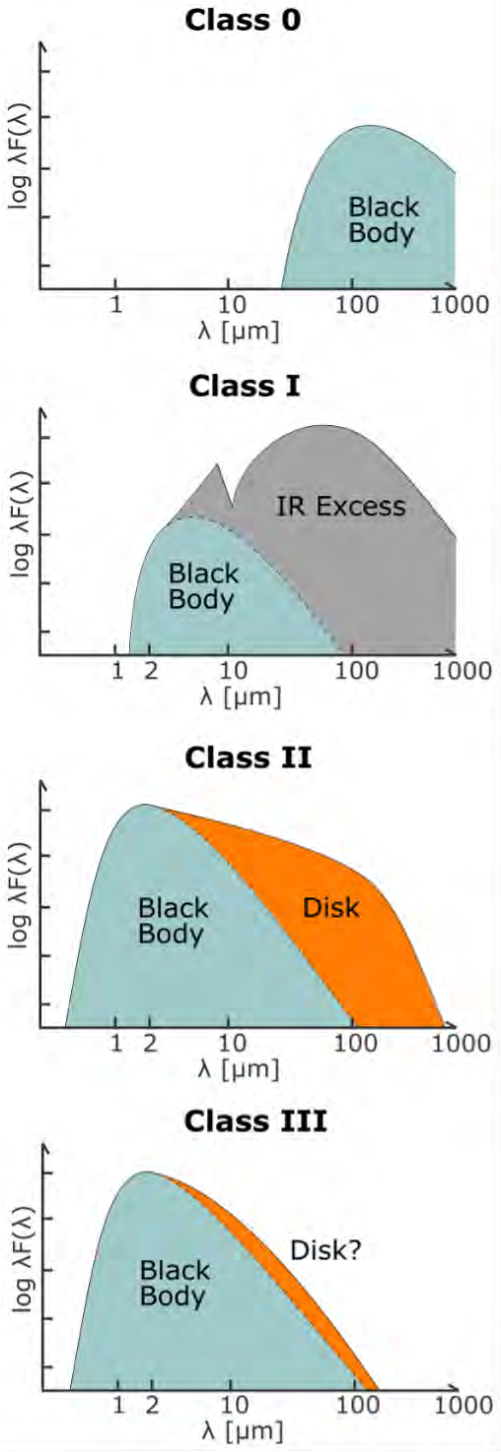

FIGURE 1.2 Illustrations of the typical SEDs seen towards the different classes of protostars. Credit: Persson (2014).

Class 0 stage (e.g., Plunkett et al., 2015; Safron et al., 2015; Sharma et al., 2020). The estimated lifespan of a Class 0 source is ≈50000 yrs (Kristensen & Dunham, 2018), making this stage a brief but highly dynamic period of a protostar.

Class I

Class I sources also have $\alpha > 0.3$ but can be differentiated from Class 0 sources by having $L_{\rm submm}/L_{\rm bol} < 0.5\%$. Likewise, Class I sources have higher bolometric temperatures with $70 \leq T_{\rm bol} \leq 650$ K. The SED of a Class I source generally peaks at far-infrared wavelengths and is associated with a large infrared excess, which is indicative of a stage where the protostar is still surrounded by an envelope (Figure 1.2). However, unlike in Class 0 sources, the envelope surrounding Class I sources is less massive, with a disk-to-envelope mass ratio of about 20–60% (Jørgensen et al., 2009).

The Class I sources continue to drive jets and outflows; however, these are generally less collimated and energetic than those in Class 0. This is indicative of the decreasing accretion rate, which can reach as low as $\sim 10^{-8}$ $M_\odot$ yr^{-1} during the Class I stage (Fiorellino et al., 2023). Nevertheless, several Class I sources have been observed undergoing luminosity outbursts, which suggests that these sources can also have periods of increased accretion (see Fischer et al., 2023, for an overview).

Class II

Class II sources have $-1.6 < \alpha < -0.3$[1] and $650 \leq T_{\rm bol} \leq 2800$ K. During this stage, most of the surrounding envelope around the protostar has either dissipated or been accreted onto the protostar and the disk. SEDs from Class II sources peak at near-infrared wavelengths and have an excess in the far-infrared and submillimeter range that can be attributed to the presence of a disk, as shown in Figure 1.2 (Lada, 1987). The disk is a primary feature of Class II sources and is often referred to as a protoplanetary disk to mark the transition of a protostar from an envelope-dominated to a disk-dominated system. High-resolution observations have shown that substructures such as rings, gaps, and spirals are ubiquitous in these disks (e.g., Andrews et al., 2018; Cieza et al., 2021). Such substructures are often thought to result from the presence of planets, which suggests that planet formation likely begins early in the Class 0/I phases. Furthermore, outflows that are fairly dominant and prominent in the earlier stages are significantly diminished in Class II sources, which indicates that there is a further decline in the accretion rate.

[1] There are some sources with $-0.3 < \alpha < 0.3$ called "Flat" sources, which are thought to be sources in transition from the Class I to Class II phase (Greene et al., 1994; Evans et al., 2009)

Class III

Class III sources have $\alpha < -1.6$ and $T_{\rm bol} \geq 2800$ K. This is the final stage in the evolution of a protostar before hydrogen burning starts and the source enters the main-sequence phase. The SED of a Class III source is mostly dominated by the stellar photosphere and only has a minimal amount of infrared and submillimeter access from the disk. This indicates that much of the material in the protoplanetary disk has been processed either by accretion onto the protostar or by the formation of large planetesimals through grain growth and coagulation at this stage (Williams & Cieza, 2011).

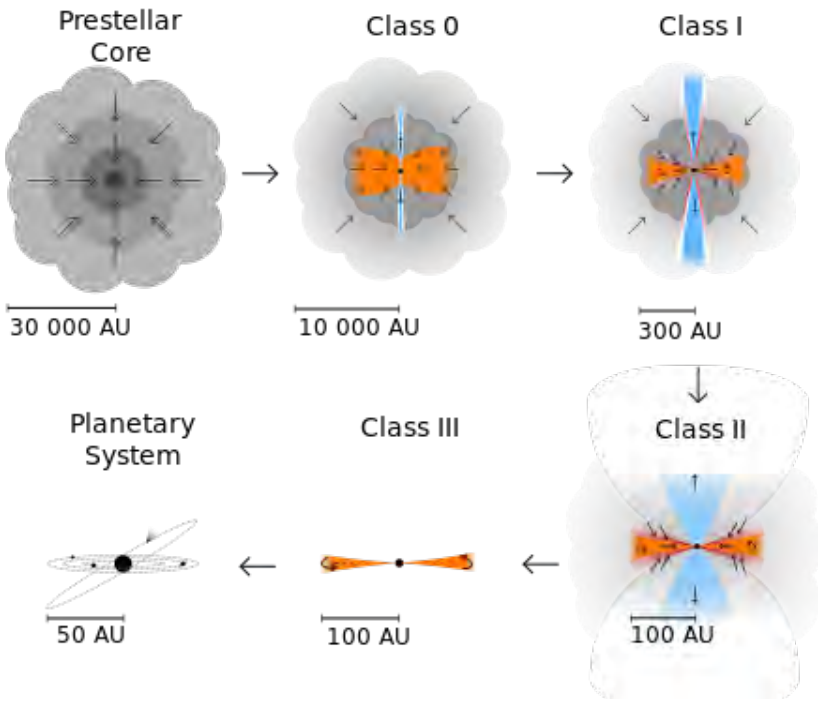

FIGURE 1.3 Schematic representation of the various phases of low-mass star formation starting with the collapse of a prestellar core and ending in the formation of a planetary system. Credit: Persson (2014).

1.3 COMPONENTS OF AN EMBEDDED PROTOSTAR

Figure 1.3 summarizes the key physical characteristics of the different classes described above, starting from the collapse of a prestellar core to the formation of a solar system. The sources in the Class 0 and Class I phases are also called *embedded sources* as these systems are still enshrouded in a thick envelope of gas and dust. The embedded nature of these protostars makes observing them quite difficult, and it is only in the past 10–15 years that we have had the necessary resolution and sensitivity to resolve them. The research in this thesis focuses on cultivating a better understanding of the physical and chemical processes of these embedded protostars. Below is a more detailed description of the major components of an embedded protostar based on our current understanding.

1.3.1 *Protostellar Core*

The protostellar core refers to the innermost region of a protostar, which houses the central nascent star that is supported by hydrostatic equilibrium. This core is the progenitor to the main-sequence star and continuously accretes material from the surrounding envelope. Throughout the protostellar stage, only hydrogen dissociation takes place in the core since the temperatures are not high enough to start nuclear fusion. The embedded phase of a protostar is characterized by the lack of emission at visible and UV wavelengths as the surrounding envelope effectively covers up the central object. This makes the core appear relatively cold and faint in the infrared and submillimeter wavelengths, as most of the emission observed comes

from light re-emitted by the surrounding envelope rather than the central object (André et al., 1993; Evans et al., 2009).

1.3.2 *Disk*

As the protostellar core collapses and accretes material, it begins to spin more rapidly in order to conserve angular momentum. Consequently, the infalling gas and dust begin to flatten and revolve around the central core, forming a disk that surrounds the protostar (Terebey et al., 1984; Shu et al., 1987). Disks around embedded sources are often also called *embedded disks* or *protostellar disks*. These disks play a crucial role in protostellar evolution as they regulate the mass accreted by the protostar and are also the sites for planet formation (Terebey et al., 1984; Shu et al., 1987). Although the question of exactly when disks form in the life cycle of a protostar is still a topic of debate, the growing number of disks observed in Class 0 sources suggests that they form early in protostellar evolution (e.g., Tobin et al., 2020; van't Hoff et al., 2023; Kido et al., 2023; Sharma et al., 2023; Aso & Sai, 2023; Sai et al., 2023; Thieme et al., 2023). Disks in Class 0 phase are relatively small with radii usually reaching only about a few tens of AU. Strong magnetic fields that appear in the core as a result of the collapse act as a "brake" and stop the disks from growing too large. In fact, numerical simulations predict that magnetic braking can become powerful enough to completely suppress the formation of disks, leading to the "magnetic braking catastrophe" (see Li et al., 2014, for a review). However, recent studies have suggested that non-ideal magnetohydrodynamics (MHD) can reduce the efficiency of magnetic braking to allow for the growth of disks (Tsukamoto et al., 2023).

As the protostar evolves, the disks grow steadily and often reach radii of several hundred AU in the Class I phase (e.g., Flores et al., 2023; Yamato et al., 2023). If the disk grows faster than the material can be accreted onto the central star, the excess buildup of material can cause the disk to become unstable and fragment into additional components. These components can lead to the formation of planetesimals or multiple systems, and the accretion of such a component onto the protostar can trigger luminosity outbursts in protostars. Recent observations of complex substructures such as rings and gaps strongly suggest such fragmentation commonly occurs in the embedded phase and may fuel early planet formation in disks (e.g., Sheehan & Eisner, 2017; Segura-Cox et al., 2020; Yamato et al., 2023).

1.3.3 *Envelope*

In an embedded source, the protostellar core is surrounded by a region of infalling gas and dust known as the envelope. This envelope serves as the primary reservoir that fuels the accretion process and is a significant contributor to the total mass of the protostellar system. The envelope can be divided into two broad regions: the outer envelope and the inner envelope regions. The outer envelope extends over thousands of AU and represents the cold and dense regions with temperatures and densities similar to those of the surrounding molecular cloud (Stahler & Palla, 2004). At these scales, the envelope generally has low turbulence and slowly drifts inwards under

the influence of gravity. The outer envelope inherits its chemistry from the prestellar core and can be traced by the similar molecules often associated with cold, dense regions of molecular clouds such as CO and NH_3 (Jørgensen et al., 2004; Bergin & Tafalla, 2007). The outer envelope regions of nearby embedded protostars usually get resolved-out when observed through high-resolution observations, as is the case with the observations presented in this thesis.

In contrast, the inner envelope region represents the material in close proximity to the protostellar core, typically within a few hundred AU. In this region, the infalling gas and dust are subject to radiative heating and stronger gravitational forces from the protostar, which results in higher temperatures and more turbulent motions. As the temperature rises, molecules that are frozen onto the grains begin to sublimate, and increased motion and densities facilitate new reaction pathways. This leads to increased chemistry in this region and also aids in the formation of complex organic molecules (COMs; see reviews by Jørgensen et al. 2020; Öberg et al. 2023).

1.3.4 *Outflows and Jets*

As material from the envelope gets accreted onto the protostar, a complex interaction occurs between the rotating, infalling material and the magnetic fields in the protostellar system. This interaction generates a strong torque that sweeps up some of the infalling gas and dust and ejects them back into the surrounding cloud as powerful outflows and jets perpendicular to the rotation of the system (Blandford & Payne, 1982). Outflows are ejections that travel at velocities ≤ 20 km s^{-1} relative to the systemic velocity (v_{sys}) of the source, while jets are ejections that travel at higher velocities, often reaching speeds of 100 km s^{-1} or higher. Both of these ejections are often observed as bipolar lobes and are crucial in regulating the angular momentum of the system by transferring excess angular momentum back into the molecular cloud. They also serve as a major feedback mechanism in the star formation process by slowing down the accretion onto the protostar and reintroducing turbulence back into the molecular cloud (Frank et al., 2014).

As mentioned in Sect. 1.2, the outflows and jets of Class 0 sources are generally more energetic than those of Class I sources, indicative of higher accretion rates in Class 0 protostars. Consequently, they are normally more collimated in Class 0 sources and carve out a smaller cavity in the envelope. As the ejecta become less powerful in the Class I (and also Class II) source, they spread out more and tend to carve out a larger cavity opening.

1.3.5 *Outflow Cavity Walls*

At the edge of the cavities carved by outflows and jets, there lies a dynamic, narrow boundary region where the infalling material of the envelope interacts with the outflowing material called the outflow cavity walls. These cavity walls are marked by increased UV radiation from the protostar, which leads to localized heating and photodissociation of molecules, facilitating new reaction pathways (e.g., Arce & Sargent, 2006; Tychoniec et al., 2021). Additionally, the material in these cavity walls gets pushed and compressed by the outflow, increasing the densities in these regions and also promoting

small-scale localized shocks (e.g., van Kempen et al., 2010; Visser et al., 2012). All of these processes make the outflow cavity walls highly active and energetic, leading to a rich and complex chemistry (Visser et al., 2012; Drozdovskaya et al., 2015).

1.3.6 *Accretion Streamers*

In the classical picture of star formation, material from the envelope is accreted axisymmetrically onto the protostar. However, recent studies have revealed that materials from the larger structures can also be deposited non-axisymmetrically by narrow filament-like structures called accretion streamers (or simply streamers) (e.g., Tobin et al., 2010; Pineda et al., 2020; Thieme et al., 2022). These streamers have relatively consistent velocity structures and have been observed at both smaller scales ($\lesssim$1000 AU; e.g., Valdivia-Mena et al. 2022; Kido et al. 2023) and larger scales ($\gtrsim$10000 AU; e.g., Pineda et al. 2020). The importance of streamers in the star formation process is still not fully understood. Nevertheless, theoretical and observational studies of streamers have shown that they can deposit material at a rate similar to the accretion rate of protostars and trigger several processes such as instability in disks, formation of substructures, episodic accretion, and late accretion in protostars (see Pineda et al., 2023, and references therein).

1.4 ASTROCHEMISTRY

As mentioned in Sect. 1.1, hydrogen and helium are the dominant components of the ISM, and the combined mass of all other heavier elements only accounts for about 1% of the total mass. Despite being such a small fraction, this 1% of material leads to a rich and diverse chemistry in the ISM. Astrochemistry studies these molecules observed in the ISM and uses them as a tool to unravel the different physical and chemical conditions of the environment in which they are found. Astrochemistry is a relatively new branch of astronomy and began only after the identification of simple molecules in the ISM in the late 1930s and early 1940s (Swings & Rosenfeld, 1937; McKellar, 1940; Adams, 1941). Since then, more than 300 different molecules have been discovered in the ISM[2], ranging from simple diatomic molecules to COMs containing 6+ atoms. Notably, most of the molecules found in the ISM have been discovered in star-forming regions, making these areas ideal laboratories for studying the formation and evolution of molecules.

[2]Complete list available on the Cologne Database for Molecular Spectroscopy (CDMS): https://cdms.astro.uni-koeln.de/classic/molecules

A primary goal of astrochemical studies in protostellar systems is to understand the various physical and chemical conditions that govern the star formation process. The observed molecules serve as excellent diagnostics for different conditions, such as temperatures, densities, and pressures, as the formation and evolution of the molecules are directly dependent on these conditions (e.g., Jørgensen et al., 2020). Moreover, the chemistry during star formation also determines the budget of molecules for planets that eventually form. Hence, understanding the astrochemistry of protostars is essential to form a complete picture of the chemistry of planets and possibly

life. Because direct, hands-on study of these molecules is not possible, the astrochemistry of protostars relies heavily on molecular spectroscopy.

1.4.1 *Molecular Spectroscopy*

The light radiated from the protostellar core of an embedded protostar gets absorbed and re-emitted by the various molecules of gas and dust in the surrounding envelope before reaching us. These molecules leave their mark on the light as spectral lines of absorption and emission. From these line profiles, we can get crucial information not only on the molecules present but also on the distribution, abundance, temperature, and density of the molecules (Herbst & van Dishoeck, 2009). Figure 1.4 shows the observed spectra towards the Class 0 source IRAS 16293-2422 with some of the key molecules highlighted. The basic principles of spectroscopy are explained in this section.

Spectroscopy relies on the fundamental principles of quantum mechanics in which energies are quantized. Atoms and molecules are quantum particles, and they have a set of quantized energy levels that they can be in at any given time. By absorbing or emitting a fixed amount of energy, they can transition around the different energy levels. Molecules have more degrees of freedom than atoms and consequently have more levels of quantized energy transitions. The transitions of a molecule can be divided into three different categories:

- **Electronic transitions:** These involve the transition of molecules between different energy levels and have typical energies observed at optical or UV wavelengths.
- **Vibrational transitions:** These involve transitions between the oscillation states of molecules, causing the bending or stretching of the molecular bonds. Vibrational transitions have typical energies observed at infrared wavelengths.
- **Rotational transitions:** These involve transitions between the different rotation states of a molecule. Rotational transitions have typical energies observed at submillimeter and millimeter wavelengths.

The total energy of a molecule is then simply the sum of energy at each state:

$$E^{total} = E^{electronic} + E^{vibrational} + E^{rotational} \tag{1.3}$$

Figure 1.5 displays the schematic diagram of the energy levels for a diatomic molecule. A molecule can absorb (or emit) a photon of a specific energy to transition to a higher (or lower) state, producing an absorption (or emission) profile in the spectra. The wavelength at which these profiles appear is unique to the molecule, thus allowing for its precise identification. Since the research in this thesis utilizes submillimeter and millimeter wavelength observations, the focus will be on rotational transition spectroscopy.

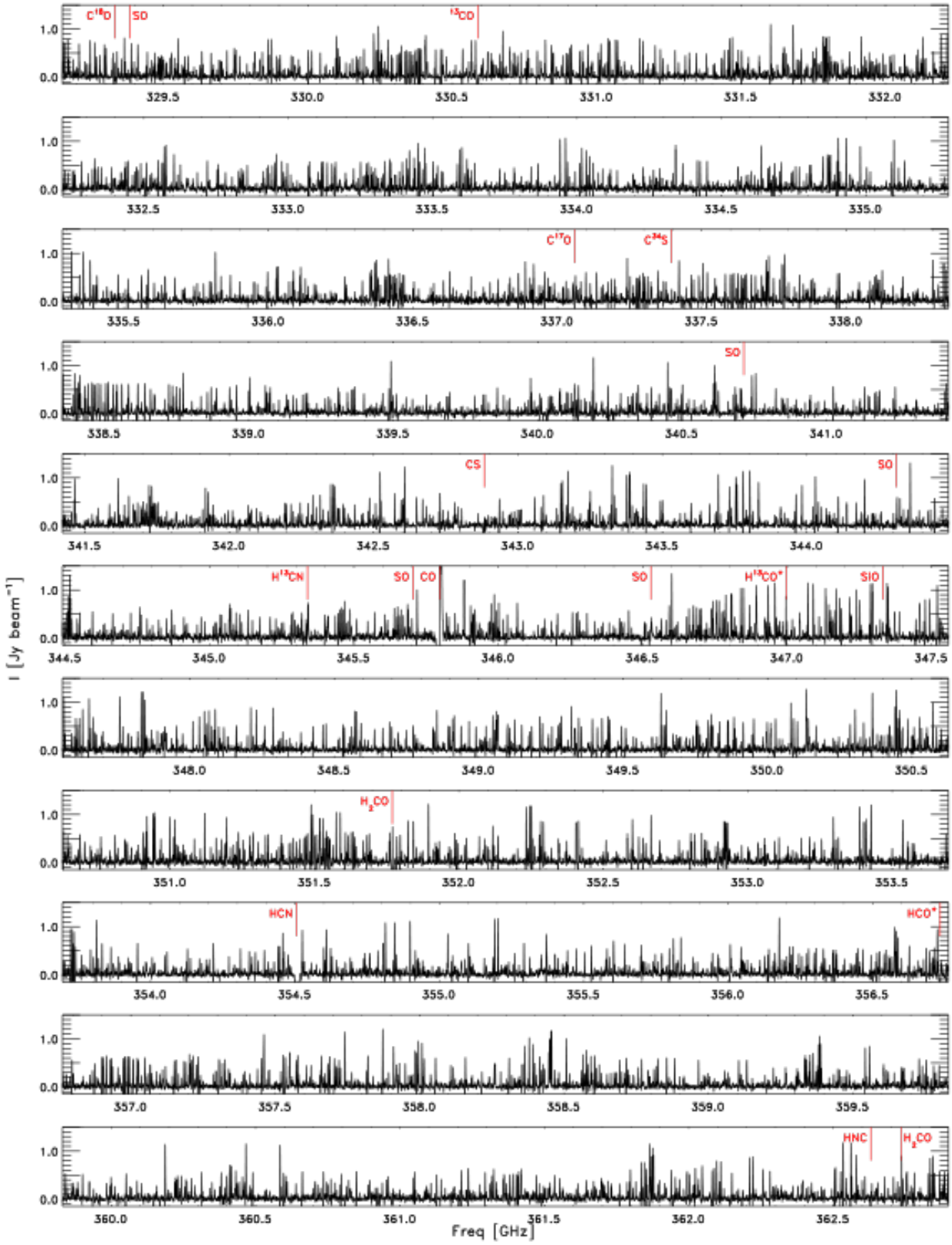

FIGURE 1.4 Spectrum of the protostar IRAS 16293-2499 obtained using the ALMA telescope. More than 10000 emission lines of several molecules were detected. The identity of a few key species are shown in red at their characteristic frequencies. Credit: Jørgensen et al. (2016).

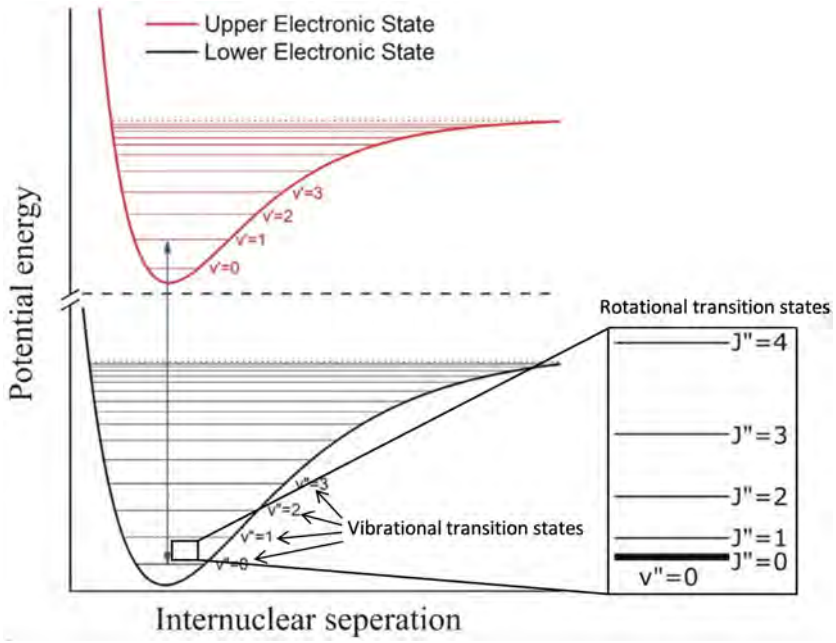

FIGURE 1.5 Schematic diagram of the electronic, vibrational, and rotational energy levels for a diatomic molecule plotted against the internuclear separation. Figure adapted from Harilal et al. (2018).

Rotational spectroscopy is a well-known technique used in radio astronomy to study the chemistry in the ISM. In fact, the vast majority (∼90%) of the molecules detected in the ISM were found using rotational spectroscopy (McGuire, 2022). The rotation energy levels of a molecule are highly dependent on its configuration and can become quite complex for larger molecules. In the simplest case of a linear molecule, the rotational energy levels can be expressed as:

$$E^{rotation} = \frac{h^2}{8\pi^2 I} J(J+1) \tag{1.4}$$

where h is the Planck constant, $J = 0, 1, 2, \ldots$ is the rotational quantum number, and I is the moment of inertia of the molecule. Using this energy, the excitation temperatures, T_{ex} of a molecule can be derived as:

$$T_{ex} = \frac{E^{rotation}}{k} \tag{1.5}$$

where k is the Boltzmann constant.

As mentioned before, the main component of the ISM is the H_2 molecule. However, since H_2 is a homonuclear molecule, it lacks a permanent electric dipole moment. Hence, the transition J=1–0 is forbidden in H_2 and J=2–0 is the ground transition instead. For this transition, $T_{ex} \approx 510$ K, which is why H_2 is not observed toward the star-forming regions where temperatures are mostly below 100 K. Therefore, we have to rely on other molecules. Fortunately, most molecules, including CO, the second most abundant molecule in the ISM, have low T_{ex} values, making them easier to detect. Table 1.1 provides the T_{ex} values for selected transitions of some of the common molecules detected toward the star-formation region.

TABLE 1.1 Summary of a few molecules that are generally observed towards protostellar systems. Adapted from Stahler & Palla (2004).

Molecule	Transition	Wavelength (mm)	T_{ex} † (K)
CO	J=1–0	2.6	5.5
CO	J=2–1	1.3	11.1
CS	J=1–0	3.1	4.7
H_2CO	$J=2_{1,2}$–$1_{1,1}$	2.1	6.8
HCO^+	J=1–0	3.1	4.3
HCO^+	J=3–2	1.1	12.8
N_2H^+	J=1–0	3.2	4.5

† $T_{ex} = E_U - E_L$

1.4.2 *Chemistry of Star-Forming Regions*

Now that the fundamentals of molecular spectroscopy have been covered, we shift the discussion to briefly explain the chemistry that gives rise to the molecular complexity observed in star-forming regions. The observation of the various molecules in the molecular clouds, although exciting, was initially puzzling. Heavier elements other than hydrogen and helium get introduced into the ISM as the gas and dust ejected from supernova explosions and other mass-loss processes, such as stellar winds of smaller stars towards the end of their life cycle. Aside from a small amount of dust particles and inert molecules such as polycyclic aromatic hydrocarbons (PAHs), most molecules are quickly (within ≈100 yr) dissociated into their atoms due to the strong UV radiation field present (Van Dishoeck et al., 1988; Herbst, 2001). Once material slowly gathers to form clouds of densities $\gtrsim 10^2$ cm^{-3}, the interior of the clouds becomes shielded from external UV radiation. This shielding allows the molecules to be synthesized in the cloud without them getting instantly destroyed by radiation.

However, the chemistry behind the formation of molecules in these clouds is quite different from the chemistry that takes place on Earth. Contrary to what their name suggests, dense clouds are much more rarefied compared to terrestrial atmospheres. So even in dense cores with densities ∼10^4 cm^{-3}, the probability of a three-body collision occurring is ≈10^{-20} (Yamamoto, 2017). Additionally, the temperatures in these dense cores are fairly low ≈10 – 20 K, so even when collisions between two particles do occur, any reactions that are endothermic or have an activation barrier do not occur. Eventually, it was found that in the cold cloud phase before the collapse starts, the chemistry is dominated by gas phase ion-molecule reactions (e.g., Herbst & Klemperer, 1973; Watson, 1974; Woods et al., 1975) and some neutral-neutral reactions (e.g., Herbst et al., 1994). Once the cloud begins to collapse, grain-surface chemistry also starts to become important.

Gas phase chemistry

The different types of gas phase reactions that can occur in the star-forming regions can be broadly divided into three categories: *bond formation, bond*

destruction, and *bond rearrangement*. The upper row of Figure 1.6 gives an overview of these reactions.

- **Bond formation:** The two major types of bond formation that can occur are radiative association and associative detachment. Radiative association reactions are those where two species collide to form an unstable molecule which emits a photon to form a stable molecule:

$$A + B \rightarrow AB + h\nu \tag{1.6}$$

  Although this type of collision is the most common, the chances of bond formation are extremely low for smaller molecules as the unstable molecule dissociates back to its initial reactants very quickly ($\tau_{diss} \sim 10^{-13}$ s; Öberg et al. 2021). Radiative association becomes more effective for larger molecules where the collision product can survive longer by distributing excess energy across the different vibrational modes of the molecules, increasing the probability of emission (Herbst, 2001; Yamamoto, 2017). For radiative association, one of the reactants is almost always hydrogen, either in atomic or molecular form, as it is the most common element for collisions to occur (Herbst & Klemperer, 1973).

  Associative detachment is a reaction where one of the reactants is an anion and the energy is carried away by an electron:

$$A^- + B \rightarrow AB + e^- \tag{1.7}$$

  These reactions are much faster than radiative association reactions but are rarer because anions produced in star-forming regions generally are quickly destroyed by photons (Millar et al., 2007).

- **Bond destruction:** Bond destruction usually occurs through photodissociation or dissociative recombination. Photodissociation is the process when a molecule absorbs UV radiation and disassociates into its components:

$$AB + h\nu \rightarrow A + B \tag{1.8}$$

  Since UV radiation is mostly absorbed by the outer layers of dense clouds, photodissociation typically only occurs at the edges of the molecular clouds or in environments with significant UV radiation, such as regions where high-mass star formation is taking place. These regions with increased UV radiation are known as photodissociation regions or photon-dominated regions (PDRs). However, even within dark clouds, some amount of photodissociation can occur in a process called cosmic ray-induced UV radiation (Prasad & Tarafdar, 1983; Gredel et al., 1989) in which cosmic rays generate a small amount of UV radiation through interaction with molecular hydrogen.

  Dissociative recombination is a reaction in which a molecular ion reacts with a free electron to produce two or more neutral species:

$$A^+ + e^- \rightarrow B + C \tag{1.9}$$

  Dissociative recombination is usually the last set of reactions that leads to the production of neutral molecules like CO, OH, H_2O, and

hydrocarbons from their ions (Herbst, 2001). Finally, bond destruction can also occur by collision of high-velocity particles in processes such as shocks.

- **Bond rearrangement:** Bond rearrangement mainly occurs through ion-molecule and neutral-neutral reactions in star-forming regions. As the name suggests, an ion-molecule reaction involves a reaction between an ion and a molecule:

$$A^+ + B \rightarrow C + D^+ \tag{1.10}$$

In the simplest case, where $A = C$ and $B = D$, the reaction simplifies to a charge exchange between the species. These ion-molecule reactions dominate the chemistry in the cold clouds prior to star formation. Molecular clouds are constantly bombarded by cosmic rays, which penetrate even the dense cores and ionize the material they encounter in their path. If the ion reaches sufficiently close to a neutral molecule, it can polarize the molecule and develop an electrostatic attraction towards it. Thus the ion and molecule collide, and the reaction proceeds. Together with dissociative recombination, the ion-molecule reaction is the major contributor to the formation of most simple molecules detected towards star-forming regions, including CO and H_2O (van Dishoeck & Black, 1986; Herbst, 2001).

Neutral-neutral reactions are exothermic reactions that occur between two neutral species and often have no or significantly low activation barrier:

$$A^+ + B \rightarrow C + D^+ \tag{1.11}$$

In cold regions of a molecular cloud, neutral-neutral reactions play an important role in the production of organic compounds such as methoxy (CH_3O), methyl formate ($HCOOCH_3$), dimethyl ether (CH_3OCH_3), and also cyanopolyynes[3] (Herbst et al., 1994; Balucani et al., 2015). Additionally, these reactions become more important in warmer regions, such as hot cores, where temperatures reach upwards of 100 K, aiding in the formation of larger molecules by overcoming the activation energy barriers.

[3] Cyanopolyynes are organic compounds with chemical formula HC_nN where $n = 3, 5, 7, \ldots$

Grain surface chemistry

The lower row of Figure 1.6 summarizes the different processes that occur on the grain surface. Although dust grains only account for ∼1% of the total mass of material present in the ISM, they play a vital role in the chemistry of star-forming regions. Primarily composed of nonvolatile silicates and carbonaceous compounds, including PAHs, dust grains generally have low temperatures (<30 K) in dense regions of dark clouds (Draine, 2003). At these low temperatures, the grains serve as energy sinks for the gas phase species, allowing for the adsorption and freeze-out of atoms and molecules onto their surfaces. Some of the species are weakly bound to the grain surfaces by van der Waals forces (physisorption), requiring less energy to be liberated back to the gas phase, while others are more strongly adsorbed

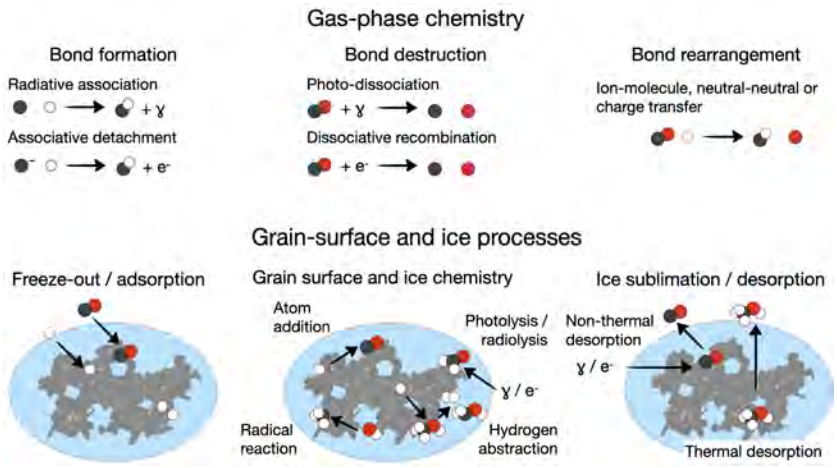

FIGURE 1.6 Illustration of the common types of gas phase (*top*) and the grain surface (*bottom*) reactions observed in the ISM. Credit: Öberg et al. (2021).

via chemical bonds (chemisorption) and require much greater energy for liberation (Shimonishi et al., 2018).

The surface of dust grains acts as a perfect catalyst for reactions to occur between the various species and leads to the production of several new species (Herbst & van Dishoeck, 2009). The atoms and molecules that get adsorbed onto the dust surfaces remain active and mobile enough for grain surface reactions to occur. These reactions proceed through one of three mechanisms: *Langmuir-Hinshelwood, Eley-Rideal,* or *Kasemo-Harris*.

- **Langmuir-Hinshelwood:** In this mechanism, both reactants are adsorbed onto the dust surface. Through quantum tunneling and/or thermal hopping, these reactants diffuse through the surface and eventually meet and react (Langmuir, 1922; Hinshelwood, 1940). This mechanism is also known as the *diffusive mechanism*.

- **Eley-Rideal:** In this mechanism, one of the reactants is adsorbed onto the dust grain while the other is still in the gas phase. The gas-phase reactant directly collides and reacts with the other reactant (Eley & Rideal, 1940). This mechanism is also known as the *direct mechanism*.

- **Kasemo-Harris:** In this mechanism, the adsorbed species retains enough of its initial kinetic energy to be able to move around the surface. The reaction then occurs when it finds another species that was previously adsorbed (Harris & Kasemo, 1981). This mechanism is also known as the *hot atom mechanism*.

One of the most important molecules that is produced through grain surface reaction is H_2. It has long been understood that in addition to gas-phase reactions, grain surface reactions are also needed to explain the observed abundance of H_2 in the ISM (Gould & Salpeter, 1963; Hollenbach & Salpeter, 1971; Wakelam et al., 2017). The formation of H_2 begins with the H atom getting adsorbed onto a grain surface. Due to high surface mobility, the H atom moves around the grain surface until it is desorbed from the grain surface or it finds another species to react with. Since hydrogen is the most common element in the dark clouds, it has the highest probability

to encounter another H atom and react to form a H_2 molecule by one of the three mechanisms discussed above. Once H_2 forms on the surface, it then quickly desorbs into the gas phase even at low temperatures of 10 K (Hollenbach & Salpeter, 1971):

$$H(g) \rightarrow H(s) \tag{1.12}$$

$$H(s) + H(s) \rightarrow H_2(s) \tag{1.13}$$

$$H_2(s) \rightarrow H_2(g) \tag{1.14}$$

Additionally, the formation of H_2O and organic molecules like H_2CO and CH_3OH which are the precursors of COMs, also proceeds through grain surface reactions. All these molecules are formed by successive hydrogenation reactions. H_2O is created by successive hydrogenation with an adsorbed O atom:

$$O \xrightarrow{+H} OH \xrightarrow{+H} H_2O \tag{1.15}$$

Likewise, H_2CO and CH_3OH are created by successive hydrogenation of CO molecules, which are produced in the gas phase and get desorbed onto dust grains when temperatures are <20 K:

$$CO \xrightarrow{+H} HCO \xrightarrow{+H} H_2CO \xrightarrow{+H} CH_3O \xrightarrow{+H} CH_3OH \tag{1.16}$$

The species adsorbed onto the grain surface stay frozen out until they receive enough energy to overcome the adsorption forces and desorb back into the gas phase. Desorption can proceed through thermal or non-thermal processes. Thermal desorption (also known as sublimation) occurs when the overall temperature of the dust grains increases and provides sufficient thermal energy to the frozen molecules to separate from the grain surface. Sublimation becomes particularly important in the inner envelope and disk regions where temperatures of dust grains are higher due to various processes such as accretion heating, viscous heating in disks, and heating from protostars, which influence the snowlines of the different molecules (e.g., van't Hoff et al., 2020; Takakuwa et al., 2024).

Alternatively, non-thermal desorption occurs through the injection of localized energies that do not uniformly raise the temperature of the grain but provide enough energy for molecules to desorb. This local heating can occur through excess energy generated during chemical reactions, cosmic-ray bombardment, or high-energy collisions with neutral molecules. Among the different types of non-thermal processes, desorption via collisions with neutral molecules is considered to be the most important one in star-forming regions and is also called sputtering. Sputtering is particularly important in shocked regions of protostellar systems (e.g., Jørgensen et al., 2004; Kristensen et al., 2010).

1.5 THIS THESIS

Despite the progress made in both our understanding of star formation and astrochemistry, there are still big unknowns that are still unanswered. Some of these big questions that are currently being explored in this field are *How and when do disks and planets form in protostellar systems? To what extent is*

material inherited from earlier stages to protoplanetary disks? Another crucial challenge is to establish the relationship between the physical evolution of protostars and astrochemistry.

These unknowns can be tackled either theoretically or observationally. This thesis uses observational methods to study the various physical and chemical aspects of the youngest sources and boost our understanding of the big questions. The observations used in this thesis were conducted using both radio interferometers and infrared observations. The next chapter goes into more detail about the various methods used to collect, process, and analyze the data.

2

Methods

"The most remarkable discovery in all of astronomy is that the stars are made of atoms of the same kind as those on the earth."
—Richard P. Feynman

The previous chapter established the theoretical framework for understanding protostellar evolution and also outlined the principles of astrochemistry as it relates to star formation. These advances have only been possible by assembling the results of decades of observational and theoretical research. This chapter is dedicated to discussing the various methods used to study protostellar systems in detail.

Section 2.1 describes the various observational techniques that are generally used to observe protostars. An emphasis is given to describing the principles of interferometric techniques and observations since the majority of the data utilized in this thesis were obtained using interferometers. Section 2.2 provides a primer on the data reduction tools and analysis techniques used in processing the observational data. It is important to note that while this section covers the core techniques relevant to this thesis, it is by no means exhaustive. Depending on the scientific goals and the observational data available, various other tools and techniques are available and are often used to observe and analyze astronomical data.

2.1 OBSERVATIONAL TECHNIQUES

2.1.1 *Dawn of Radio and Infrared Astronomy*

The light emitted by celestial objects forms the basis for all astronomical studies. Astronomers are able to extract valuable information about these distant objects by carefully observing and analyzing the light coming from them. For much of human history, observation of celestial bodies was restricted to optical telescopes that operate at visible wavelengths. Following the publication of Maxwell's equations in the 19^{th} century (Maxwell, 1865), it became clear that visible light is only a small fraction of the electromagnetic radiation and stars can be observed in a wide range of wavelengths. However, observing at wavelengths beyond the visible spectrum posed additional challenges as the atmosphere absorbs and blocks a significant portion of the radiation (see Figure 2.1). Although this atmospheric absorption is valuable for life to survive as it blocks harmful radiation from reaching the Earth's surface, it acts as a deterrent for astronomical observations.

Methods to overcome the challenge of atmospheric opacity were discovered in the 20^{th} century. In 1931, Karl G. Jansky observed radio emissions coming from outside the solar system at a wavelength of $\sim$15 m (Jansky,

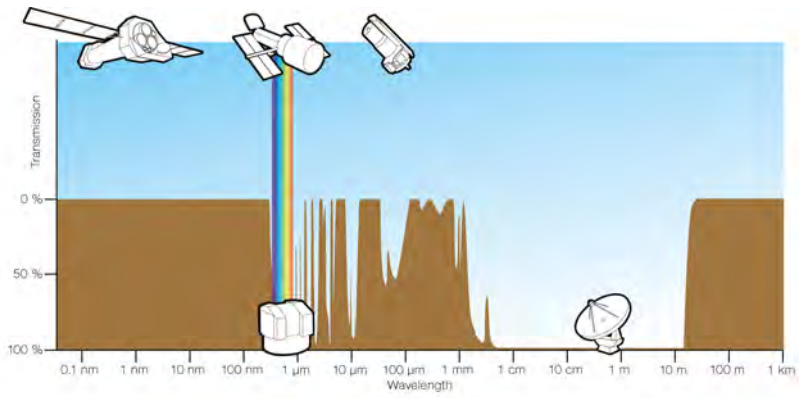

FIGURE 2.1 Illustration depicting the transparency of the Earth's atmosphere at various wavelengths of electromagnetic radiation. Except for the optical, radio, and a few regions at infrared wavelengths, the atmosphere is mostly opaque to radiation at other wavelengths. Credit: ESA/Hubble/F. Granato.

1933). This observation showed that the Earth's atmosphere is transparent to emission at radio wavelengths (Figure 2.1), and quickly established radio telescopes as a powerful new technique to observe distant objects. Likewise, the first airborne and space-based infrared telescopes were also launched in the same century (e.g., *Infrared Astronomical Satellite* (IRAS); Neugebauer et al. 1984, *Infrared Space Observatory* (ISO); Kessler et al. 1996). By placing these telescopes above much of the atmosphere of the Earth, astronomers were able to circumvent the limitations presented by the atmospheric window and observe in a wider range of wavelengths.

As mentioned in Section 1.1, the inner regions of GMCs–where star formation takes place–are veiled in a thick layer of gas and dust, making them only observable at infrared and radio wavelengths. The advent of radio and infrared telescopes was thus crucial in observing these regions, essentially starting the studies of star and planet formation as a new branch of astronomy. During the several decades following their inception, advancement in technology and instrumentation has resulted in significant new improvements in sensitivity, bandwidth, and spatial resolution of new facilities. The research on star formation has consequently also benefited from these advancements. For example, space-based infrared telescopes like *Spitzer* (Werner et al., 2004) and *Herschel* (Pilbratt et al., 2010), have been used to catalog and analyze all protostars that are observable within the nearest 500 pc (see Dunham et al., 2014, and references therein). Likewise, modern radio telescopes have been used to observe dust and gas emissions toward protostars, which help to determine important parameters such as its disk and envelope mass (e.g., Jørgensen et al., 2009; Tobin et al., 2015; Andersen et al., 2019), chemical composition (e.g., Tychoniec et al., 2021; Yang et al., 2021), and magnetic fields and turbulence (e.g., Hull et al., 2017; Maury et al., 2018; Huang et al., 2024).

Both infrared and (sub)millimeter wavelength observations are useful in probing distinct conditions and components within star-forming regions. Near to mid-infrared regimes (up to ∼30 μm) are accessible with telescopes like *Spitzer* and *James Webb Space Telescope* (JWST), and trace warm dust, hot gas-phase (rovibrational[1]) transitions, and solid-state features (ices).

[1]A transition in which both the rotational and vibrational energy level changes

Most of the protostars in nearby star-forming regions were identified using such space-based near to mid-infrared telescopes (e.g., Lada & Wilking, 1984; Evans et al., 2009). More recently, the JWST has been employed to investigate molecular ice contents of protostars (e.g., Beuther et al., 2023) and study candidate protoplanets (e.g., Wagner et al., 2024). On the other hand, (sub)millimeter wavelength observations ($\gtrsim$300 μm) trace rotational transitions of molecules at lower temperatures as well as the cold dust regions. Bridging the gap between these two regimes are far-infrared observations with telescopes like *Herschel* that are able to capture the peak of the emission from protostars at wavelengths of $\sim$100 – 200 μm. Together, these observations are highly complementary and provide valuable information about different aspects of the star-formation process.

The different types of radio wavelength observational facilities available for the study of protostellar systems can be broadly divided into two categories: *single-dish telescopes* and *interferometers*. Both techniques have their own merits and play crucial roles in forming a comprehensive picture of star formation and evolution. This thesis also utilizes observational data collected using an infrared telescope and a radio wavelength interferometer.

2.1.2 *Single-dish observations*

FIGURE 2.2 Examples of single-dish radio telescopes. IRAM 30 m telescope located at the Sierra Nevada Mountains in Spain (*left*; Credit: IRAM) and the APEX 12 m telescope located at the Chajnantor plateau in Chile (*right*; Credit: K.Zacher, ESO.).

As suggested by its name, single-dish observations are carried out by telescopes that use only one antenna. Despite the increasing popularity of radio interferometers, single-dish radio telescopes such as the 15 m *James Clerk Maxwell Telescope* (JCMT), the 12 m *Atacama Pathfinder EXperiment* (APEX), and the 30 m *Institut de Radioastronomie Millimétrique* (IRAM) telescope are still relevant and commonly used. Figure 2.2 displays the IRAM telescope and the APEX telescope as examples of single-dish radio telescopes still currently in use.

Single-dish telescopes have been invaluable in the studies of protostellar systems. More than half of the molecules detected towards the ISM and protostellar regions were found using single-dish radio telescopes (McGuire, 2022). Although single-dish radio telescopes lack the spatial resolution of interferometers, they are quite sensitive to the more extended structures. As such, they are frequently used to observe the large-scale structures of the star-forming regions (e.g., Carlhoff et al., 2013; Stutz et al., 2013). Furthermore, they can more accurately determine the total flux coming from

a region as they do not suffer from the "missing flux problem" (Kwon et al., 2009).

2.1.3 *Interferometric observations*

The maximum angular resolution achievable by an antenna is given by the Rayleigh criterion:

$$\theta_{max} \approx 1.22\frac{\lambda}{D} \tag{2.1}$$

where λ is the wavelength of observation and D is the diameter of the antenna (Rayleigh, 1879). This criterion shows that in order to observe an object at a higher resolution, either the observation must be conducted at shorter wavelengths or the diameter of the telescope must be increased. Since protostellar systems are only observable in the infrared and radio wavelengths, going to lower wavelengths is not an option. The only choice remaining to astronomers is to increase the diameter of the telescopes. The largest fully steerable single-dish telescope is the Green Bank Telescope (GBT), which has a diameter of 100 m and can observe at a wavelength of 2.6 mm. Building any larger is extremely challenging and impractical. Using Equation 2.1, the maximum angular resolution achievable by the GBT is $\sim 6\farcs5$. When observing a nearby protostellar system at 150 pc, this translates to an angular resolution of $\sim$1000 AU. Hence, while this resolution is desirable to observe the large-scale cold clouds, it is insufficient to observe the inner envelope and disk regions of protostars.

This angular resolution limitation experienced by a single-dish telescope can be rectified by using interferometry. Figure 2.3 displays an illustration of how interferometry works in a playful way. In practice, interferometry is a technique that combines the signals from an array of telescopes together using interference, allowing them to operate as a single, larger telescope. In an interferometer, Equation 2.1 gets modified to:

$$\theta_{max} \approx 1.22\frac{\lambda}{B_{max}} \tag{2.2}$$

where the denominator changes from the diameter of the individual antenna to the largest distance between the antennas of an array, B_{max}. The distances between the antennas of an interferometer are also called *baselines*. By placing antennas over a large distance apart, interferometers can achieve a much higher angular resolution, which allows astronomers to observe significantly smaller structures. Therefore, interferometers are extremely useful and frequently used to observe the inner regions of protostellar systems. Although interferometers are also used in infrared and optical wavelengths (e.g., the Cambridge Optical Aperture Synthesis Telescope (COAST) and the Very Large Telescope Interferometer (VLTI)), they are most commonly used in radio wavelengths. The terms interferometer and radio interferometer can be used interchangeably in this thesis. The characteristics and features of this interferometer are described below.

Two-element interferometer

The basics of interferometry can be explained with the simplest case of an interferometer consisting of only two antennas. Figure 2.4 shows an

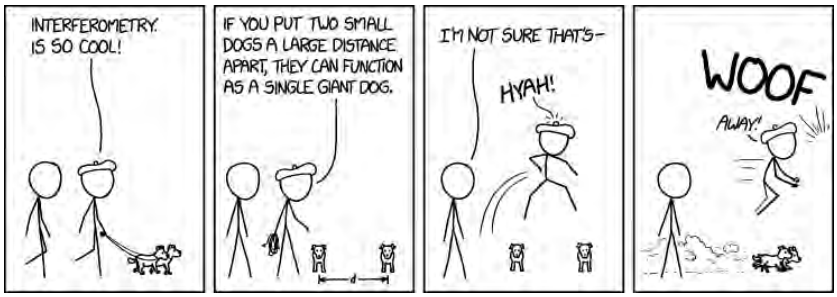

FIGURE 2.3 A comic panel explaining the basics of interferometry. Credit: XKCD Comics.

illustration of such an interferometer made up of only antennas A_1 and A_2 separated by the distance $\vec{B}$. Both antennas are observing the same object in the sky in the direction of the unit vector $\vec{s}$. The radiation coming from the object arrives as a plane wave reaching A_1 first and then A_2 after a small time delay given by:

$$\tau = \frac{\vec{B} \cdot \vec{s}}{c} \tag{2.3}$$

where c is the speed of light. This electromagnetic radiation of amplitude E induces a voltage in each antenna receiver:

$$U_1 \propto E e^{i\omega t} \tag{2.4}$$

$$U_2 \propto E e^{i\omega(t-\tau)} \tag{2.5}$$

The voltage signals received from each antenna are multiplied and then averaged in the correlator to obtain a quantity called the correlator response:

$$R(\tau) \propto \frac{1}{2} E^2 e^{i\omega\tau} \tag{2.6}$$

This correlator response is a function of τ, which itself varies over time as the rotation of the Earth constantly changes the direction of $\vec{s}$. Consequently, the response measures the change in the interference patterns as a function of time. According to the van Cittert-Zernike theorem, the antenna response can be converted into a function of the brightness distribution of the source, I, and the effective collecting area of the telescope, A (van Cittert, 1934; Zernike, 1938). Redefining the coordinate system, this expression changes as:

$$V(u,v) = \int_{-\infty}^{\infty}\int_{-\infty}^{\infty} A(x,y) I(x,y) e^{i2\pi(ux+vy)} \mathrm{d}x\mathrm{d}y \tag{2.7}$$

Here, $V(u,v)$ is the visibility function on the u,v plane, where u describes the baselines in one direction and v describes the baselines in a perpendicular direction to u. $V(u,v)$ is a complex quantity with an amplitude and a phase that holds a specific piece of information on the brightness of the measured source in the x,y plane. The shorter baselines that are closer to the origin in the u,v plane correspond to the larger-scale structure on the spatial scale of the source brightness and vice versa. Looking at the expression in Equation 2.7, it is clear that $V(u,v)$ is simply the Fourier transform of the term $A(x,y)I(x,y)$. By applying the inverse Fourier transformation, the

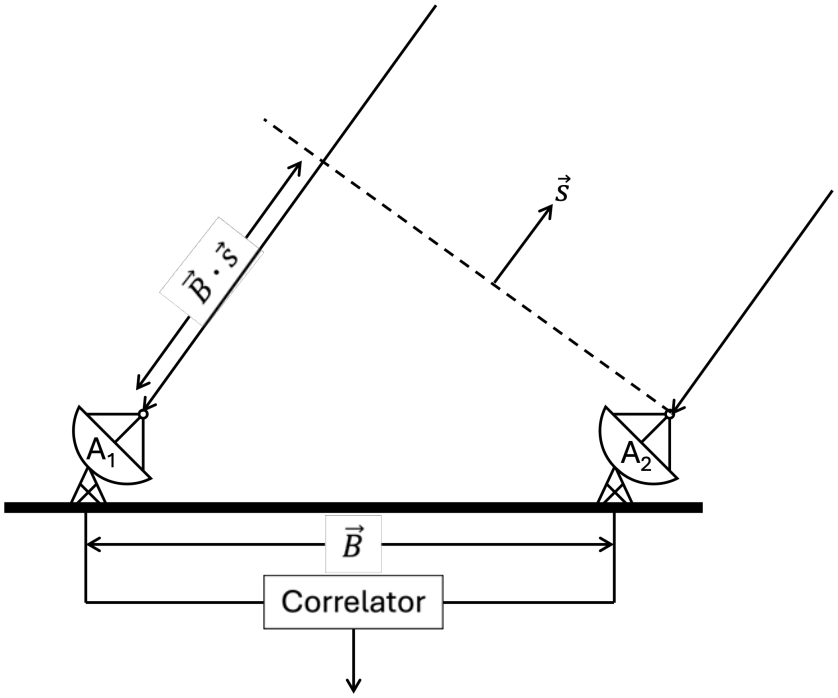

FIGURE 2.4 Schematic diagram of a two-element interferometer separated by the baseline $\vec{B}$. Both antennas are observing the same region of the sky and due to the longer path antenna A_1 experiences a geometric time delay in the signal observed.

image produced gives a modified version of the brightness distribution:

$$I'(x,y) = A(x,y)I(x,y) = \int_{-\infty}^{\infty}\int_{-\infty}^{\infty} V(u,v)e^{-i2\pi(ux+vy)}\mathrm{d}u\mathrm{d}v \tag{2.8}$$

To recover the entirety of the source brightness using Equation 2.8, the u,v plane must be completely filled. If only short-baseline data are present, only large-scale structures are recovered, and finer details are lost. Likewise, if only long-baseline data are present, then only small-scale structures are recovered. This is shown in Figure 2.5. In practice, the u,v plane is not a continuous field but a set of discrete points that correspond to individual baselines. The more number of points on the u,v field, the better the coverage on the u,v field and the better the source brightness image. For N antennas, N(N-1) baselines are present. As the Earth rotates, the position of the baseline changes, filling up more points on the u,v field. Hence, longer observation times allow for more comprehensive coverage in the u,v plane, ensuring a better image is recovered.

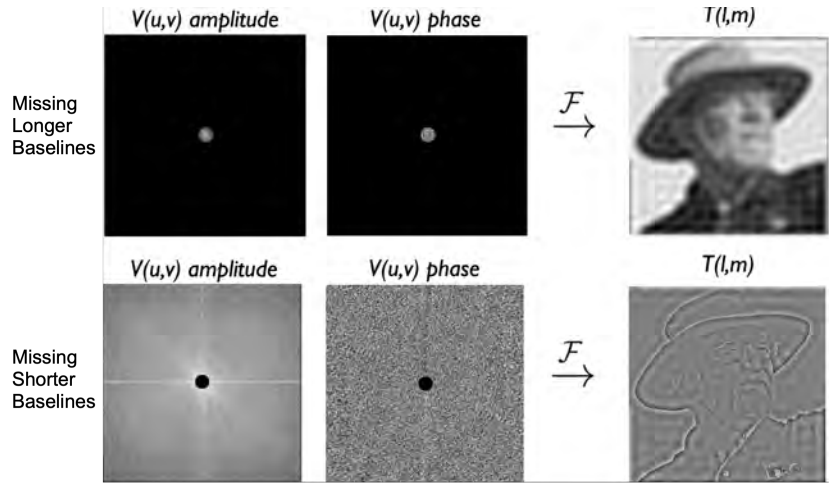

FIGURE 2.5 Illustration showing the impact of missing baselines on the final image. When only shorter baseline data are available, the image retains large-scale features but loses the finer details on the final image. On the other hand, if only longer baselines are present, then the final image loses the large-scale features. Credit: David J Wilner, 14^{th} Synthesis and Imaging Workshop.

2.2 WORKING WITH INTERFEROMETRIC DATA

Real-world interferometers are much more complex than the simplified two-element interferometer described above. Actual interferometers are typically comprised of several antennas and have multiple baselines. Additionally, the u, v coverage of the visibilities are often only partially sampled as the observations are generally conducted in discrete intervals, typically spanning over a few tens of seconds. This process is then repeated multiple times until the desired sensitivity is reached or the u, v coverage is satisfactory according to the science goals. Due to the discrete nature of the observations, the image of the source brightness is instead obtained through discrete Fourier transform (DFT) of the visibilities.

The DFT of the u, v plane gives a point spread function (PSF) commonly referred to as the *dirty beam*, $B_D(x, y)$. This dirty beam essentially displays the response of the interferometer to a point source due to the incomplete u, v coverage and is characterized by a central peak and additional smaller peaks called sidelobes as a result of the gaps in the u, v sample. The dirty beam is convolved to the theoretical true image to give the dirty image, $I_D(x, y)$:

$$I_D(x, y) = B_D(x, y) \otimes I(x, y) \tag{2.9}$$

Where $\otimes$ denotes the convolution function. This dirty image is equivalent to the raw image generated by performing discrete inverse Fourier transformation of the obtained visibilities. Figure 2.6 shows the relationship between the u, v sampling, the dirty beam, and the dirty image. As seen in the dirty image of Figure 2.6, the sidelobes of the dirty beam can appear as artificial structures around the true source. Additionally, the dirty beam can also distort any extended structure that might be present. To remove the effects of the dirty beam and to prevent these sidelobes from leading to false results, the dirty image must undergo further processing. Furthermore, the visibilities also contain contamination due to atmospheric and instrumen-

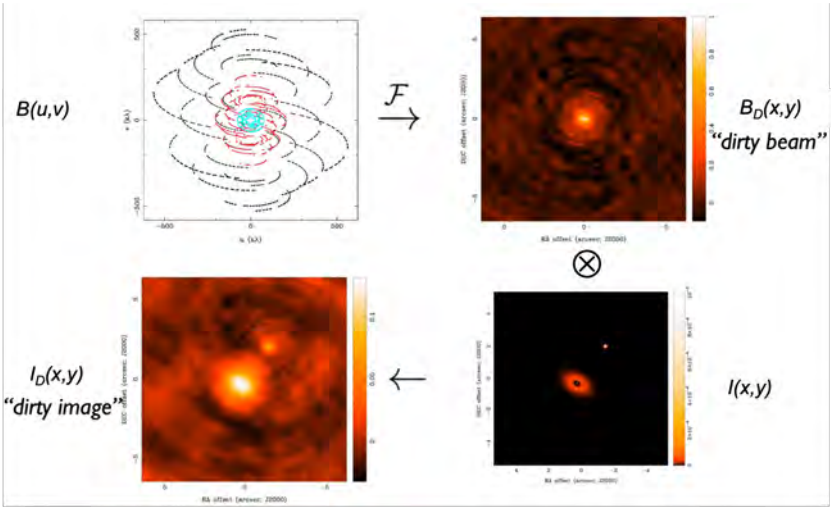

FIGURE 2.6 An example of how the dirty beam and the dirty image are generated. The Fourier transform of the u, v grid gives the dirty beam. This dirty beam is then convolved with the true sky brightness of the image producing a dirty image. Credit: D. J. Wilner, 14^{th} Synthesis and Imaging Workshop.

tal effects. These contaminations must be removed from the visibilities to ensure accurate results.

2.2.1 *Calibration and imaging*

The primary goal of calibration in interferometry is to identify and correct the various atmospheric and instrumental contaminations in the observed visibility data. Likewise, calibration also aligns the phases and amplitudes of the different antenna responses, ensuring that the collected data from all antennas are consistent and representative of the observed target. Calibration of the observed data is performed using calibrators, which are bright, compact astronomical sources whose positions and fluxes are well known. In radio interferometry, such calibrators are usually planets, moons, or quasars. In a typical observation, at least two different sources are used as primary and secondary calibrators. These calibrators are observed during the same observing run as the target source. Generally, the primary calibrator is observed at the beginning and at the end of the observation, while the secondary calibrator is observed in fixed intervals between the observation of the target source. This approach allows for different calibration steps:

- **Bandpass calibration:** The bandpass calibration corrects the changes in the signal of an antenna as a function of frequency. Such changes can be caused by delays in the instruments, such as amplifiers and filters, delays due to slight differences in cable length leading to a small phase delay, or atmospheric variations changing the signal response. Typically, a bright source with high signal-to-noise (SNR) and relatively line-free spectra like a quasar is chosen for bandpass calibration. The calibrator is observed across the full frequency range of the bandpass, and its observed response is compared with its documented response. Any variations found are corrected, and the same corrections are also applied to the target source observations.

- **Gain calibration:** The gain of an antenna is a complex mathematical function consisting of both phase and amplitude components that represents the antenna response to the incoming signals. Gain calibration thus involves identifying and correcting for any temporal variations in both phase and amplitude of the observations. These variations can be caused by both instrumental effects, such as errors in antenna positioning and pointing, or atmospheric effects, such as variations in the water vapor levels in the atmosphere during observation. Ideally, gain calibrators are bright sources such as quasars that are close to the target source so that any errors caused by local atmospheric conditions are reflected on the calibrator observations as well.

- **Flux calibration:** The signals measured by the antennas are measured in terms of the antenna temperatures, typically measured in Kelvin (K). The process of converting these antenna temperatures into absolute flux scales, usually measured in Jansky (Jy), is known as flux calibration. Flux calibrators are typically unresolved sources with well-measured and stable flux densities, such as planets or moons. Quasars are also used occasionally, and sometimes the same source can double as both flux and bandpass calibrators. By comparing the antenna response to the known flux density of the calibrator, a scaling factor is determined to convert the temperature units to absolute flux units. This scaling factor is then applied to the temperature response to obtain the flux densities of the target source.

- **Self-calibration :** In addition to using external calibrators, the observed target itself can also be used as a reference to improve the amplitude and phase calibration solutions. This is an iterative process that consists of several steps. First, an initial model of the observed visibility is created after standard calibration steps (bandpass, gain, and flux calibrations). This model is then used to perform adjustments in the complex gains of each antenna response. Then a new model is generated, and the process is repeated until the SNR of the observations stops improving. Self-calibration is a powerful process as it can correct for fast and tiny changes in the instrument response and atmosphere that are missed by gain calibration and also help reduce artifacts from the final image.

Once the observed visibilities are properly calibrated, they are now ready to be imaged. At this stage, it is common to apply a weighing parameter, $g(u,v)$, to each of the visibility measurements. Since the u,v grid is only partially filled, $g(u,v)$ determines how each visibility measurement is weighted during the final reconstruction of the image. Selecting an appropriate weighing parameter is crucial, as this influences the sensitivity, noise levels, and resolution of the final image by creating a balance between the visibilities obtained from longer and shorter baselines. There is no single universally "correct" choice for $g(u,v)$ and its chosen value depends on the scientific objectives. However, *natural, uniform,* and *Briggs* are some of the few weighing schemes that are most widely used.

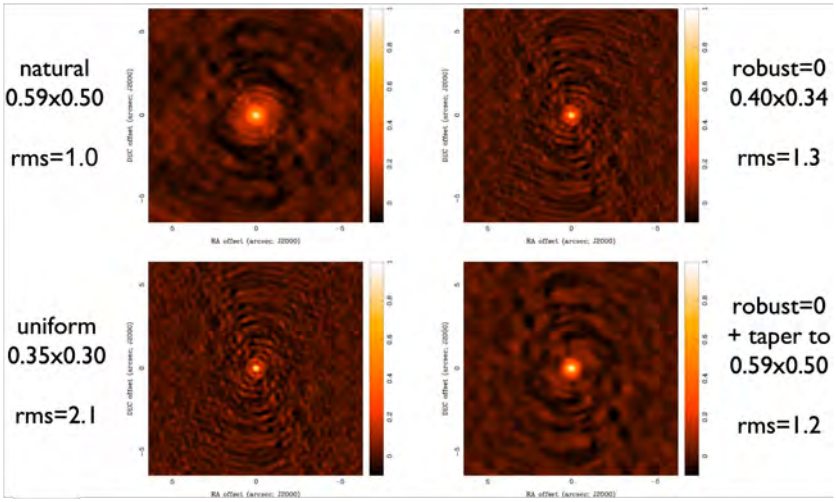

FIGURE 2.7 Plots illustrating how the dirty beam and the rms noise level change with the use of the different weighting schemes. Credit: David J Wilner, 14^{th} Synthesis Imaging Workshop.

In natural weighting, each visibility point is given the same weight. This effectively gives more weight to the densely populated area in the u, v plane. Since more short baselines are present than long baselines, images created with this approach will be more sensitive to large-scale structures. Natural weighting provides the highest SNR of the image at the cost of angular resolution. Uniform weighting is essentially the opposite of natural weighting. Here, each u, v grid is given the same weight, thus giving more weight to the less populated regions (i.e., longer baselines) and less weight to densely populated cells (i.e. shorter baselines). Images produced with uniform weighting will be more sensitive to small-scale structures but will also have a higher noise level. A flexible approach was proposed as a compromise between the natural and uniform weighting called the Briggs weighting (Briggs, 1995). This approach, also known as *robust weighting*, uses a parameter called the robust value between –2 and +2 to weigh the visibilities. Robust value of –2 approaches uniform weighting, and +2 approaches natural weighting, with robust value of 0 providing a balance between sensitivity and resolution.

The above weighting schemes can also be supplemented by applying an additional Gaussian tapering to weight down the longer baselines. This increases sensitivity to larger structures and also helps reduce noise by suppressing small-scale artifacts but leads to the loss of angular resolution. Figure 2.7 displays an example of how the dirty beam of an observation changes with the different weighing schemes. Including $g(u, v)$ with the visibility gives us the relationship of the dirty image, I_D to the visibility:

$$I_D(x, y) = \sum_k g(u_k, v_k) V(u_k, v_k) e^{-i2\pi(u_k x + v_k y)} \tag{2.10}$$

As shown in Equation 2.9, this dirty image represents the true brightness distribution convoluted to the dirty beam. The process of creating the final source brightness image by separating the effects of the dirty beam from the dirty image is known as deconvolution. Although there are several deconvolution techniques available, the most commonly used technique is

the CLEAN algorithm (Högbom, 1974), which has also been adopted for the observations used in this thesis. CLEAN is an iterative algorithm and works under the assumption the source brightness can be approximated by a series of point sources. The general steps followed by the algorithm are described below and illustrated in Figure 2.8.

1. Initialize a new empty CLEAN component map.
2. Identify the peak emission in the dirty image.
3. Subtract a factor of the dirty beam shape from the position of the peak emission identified in step 2. The dirty image left after the subtraction is called the residual image.
4. Add this subtracted point source to the CLEAN component map.
5. Repeat steps 2, 3, and 4 until the peak emission in the residual map reaches below a certain threshold.
6. Estimate the main lobe of the dirty beam by a 2D Gaussian function known as the CLEAN beam. Convolve the CLEAN beam with the CLEAN component map.
7. Add the remaining residual map to the new convolved map, finally creating the CLEAN image.

This final CLEAN in an image has information about the source brightness and is mostly free of artifacts from the dirty beam. This is the image used for further analysis. The CLEAN algorithm works best with bright, compact sources and is perfect for the deconvolution of protostellar sources. For extended or low-brightness sources, modified versions of the CLEAN algorithm or other deconvolution methods are used (see Multi-Scale CLEAN; Wakker & Schwarz (1988); Cornwell (2008) and Maximum Entropy Method; Wernecke & D'Addario (1977) for further details). The calibration and imaging of the ALMA observational data used in this thesis is performed using the Common Astronomy Software Applications (CASA) package McMullin et al. (2007).

2.2.2 *Moment Maps*

Each ALMA observation towards a source contains information about its dust continuum and any spectral lines present due to the various molecular gas emissions. Therefore, two types of CLEAN images are created after the calibration and imaging process: a 2D continuum map and a 3D spectral line cube. So in addition to the sky coordinates, the spectral line cube also contains a third frequency (or velocity) axis. This means that the 3D cube contains a spectra at each pixel of the map. With high-resolution imaging of ALMA containing a few hundred to thousands of pixels along each axis, inspecting and analyzing all of the spectra becomes impractical.

Moment maps provide a great alternative to quickly extract key information about the spectral lines observed and use it for analysis. It collapses the 3D cube in one axis to create a 2D image focusing on one key aspect, aiding

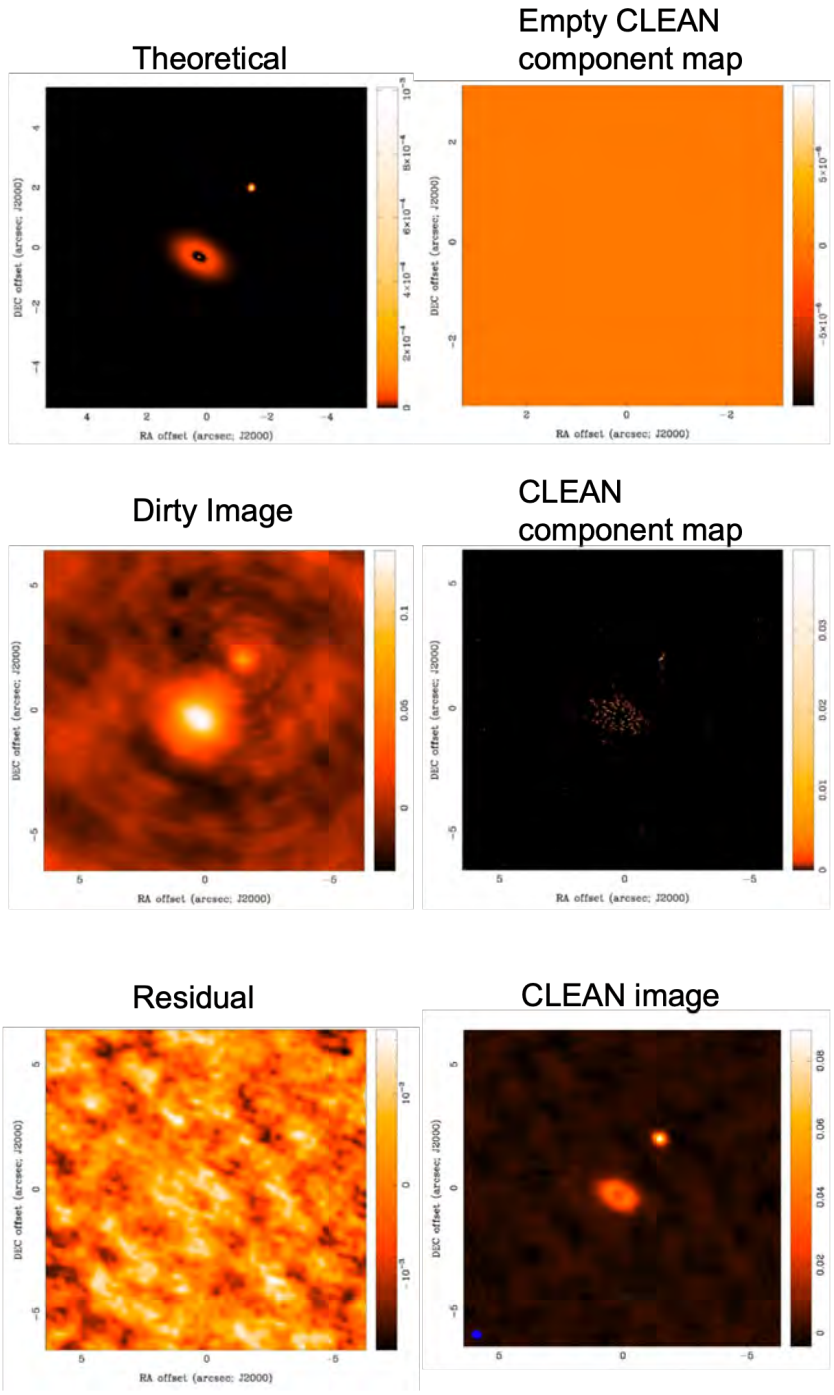

FIGURE 2.8 Figures displaying the various steps of creating a CLEAN image using the CLEAN algorithm. Credit: David J Wilner, 14^{th} Synthesis Imaging Workshop.

in the visualization of the spatial and kinematic structure of the molecular emission towards the source. Several moment maps are available and are numbered from –1 to 11. However, the most commonly used are moments 0, 1, 8, and 9. This thesis also makes use of these moment maps for most of the spectral line observation analysis presented in Chapters 4 and 5. Examples of each of moment maps 0, 1, 8, and 9 are given in Figure 2.9 and their features and uses are described below. All of these moment maps are generated using the `immoments` task in the CASA package.

- **Moment 0:** Moment 0 maps, also called integrated intensity maps, display the sum of all emissions in each pixel along the frequency axis. It roughly gives the relative amount of gas present at each pixel towards the observed source. These maps can be helpful to study the spatial extent and the concentration of the gas towards the observed region.

- **Moment 1:** Moment 1 maps, also called mean-velocity maps, display the intensity-weighted average velocity along the frequency axis observed at each pixel. This map essentially shows the bulk motion of the gas. By comparing the moment 1 map with the systemic velocity of the source, it can be determined if a section of the gas is moving towards us (indicated by blue-shifted emission) or away from us (indicated by red-shifted emission). Moment 1 maps can help in the study of the rotation in protostellar systems.

- **Moment 8:** Moment 8 maps display the maximum value of the spectrum at each pixel. These maps are useful in determining regions of strongest emission towards the source, which can help identify the various chemical processes leading to the strong emission. Typically, the regions that have higher moment 8 values are also the regions with concentrated moment 0 emission. However, there are exceptions to this, as can be seen in Figure 2.9.

- **Moment 9:** Moment 9 maps display the velocity of the maximum value of the spectrum at each pixel. These maps convey the kinematics of regions with the highest emissions, offering insights into the various physical and chemical processes in the region.

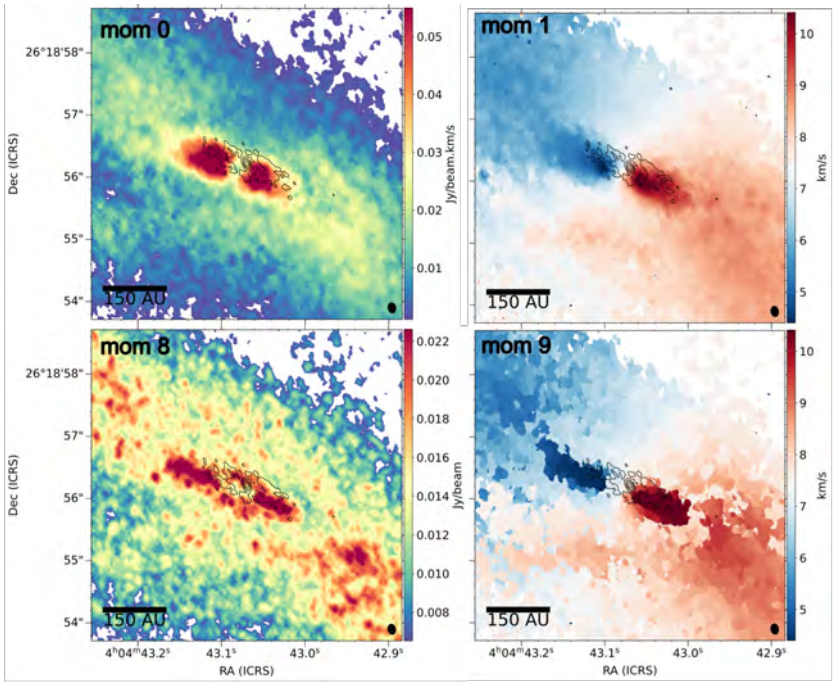

FIGURE 2.9 An example of the different moment maps for the molecular emission of $C^{18}O$ ($J = 2–1$) observed towards the protostellar source L1489IRS.

2.3 INSTRUMENTS USED IN THIS THESIS

In this section, I provide a brief introduction to the instruments that were used to collect the observational data used in this thesis. Modern telescopes now provide both pipeline-calibrated results as well as raw datasets, allowing researchers to work with preprocessed data or perform their own data reduction. For this thesis, I conducted the reduction of the raw datasets myself, as it is an important skillset to have as an observational astronomer.

2.3.1 *Infrared Telescope*

This thesis uses far-infrared observations carried out by the *Stratospheric Observatory For Infrared Astronomy* (SOFIA) to observe high–J CO rotation transitions in the far-infrared towards the highly energetic SVS13 system (Chapter 6). SOFIA was an airborne observatory that used a modified Boeing 747 to carry a 2.7 m reflecting infrared telescope. Figure 2.10 shows the SOFIA telescope in operation. It operated at an altitude of 39000–45000 ft (12 – 14 km), avoiding ∼99% of the water vapor in the Earth's atmosphere that blocks most infrared radiation. The data was collected using the Far Infrared Field-Imaging Line Spectrometer (FIFI-LS) instrument (Colditz et al., 2018; Fischer et al., 2018).

2.3.2 *Radio Interferometer*

The observational data used in Chapters 4 and 5 of this thesis were collected using the Atacama Large Millimeter/submillimeter Array (ALMA). ALMA is one of the largest and most powerful radio interferometers in the world. It is located on the Chajnantor plateau of the Chilean Andes at an altitude

FIGURE 2.10 The SOFIA telescope in flight with its telescope cavity open for observation. Credit: NASA/Jim Ross.

of 5000 m above sea level. The array is made up of a total of 66 high-precision antennas, 54 of which are 12 m antennas, and the remaining 12 of them are 7 m antennas. Fifty of the 12 m antennas can be arranged in different configurations, with baselines reaching up to 16 km to conduct high-resolution observations. The remaining four 12 m antennas and the twelve 7 m antennas are called the Atacama Compact Array (ACA). The antennas in the ACA are fixed and are dedicated to the observation of large-scale extended structures. ALMA has a total of 10 receiver bands and is able to observe at wavelengths of 0.35 mm to 8.6 mm, allowing it to achieve an extremely high angular resolution of up to $0\farcs0048$ with the 12 m array.

Since its Early Science Operations in September 2011, ALMA has been at the forefront of radio astronomy and has led to many important discoveries in different fields, including the field of star and planet formation. ALMA was the first instrument to provide observational confirmation of substructures in protoplanetary disks (ALMA Partnership et al., 2015), which are thought to result from ongoing planet formation. ALMA has also been able to detect a circumplanetary disk around a protoplanet still forming in the gap of a protostellar disk (Benisty et al., 2021). Likewise, with its improved sensitivity, ALMA has shown that even the youngest protostars are full of COMs (Jørgensen et al., 2016; Yang et al., 2021). It would not be wrong to say that ALMA has revolutionized our understanding of star and planet formation processes.

FIGURE 2.11 The various antennas of the Atacama Large Millimeter/submillimeter Array located on the Chajnantor plateau in the Chilean Andes. Credit: EFE/Ariel Marinkovic.

3

Research Context and Overview

"What is now proved was once only imagined."
—William Blake

The formation of stars and planets is a highly dynamic and complex process that requires both observational and computational techniques to study its mechanisms in detail. In recent decades, improvements in modern observing techniques, especially the dawn of ALMA, have led to several new important advancements. Substructures within protoplanetary disks, such as rings and gaps, are now routinely resolved (Andrews et al., 2018; Cieza et al., 2021), observational evidence of streamers and outbursts has become increasingly common (Pineda et al., 2023; Fischer et al., 2023), and direct detections of active planet formation in protoplanetary disks have started to appear (Benisty et al., 2021). Despite these incredible breakthroughs, many fundamental questions still remain unanswered, particularly towards the youngest, most embedded sources, where the physical and chemical processes are obscured within dense envelopes.

Some of the key questions that are still outstanding in the field, as touched upon in the previous chapters are:

- Are Keplerian disks common in the youngest protostellar sources?
- How and when do substructures begin to appear in protostellar disks?
- What are the various physical and chemical processes that govern the star-formation process during the embedded stages, and is it possible to constrain them?
- Can the molecular emissions observed towards the embedded sources be used as diagnostics of the various components at disk scales?

The work presented in this thesis aims to address these questions by using observational techniques to investigate the earliest embedded phases of star formation. The majority of the research presented in this thesis has been conducted in the context of the ALMA Large program *Early Planet Formation in Embedded Disk* (eDisk), with the results presented in Chapters 4 and 5 contributing directly to the findings of the eDisk program. The following section provides a short overview of the eDisk program and highlights the main results obtained from various studies within the project. For a more detailed description of the motivations, methods, and results of the eDisk program, see Ohashi et al. (2023) and references therein.

3.1 ALMA LARGE PROGRAM EARLY PLANET FORMATION IN EMBEDDED DISK (EDISK)

3.1.1 *Introduction, Motivation, and Ancillary Contributions*

The iconic observation of the HL Tau protostar, filled with multiple gaps and rings, showcased the capabilities of ALMA in studying the earliest stages of protostellar evolution (ALMA Partnership et al., 2015). Following this groundbreaking result, multiple programs have employed ALMA to conduct high-resolution and high-sensitivity observations of nearby protostellar systems, which has revealed that such substructures are ubiquitous in Class II disks (Andrews et al., 2018; Cieza et al., 2021). These substructures are often thought to be carved by embedded planets that are actively forming within the protoplanetary disks of these Class II sources (Dong et al., 2015; Zhang et al., 2018). These results suggest that planet formation likely begins earlier in the embedded phases of protostellar evolution. This is further backed by the fact that the mass reservoirs of Class II sources are generally insufficient to form giant planets (Tychoniec et al., 2020). These results raise an obvious question: *At what point do planets start forming in disks?*

The ALMA Large program eDisk attempts to answer this question by observing 19 embedded Class 0 and I protostars. The primary aim of eDisk is to search for signatures of Keplerian disks and potential substructures that are indicative of planet formation within these systems. The sources were chosen from nearby (< 200 pc) star-forming regions with relatively high luminosities ($L_{\rm bol} > 0.1 L_{\odot}$). The eDisk program is a global project that currently consists of over 40 scientists from 15 institutions in 6 different countries and is spearheaded by principal investigator Nagayoshi Ohashi and co-principal investigators Jes K. Jørgensen and John J. Tobin.

One of the major contributions I made to the initial overview paper was to construct new, updated SED plots for all eDisk sources. These SEDs are crucial to calculate the $T_{\rm bol}$ and $L_{\rm bol}$ values of sources. $T_{\rm bol}$ and $L_{\rm bol}$ values are fundamental properties of the sources and are essential for the classification of the sources and for the analysis of the results. The SEDs were created by compiling the latest photometric and spectral line data available in the infrared and submillimeter available for each target. The values of bolometric temperatures ($T_{\rm bol}$) and bolometric luminosities ($L_{\rm bol}$) for the eDisk sample were then derived by using these updated SEDs and the revised distances from the latest Gaia measurements (Zucker et al., 2020). The SEDs obtained for the eDisk program are shown in Figure 3.1 and the distances, $T_{\rm bol}$, and $L_{\rm bol}$ values are also reported in Table 3.1 along with some key results obtained from continuum observations of the sources.

TABLE 3.1 eDisk Sample Summary and Physical Parameters of Continuum Emission. Adapted from Table 1 and Table 3 of Ohashi et al. (2023).

Source name	ICRS R.A. (h m s)	ICRS Dec. (d m s)	Class	Distance (pc)	$T_{\rm bol}$ (K)	$L_{\rm bol}$ ($L_\odot$)	Peak I_ν, T_b (mJy beam^{-1}, K)	F_ν (mJy)	Inc. (deg)	References
(1)	(2)	(3)	(4)	(5)	(6)	(7)	(8)	(9)	(10)	(11)
L1489 IRS	04:04:43.080	+26:18:56.12	I	146	213	3.4	5.4, 21	91	71	(1)
IRAS 04166+2706	04:19:42.505	+27:13:35.83	0	156	61	0.4	9.6, 133	71	47	(2)
IRAS 04169+2702	04:19:58.477	+27:09:56.82	I	156	163	1.5	4.3, 64	101	44	(3)
IRAS 04302+2247	04:33:16.499	+22:53:20.23	I	160	88	0.43	1.1, 14	183	84	(4)
L1527 IRS	04:39:53.878	+26:03:09.43	0	140	41	1.3	4.3, 69	139	75	(5)
Ced 110 IRS4	11:06:46.369	–77:22:32.88	0	189	68	1.0	5.8, 79	80	75	(6)
BHR 71 IRS2	12:01:34.008	–65:08:48.08	0	176	39	1.1	8.7, 65	14	31	(7)
BHR 71 IRS1	12:01:36.476	–65:08:49.37	0	176	66	10	26, 170	384	39	(7)
IRAS 15398-3359	15:43:02.232	–34:09:06.96	0	155	50	1.4	5.9, 93	7.9	51	(8)
GSS 30 IRS3	16:26:21.715	–24:22:51.09	0	138	50	1.7	6.4, 56	124	72	(9)
Oph IRS 43	16:27:26.906	–24:40:50.81	I	137	193	4.1	3.3, 62	11	78	(10)
IRAS 16253-2429	16:28:21.615	–24:36:24.33	0	139	42	0.16	5.1, 40	12	68	(11)
Oph IRS 63	16:31:35.654	–24:01:30.08	I	132	348	1.3	5.8, 170	280	47	(12)
IRAS 16544-1604	16:57:19.643	–16:09:24.02	0	151	50	0.89	4.1, 103	52	73	(13)
R CrA IRS 5N	19:01:48.480	–36:57:15.39	0	147	59	1.4	5.5, 94	99	65	(14)
R CrA IRS 7B	19:01:56.420	–36:57:28.66	I	152	88	5.1	18, 195	339	68	(15)
R CrA IRAS 32	19:02:58.722	–37:07:37.39	0	150	64	1.6	4.9, 153	80	69	(16)
TMC-1A[a]	4:39:35.202	+25:41:44.22	I	137	183	2.3	5.0, 187	184	52	(17)
B335[a]	19:37:00.900	+07:34:09.81	0	165	41	1.4	5.0, 243	29	37	(17)

Notes. Column (1): target names. Column (2): right ascension of the continuum emission measured with single 2D Gaussian fittings. For L1489 IRS 2D Gaussian fittings with two components were performed because single 2D Gaussian fittings did not provide a solution. Column (3): decl. of the continuum emission measured with single 2D Gaussian fittings. For L1489 IRS 2D Gaussian fittings with two components were performed because single 2D Gaussian fittings did not provide a solution. Column (4): evolutionary stage classification based on $T_{\rm bol}$. Column (5): distance to the source based on recent Gaia measurements. Column (6): bolometric temperature rederived from the newly compiled SED. Column (7): bolometric luminosity rederived from the newly compiled SED. Column (8): peak intensity of the continuum emission and its brightness temperature estimated with the full Plank function. Column (9): integrated flux density of the continuum emission measured with single 2D Gaussian fittings. For L1489 IRS 2D Gaussian fittings with two components were performed because single 2D Gaussian fittings did not provide a solution. Column (10): inclination angle of the continuum emission estimated from the ratio of the major and minor axes of the continuum emission. Column (11): references from the eDisk program.

[a] For these sources, we used only ALMA archival data without new observations.

References. (1) Yamato et al. 2023; (2) Phuong et al. 2024; (3) Han et al. 2024; (4) Lin et al. 2023; (5) van't Hoff et al. 2023; (6) Sai et al. 2023; (7) Gavino et al. 2024; (8) Thieme et al. 2023; (9) Santamaría-Miranda et al. 2024; (10) Narayanan et al. 2023; (11) Aso & Sai 2023; (12) Flores et al. 2023; (13) Kido et al. 2023; (14) Sharma et al. 2023; (15) Takakuwa et al. 2024; (16) Encalada et al. 2024; (17) Ohashi et al. 2023

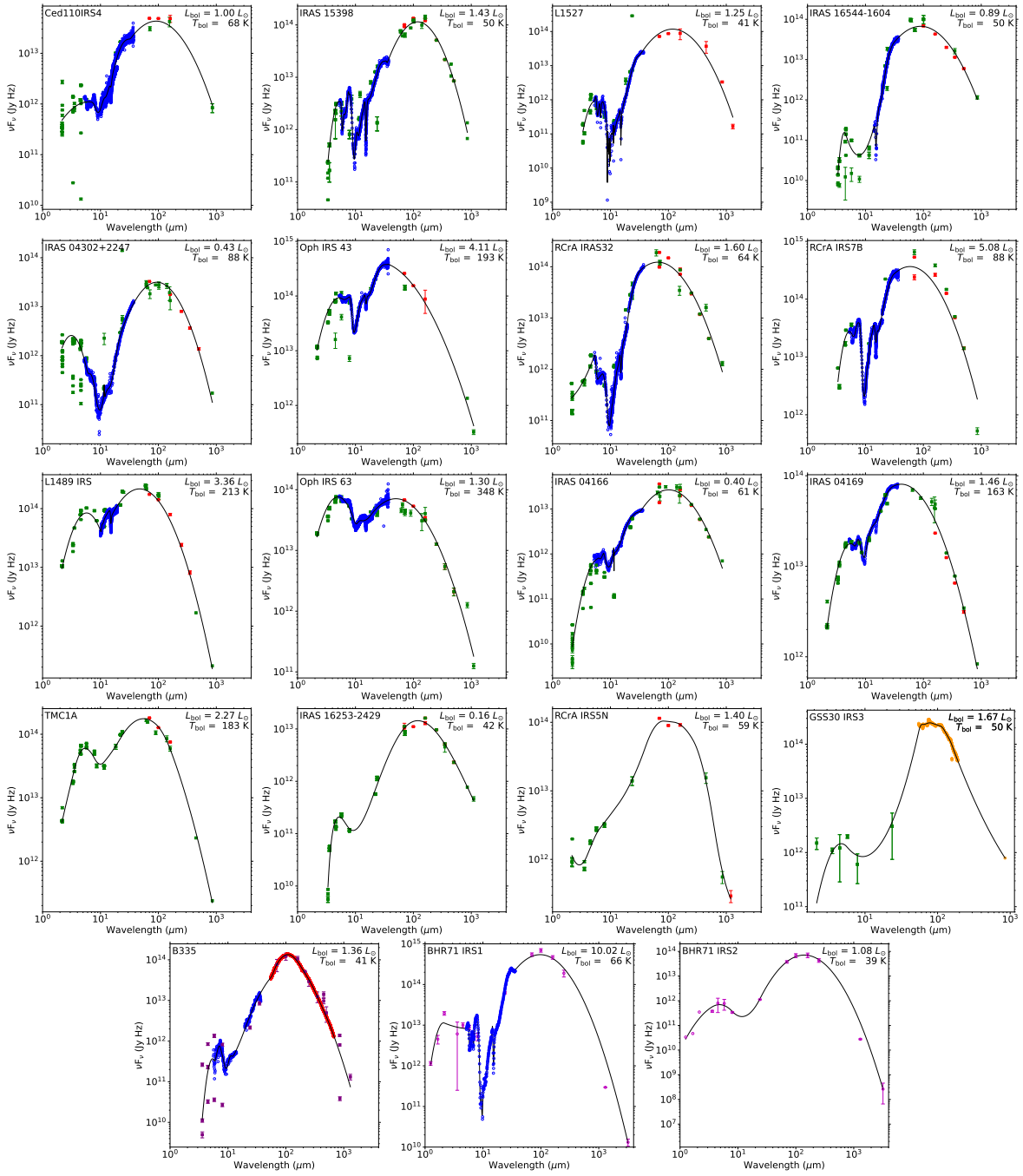

FIGURE 3.1 Spectral energy distributions from the eDisk sources. The SED Photometric data and spectroscopic data are shown in filled squares and empty circles, respectively. The black line represents the spline fit of the SED values used to calculate each source's L_{bol} and T_{bol}. Credit: Ohashi et al. (2023).

3.1.2 *Summary of Key Results*

The eDisk observations have led to several important results, improving our understanding of the physical and chemical processes present in the embedded phases of star formation. Here I highlight some of the most notable findings from the analysis of the observational data.

Figure 3.2 shows the gallery of continuum emission obtained for all eDisk sources. These observations reveal that all sources are spatially resolved and exhibit flattened disk-like structures, suggesting the continuum emission tracing the disks surrounding the targeted protostars. Additionally, there is a huge diversity in the extent of the continuum emission between the sources that spans over two orders of magnitude. Despite this variation, no apparent correlation is observed between the sizes of the continuum and the $L_{\rm bol}$ or $T_{\rm bol}$ of the source. Initially, all the eDisk sources were thought to be single systems. However, the high-resolution continuum observations revealed that 4 of the sources, Ced 110 IRS4, Oph IRS 43, R CrA IRS 7B, and R CrA IRS 32, are in fact close binary systems.

Continuum emissions from several sources also show relatively high intensities, often reaching peak brightness temperatures upwards of 100 K (see Table 3.1). Such high temperatures are in stark contrast to the observations towards Class II disks (Andrews et al., 2018; Villenave et al., 2020) and cannot be explained solely by passive heating from the central source. Results from radiative transfer models show that the inclusion of viscous accretion heating is essential to recreate the observed intensities (Takakuwa et al., 2024). This suggests that the protostellar disks in the eDisk sources are self-luminous.

Unlike Class II disks that frequently exhibit substructures in their continuum, most eDisk sources appear relatively smooth. In fact, clear substructures, such as rings and gaps, are only identified in L1489 IRS and Oph IRS 63 (Flores et al., 2023; Yamato et al., 2023). Both of these sources are Class I objects and have the two highest $T_{\rm bol}$ values within the eDisk sample, implying that they are the most evolved systems among the targeted sources. These results suggest that substructures in disks likely form very quickly when protostars evolve from the embedded phase to the Class II phase. Alternatively, the absence of substructures can also be explained by optically thick continuum emission obscuring any substructures present in the disk midplane. The optically thick nature of the continuum emission is supported by the observation of brightness asymmetry along the minor axis of several eDisk sources (e.g., van't Hoff et al., 2023). Embedded disks are typically more flared than Class II disks, as most dust has not yet settled into the midplane. The dust scale height for IRAS 04302 at the radius of 100 au is estimated to be $\sim$6 au, significantly larger than the typical value of $\sim$0.5 au for Class II disks (Lin et al., 2023). Figure 3.3 presents a schematic representation of a flared disk viewed at an inclination of 70° to help explain the observed brightness asymmetry. In this scenario, the near side of the disk appears dimmer as this emission originates from the colder disk midplane, whereas the far side appears brighter as this emission originates from the warm disk surface regions (Takakuwa et al., 2024).

In addition to the continuum emission, numerous spectral lines, including $C^{18}O$, are also detected toward the eDisk sources. The $C^{18}O$ emission is typically concentrated around the position of the continuum and often displays a clear velocity gradient along the major axis of the continuum. Such a velocity gradient is indicative of a rotation motion in the system. Position-velocity (PV) analysis of $C^{18}O$ emission towards the eDisk sources shows that Keplerian rotation is common even in Class 0 sources (e.g., Aso & Sai, 2023; van't Hoff et al., 2023; Kido et al., 2023; Sai et al., 2023; Thieme et al., 2023). This result implies that disks are common even in the youngest sources. In addition to $C^{18}O$, several other molecules are seen towards the eDisk sources, providing complementary insights into the physical and chemical conditions within these systems. The results from these molecular lines will be explored in greater detail in Chapter 5.

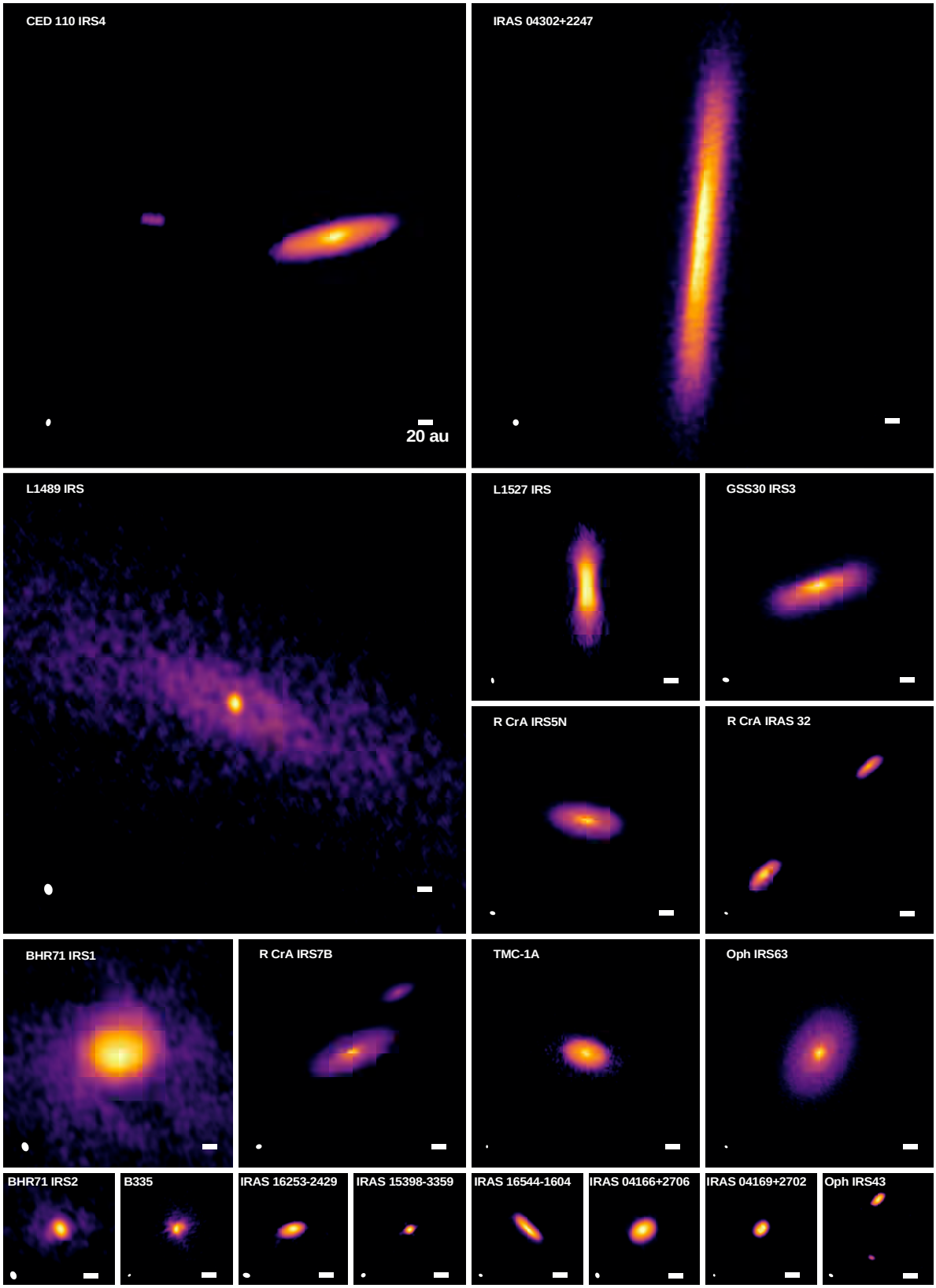

FIGURE 3.2 Gallery of continuum maps obtained towards the eDisk sources. All maps are shown in the same linear scale. The beam size is shown on the bottom left, and the scale of 20 au is shown in the bottom right of each image. Credit: Ohashi et al. (2023).

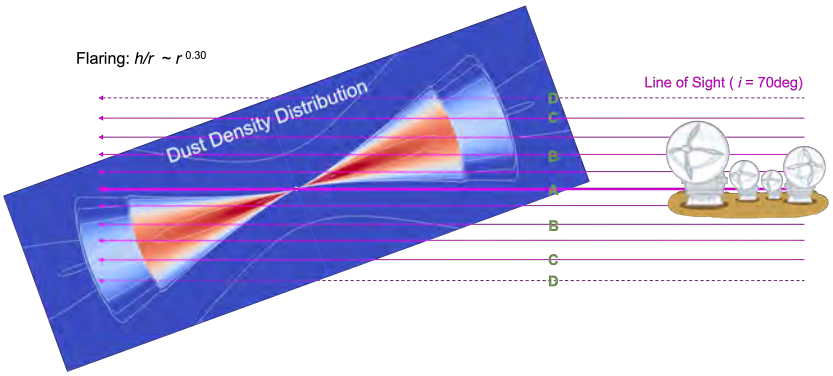

FIGURE 3.3 Schematic view of the observation of a flared disk at an inclination of 70° to the line of sight of the observer. Credit: Takakuwa et al. (2024).

3.2 PUBLICATIONS

The results of this thesis are presented in three closely related scientific papers. This section provides an overview of these papers and also highlights their overall conclusions. The papers are:

1. Sharma, R., Jørgensen, J. K., Gavino S., et al., 2023, "Early Planet Formation in Embedded Disks (eDisk). IX. High-resolution ALMA Observations of the Class 0 Protostar R CrA IRS5N and Its Surroundings". ApJ, 954, 69.

2. Sharma, R., Jørgensen, J. K., van' t Hoff, M. R. L., et al. 2024, "Early Planet Formation in Embedded Disks (eDisk). XX. Constraining the Chemical Tracers of Young Protostellar Sources". Submitted to A&A.

3. Sharma, R., Tobin, J. J., Jørgensen, J. K., 2024, "High–J CO Observations with SOFIA FIFI-LS: Characterizing Warm Gas in the SVS13 Region". In preparation.

3.2.1 *Paper I: Early Planet Formation in Embedded Disks (eDisk) IX: High-resolution ALMA Observations of the Class 0 Protostar R CrA IRS5N and Its Surroundings*

The first paper presents a comprehensive analysis of the continuum and spectral line observations obtained with ALMA towards IRS5N, a Class 0 protostar in the Corona Australis molecular cloud. The observations were conducted at a wavelength of 1.3 mm and achieved an angular resolution of $\sim$0.″05 ($\sim$8 au) towards the source. The continuum images show the presence of a well-resolved and flattened disk-like structure with a radius of $\sim$62 au. Although the continuum emission does not show any apparent substructures, Gaussian fitting revealed the presence of a brightness asymmetry in the minor axis of the disk as seen towards other eDisk sources, as mentioned in Section 3.1.2. From the continuum brightness, the disk mass for IRS5N is estimated to be 6.65 $\times$ 10^{-3} $M_{\odot}$ and 0.02 $M_{\odot}$ at dust temperatures of 47 K and 20 K, respectively.

PV analysis of the $C^{18}O$ emission reveals the presence of a Keplerian disk rotating around a central protostellar source of $\sim$0.3 $M_{\odot}$. Emissions from

other molecules such as ^{12}CO and ^{13}CO are also detected towards IRS5N. However, these emissions do not appear to trace any outflows or cavity walls but seem to be affected by emissions from the surrounding environment.

In addition to IRS5N, the observations also detect IRS5, another nearby protostar located approximately 10″away from IRS5N. Although IRS5 was not an official source targeted by the eDisk program, interesting results have been observed towards this source. IRS5 is a close binary protostar with a projected separation of ∼130 au between its primary source, IRS5a, and its secondary, IRS5b. IRS5a is resolved in the continuum observations with a compact disk of radius ∼13 au and an estimated disk mass of 3.20×10^{-4} $M_\odot$ and 9.18×10^{-4} $M_\odot$ at dust temperatures of 47 K and 20 K, respectively. Notably, the ^{12}CO channel maps towards IRS5 reveal emission originating from IRS5b streaming onto a disk-like structure around IRS5a, possibly tracing the transport of material between the two components.

3.2.2 *Paper II: Early Planet Formation in Embedded Disks (eDisk). XX: Constraining the Chemical Tracers of Young Protostellar Sources*

The second paper builds on the study of the individual sources of the eDisk program. It systematically compiles all the molecular emissions observed towards the eDisk sources to identify key chemical tracers associated with the various components of the observed protostars at disk scales. This is achieved by generating moment 8 and 9 maps for each molecule targeted in all sources. Protostellar outflows are prominently detected in 15 of the 19 sources and are traced primarily by emissions in ^{12}CO and ^{13}CO. In a few Class 0 sources, evidence of more collimated jets is also observed in emissions of SiO and high-velocity channel maps of ^{12}CO. These outflows and jets carve out a cavity in the surrounding envelope and interact with the infalling material to create the outflow cavity walls, often delineated by emissions of c−C_3H_2 and H_2CO in addition to the CO isotopologues.

The inner envelope and disk regions are commonly traced by high-density tracers such as ^{13}CO, C^{18}O, and SO. Even within the inner envelope and disk regions, emissions in CH_3OH and DCN are mostly confined to the innermost regions of Class 0 sources, likely originating from the inner disk surface and hot core regions. The dust temperatures in these regions can rise upwards of $\sim$ 70 K, sufficient enough to sublimate these molecules from the dust surfaces into the gas phase. Additionally, emissions from C^{18}O, SO, and H_2CO also trace accretion streamers towards 5 sources, indicating the presence of non-axisymmetic infall in the embedded phases. Among the various molecules targeted by eDisk observations, the emissions from SO and H_2CO display complex and diverse morphologies between the sources. For example, in some sources, they appear as patches in the outflow regions, while in others, they trace rotation in the inner envelope and disk regions. These varied morphologies suggest the presence of multiple formation and excitation pathways for SO and H_2CO, highlighting the importance of understanding chemistry during the star-formation process.

3.2.3 *Paper III: High−J CO Observations with SOFIA FIFI-LS: Characterizing Warm Gas in the SVS13 Region*

The third paper shifts focus from radio wavelength observations to far-infrared observations, using the SOFIA telescope to investigate molecular emissions from high-excitation rotational transitions of CO towards SVS13-A, HH-7, and SVS13-C, all located in the highly energetic NGC 1333 cluster. Observations were conducted between the wavelengths 76 and 187 μm, targeting several high−J CO rotational transitions ranging from $J = 14-13$ to $J = 34-33$. These high−J CO lines are better diagnostics of the warm gas components in protostellar systems and also provide valuable insights into the physical processes of the emitting regions (e.g., Manoj et al., 2013; Karska et al., 2018; Yang et al., 2018).

The 14–13 and 17–16 transitions are consistently detected towards all three sources and have similar intensities. This suggests that these emissions likely originate from similar processes that heat the gas globally throughout the region. On the other hand, emissions from transitions 21–20 or higher are only observed towards some sources. This suggests these higher transitions likely originate from localized processes such as spot shocks in these regions. Rotational diagrams constructed from the observed flux reveal the presence of warm gas components of ∼200 K in SVS13-A and ∼250 K in HH-7 and SVS13-C. Additionally, a possible hot gas component is also seen towards SVS13-A with a temperature of ∼500 K.

3.2.4 *Overall Conclusions*

In the big picture of star and planet formation, the main conclusions from this thesis are:

- The high-resolution and high-sensitivity ALMA observations reveal that Keplerian disks and outflows are common even in very young, embedded protostars. The disk of IRS5N and indeed the majority of eDisk sources appear smooth and do not exhibit any clear signs of substructures. Assuming optically thin emission, the disk masses can be estimated. However, the high brightness temperatures and asymmetry observed in the minor axis of the continuum suggest that the disks are optically and geometrically thick and the smaller dust grains have not completely settled onto the disk midplane.

- The embedded phase of protostellar evolution is marked by a rich and varied chemistry. The different molecules observed in these sources establish the initial chemical budget for planet formation and can also be used as a diagnostic tool to identify the various components of an embedded system such as disks, envelopes, outflows, and accretion streamers.

- The molecules also provide crucial information about the various processes that occur in a protostellar system. For example, molecules that display a velocity gradient near the protostar reveal the dynamics of disk rotation, while knots seen in molecular emission in the outflow direction can indicate previous episodic accretion. Certain molecules,

such as SiO and DCN, are exclusively seen towards Class 0 sources, making them possible identifiers of the youngest protostellar systems. Investigating their formation and evolution mechanisms can help test their potential as a tracer of the evolutionary stage of embedded sources.

- Infrared observations provide crucial complementary information to those of the millimeter observations. Far infrared observations of high–J rotational transition of CO lines probe the warm and hot gas components, shedding light into the various cooling mechanisms present in protostellar systems that dissipate energy back into the molecular cloud.

3.3 FUTURE OUTLOOK

The results presented across the three papers included in this thesis open up several new avenues that can be explored for future projects. In this section, I detail some of the future studies that are ongoing or are in the advanced stages of planning and also present some ideas that can be pursued for upcoming future projects.

Mass accumulation in an embedded protostar is not a constant process but is instead marked with intermittent periods of intense accretion called episodic accretion bursts. Knots and clumps that appear in the direction of jets and outflows are thought to be evidence of previous outbursts in protostars (Plunkett et al., 2015; Vorobyov et al., 2018). Such clumps are seen in molecular lines of several sources targeted in Paper II. Additionally, the HH-7 region in Paper III represents an intense outflow clump, likely resulting from a previous outburst in the SVS13-A protostar. Therefore, studying protostars that are currently ongoing an outburst offers a unique opportunity to examine these processes in detail. With this motivation, we have obtained high-resolution ALMA observations of the outbursting Class 0 protostar HOPS-383 located in the Orion molecular cloud. I am the principal investigator for these observations, and this project will aid in addressing the mechanisms and implications of outbursts in embedded sources. This study is a direct follow-up to the initial HOPS-383 study presented in Sharma et al. (2020), but has similar observational parameters as the eDisk observations, allowing us to compare the results of a protostar that is currently ongoing accretion outburst with those that are in a quiescent stage from the eDisk sources.

Another project that currently is in the pipeline involves using theoretical models and simulations to explain the chemistry of the various molecular lines observed in the eDisk sources. This project directly builds on the results from Paper II, where it was found that certain molecules such as SiO are predominantly only observed towards Class 0 sources, and emissions from a few molecules such as SO and H_2CO suggest multiple formation and excitation pathways are active for these molecules. The proposed study will use a modified version of the adaptive mesh refinement code RAMSES (Teyssier, 2002; Haugbølle et al., 2018) to simulate the physical evolution over time as accretion proceeds on a Class 0 protostar whose molecular

abundances resemble those of the eDisk observations. The outcomes of these simulations will allow us to assess how the molecular abundances vary as the physical conditions of the system change over time and evaluate whether these physical variations alone can explain the observed differences among the sources. The project will proceed to advanced chemical modeling with full reaction pathways using tools like the Nautilis Multi-Grain Code (NMGC; Iqbal & Wakelam 2018) or the LIne Modeling Engine (LIME; Brinch & Hogerheijde 2010) if the physical models alone are insufficient to explain the observations.

An intriguing result obtained from Paper I is the bridge-like structure appearing in the ^{12}CO channel maps of the binary source IRS5. This feature appears to trace the transport of material between the components (Sadavoy et al., 2018; Jørgensen et al., 2022). Dedicated high-resolution and high-sensitivity observation of this binary source will provide a better constraint on this structure and also help us understand the dynamics of the evolution in close binary systems. We plan to submit an ALMA proposal to observe IRS5 to map the gas and dust structure towards the source.

In addition to these already planned projects, there are several other directions that could be taken as a follow-up to the studies presented in this thesis. The successful launch of the *James Webb Space Telescope* (JWST) has opened up new opportunities for observing embedded systems at near- and mid-infrared wavelengths. These observations are sensitive to the molecular ices present in protostellar systems and can provide additional constraints on the grain-surface chemistry of various molecules. Likewise, the upcoming *next generation Very Large Array* (ngVLA) and the *Square Kilometer Array* (SKA) will provide opportunities to observe at centimeter wavelengths, where spectra of COMs will be less crowded and suffer less from line blending and confusion, making them easier to identify. Combining these multi-wavelength observations from near-infrared to centimeter wavelengths will provide a more comprehensive understanding of the star and planet formation processes.

3.4 OWN CONTRIBUTIONS VERSUS CONTRIBUTIONS OF COLLABORATORS

This section outlines the contributions I made, as well as the contributions of the co-authors to the papers presented in Chapters 4, 5, and 6.

Paper I. The raw datasets used in this paper were obtained from ALMA observations of the IRS5N source, conducted as part of the eDisk program. I performed the full data reduction for IRS5N by following the data reduction scripts developed for the eDisk observations by John J. Tobin and Patrick Sheehan. I also performed the subsequent analysis of the data and led the discussion of the results. I created all of the figures and tables used in the paper and wrote the entirety of the paper with the exception of the last paragraph of Section 4.3.2, which was contributed by Jes K. Jørgensen. Co-authors Jes K. Jørgensen and Sacha Gavino gave substantial inputs and suggestions to improve the analysis and writing of the paper. Other co-authors also contributed with important discussions and additional comments to help

improve the draft of the paper as a whole. Any changes made to the paper based on the comments were implemented by me.

Paper II. This paper focuses on the analysis of ALMA spectral line observations for all 19 sources included in the eDisk program. Most of the datasets were re-reduced by John J. Tobin to ensure uniformity and consistency across all sources. New images were created using the robust weighting of 2 (see Section 2.2.1). Following this re-reduction, I compiled the entire dataset, generated the moment maps for all sources, and led the subsequent analyses and discussions of the results. I created all the figures and tables used in the paper. I wrote the entire paper by myself, incorporating the insights provided by co-authors during our biweekly discussions. Specifically, Jes K. Jørgensen, Merel L. R. van' t Hoff, and Jeong-Eun Lee greatly helped in the interpretation of the results. All co-authors contributed with constructive comments on the draft to help refine and improve the paper. Any changes made to the paper based on the comments were implemented by me. Additionally, as a complement to this paper, I also developed an interactive webpage where users can explore all the moment maps generated for this paper online (see Section 5.3).

Paper III. This paper is based on far-infrared spectroscopic data obtained using the SOFIA telescope. The pipeline-calibrated datasets were retrieved from the SOFIA archival database. I processed the downloaded data by correcting for atmospheric transmission and subtracting the continuum to create the final spectra. I also conducted all subsequent analyses, created the figures and tables, and wrote the entire paper. Jes K. Jørgensen and John J. Tobin provided valuable comments and suggestions on the interpretation and to improve the draft of the paper. Any changes made to the paper based on the comments were implemented by me.

4

Early Planet Formation in Embedded Disks (eDisk) IX: High-resolution ALMA Observations of the Class 0 Protostar R CrA IRS5N and its surrounding

Rajeeb Sharma[1], Jes K. Jørgensen[1], Sacha Gavino[1], Nagayoshi Ohashi[2], John J. Tobin[3], Zhe-Yu Daniel Lin[4], Shigehisa Takakuwa[2,5], Chang Won Lee[6,7], Jinshi Sai (Insa Choi)[2], Woojin Kwon[8,9], Itziar de Gregorio-Monsalvo[10], Alejandro Santamaría-Miranda[10], Hsi-Wei Yen[2], Yuri Aikawa[11], Yusuke Aso[6], Shih-Ping Lai[2,12,13,14], Jeong-Eun Lee[15], Leslie W. Looney[16], Nguyen Thi Phuong[6,17], Travis J. Thieme[12,13,14], Jonathan P. Williams[18]

[1] Niels Bohr Institute, University of Copenhagen, Øster Voldgade 5–7, 1350, Copenhagen K, Denmark
[2] Academia Sinica Institute of Astronomy & Astrophysics, 11F of Astronomy-Mathematics Building, AS/NTU, No.1, Sec. 4, Roosevelt Rd, Taipei 10617, Taiwan, R.O.C.
[3] National Radio Astronomy Observatory, 520 Edgemont Rd., Charlottesville, VA 22903 USA
[4] University of Virginia, 530 McCormick Rd., Charlottesville, Virginia 22903, USA
[5] Department of Physics and Astronomy, Graduate School of Science and Engineering, Kagoshima University, 1-21-35 Korimoto, Kagoshima, Kagoshima 890-0065, Japan
[6] Korea Astronomy and Space Science Institute, 776 Daedeok-daero Yuseong-gu, Daejeon 34055, Republic of Korea
[7] University of Science and Technology, 217 Gajeong-ro Yuseong-gu, Daejeon 34113, Republic of Korea
[8] Department of Earth Science Education, Seoul National University, 1 Gwanak-ro, Gwanak-gu, Seoul 08826, Republic of Korea
[9] NU Astronomy Research Center, Seoul National University, 1 Gwanak-ro, Gwanak-gu, Seoul 08826, Republic of Korea
[10] European Southern Observatory, Alonso de Cordova 3107, Casilla 19, Vitacura, Santiago, Chile
[11] Department of Astronomy, Graduate School of Science, The University of Tokyo, 7-3-1 Hongo, Bunkyo-ku, Tokyo 113-0033, Japan

[12] Institute of Astronomy, National Tsing Hua University, No. 101, Section 2, Kuang-Fu Road, Hsinchu 30013, Taiwan
[13] Center for Informatics and Computation in Astronomy, National Tsing Hua University, No. 101, Section 2, Kuang-Fu Road, Hsinchu 30013, Taiwan
[14] Department of Physics, National Tsing Hua University, No. 101, Section 2, Kuang-Fu Road, Hsinchu 30013, Taiwan
[15] Department of Physics and Astronomy, Seoul National University, 1 Gwanak-ro, Gwanak-gu, Seoul 08826, Korea
[16] Department of Astronomy, University of Illinois, 1002 West Green St, Urbana, IL 61801, USA
[17] Department of Astrophysics, Vietnam National Space Center, Vietnam Academy of Science and Techonology, 18 Hoang Quoc Viet, Cau Giay, Hanoi, Vietnam
[18] Institute for Astronomy, University of Hawai'i at Mānoa, 2680 Woodlawn Dr., Honolulu, HI 96822, USA

Published in The Astrophysical Journal, vol. 954, page 69, Sept 2023

Abstract

We present high-resolution, high-sensitivity observations of the Class 0 protostar RCrA IRS5N as part of the Atacama Large Milimeter/submilimeter Array (ALMA) large program Early Planet Formation in Embedded Disks (eDisk). The 1.3 mm continuum emission reveals a flattened continuum structure around IRS5N, consistent with a protostellar disk in the early phases of evolution. The continuum emission appears smooth and shows no substructures. However, a brightness asymmetry is observed along the minor axis of the disk, suggesting the disk is optically and geometrically thick. We estimate the disk mass to be between 0.007 and 0.02 $M_\odot$. Furthermore, molecular emission has been detected from various species, including $C^{18}O$ (2–1), ^{12}CO (2–1), ^{13}CO (2–1), and H_2CO ($3_{0,3}-2_{0,2}$, $3_{2,1}-2_{2,0}$, and $3_{2,2}-2_{2,1}$). By conducting a position-velocity analysis of the $C^{18}O$ (2–1) emission, we find that the disk of IRS5N exhibits characteristics consistent with Keplerian rotation around a central protostar with a mass of approximately 0.3 $M_\odot$. Additionally, we observe dust continuum emission from the nearby binary source, IRS5a/b. The emission in ^{12}CO toward IRS5a/b seems to emanate from IRS5b and flow into IRS5a, suggesting material transport between their mutual orbits. The lack of a detected outflow and large-scale negatives in ^{12}CO observed toward IRS5N suggests that much of the flux from IRS5N is being resolved out. Due to this substantial surrounding envelope, the central IRS5N protostar is expected to be significantly more massive in the future.

4.1 INTRODUCTION

Protostellar disks form as an outcome of the conservation of angular momentum during the gravitational collapse of the dust and gas in the envelope surrounding young stars (e.g., Terebey et al., 1984; McKee & Ostriker, 2007). These disks not only regulate the mass accreted onto the protostar but also provide the necessary ingredients for planet formation (Testi et al., 2014). Recent Atacama Large Milimeter/submilimeter Array (ALMA) observations with high spatial resolution have discovered that substructures such as gaps and rings are common in the dust emission of Class II young stellar object disks (ALMA Partnership et al., 2015; Andrews et al., 2018; Cieza et al., 2021). While these structures can be attributed to features such as snowlines and dust traps (Zhang et al., 2015; Gonzalez et al., 2017), they are largely thought to be indications of embedded planets (Dong et al., 2015; Zhang et al., 2018). The direct imaging of possible protoplanets in the gap of the continuum emission of the protostar PDS 70 further supports this idea (Keppler et al., 2018; Isella et al., 2019; Benisty et al., 2021).

Recent studies have shown that the mass reservoir of Class II disks is generally insufficient to form giant planets (Tychoniec et al., 2020). This suggests that planet formation is already well underway by the time a protostar reaches the Class II (T Tauri) phase. Interferometric observations over the last decade have shown that protostellar disks can be found in younger Class 0/I protostars (e.g., Tobin et al., 2012; Brinch & Jørgensen, 2013; Ohashi et al., 2014; Sheehan & Eisner, 2017; Sharma et al., 2020; Tobin et al., 2020). These disks are generally found to be larger and possibly more turbulent compared to disks around more evolved sources (Sheehan & Eisner, 2017; Tychoniec et al., 2020). Furthermore, evidence of substructures has been observed in a handful of embedded Class I sources (e.g., Sheehan & Eisner, 2017; Segura-Cox et al., 2020; Sheehan et al., 2020). These results, combined with the ubiquity of substructures in Class II disks, suggest that planet formation likely begins earlier during the Class 0/I phase when the disk is still embedded in its natal envelope.

To constrain how and when substructures form in young ($\lesssim$1 Myr old) protostellar disks and ultimately understand their nature, a sample of 19 nearby Class 0/I protostellar systems have been studied with ALMA as part of the Large Program Early Planet Formation in Embedded Disks (eDisk; Ohashi et al., 2023). One of these deeply embedded protostars located in the R Coronae Australis (R CrA) region, the most active star formation region in the Corona Australis molecular cloud, is the Class 0 source RCrA IRS5N (hereafter IRS5N; Harju et al. 1993; Chini et al. 2003). IRS5N (also referred to as CrA-20; Peterson et al., 2011) is part of a group of a dozen deeply embedded young stellar objects (YSOs) in a cluster dubbed the Coronet in the R CrA region (Taylor & Storey, 1984). Traditionally, the cluster is estimated to be at a distance of $\sim$ 130 pc. However, from the recent *Gaia* DR2 parallax measurements, the distance to the cluster has been updated to 147 $\pm$ 5 pc (Zucker et al., 2020), which we have adopted for this paper. This value is consistent with the distance of 149.4 $\pm$ 0.4 pc measured recently by Galli et al. (2020).

The Coronet has been extensively observed from X-rays to radio wave-

lengths (e.g., Peterson et al., 2011; Lindberg et al., 2014; Sandell et al., 2021, see also review by Neuhäuser & Forbrich 2008). Based on *Spitzer* photometry of the Coronet, IRS5N was first classified as a Class I source (Peterson et al., 2011), which was later updated to Class 0 with the addition of *Herschel* and JCMT/SCUBA data (Lindberg et al., 2014). From a recent reanalysis of the spectral energy distribution (SED) of IRS5N utilizing the most recent photometry and the updated Gaia distance above, we find its bolometric temperature ($T_{\rm bol}$) = 59 K and its bolometric luminosity ($L_{\rm bol}$) = 1.40 $L_\odot$ (Ohashi et al., 2023). Up to now, the highest angular resolution observations of IRS5N at submillimeter wavelengths so far were from the Submillimeter Array (SMA) in the compact configuration at a resolution of $4\farcs6 \times 2\farcs6$ (Peterson et al., 2011). In this paper, part of the series of first-look papers from eDisk, we present the first high-angular resolution ($\sim 0\farcs05$), high-sensitivity continuum and spectral line observations toward IRS5N using ALMA. The field-of-view of our ALMA observations of IRS5N also captures the nearby binary protostar, IRS5 a and b. IRS5 (also known as R CrA 19; Peterson et al. (2011)) was first reported in Taylor & Storey (1984) and later found to be a binary (Chen & Graham, 1993; Nisini et al., 2005).

The paper is structured as follows: The observations and the data reduction process are described in Sect. 4.2. The empirical results from the observations of the disk continuum and the molecular line emission are presented in Sect. 4.3. The implications of the results are discussed in Sect. 4.4 and the conclusions are presented in Sect. 4.5.

4.2 OBSERVATIONS AND DATA REDUCTION

IRS5N was observed as part of the eDisk ALMA large program (2019.1.00261.L, PI: N. Ohashi) in Band 6 at 1.3 mm wavelength. The short-baseline observations were conducted on 2021 May 4 and on 2021 May 15 for a total on-source time of ∼76 minutes. The long-baseline observations were made between 2021 August 18 and October 2 for a total on-source time of ∼256 minutes. The shortest and the longest projected baselines were 15 m and 11,615 m, respectively. Along with the continuum, molecular line emissions from ^{12}CO, ^{13}CO, C^{18}O, SO, SiO, DCN, c-C_3H_2, H_2CO, CH_3OH, and DCN were also targeted. A detailed description of the observations along with the spectral setup, correlator setup, and calibration is provided in Ohashi et al. (2023).

The ALMA pipeline-calibrated long- and short-baseline data were further reduced and imaged using the Common Astronomy Software Application (CASA) 6.2.1 (McMullin et al., 2007). The source position was estimated by calculating the continuum peak position for each execution block and aligned to a single phase center when calculating the scaling between the execution blocks. The self-calibration was carried out using the native phase centers of the observations. The short-baseline data were initially self-calibrated with six rounds of phase-only calibration followed by three rounds of phase and amplitude calibration. Then, the long-baseline data were combined with the self-calibrated short-baseline data, and four more rounds of phase-only calibration were performed on the combined data. The solutions of the

Table 4.1. Overview of the continuum and the detected molecular lines

Continuum/Molecules	Transition	robust	Frequency (GHz)	Beam ($''$)	P.A. ($^\circ$)	Δv (km s^{-1})	RMS (mJy beam^{-1})
Continuum	–	0.5	225.000000	0.05 × 0.03	60	–	0.016
$C^{18}O$	$J = 2$–1	0.5	219.560354	0.11 × 0.08	83.8	0.167	1.636
^{12}CO	$J = 2$–1	0.5	230.538000	0.11 × 0.08	85.9	0.635	0.987
^{13}CO	$J = 2$–1	2.0	220.398684	0.15 × 0.11	-87.3	0.167	2.104
H_2CO	$J_{K_a,K_c} = 3_{0,3} - 2_{0,2}$	2.0	218.222192	0.14 × 0.11	-86.6	1.34	0.499
H_2CO	$J_{K_a,K_c} = 3_{2,1} - 2_{2,0}$	2.0	218.760066	0.15 × 0.11	-86.8	0.167	1.471
H_2CO	$J_{K_a,K_c} = 3_{2,2} - 2_{2,1}$	2.0	218.475632	0.17 × 0.13	-86.6	1.34	0.529

continuum self-calibration are applied to the spectral line data as well.

The final continuum images were created with a range of robust parameters from -2.0 to 2.0. We adopt the robust value of 0.5 for the continuum image in this paper, providing a balance between sensitivity and resolution. This resulted in a synthesized beam of $0\farcs052 \times 0\farcs035$ and an rms noise of 16 μJy beam^{-1}. The spectral line images are created with robust parameters of 0.5 and 2.0 with *uvtaper* = 2000 kλ. We adopt robust 0.5 for most of the spectral lines except for the ^{13}CO and H_2CO lines, where we adopt robust 2.0 to increase the signal-to-noise ratio. The details of the continuum observations and the detected spectral lines are summarized in Table 4.1.

4.3 RESULTS

4.3.1 *Dust continuum emission*

Figure 4.1 shows the continuum images from the ALMA data at 1.3 mm. Figure 4.1(a) displays the large-scale view of the continuum emission from the region, and the remaining panels show the zoom-in of the IRS5N and the IRS5 protostars.

Figure 4.1(b) shows the zoomed-in view of the IRS5N continuum image. The image shows a well-resolved flattened dust structure, which likely traces the disk surrounding the central protostar. The brightest emission of the disk is concentrated at its geometrical center with a peak intensity of 5.53 mJy beam^{-1} as measured from the emission map corresponding to a brightness temperature of ∼94 K, calculated with the full Planck function. The brightness temperature of 94 K is relatively high for a protostar with L_{bol} = 1.4 $L_\odot$ and deviates from the traditional assumptions of protostars generally derived from Class II disks (Kusaka et al., 1970; Chiang & Goldreich, 1997; Huang et al., 2018). One likely explanation for this high-brightness temperature is that IRS5N experiences self-heating through accretion luminosity, which has also been seen on other eDisk sources and further explored in Takakuwa et al. (in prep.). The total integrated flux density of IRS5N is 101 mJy, measured by integrating pixels where intensity is above 3σ. The

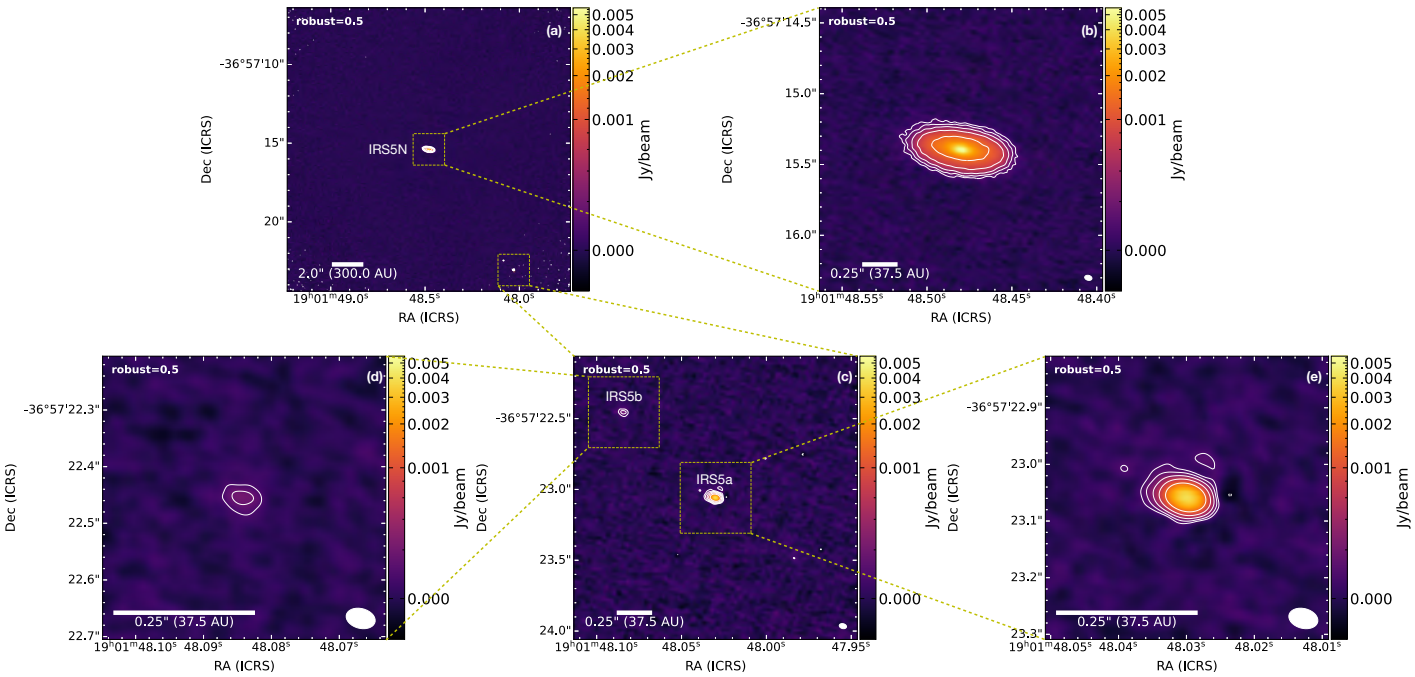

FIGURE 4.1 (a) 1.3 mm continuum images of R CrA IRS5N and IRS5 sources with a robust paramater of 0.5. (b) Zoomed-in view of the IRS5N disk. (c) Zoomed-in view of IRS5a and its companion IRS5b. (d) and (e) show further zoomed-in views of the individual sources of the IRS5 binary. The contour levels are 5σ, 10σ, 20σ, 40σ, and 80σ with $\sigma = 0.016$ mJy beam^{-1}. The synthesized beam is shown in white in the bottom right corner with a beam size of $0\farcs052 \times 0\farcs035$ and a position angle of 75.4°. The color stretch used for the images is arcsinh to cover the dynamic range between the sources.

geometrical peak position of IRS5N is $19^{h}01^{m}48\farcs48$, $-36°57'15\farcs39$. The full width at half maximum (FWHM) of IRS5N is estimated to be ∼62 au from the Gaussian fit model of the continuum emission. The deconvolved size enables us to estimate the inclination, i, of the IRS5N disk to be ∼65° calculated from $i = \arccos(\theta_{\rm min}/\theta_{\rm maj})$, where $\theta_{\rm min}$ and $\theta_{\rm max}$ are the FWHM of the minor and major axes respectively.

Figure 4.1(c) shows the zoomed-in view of the binary source IRS5, with panels (d) and (e) showing the zoom-in of IRS5b and IRS5a, respectively. Nisini et al. (2005) first reported a separation of $\sim 0\farcs6$ between the two components based on pre-images with a relatively coarse pixel size of 0.14 arcsec/pixel. The pre-images were taken as part of preparations for spectroscopic observations using the ISAAC instrument of the Very Large Telescope (VLT). Our current high-resolution ALMA observations reveal that IRS5a and IRS5b have a projected separation of $\sim 0\farcs9$ (∼132 au at a distance of 147 pc). This difference between the previous and the new separation may be due to a combination of the proper motions of the sources, and the confusion from the scattered light in the infrared observations. The peak position of IRS5a as measured with Gaussian fitting is $19^{h}01^{m}48\farcs030$, $-36°57'23\farcs06$. We adopt this position as the coordinate of IRS5a. IRS5a is peaked at the center with a peak intensity of 3.87 mJy beam^{-1} or ∼62 K and a flux density of 4.85 mJy. The secondary source, IRS5b, is much smaller and fainter than IRS5a. The peak position of IRS5b as measured with Gaussian fitting is

$19^h01^m48^s.084$, $-36°57'22''.46$. It has a peak intensity of ∼0.20 mJy beam^{-1} or ∼3 K and a flux density of 0.26 mJy. The flux density of IRS5 was also measured by integrating above the 3σ level over a region surrounding the individual continuum sources. From our observations, IRS5a is marginally resolved whereas IRS5b is not resolved.

4.3.2 *Disk and envelope masses*

The dust continuum emission with ALMA can be used to estimate the mass of the total disk structure surrounding the sources. Assuming optically thin emission, well-mixed gas and dust, and isothermal dust emission, the dust mass can be derived from

$$M_{\rm dust} = \frac{D^2 F_\lambda}{\kappa_\lambda B_\lambda(T_{\rm dust})}, \tag{4.1}$$

where D is the distance to the source (∼147 pc) and $T_{\rm dust}$ is the temperature of the disk. F_λ, κ_λ, and B_λ are the flux density of the disk, dust opacity, and the Planck function at the wavelength λ, respectively. Typically, for Class II disks, $T_{\rm dust}$ is often taken to be a fixed temperature of 20 K independent of the total luminosity (e.g., Andrews & Williams, 2005; Ansdell et al., 2016). However, for younger, more embedded Class 0/I disks, Tobin et al. (2020) found through radiative transfer modeling that the dust temperature scales as

$$T_{\rm dust} \approx 43{\rm K}\left(\frac{L_{bol}}{1L_\odot}\right)^{0.25}, \tag{4.2}$$

For IRS5N with a bolometric luminosity of 1.40 $L_\odot$ Equation (4.2) yields $T_{\rm dust} = 47$ K.

We estimate the disk masses using both dust temperatures. We adopt $\kappa_{1.3{\rm mm}} = 2.30$ cm^2 g^{-1} from dust opacity models of Beckwith et al. (1990) and assume a canonical gas-to-dust ratio of 100:1 to calculate disk masses using Equation (4.1). The resulting total disk mass for IRS5N is 0.019 $M_\odot$ for a dust temperature of 20 K and 6.65×10^{-3} $M_\odot$ for a dust temperature of 47 K. The scaled dust temperature of IRS5a is similar to that of IRS5N, as Lindberg et al. (2014) found $L_{\rm bol}$ of IRS5a to be 1.7 $L_\odot$. Disk masses are also derived for the binary, IRS5. The estimated disk masses for all the continuum sources are presented in Table 4.2. It is important to note that the disk masses calculated using Equation (4.1) represent lower limits, as the continuum emission is most likely optically thick (see Section 4.4).

For comparison, we estimate the mass of the envelope around IRS5N using a simple 1D dust radiative transfer model. We adopt a single power-law density profile, $n \propto r^{-1.5}$ corresponding to material in free-fall between inner and outer radii of 100 and 10,000 au, respectively, and take the bolometric luminosity of the source determined from the full SED as the sole (internal) heating source of the dust. The dust radiative transfer model then calculates the temperature-profile of the dust in the envelope self-consistently and predicts the SED of the resulting source emission. To constrain the envelope mass we then fit the long wavelength ($\lambda > 60$ μm) part of the spectral energy distribution of IRS5N. This method allows for a slightly more robust way of determining the envelope mass than simply adopting a single

Table 4.2. Estimated disk masses of continuum emission sources.

Source	Flux Density	Gas+Dust Mass	
		20 K	47 K
	(mJy)	($M_\odot$)	($M_\odot$)
IRS5N	100.65	0.019	6.65×10^{-3}
IRS5a	4.85	8.92×10^{-4}	3.20×10^{-4}
IRS5b	0.26	4.73×10^{-5}	–

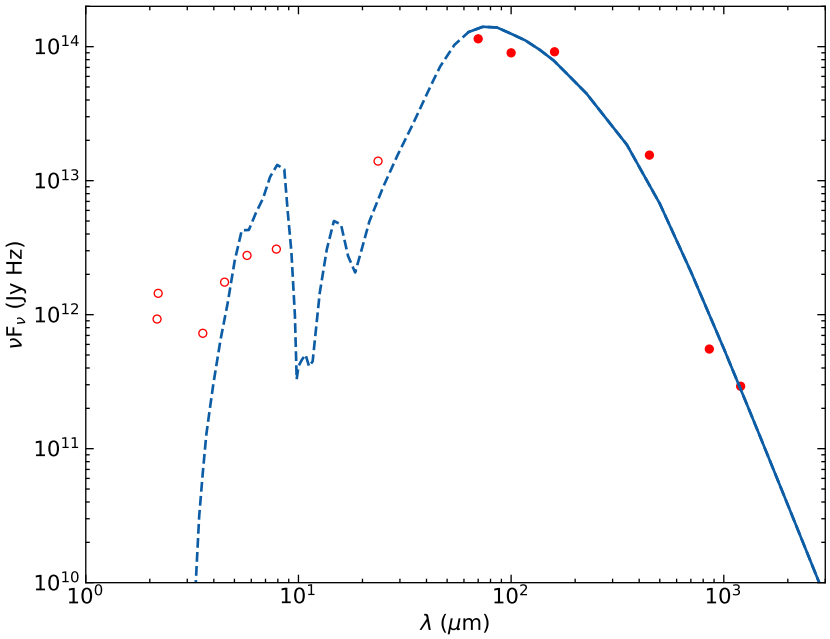

FIGURE 4.2 Fitting of the SED of IRS5N with a 1D radiative transfer model. Filled red circles represent SED values over 60 μm which are fitted by the model. Open red circles represent the remaining SED values used as input. The solid blue line represents the fit given by the model. The dashed blue line represents that the model does not fit this part of the SED.

submilimeter flux point and isothermal dust as it provides an estimate of the temperature of the dust taking into account the source luminosity (e.g., Jørgensen et al., 2002; Kristensen et al., 2012). The resulting fit of the envelope model is shown in Fig. 4.2 with the envelope mass constrained to be 1.2 $M_\odot$. The estimated uncertainty on the fitted envelope mass is comparable to the flux calibration uncertainty, typically about 20% for the measurements used here. However, systematic uncertainties of the adopted simplified physical structure of the envelope and the dust opacity laws will likely dominate over this. It is worth emphasizing that this simplified model is not expected to, and does not, fit the emission at wavelengths shorter than 60 μm due to the complex geometry of the system at small scales and contributions from scattering.

4.3.3 *Molecular lines*

Among the molecules mentioned in Section 4.2, emission is detected in $C^{18}O$, ^{12}CO, ^{13}CO, and H_2CO molecules in our observations. Figure 4.3 presents an overview of the integrated-intensity (moment-0) and mean-velocity (moment-1) maps of all the detected molecules toward IRS5N and IRS5. The moment 1 maps were generated by integrating the regions where $I_\nu \geq 3\sigma$, where σ is the rms per channel. The maps for $C^{18}O$and ^{12}CO were made using a robust parameter of 0.5, while the maps for the remaining molecules were made using a robust parameter of 2.0. The channel maps of all the observed molecules around IRS5N are shown in Appendix 4.A.

It is worth emphasizing that large-scale negative components are visible in the channel maps of the molecules, particularly of the CO isotopologues. These negative components indicate that a significant amount of extended flux originating from the large-scale structures surrounding the sources is being resolved out. While it is crucial to analyze these structures to build a comprehensive picture of the physics and chemistry of the system, we are constrained by the limitations of our high-resolution observations. The maximum recoverable scale, (θ_{MRS}) of our observations was 2.″91. Hence, this study focuses only on small-scale structures, such as the disk and envelope of individual systems.

$C^{18}O$

Figure 4.4 shows the zoomed-in integrated moment 0 and moment 1 maps of the $C^{18}O$(2–1) emission around IRS5N. The moment 0 map shows a flattened structure along with a velocity gradient extended along the major axis of the disk, traced by the continuum emission. The size of the gas disk radius from the $C^{18}O$emission is comparable to that of the disk continuum and has a hole at the protostar position. Based on the consistency between the $C^{18}O$emission and the continuum emission, the radius of the disk can be assumed to be the same as the FWHM of the continuum, ∼62 au. The hole at the protostellar position has negative intensities below 3σ at 5.35 km s^{-1} – 6.02 km s^{-1} (see Figure 4.13, 4.19). The deficit likely results from continuum over-subtraction due to the $C^{18}O$emission being relatively weak compared to the bright continuum emission.

The moment 1 map of the $C^{18}O$emission shows that the blue- and the red-shifted velocities have a distinct separation along the eastern and western sides, respectively. Such a velocity profile is consistent with a rotating disk. The position-velocity (PV) analysis of the $C^{18}O$emission is presented in Section 4.4.

^{12}CO and ^{13}CO

Figure 4.5 shows zoomed-in moment 0 and moment 1 maps of ^{12}CO (2–1) and ^{13}CO (2–1) emission near IRS5N. While the ^{12}CO emission shows extended emission around IRS5N, it does not seem to trace any obvious outflow/jet associated with the protostar, which is puzzling. The spiral structure seen towards the west of the protostar is blue-shifted and seems to trace infalling material onto the protostellar disk (see channel maps; Figure 4.14).

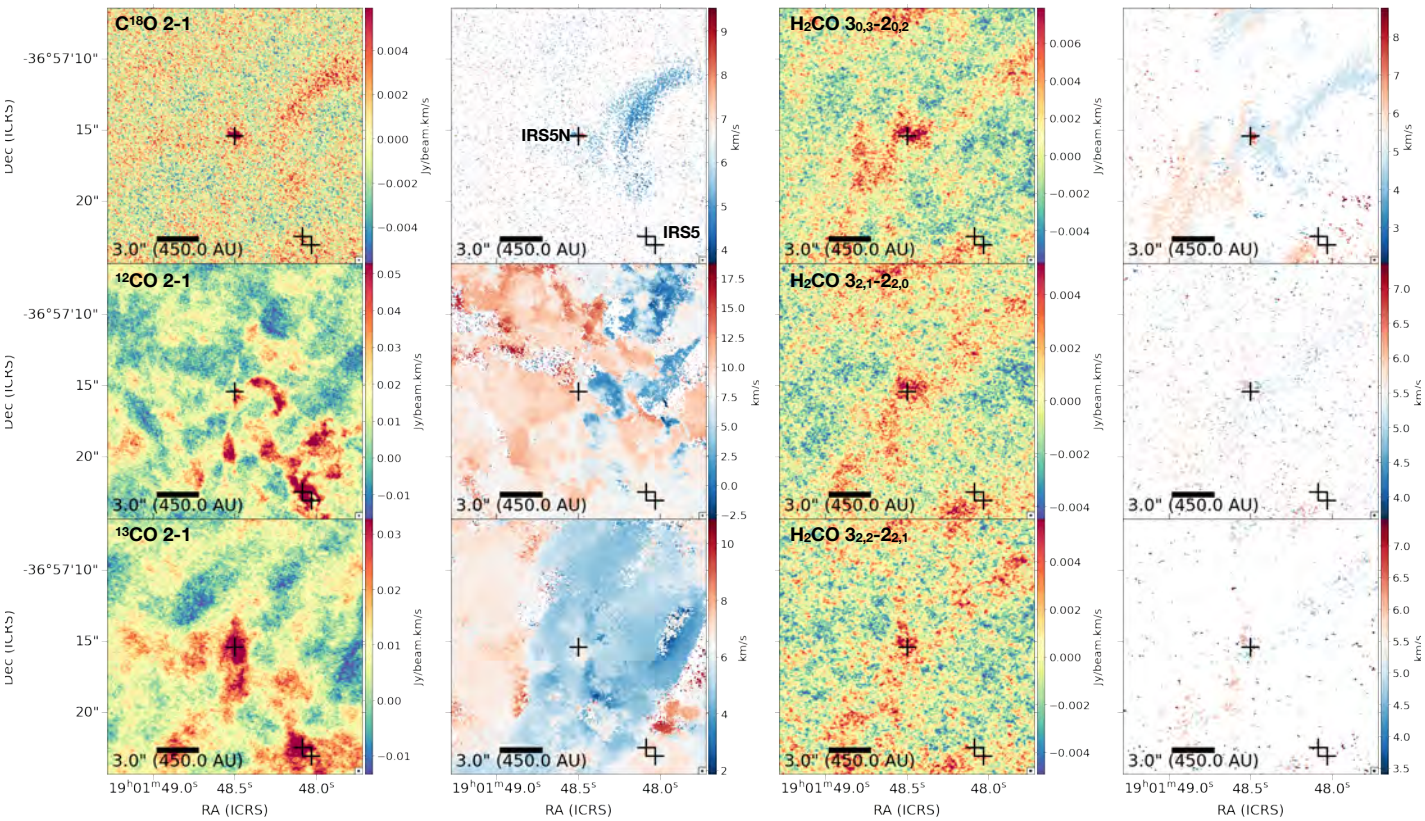

FIGURE 4.3 Overview of all the molecular lines detected towards IRS5N and IRS5. For each molecule, the moment 0 map is shown on the left and the moment 1 map is shown on the right. The cross marks show the peak of the continuum emission of IRS5N and the binary IRS5. The maps are created by integrating over the velocity ranges of 3.68 – 9.53 km s^{-1}, -5.38 – 20.65 km s^{-1}, 0.51 – 12.03 km s^{-1}, 2.06 – 8.76 km s^{-1}, 3.68 – 7.36 km s^{-1}, and 3.40 – 7.42 km s^{-1} for $C^{18}O$, ^{12}CO, ^{13}CO, H_2CO ($3_{0,3}$–$2_{0,2}$), H_2CO ($3_{2,1}$–$2_{2,0}$), and H_2CO ($3_{2,2}$–$2_{2,1}$) respectively. The synthesized beam is shown in black at the bottom right corner of each image, enclosed by a square.

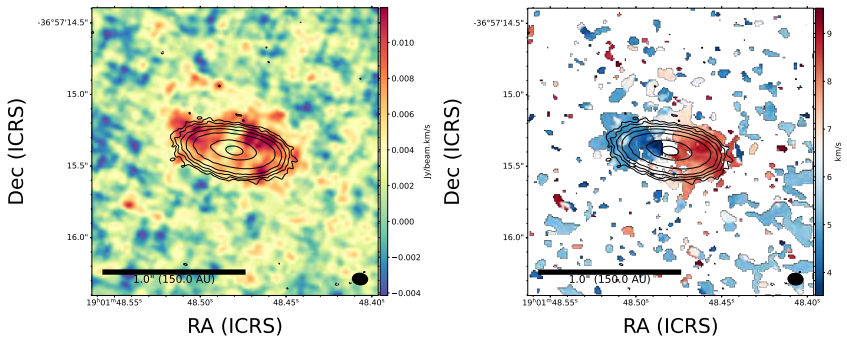

FIGURE 4.4 Zoomed-in moment 0 map (*left*) and moment 1 map (*right*) of the $C^{18}O$(J=2–1) emission towards IRS5N created with the robust value of 0.5. The overlaid contours show continuum emission from 3σ to 192σ, with each contour doubling the previous σ level. The maps are created by integrating over the velocity ranges of 3.68 – 9.53 km s^{-1}. The synthesized beam size for the $C^{18}O$emission is 0.″11 × 0.″08.

Additionally, extended emission is seen in the surrounding of IRS5N, some of which likely originates from the protostar. In contrast, the ^{13}CO plot shows some emission in the north-south direction of the protostar but this emission is mostly observed in red-shifted velocity channels (Figure 4.21). The channel maps of ^{13}CO also show an apparent deficit near the proto-

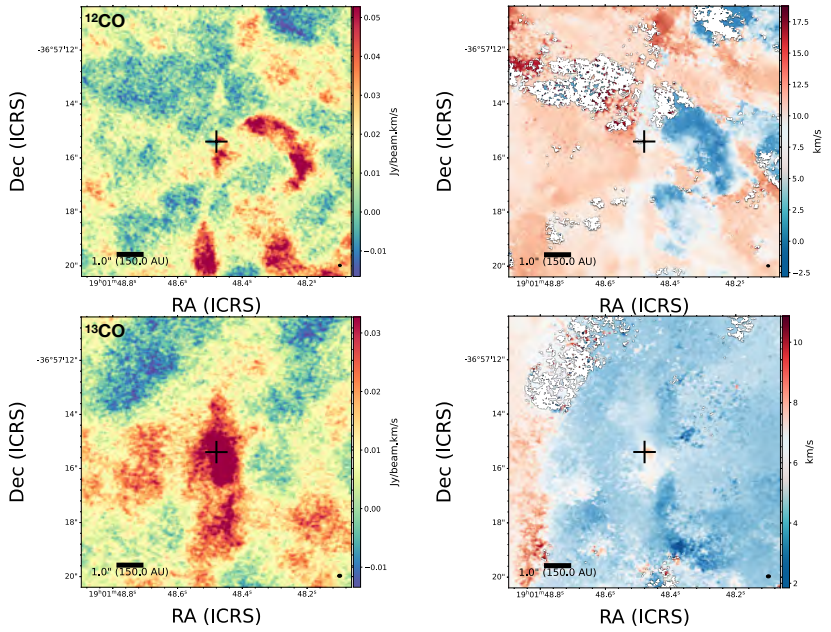

FIGURE 4.5 Zoomed-in moment 0 (*left*) and moment 1 (*right*) maps of ^{12}CO (*top*) and ^{13}CO (*bottom*) emission. The maps are created by integrating over the velocity ranges of -5.38 – 20.65 km s^{-1} and 0.51 – 12.03 km s^{-1} for ^{12}CO and ^{13}CO , respectively. The cross represents the peak position of the IRS5N continuum. Synthesized beam is shown in black at the bottom right corner of each image.

stellar position at the velocity range of 5.02 km s^{-1} – 6.19 km s^{-1} which is much more prominent than the deficit seen on the C^{18}Ochannel maps (Figure 4.19). This is most likely due to the continuum over-subtraction, similar to that of the C^{18}Oemission. This suggests that the ^{13}CO emission is extended and somewhat optically thick, leading it to become resolved-out as $\theta_{MRS} = 2\farcs91$. The moment maps of ^{12}CO and ^{13}CO reveal the complex nature of the emission around IRS5N.

We also detected molecular emission in ^{12}CO (2–1) and ^{13}CO (2–1) towards IRS5. Figure 4.6 (a) shows the moment 0 maps of ^{12}CO emission around IRS5a and IRS5b. The ^{12}CO emission around IRS5a is compact, with no visible outflow structure. In contrast, bright, elongated emission is observed toward IRS5b in the east-west direction, possibly tracing an outflow from IRS5b. The emission has a velocity gradient and relatively high velocities from -1.58 km s^{-1} – 2.23 km s^{-1} and 9.85 km s^{-1} – 13.03 km s^{-1} as shown in the ^{12}CO channel maps in Figure 4.7. Additionally, bright extended emission is also seen around IRS5b which connects its way into IRS5a. Based on the ^{12}CO emission towards the IRS5 binary, we estimate its systemic velocity to be ∼6.50 km s^{-1}. The channel maps show that the blue-shifted emission seems to emanate from IRS5b and stream onto IRS5a as the velocity increases. Similar stream- or bridge-like features are observed toward other protostellar binaries (e.g., Sadavoy et al., 2018; van der Wiel et al., 2019; Jørgensen et al., 2022) and may trace transport of material between the companions triggered by interactions during their mutual orbits (e.g., Kuffmeier et al., 2019; Jørgensen et al., 2022). The streaming emission appears to end in a disk-like structure around IRS5a, seen in channel maps of 6.68 km s^{-1} – 9.85 km s^{-1}. Notably, this structure is

much larger than the observed size of the dust continuum structure of IRS5a seen in Figure 4.1, indicating it likely traces the inner envelope surrounding the disk. Additionally, in channel maps ranging from 7.31 km s^{-1} to 8.58 km s^{-1}, extended emission possibly tracing an outflow is seen towards the southeast of IRS5a. Conversely, the ^{13}CO emission in Figure 4.6 (b) traces the extended mutual envelope material surrounding both sources. The emission is much brighter towards IRS5b than IRS5a, with the brightness peak towards the southwest of IRS5b.

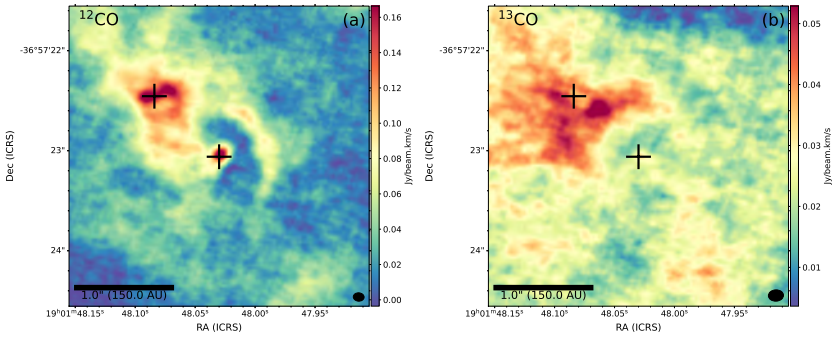

FIGURE 4.6 Zoomed-in moment 0 maps of ^{12}CO emission (a) around the IRS5 binary source and ^{13}CO emission (b) around the IRS5 binary source. The crosses represent the peak position of the continuum emission of IRS5a and IRS5b sources. The maps are created by integrating over the velocity ranges of -4.75–14.93 km s^{-1} and 2.85 – 9.86 km s^{-1} for ^{12}CO and ^{13}CO , respectively. Synthesized beam is shown in black at the bottom right corner of each image.

H_2CO

In addition to the CO isotopologues, we also detect emission from three H_2CO lines towards IRS5N. Figure 4.3 shows that the emission structure of the three transitions are similar to one another, with most of the emission surrounding the disk and inner envelope with extended emission towards the northwest and southeast direction of the source. There is a slight velocity difference between the two sides of the extended source as shown by the moment 1 maps. The $3_{0,3}$–$2_{0,2}$ transition has the lowest upper-level energy and is also the strongest, as expected. A magnified view of the moment 0 and moment 1 maps of the brightest transition of H_2CO, $3_{0,3}$–$2_{0,2}$, is shown in Figure 4.8. The zoomed-in maps reveal that besides the large-scale emission, some red-shifted emission is visible towards the west of the disk, similar to that of the C^{18}O emission (see Figure 4.4), but appears to lack the corresponding blue-shifted counterpart, suggesting asymmetric distribution of the chemical composition of the disk/envelope system.The velocity channel maps show that there is negative emission at the position of the protostar which again is likely caused by continuum over-subtraction (see Figure 4.16, 4.22). However, the large-scale negatives seen in the velocity channel maps suggest that a significant amount of flux is getting resolved out.

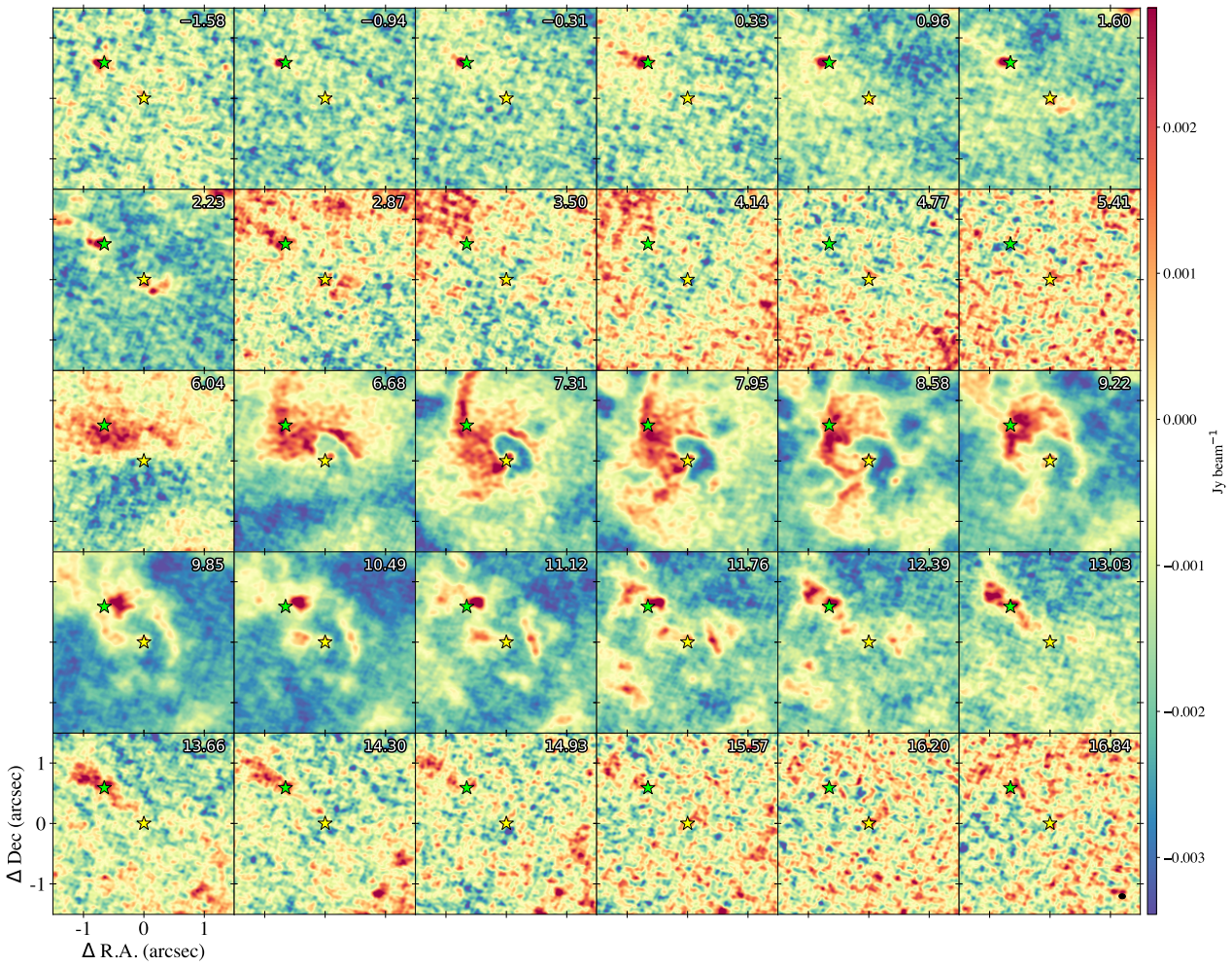

FIGURE 4.7 Channel maps showing the ^{12}CO emission around the two sources of the IRS5 system. The yellow star and the green star show the peak position of the continuum emission of IRS5a and IRS5b, respectively. The numbers at the top show the corresponding velocity of each channel map. Synthesized beam is shown in black at the bottom right corner of the final channel map.

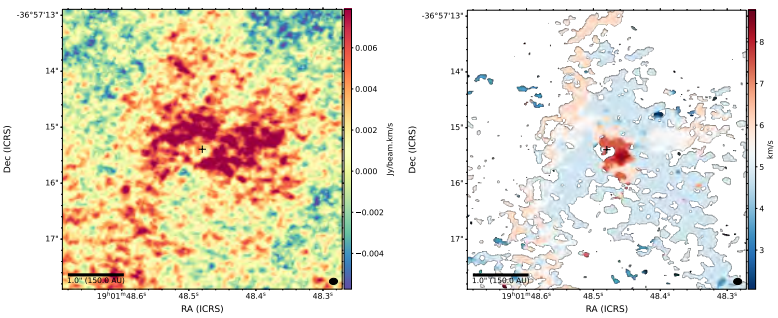

FIGURE 4.8 Same as Figure 4.5 but for H_2CO ($3_{0,3}$–$2_{0,2}$) instead. The maps are created by integrating over the velocity ranges of 2.06 – 8.76 km s^{-1}.

4.4 ANALYSIS AND DISCUSSION

4.4.1 *Continuum Modeling*

As shown in Figure 4.1, even though we sufficiently resolve the disk of IRS5N, no apparent substructures can be identified in the continuum emission. IRS5a also appear to be relatively smooth, while IRS5b is not resolved.

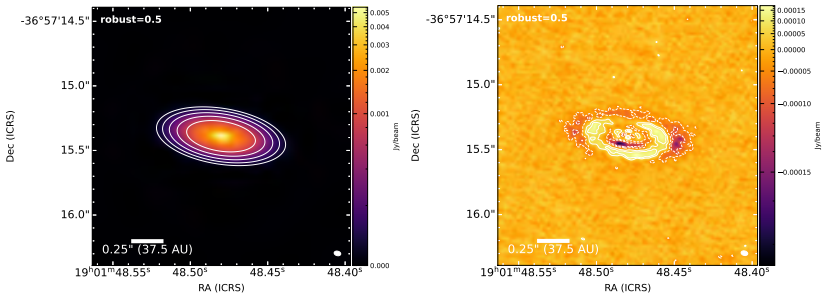

FIGURE 4.9 IRS5N disk model (*left*) and residual (*right*) created using double Gaussian components. Contours show the 3σ, 6σ, 12σ, 24σ and 48σ. The dashed contours indicate negative intensity. The white ellipse on the bottom right corner of each image shows the synthesized beam.

Figure 4.9 shows the best-fit model and its corresponding residual of the continuum emission of IRS5N made with CASA task `imfit`. The model was created using two 2D Gaussian components as a single Gaussian model misses a lot of emission of the continuum. The residual image and the intensity plots in Figure 4.10 show that the double-component model is able to recover most of the continuum emission. The fitting results of both models are provided in Table 4.3. The parameters of the disk continuum such as its peak position, P.A., and i do not change significantly between the two components of the model. It is important to note that the residuals are a result of the model not representing the structure of the emission and can not necessarily be taken as evidence of the presence of substructures in the distribution of material within the dusty disk. The residual image shows that there is some asymmetry in the direction of the minor axis (North-South). The disk appears to be brighter in the south compared to the north. Such asymmetry in the minor axis is observed in several eDisk sources (Ohashi et al., 2023). This can be attributed to the geometrical effects of optically thick emission and flaring of the disk (Takakuwa et al., in prep.). The north side of the disk is more obscured compared to the south which is expected to be on the far side of the disk with $i \sim 65°$, where 90° represents the completely edge-on case.

We also fit the continuum emission for both sources in the IRS5 system. Figure 4.11 shows the model and the residual created of IRS5a and IRS5b after subtracting a single 2D Gaussian. The model is able to reasonably capture the majority of the continuum emission from both sources as seen from the residual images. The results of the fitting are provided in Table 4.3.

4.4.2 *Kinematics of the disk: Position-velocity diagram*

The kinematics of the protostellar disk are investigated with position-velocity (PV) diagrams of molecular line emission that trace the disk. For IRS5N,

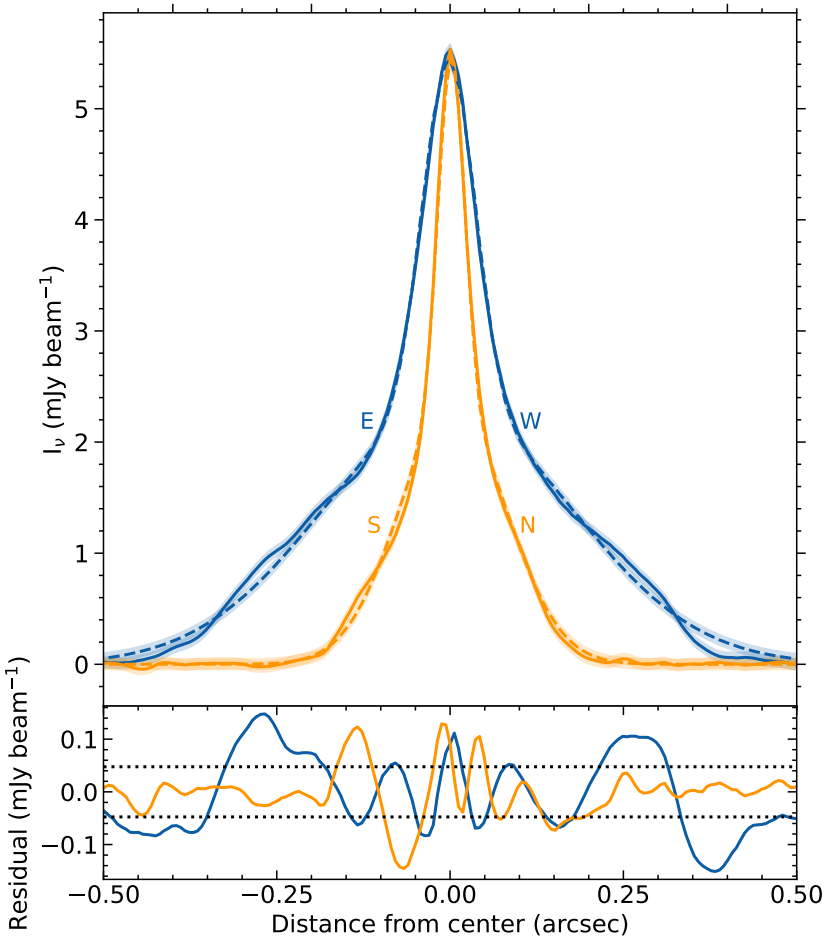

FIGURE 4.10 Intensity profiles of the 1.3 mm continuum emission of IRS5N shown in Figure 4.1(b) and double Gaussian component model shown in Figure 4.9. The solid line represents the observed emission and the dashed line represents the model. The blue lines indicate the intensity along the major axes and the orange lines represent the intensity along the minor axes. The smaller plot at the bottom shows the residual intensity after subtracting the model from the observation. The shaded region and the horizontal dotted lines indicate $\pm 3\sigma$ uncertainties with $\sigma = 0.016$ mJy beam^{-1}.

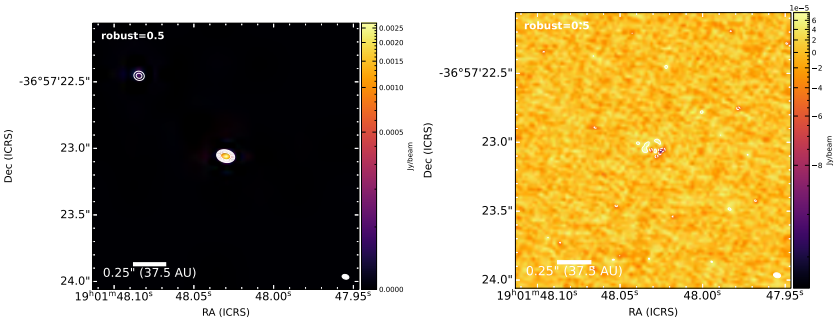

FIGURE 4.11 Same as Figure 4.10 but for IRS5a binary source with the model made with a single Gaussian peak for each continuum emission observed.

$C^{18}O$is the only molecule where evidence of rotation is seen in the protostellar disk (see Figure 4.3). $C^{18}O$is much less optically thick and is a better disk tracer than other CO isotopologues, making it an excellent species for PV analysis. Figure 4.12 shows the PV diagram of IRS5N in $C^{18}O$along the major axis of the disk. The PV diagram shows that the blue-shifted emission and

TABLE 4.3 Best-fit parameters.

Parameter	Single Gaussian Component			Double Gaussian Components	
	IRS5N	IRS5a	IRS5b	IRS5N	
				Component 1	Component 2
R.A (h:m:s)	19:01:48.480	19:01:48.030	19:01:48.084	19:01:48.480	19:01:48.480
Dec (d:m:s)	-36:57:15.39	-36:57:23.06	-36:57:22.46	-36:57:15.39	-36:57:15.39
Beam size ($''$)	0.05 × 0.03	0.05 × 0.03	0.05 × 0.03	0.05 × 0.03	0.05 × 0.03
Beam P.A. (°)	75.44	75.44	75.44	75.44	75.44
$\theta_{\rm maj}$ (mas) †	373.7 ± 7.1	22.91 ± 0.95	46 ± 16	73.58 ± 1.69	423.9 ± 3.0
$\theta_{\rm min}$ (mas) †	156.7 ± 2.9	16.82 ± 0.56	40 ± 26	28.32 ± 0.76	179.4 ± 1.3
P.A. (°) †	81.10 ± 0.76	84.7 ± 5.7	174 ± 54	81.22 ± 0.80	81.08 ± 0.29
Inclination (°)	65.21 ± 0.70	42.76 ± 3.29	29.59 ± 74.38	67.36 ± 0.84	64.96 ± 0.27
Peak Intensity (mJy beam^{-1})	2.970 ± 0.054	3.893 ± 0.020	0.174 ± 0.00022	3.172 ± 0.039	2.286 ± 0.016
Flux Density (mJy)	99.1 ± 1.9	4.727 ± 0.041	0.361 ± 0.00063	7.09 ± 0.12	98.30 ± 0.69

† Values are deconvolved from the beam.

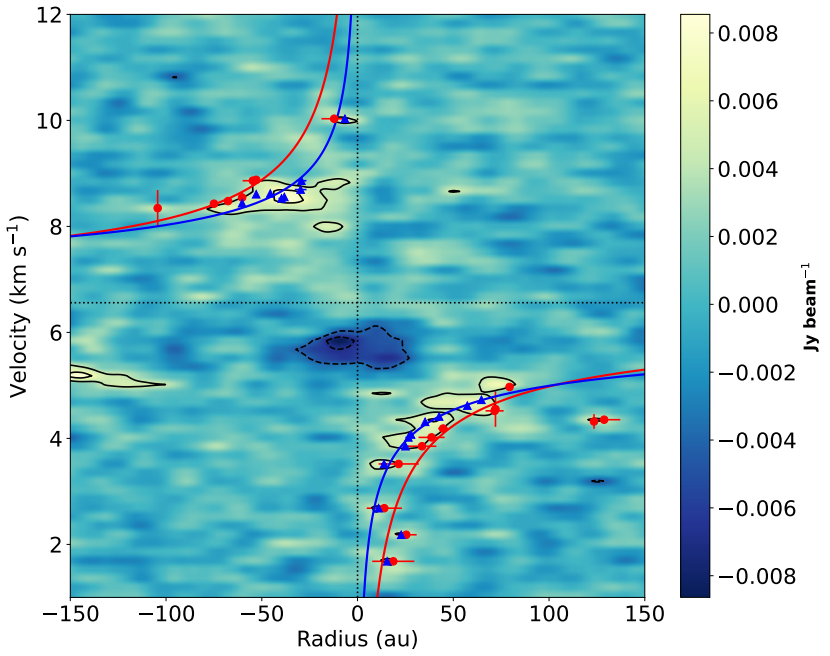

FIGURE 4.12 PV diagram of $C^{18}O$emission towards IRS5N cut along its major axis. The points derived using the "edge" and "ridge" methods and their corresponding rotation curves are shown in blue and red, respectively. The black contours start at 3σ level and increase every 2σ. Dashed contours show the corresponding negative contours.

the red-shifted emission are separated in the northeast and the southwest, respectively.

The PV diagram was fitted using the `pvanalysis` package of the Spectral Line Analysis/Modeling (SLAM)[1] code (Aso & Sai, 2023) to investigate the nature of the rotation. The details of the fitting procedure are given in Ohashi et al. (2023), but a short description is provided here. The code determines the corresponding position at a given velocity using the PV diagram and calculates two types of representative points known as the edge and the ridge. The ridge is defined as the intensity-weighted mean calculated with

[1] https://github.com/jinshisai/SLAM

Table 4.4. PV fitting results for $C^{18}O$with SLAM

Fitting method	Edge	Ridge
R_b (au)	76.98 ± 2.30	42.80 ± 0.44
p_{in}	0.554 ± 0.047	0.379 ± 0.012
v_{sys} (km s^{-1})	6.564 ± 0.024	6.507 ± 0.008
M_{in} ($M_\odot$)	0.398 ± 0.041	0.184 ± 0.008

emission detected above a given threshold, while the edge corresponds to the outermost contour defined by a given threshold. For the analysis of the PV diagram of the $C^{18}O$emission around IRS5N, a threshold of 3σ level was used, where $\sigma = 1.636$ mJy $beam^{-1}$. The edge and the ridge are then fit separately with a single power-law function given by

$$V_{\rm rot} = V_b \left(\frac{R}{R_b}\right)^{-p} + V_{sys}, \tag{4.3}$$

where $V_{\rm rot}$ is the rotational velocity, R_b is the break radius, V_b is the rotational velocity at R_b, p is the power-law index, and V_{sys} is the systemic velocity of the system.

The fitting results of the SLAM code are summarized in Table 4.4. Here, the ridge points are calculated using the 1D intensity weighted mean profile, called "mean" fitting method. However, the ridge points can also be calculated using the center of the Gaussian fitting. Using this "Gaussian" fitting method, we get $R_b = 39.75 \pm 0.76$ au, $p_{in} = 0.515 \pm 0.029$, $v_{sys} = 6.464 \pm 0.020$ km s^{-1}, and $M_{in} = 0.246 \pm 0.015$ ($M_\odot$), which are consistent to the values derived from the "mean" method. In the case of both the edge and ridge methods, the value of p_{in} is found to be close to 0.5, suggesting that the disk of IRS5N is already in Keplerian rotation. Typically, Keplerian rotation is commonly observed in more evolved sources (Simon et al., 2000). However, recent studies have found that some Class 0 sources already possess Keplerian disks (e.g. Tobin et al., 2012; Ohashi et al., 2014, 2023). In both the ridge and the edge methods, Keplerian rotation is observed out to a radius of ∼40 au and ∼76 au, respectively. The FWHM of the disk continuum falls well within this range, indicating that it could serve as a reliable indicator of the disk size of IRS5N. Under this assumption, the mass of the central source of IRS5N is estimated to be 0.398 ± 0.041 $M_\odot$ and 0.184 ± 0.008 $M_\odot$ for the edge and the ridge cases, respectively. The actual mass of the central source likely lies between these two estimates, approximately 0.3 $M_\odot$ (Maret et al., 2020). This shows that with a stellar mass of ∼0.3 $M_\odot$ compared to a disk mass of $\sim 0.007 - 0.02 M_\odot$ and an envelope mass of 1.2 $M_\odot$, IRS5N is a deeply embedded protostar.

The stability of the disk against gravitational collapse can be estimated by using Toomre's Q parameter

$$Q = \frac{c_s \Omega}{\pi G \Sigma}, \tag{4.4}$$

where c_s is the sound speed, $\Omega = GM_*/R^3$ is the differential rotation value of a Keplerian disk at the given radius R, M_* is the mass of the protostar, G is the gravitational constant, and Σ is the surface density. A disk is considered gravitationally stable if $Q > 1$, while $Q < 1$ suggests that the disk may be prone to fragmentation. This equation can also be expressed in the form given by Kratter & Lodato (2016) and Tobin et al. (2016) as

$$Q \approx 2\frac{M_* H}{M_d R}, \tag{4.5}$$

where $H = c_s/\Omega$, M_d is the mass of the disk, and R is the radius of the disk. For IRS5N with $M_* = 0.3\ M_\odot$ and $R = 62$ au, we find $Q \approx 3.5$ and 15 for disk masses of $0.019\ M_\odot$ and $6.65 \times 10^{-3} M_\odot$ at 20 K and 47 K, respectively. This implies that the disk of IRS5N is gravitationally stable.

4.4.3 *The low molecular emission around IRS5N*

In Section 4.3, we mention that although we see extended emission in ^{12}CO and ^{13}CO in the region around IRS5N, we do not see any clear signs of outflow in these molecules. Emission is also not detected in SiO (J=5–4) or SO (J=6_5–5_4), both of which are known tracers of outflow and shocks (e.g., Schilke et al., 1997; Wakelam et al., 2005; Ohashi et al., 2014; Sakai et al., 2014). This is in contrast to most known young Class 0/I sources, where observations of a prominent outflow have become ubiquitous. Additionally, most of the emission detected in H_2CO, the only other molecule besides the CO isotopologues detected around IRS5N, is at a tentative level of $3\sigma - 5\sigma$.

The curious case of low emission around IRS5N has also been noted by previous studies (Nutter et al., 2005; Lindberg et al., 2014). Lindberg et al. (2014) specifically noted that only marginal residuals remained in the *Herschel*/PACS maps of the region when assuming that all emission originated from the IRS5 source. Recent studies suggest that previously thought young Class 0 objects exhibiting weak molecular line emission and lack prominent high-velocity outflow structures may actually be potential candidates for first hydrostatic core (FHSC) (Busch et al., 2020; Maureira et al., 2020; Dutta et al., 2022). These FHSC objects, however, have a relatively short lifetime of $\sim 10^3$ yr and simulations predict their luminosities to be $\sim 0.1\ L_\odot$ with the mass of the central source of $\lesssim 0.1\ M_\odot$ (Commerçon et al., 2012; Tomida et al., 2015; Maureira et al., 2020). Considering that IRS5N has a bolometric luminosity of $1.40\ L_\odot$ and a protostellar mass of $0.3\ M_\odot$, it has already progressed well beyond the FHSC stage and this most likely is not the explanation for the observed low emission and lack of outflow. Nonetheless, given the presence of a massive envelope of $\sim 1.2\ M_\odot$ surrounding IRS5N, it is likely to become much more massive in the future.

The peculiarity of the molecular emission characteristics of IRS5N are most likely explained by the complexity of the Coronet region. IRS7B, another YSO source of eDisk from the Coronet region, also seems to lack an outflow in the spectral lines (Ohashi et al., 2023). The Coronet hosts numerous YSOs and Molecular Hydrogen emission-line Objects (MHOs) with more than 20 Herbig-Haro (HH) objects (see Wang et al., 2004, and references therein). Such an environment might be affecting the molecular emission seen from these sources. ^{12}CO, being optically thick, is the most

affected. We do observe ^{13}CO emission in the North-South direction of the source, roughly in the direction where the outflow is expected. However, this is only seen at low velocity, red-shifted channel maps. C^{18}Oappears to be the least affected among the CO isotopologues as it is the most optically thin of the three and is not as hidden behind the optically thick emission from the cloud like ^{12}CO and ^{13}CO making it mostly sensitive to the inner disk where the CO is evaporated from the dust grains (Jørgensen et al., 2015).

4.5 CONCLUSIONS

We have presented high-resolution, high-sensitivity observations of the protostar IRS5N and its surroundings as part of the eDisk ALMA Large program. Our ALMA band 6 observation had a continuum angular resolution of $\sim 0\farcs05$ ($\sim$8 au) and molecular line emission from C^{18}O, ^{12}CO, ^{13}CO, and H_2CO. The main results of the paper are as follows:

1. The 1.3 mm dust continuum emission traces protostellar disks around IRS5N and IRS5. The continuum emissions appear smooth, with no apparent substructures in either source. However, the disk of IRS5N shows brightness asymmetry in the minor axis, with the southern region appearing brighter than the northern region. The asymmetry can be attributed to the geometrical effects of optically thick emission and flaring of the disk.
2. IRS5N has a disk radius of $\sim$62 au elongated along the northeast to southwest direction with a P.A. of 81.10°. IRS5a has a much smaller disk radius of $\sim$13 au with a P.A. of $\sim$85°. The disk of IRS5b remains unresolved. Using the total integrated intensity of each source and assuming a temperature of $T = 20$ K, which is a typical dust temperature for Class II disks, the estimated disk masses for IRS5N, IRS5a, and IRS5b are 0.02, 9.18×10^{-4}, and 6.48×10^{-5} $M_\odot$, respectively. At a temperature of $T = 47$ K based on radiative transfer, the estimated disk masses for IRS5N and IRS5a are 6.65×10^{-3} and 3.20×10^{-4} $M_\odot$, respectively.
3. Disk rotation is observed in the C^{18}O emission around IRS5N, with the blue- and red-shifted emission separated along the major axis of the disk. PV analysis of the emission reveals the disk is in Keplerian rotation. The stellar mass of the central source of IRS5N is estimated to be $\sim$0.3 $M_\odot$.
4. Using a 1D dust radiative transfer model, the estimated envelope mass around IRS5N is 1.2 $M_\odot$. The envelope mass is much greater than the disk mass of 0.02 $M_\odot$ and stellar mass of 0.3 $M_\odot$ indicating IRS5N is a highly embedded protostar.
5. The ^{12}CO and ^{13}CO maps towards IRS5N are complex and lack any apparent indication of an outflow or cavity. In contrast, the ^{12}CO maps around IRS5 show emission streaming from IRS5b to IRS5a, tracing the gas connecting to the disk-like structure around the latter. This observation potentially suggests material transport between the two sources.

ACKNOWLEDGMENTS

This paper makes use of the following ALMA data: ADS/ JAO.ALMA#2019.1.00261.L. ALMA is a partnership of ESO (representing its member states), NSF (USA), and NINS (Japan), together with NRC (Canada), MOST and ASIAA (Taiwan), and KASI (Republic of Korea), in cooperation with the Republic of Chile. The Joint ALMA Observatory is operated by ESO, AUI/NRAO, and NAOJ. The National Radio Astronomy Observatory is a facility of the National Science Foundation operated under cooperative agreement by Associated Universities, Inc. R.S, J.K.J, and S.G. acknowledge support from the Independent Research Fund Denmark (grant No. 0135-00123B). S.T. is supported by JSPS KAKENHI grant Nos. 21H00048 and 21H04495. This work was supported by NAOJ ALMA Scientific Research Grant Code 2022-20A. L.W.L. acknowledges support from NSF AST-2108794. J.J.T. acknowledges support from NASA XRP 80NSSC 22K1159. N.O. acknowledges support from National Science and Technology Council (NSTC) in Taiwan through grants NSTC 109-2112-M-001-051 and 110-2112-M-001-031. S.P.L. and T.J.T. acknowledge grants from the National Science and Technology Council of Taiwan 106-2119-M-007-021-MY3 and 109-2112-M-007-010-MY3. I.d.G. acknowledges support from grant PID2020-114461GB-I00, funded by MCIN/AEI/ 10.13039/501100011033. Z.Y.D.L. acknowledges support from NASA 80NSSCK1095, the Jefferson Scholars Foundation, the NRAO ALMA Student Observing Support (SOS) SOSPA8-003, the Achievements Rewards for College Scientists (ARCS) Foundation Washington Chapter, the Virginia Space Grant Consortium (VSGC), and UVA research computing (RIVANNA). Z.-Y.L. is supported in part by NASA NSSC20K0533 and NSF AST-1910106. W.K. was supported by the National Research Foundation of Korea (NRF) grant funded by the Korea government (MSIT; NRF-2021R1F1A1061794). C.W.L. is supported by the Basic Science Research Program through the National Research Foundation of Korea (NRF) funded by the Ministry of Education, Science and Technology (NRF- 2019R1A2C1010851), and by the Korea Astronomy and Space Science Institute grant funded by the Korea government (MSIT; Project No. 2023-1-84000). H.-W.Y. acknowledges support from the National Science and Technology Council (NSTC) in Taiwan through the grant NSTC 110-2628-M-001-003- MY3 and from the Academia Sinica Career Development Award (AS-CDA-111-M03). Y.A. acknowledges support by NAOJ ALMA Scientific Research Grant code 2019-13B, Grant-in-Aid for Transformative Research Areas (A) 20H05844 and 20H05847. J.E.L. is supported by the National Research Foundation of Korea (NRF) grant funded by the Korean government (MSIT; grant No. 2021R1A2C1011718). J.P.W. acknowledges support from NSF AST-2107841.

4.a CHANNEL MAPS

Figure 4.13–4.18 show the selected large-scale channel maps of ^{12}CO, ^{13}CO, C^{18}O, and H_2CO emission observed toward IRS5N. Figure 4.19–4.24 show the zoomed-in view of the molecular emissions observed.

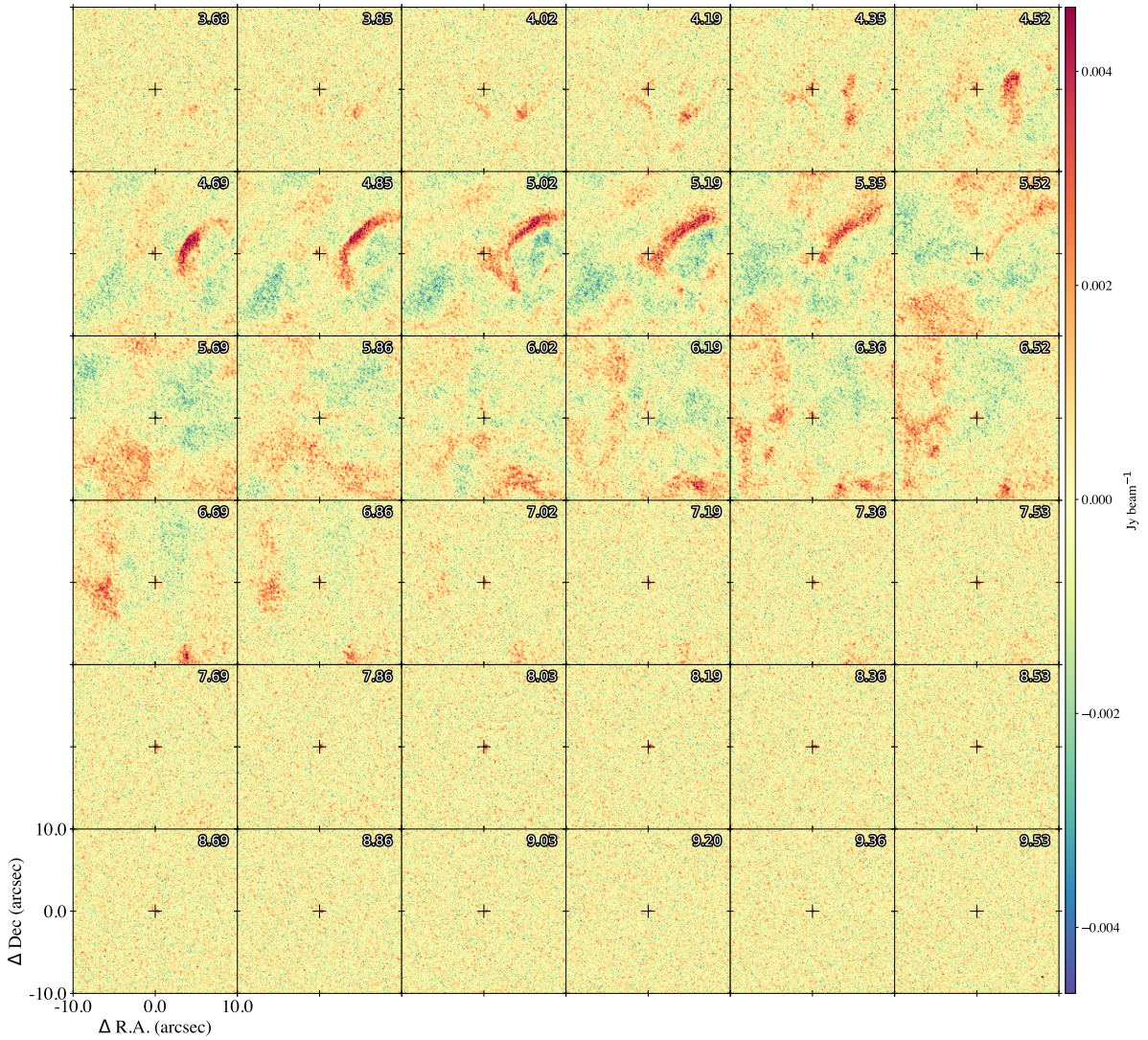

FIGURE 4.13 Selected channel maps showing the $C^{18}O$ (2–1) emission around IRS5N. The numbers at the top show the corresponding velocity of each channel map. The cross shows the peak position of the IRS5N continuum. Synthesized beam is shown in black on the bottom right corner of the final channel.

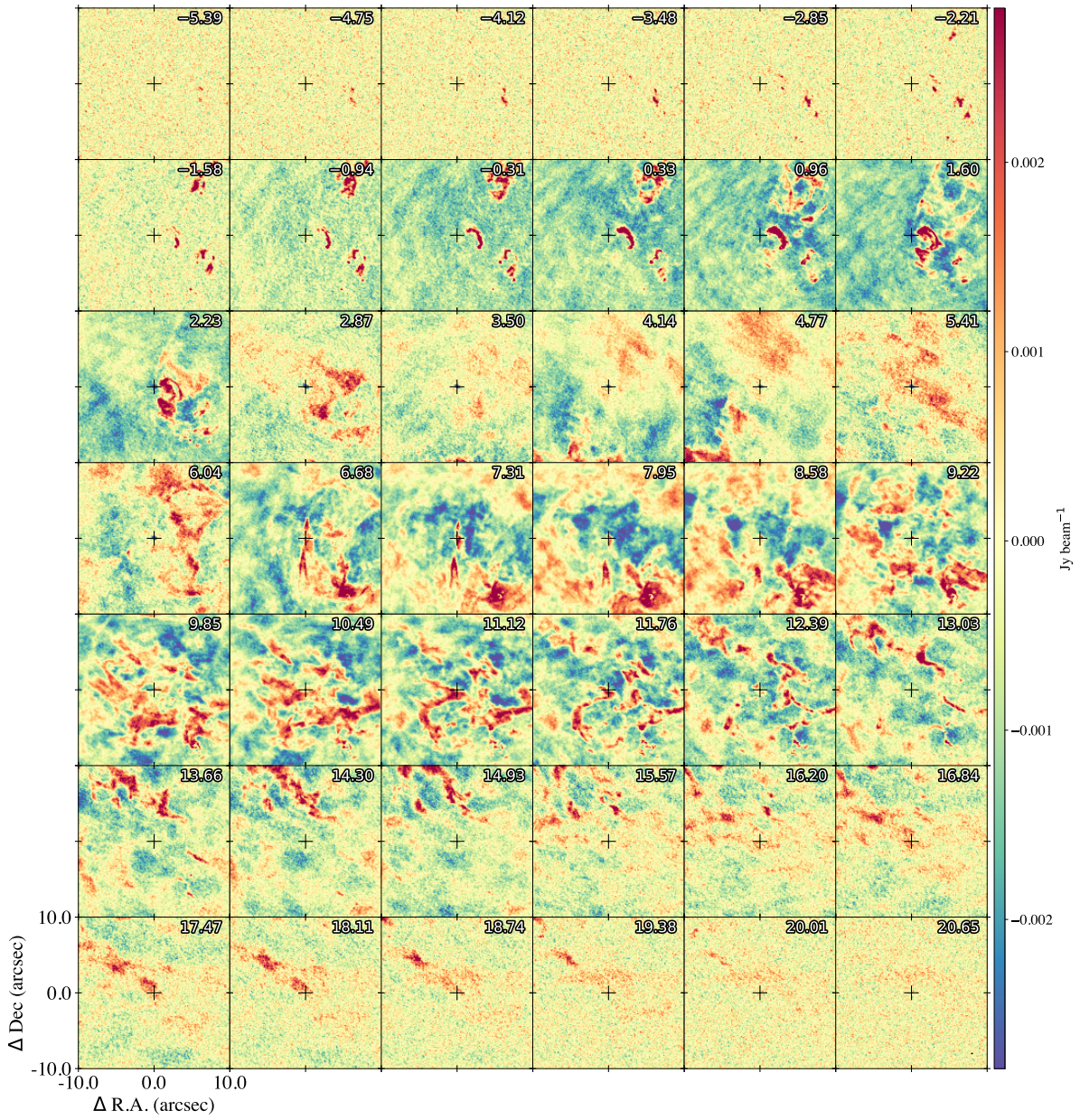

FIGURE 4.14 Same as Figure 4.13 but for ^{12}CO (2–1) instead.

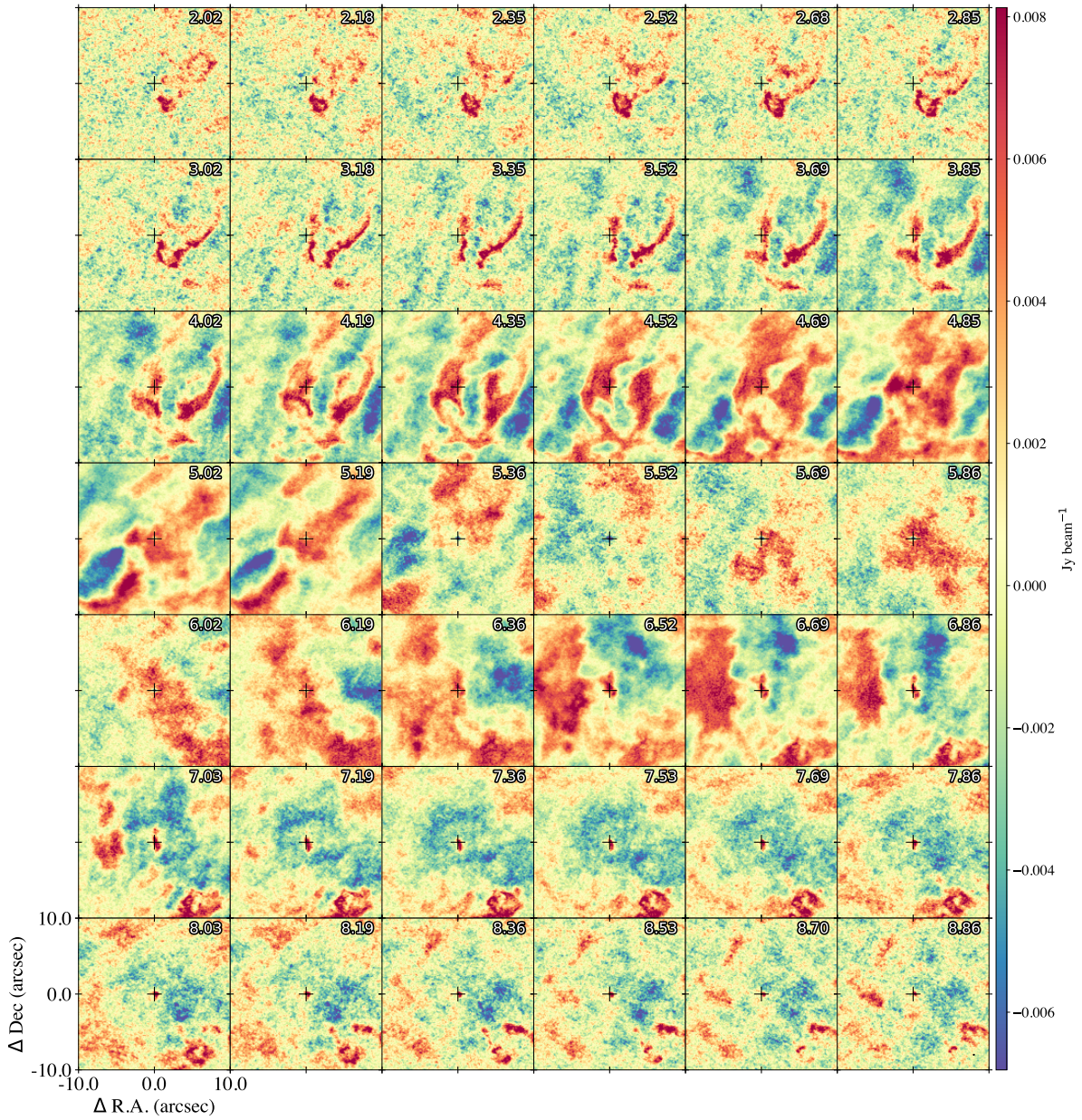

FIGURE 4.15 Same as Figure 4.13 but for ^{13}CO (2–1) instead.

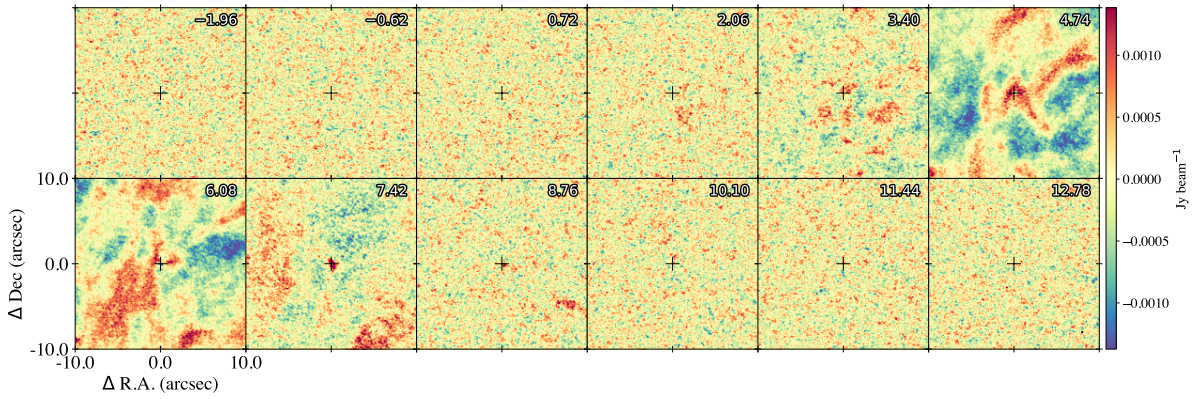

FIGURE 4.16 Same as Figure 4.13 but for H_2CO ($3_{0,3}$–$2_{0,2}$) instead.

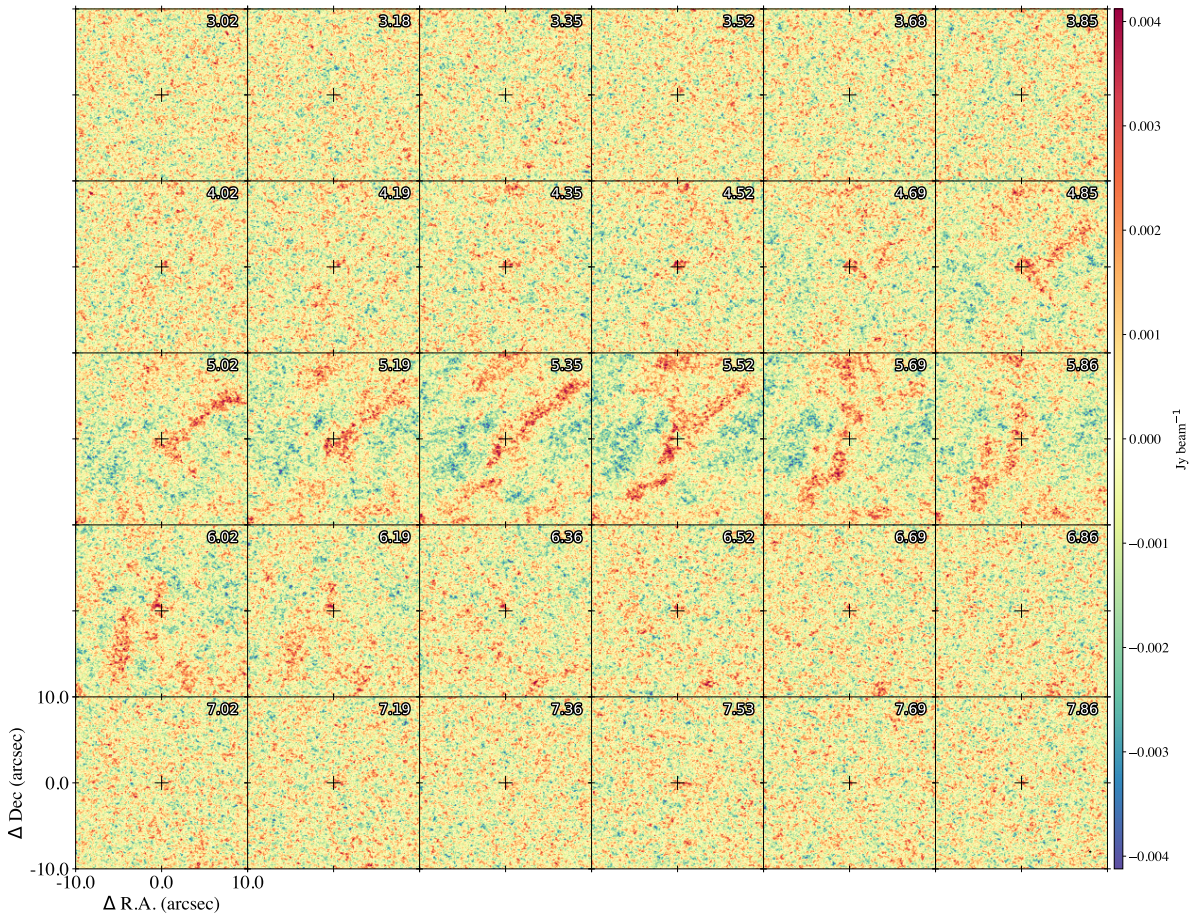

FIGURE 4.17 Same as Figure 4.13 but for H_2CO ($3_{2,1}$–$2_{2,0}$) instead.

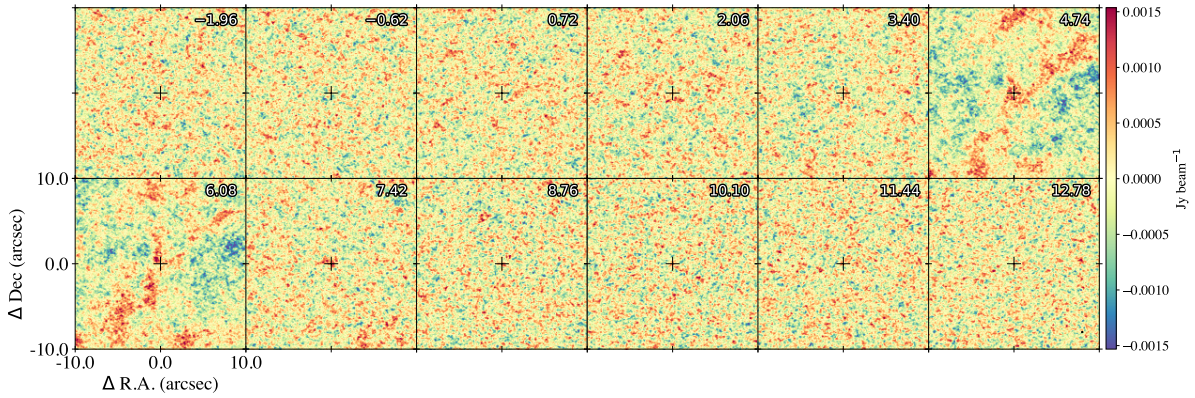

FIGURE 4.18 Same as Figure 4.13 but for H_2CO ($3_{2,2}$–$2_{2,1}$) instead.

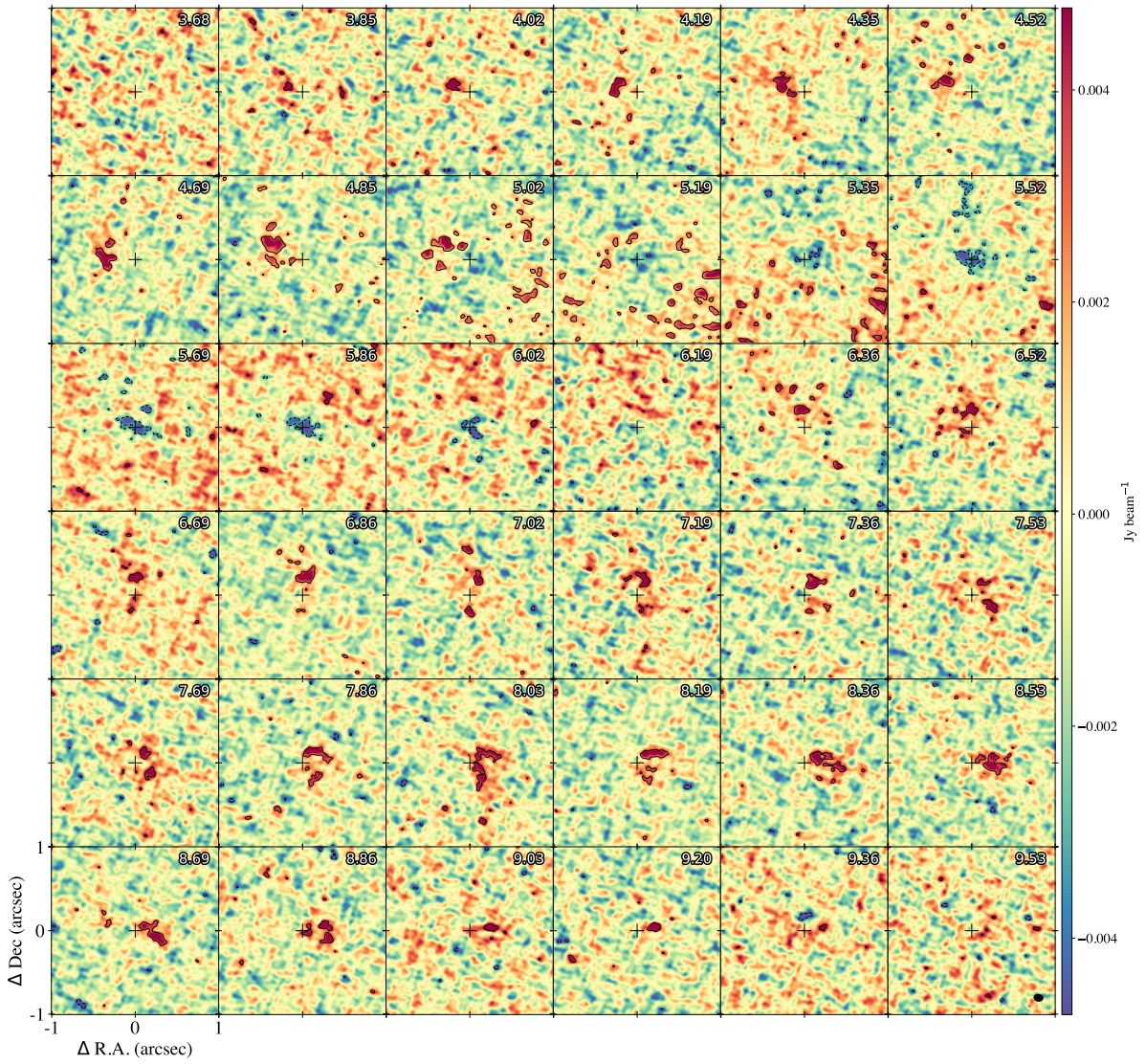

FIGURE 4.19 Channel maps showing the zoomed-in view of the $C^{18}O$ (2–1) emission around IRS5N. The numbers at the top show the corresponding velocity of each channel map. The solid contours represent the 3σ level and the dashed lines show the -3σ level. The cross shows the peak position of the IRS5N continuum. Synthesized beam is shown in black on the bottom right corner of the final channel.

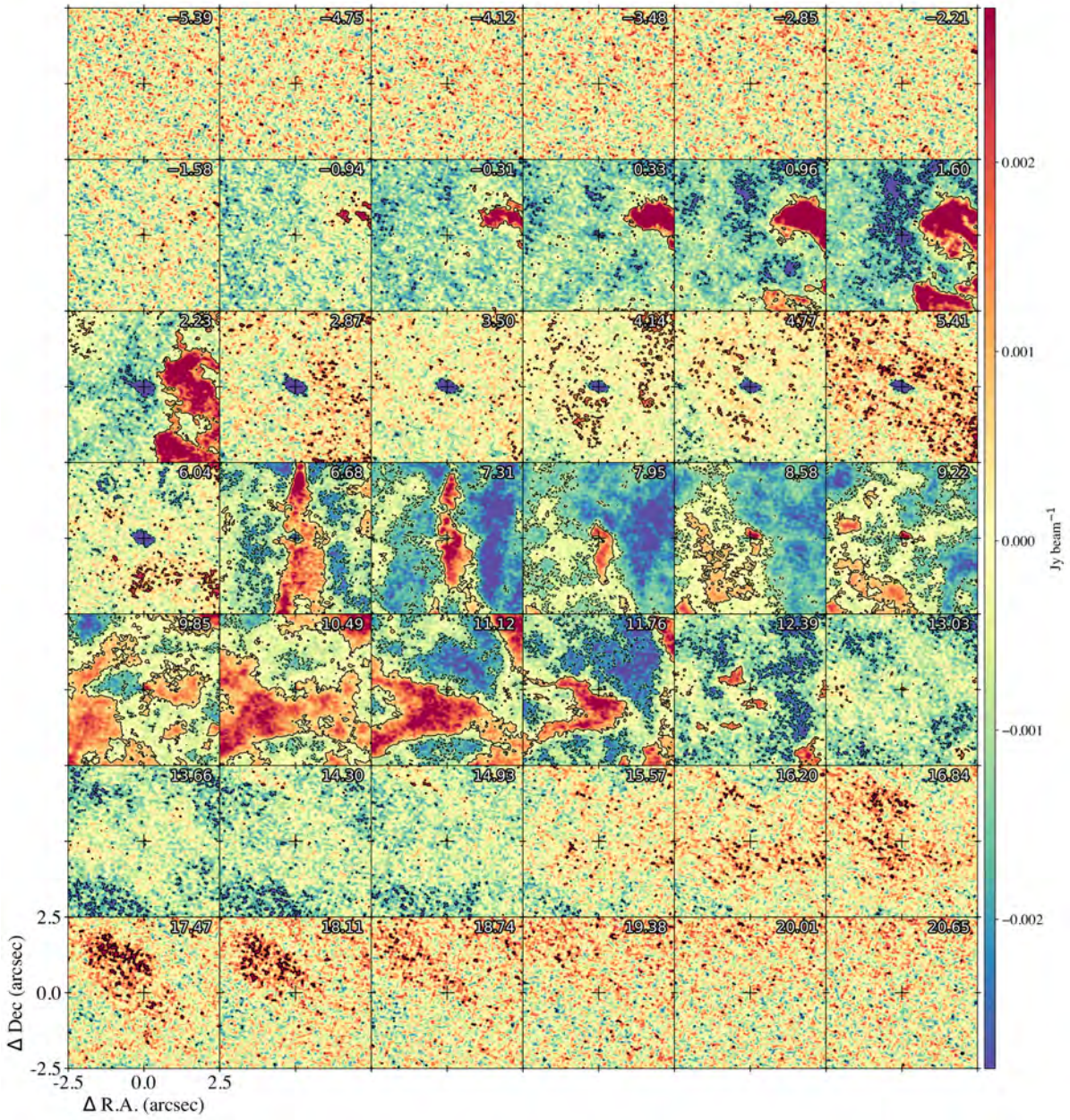

FIGURE 4.20 Same as Figure 4.19 but for ^{12}CO (2–1) instead.

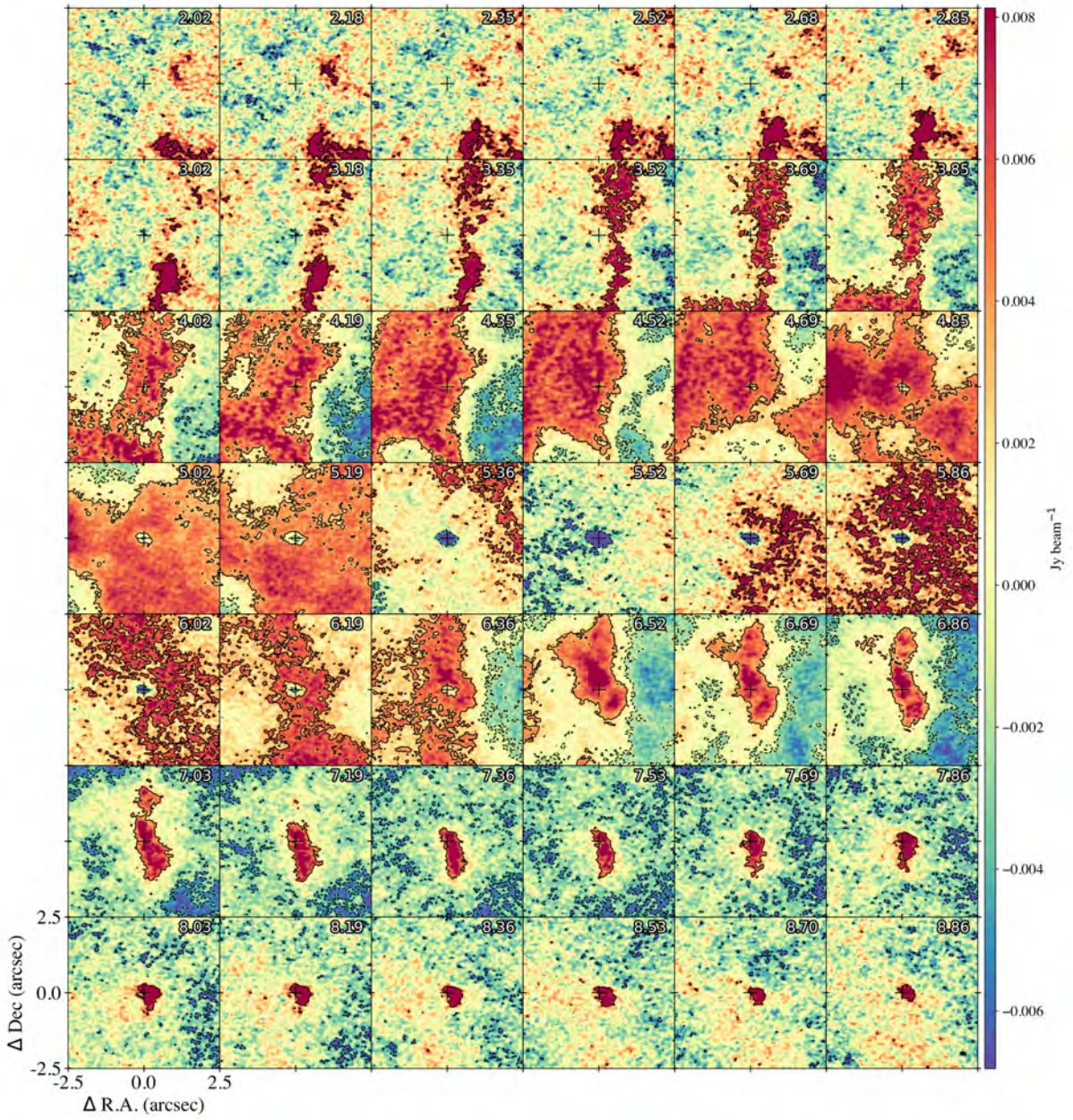

FIGURE 4.21 Same as Figure 4.19 but for ^{13}CO (2–1) instead.

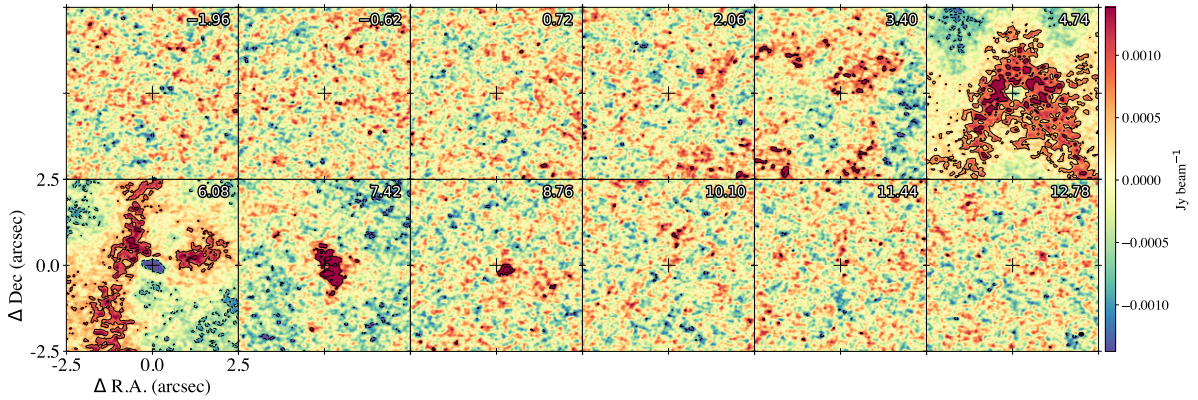

FIGURE 4.22 Same as Figure 4.19 but for H_2CO ($3_{0,3}$–$2_{0,2}$) instead.

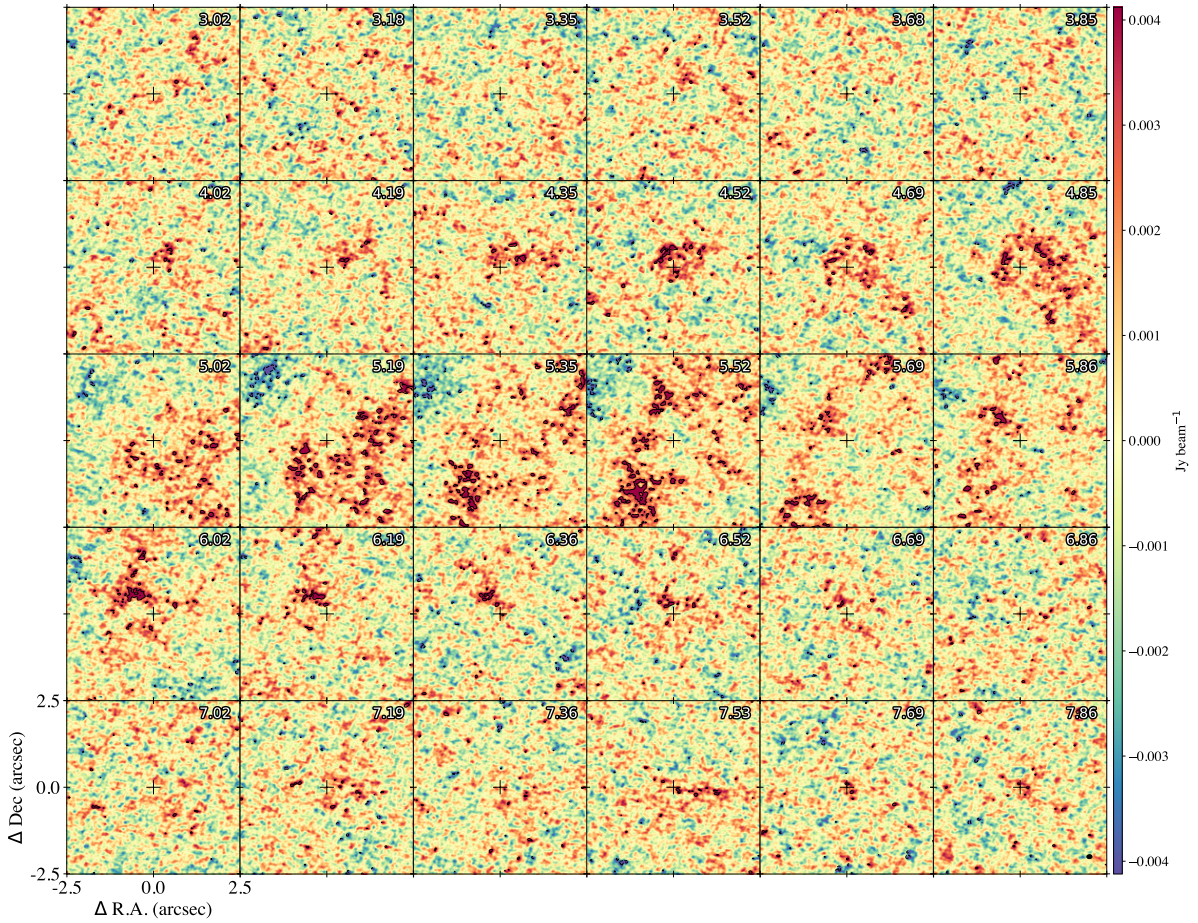

FIGURE 4.23 Same as Figure 4.19 but for H_2CO ($3_{2,1}$–$2_{2,0}$) instead.

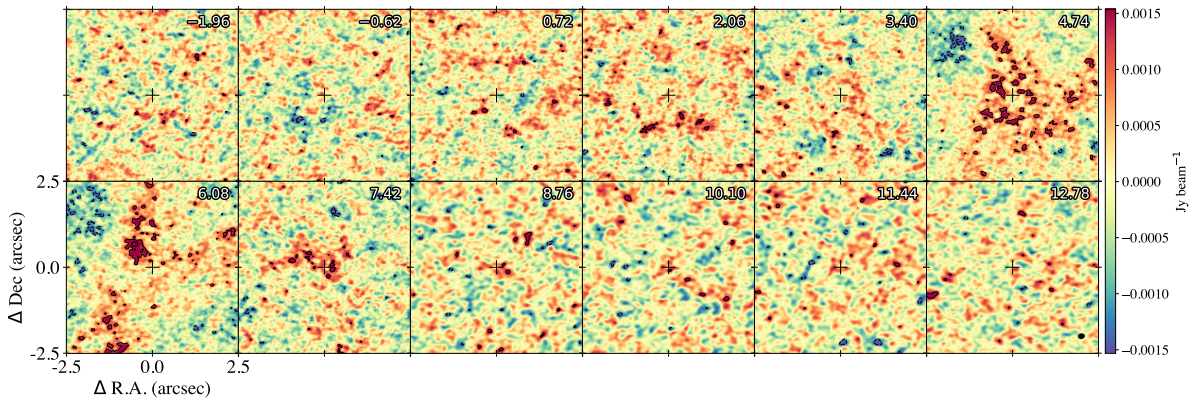

FIGURE 4.24 Same as Figure 4.19 but for H_2CO ($3_{2,2}$–$2_{2,1}$) instead.

5

Early Planet Formation in Embedded Disks (eDisk). XX: Constraining the Chemical Tracers of Young Protostellar Sources

Rajeeb Sharma[1], Jes K. Jørgensen[1], Merel L. R. van 't Hoff[2,3], Jeong-Eun Lee[4], Yuri Aikawa[5], Sacha Gavino[1,6], Yao-Lun Yang[7], Nagayoshi Ohashi[8], John J. Tobin[9], Patrick M. Koch[8], Zhi-Yun Li[10], Leslie W. Looney[9,11], Mayank Narang[8], Suchitra Narayanan[12], Travis J. Thieme[8]

[1] Niels Bohr Institute, University of Copenhagen, Jagtvej 155A, 2200 Copenhagen N., Denmark
[2] Department of Astronomy, University of Michigan, 1085 S. University Ave., Ann Arbor, MI 48109-1107, USA
[3] Department of Physics and Astronomy, Purdue University, 525 Northwestern Avenue, West Lafayette, IN 47907, USA
[4] Department of Physics and Astronomy, SNU Astronomy Research Center, Seoul National University, 1 Gwanak-ro, Gwanak-gu, Seoul 08826, Korea
[5] Department of Astronomy, Graduate School of Science, The University of Tokyo, 113-0033 Tokyo, Japan
[6] Dipartimento di Fisica e Astronomia, Università di Bologna, Via Gobetti 93/2, 40122 Bologna, Italy
[7] RIKEN Cluster for Pioneering Research, Wako-shi, Saitama, 351-0198, Japan
[8] Institute of Astronomy and Astrophysics, Academia Sinica. 11F of Astronomy-Mathematics Building, AS/NTU No.1, Sec. 4, Roosevelt Rd, Taipei 106216, Taiwan, R.O.C.
[9] National Radio Astronomy Observatory, 520 Edgemont Rd., Charlottesville, VA 22903 USA
[10] University of Virginia, 530 McCormick Rd., Charlottesville, Virginia 22904, USA
[11] Department of Astronomy, University of Illinois, 1002 West Green St, Urbana, IL 61801, USA
[12] Institute for Astronomy, University of Hawai'i at Mānoa, 2680 Woodlawn Dr., Honolulu, HI 96822, USA

Submitted to Astronomy and Astrophysics

Abstract

Context. Recent studies indicate that the formation of planets in protoplanetary disks begins early in the embedded Class 0/I phases of protostellar evolution. The physical and chemical makeup of the embedded phase can provide valuable insights into the process of star and planet formation.

Aims. This study aims to provide a thorough overview of the various morphologies for molecular emissions observed on disk scales ($\lesssim$100 au) toward nearby embedded sources.

Methods. We present high angular resolution ($0\farcs1$, $\sim$15 au) molecular line emissions for ^{12}CO, ^{13}CO, C^{18}O, SO, SiO, DCN, CH_3OH, H_2CO, and c–C_3H_2 towards 19 nearby protostellar sources in the context of the Atacama Large Millimeter/submillimeter Array (ALMA) Large Program "Early Planet Formation in Embedded Disks (eDisk)".

Results. Emissions in ^{12}CO are seen towards all sources and primarily trace outflowing materials. A few sources also show high-velocity jets in SiO emission and high-velocity channel maps of ^{12}CO. The ^{13}CO and C^{18}O emissions are well-known tracers of high-density regions and trace the inner envelope and disk regions with clear signs of rotation seen at continuum scales. The large-scale emissions of ^{13}CO also delineate the outflow cavity walls where the outflowing and infalling materials interact with each other, and exposure to UV radiation leads to the formation of hydrocarbons such as c–C_3H_2. Both DCN and CH_3OH, when detected, show compact emissions from the inner envelope and disk regions that peak at the position of the protostar. The CH_3OH emissions are contained within the region of DCN emissions, which suggests that CH_3OH traces the hot core regions. Both SO and H_2CO show complex morphology among the sources, suggesting that they are formed through multiple processes in protostellar systems.

5.1 INTRODUCTION

The formation of low-mass stars like our Sun begins with the gravitational collapse of dense prestellar cores in cold molecular clouds. As the temperature and the pressure increase, the collapsing core eventually forms a protostar, signaling a shift from the prestellar to the protostellar phase. In the earliest phases of protostellar evolution – the Class 0 and Class I stages – the protostar is embedded in an infalling envelope that accounts for a substantial fraction of the mass of the system (Lada & Wilking, 1984; André et al., 1993, 2000). This embedded nature of these young sources has long proved to be an obstacle for directly observing protostellar disks. Consequently, most studies in the past have focused predominantly on the

studies of disks in more evolved Class II sources, where most of the envelope has been accreted or dissipated.

Over its first decade of operations, the Atacama Large Millimeter/submillimeter Array (ALMA) has revolutionized studies of the inner regions of envelopes and structures of protoplanetary disks surrounding young stars in their earliest stages. Figure 5.1 presents an overview of our current understanding of the different components of an embedded protostar, such as its disk, envelope, outflow, etc. These components play an important role during the formation of the protostar and the planets. For instance, protostellar disks regulate the mass accreted by the protostar from the envelope and provide the necessary conditions for the dust grain growth that seeds planet formation (Testi et al., 2014; Maury et al., 2019). Likewise, protostellar outflows and winds eject mass back into the molecular cloud, decreasing the protostar's efficiency of mass accretion and replenishing the turbulent motions via feedback mechanisms (Arce et al., 2007; Nakamura & Li, 2014).

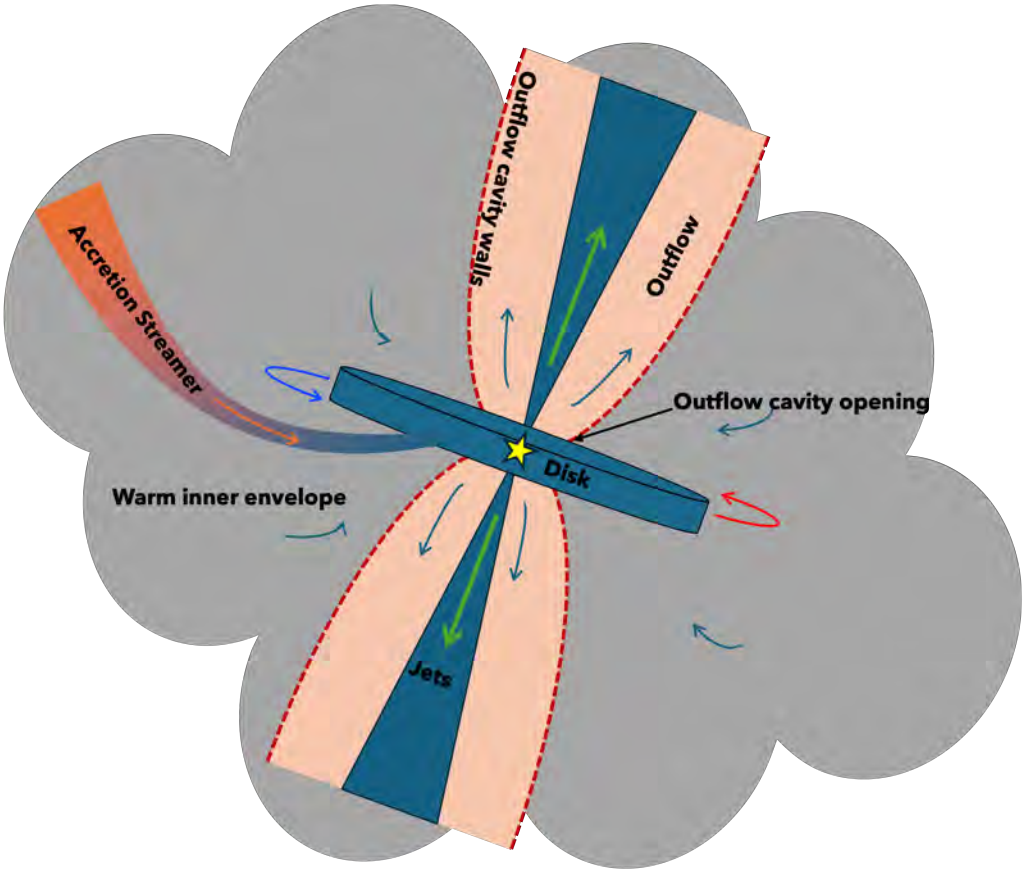

FIGURE 5.1 Cartoon image illustrating the different components present in an embedded protostellar system.

Understanding and characterizing the components of young protostellar systems in detail is therefore crucial in forming a comprehensive picture of star and planet formation. One way to achieve this is to study the molecular line emissions that trace the various components within a protostellar system. These molecules serve as a powerful diagnostic tool for these components and provide valuable insight into the various physical and chemical processes that occur during the formation of stars and planets.

The chemical makeup of a protostellar system is both complex and dynamic. Initially, much of the chemistry of a system is at least partially inherited from the prestellar core and infalling envelope, where most molecules are primarily frozen onto the dust grains (Pontoppidan et al., 2014; Boogert et al., 2015). As the protostar evolves, the wide range of temperatures, densities, and physical processes occurring within its structures facilitate multiple new reaction pathways. Consequently, the original chemical composition undergoes significant changes, giving rise to a variety of new species ranging from basic diatomic molecules to complex organic molecules (COMs) (e.g., see reviews by Herbst & van Dishoeck, 2009; Jørgensen et al., 2020; Öberg et al., 2021).

Astrochemical studies have long aimed to enhance our understanding of protostellar systems through molecular observations. This goal involves two primary objectives: First, to identify unique chemical tracers of specific components of protostellar systems on different spatial scales and in various evolutionary stages of young stars. Second, to thoroughly investigate the chemistry of these various components. An attempt at doing this systematically using ALMA was presented by Tychoniec et al. (2021), who examined the spectral line emissions of various molecules towards 16 Class 0/I protostars in nearby star-forming regions. By combining high-resolution spectral line data from several ALMA observations at different wavelengths (ALMA's Bands 3, 5, and 6), they analyzed emissions from several molecules and developed a comprehensive reference of molecules that traces the various morphologies in Class 0/I sources.

In this work, we present high-resolution ALMA spectral line observations of 19 nearby Class 0 and I protostars from the *Early Planet Formation in Embedded Disks (eDisk)* survey (Ohashi et al., 2023). This work extends on the findings from Tychoniec et al. (2021), offering two key advantages over the previous study. First, unlike the sources in Tychoniec et al. (2021), which were drawn from various studies, the eDisk program utilizes a uniform and well-characterized sample of sources, all observed in the same manner. This provides a more consistent and reliable baseline for comparison between the different sources. Second, the eDisk observations achieve higher spatial resolutions compared to those in the previous study ($\sim$0.″1 compared to $\sim$0.″5 – 3″). This enables us to investigate the physical and chemical processes in the innermost regions of protostellar disks.

Initial results from continuum observations and kinematic analyses of individual eDisk sources have already been presented in a series of first-look papers. These papers show that in contrast to Class II sources, where rings and gaps are ubiquitous, clear substructures are only seen in 2 out of the 19 sources, L1489IRS (Yamato et al., 2023) and OphIRS63 (Flores et al., 2023). Additionally, position velocity (PV) analyses of spectral line emissions have shown that Keplerian-rotating disks are common even in the youngest Class 0 protostars (Aso & Sai, 2023; van 't Hoff et al., 2018; Kido et al., 2023; Sai et al., 2023; Sharma et al., 2023; Thieme et al., 2023). However, while these first-look papers have discussed cases of specific sources, a comprehensive synthesis of the data that identifies and contrasts the different chemical tracers across the entire sample is still lacking. This paper aims to address this gap by systematically analyzing the molecular tracers across all eDisk

sources, providing a holistic view of the molecular tracers in early protostellar systems.

The paper is structured as follows. Sect. 5.2 briefly describes the observations and data reduction processes. The empirical results from the observations of the molecular line emissions are presented in Sect. 5.3. The implications of the results are discussed in Sect. 5.4 and the conclusions are presented in Sect. 5.5.

5.2 OBSERVATIONS

Observations for the sources were conducted in multiple sessions that spanned April 2021 to July 2022 as part of the eDisk ALMA Large program (2019.1.00261.L, PI: N. Ohashi) in Band 6 at a wavelength of 1.3 mm, with supplemental data obtained from the ALMA DDT observations (2019.A.00034.S, PI: J. Tobin). The projected baselines of the observations ranged from 15 m to 12594.5 m, allowing for spatial resolutions of $\sim 0\farcs04$ for the continuum and $\sim 0\farcs1$ for the spectral lines, with slight variations among the sources due to differences in observing conditions and exact array configurations. The spectral setup was set up to probe the dust continuum and a suite of molecular species, including ^{12}CO, ^{13}CO, C^{18}O, SO, SiO, DCN, $c-C_3H_2$, H_2CO, and CH_3OH. Table 5.1 provides an overview of these targeted molecules, together with the velocity resolutions at which they were observed.

Both short and long baseline data were obtained for all sources in our sample, with the exception of OphIRS63, for which only short baseline data could be obtained due to scheduling constraints. The short baseline observations increase the maximum recoverable scale, (θ_{MRS}), of our observations to $\approx 3''$, allowing us to investigate the relatively extended emissions around the sources. A detailed description of the observational parameters, including specific observation dates, number of antennas used, precipitable water vapor levels, and the complete spectral and correlator setups, can be found in Ohashi et al. (2023).

The data were initially calibrated using the standard ALMA pipeline calibrations, which involved bandpass, flux, and phase calibrations. Subsequent reduction and imaging were performed using the Common Astronomy Software Application (CASA; McMullin et al., 2007) version 6.2.1, following a script developed for the eDisk Large program (Tobin, 2023). To enhance the data quality and signal-to-noise ratio, both phase-only and phase and amplitude self-calibration were applied to the continuum data. The number of self-calibrations applied varied by source. The spectral line cubes were then generated by subtracting the continuum emission from the visibility data using the CASA task *uvcontsub*. The derived solutions from the continuum self-calibrations were also applied to the line data. For each source, the final continuum images were created with a range of robust parameters from -2.0 to 2.0, and the line images were created with robust parameters of 0.5 and 2.0. We adopted the robust value of 2.0 for both the continuum contours and the spectral line images used in this work to increase the signal-to-noise ratio, particularly of the weaker spectral line emissions. For OphIRS63, which only has short baseline observations, we adopt the robust value of 0.5. This choice allowed us to keep the beam sizes of its line observations within

TABLE 5.1 Summary of spectral line transitions covered

Molecule	Transition	Rest Frequency (GHz)	Velocity Resolution (km s^{-1})	E_{up} (K)	RMS range† (mJy $beam^{-1}$)
^{12}CO	2–1	230.53800	0.635	16.6	0.83 – 2.14
^{13}CO	2–1	220.398684	0.167	15.9	1.58 – 4.61
$C^{18}O$	2–1	219.560354	0.167	15.8	1.36 – 3.49
SiO	5–4	217.10498	1.340	31.3	0.52 – 1.80
SO	6_5–5_4	219.949442	0.167	35.0	1.75 – 4.33
CH_3OH	4_2–3_1, E	218.440063	1.340	45.6	0.46 – 1.24
DCN	3–2	217.238538	1.340	20.9	0.51 – 1.68
H_2CO	$3_{0,3}$–$2_{0,2}$	218.222192	0.167	21.0	0.45 – 1.14
H_2CO	$3_{2,1}$–$2_{2,0}$	218.760066	1.340	68.1	1.30 – 3.26
H_2CO	$3_{2,2}$–$2_{2,1}$	218.475632	1.340	68.1	0.45 – 1.24
c-C_3H_2[a]	$6_{0,6}$–$5_{1,5}$	217.822148	1.340	38.6	0.47 – 1.36
c-C_3H_2[a]	$6_{1,6}$–$5_{0,5}$	217.822148	1.340	38.6	0.47 – 1.36
c-C_3H_2	$5_{1,4}$–$4_{2,3}$	217.940046	1.340	35.4	0.53 – 1.16
c-C_3H_2	$5_{2,4}$–$4_{1,3}$	218.160456	1.340	35.4	0.45 – 1.19

† This range represents the range of the RMS values obtained towards different sources.
[a] These two lines are blended in eDisk observations.

a factor of $\lesssim$2-3 of the other sources without significantly compromising the signal-to-noise ratio of the images.

In addition, comparable data for the protostars TMC1A (2015.1.01415.S; Bjerkeli et al., 2016; Harsono et al., 2018) and B335 (2013.1.00879.S, 2017.1.00288.S; Yen et al., 2015; Bjerkeli et al., 2019) were taken from the ALMA archive. These raw datasets for these sources were reduced and imaged using the same script developed for the eDisk Large program to ensure consistency.

5.3 RESULTS

Table 5.2 provides a summary of the continuum observations for the eDisk sample. All sources are located within 200 pc and have inclinations greater than 30 degrees, offering favorable viewing angles to study the disks. The bolometric luminosities (L_{bol}) of these sources range from 0.16 $L_\odot$ to 10 $L_\odot$, with a median value of $\sim$1 $L_\odot$, reflecting a diverse set of protostellar objects. In order to characterize the different morphologies and the kinematics observed towards the eDisk sources, we create peak intensity (moment 8) and peak velocity (moment 9) maps for each of the targeted molecules. These maps are made only using pixels where emissions are detected at a level of $\geq 3\sigma$. Figure 5.2 presents an overview of the overall detection statistics, detailing the number of sources that display emissions for each molecule on the left and the number of molecules detected towards each source on the right. Certain molecules such as CO isotopologues, SO, and H_2CO are found throughout the sample, while molecules such as SiO, DCN, and CH_3OH are predominantly detected towards the Class 0 sources.

In this section, we explore the origins of each of the molecules observed towards the eDisk sources along with representative plots. For the purpose

TABLE 5.2 Summary of the eDisk sources

Source Name	Hereafter	Class	Distance (pc)	T_{bol} (K)	L_{bol} ($L_\odot$)	Inclination (°)	References
BHR 71 IRS1	BHR71 IRS1	0	176	66	10	39	(1)
BHR 71 IRS2	BHR71 IRS2	0	176	39	1.1	31	(1)
Ced110 IRS4[a]	Ced110IRS4	0	189	68	1.0	75	(2)
GSS30 IRS3	GSS30IRS3	0	138	50	1.7	72	(3)
IRAS 04166+2706	IRAS04166	0	156	61	0.4	47	(4)
IRAS 15398–3359	IRAS15398	0	155	50	1.4	51	(5)
IRAS 16253–2429	IRAS16253	0	139	42	0.16	68	(6)
IRAS 16544–1604	IRAS16544	0	151	50	0.89	73	(7)
L1527 IRS	L1527	0	140	41	1.3	75	(8)
R CrA IRAS 32[a]	IRAS32	0	150	64	1.6	69	(9)
R CrA IRS5N	IRS5N	0	147	59	1.4	65	(10)
IRAS 04169+2702	IRAS04169	I	156	163	1.5	44	(11)
IRAS 04302+2247	IRAS04302	I	160	88	0.43	84	(12)
L1489 IRS	L1489	I	146	213	3.4	71	(13)
Oph IRS43[a]	OphIRS43	I	137	193	4.1	78	(14)
Oph IRS63	OphIRS63	I	132	348	1.3	47	(15)
R CrA IRS7B[a]	IRS7B	I	152	88	5.1	68	(16)
B335	B335	0	165	41	1.4	37	(9)
TMC-1A	TMC1A	I	137	183	2.3	52	(9)

[a] These sources have close binaries. The inclination angle for these binaries are based on their primary companion.

References. 1) Gavino et al. (2024); (2) Sai et al. (2023); (3) Santamaría-Miranda et al. (2024); (4) Phuong et al. (2024); (5) Thieme et al. (2023); (6) Aso & Sai (2023); (7) Kido et al. (2023); (8) van't Hoff et al. (2023); (9) Ohashi et al. (2023); (10) Sharma et al. (2023); (11) Han et al. (2024); (12) Lin et al. (2023); (13) Yamato et al. (2023); (14) Narayanan et al. (2023); (15) Flores et al. (2023); (15) Takakuwa et al. (2024); (16) Ohashi et al. (2023).

of this study, we rely exclusively on the results seen in the moment 8 and moment 9 plots to identify and define the different components. While only a few representative plots providing key insights into the emission morphology of each source are highlighted in the main text, the complete maps of all sources for each molecule are shown in Appendices 5.A and 5.B. Furthermore, for ease of access and exploration, an interactive version of all the molecular maps for each source is available on the website `https://edisk-app.streamlit.app`.

5.3.1 ^{12}CO

^{12}CO (2–1) emissions are detected towards all eDisk sources. Apart from IRS5N, Ced110IRS4, IRS7B, and OphIRS43, these emissions are primarily associated with molecular outflows and also delineate the walls of the outflow cavities. Figure 5.3 presents moment 8 maps that display the large-scale emission of ^{12}CO (2–1) towards ten eDisk sources. These maps reveal the different varieties of outflows observed in our sample. Most sources exhibit

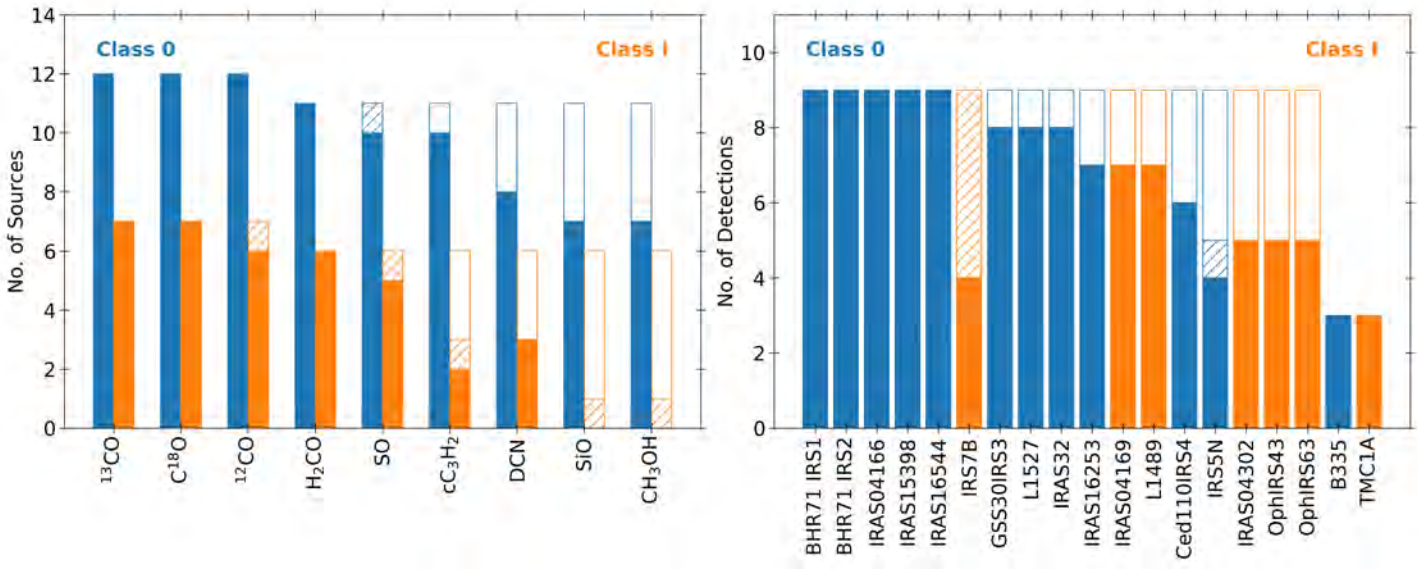

FIGURE 5.2 Overview of the detection statistics showcasing plots illustrating the number of sources where emissions of each molecule are observed (*left*) and number of molecules observed towards each source (*right*). The dashed regions represent cases where emissions are observed towards a source but are unlikely to be associated with that source.

wide-angle outflows that generally display curvature or have shoulder-like structures and deviate from being strictly conical. The outflow towards IRAS15398 is much more collimated compared to the other sources.

The origin of the outflows appears to be deep within the inner disk region, very close to the corresponding positions of the protostars. The emissions are generally perpendicular to the major axis of the elongated continuum emission and typically exhibit distinct velocity gradients with red- and blue-shifted emissions tracing individual outflow lobes (see Figure 5.15). The outflow originating from the main source of the close binary system IRAS32 appears to interact and blend with the material surrounding the secondary source. In addition to the outflow, the warm inner envelope and disk regions surrounding the continuum can also be traced by the ^{12}CO emission, especially in the velocity channels close to the systemic velocity (v_{sys}) of the source. These emissions likely originate from CO molecules sublimating off dust grains in the inner envelope and disk regions. This can occur due to the presence of viscous accretion heating that raises the dust temperatures above 20 K, the sublimation point of CO, even towards the midplane of the disk (Takakuwa et al., 2024).

The ^{12}CO emissions towards the sources Ced110IRS4, OphIRS43, IRS7B, and IRS5N do not appear to trace any apparent outflow or jets associated with the protostar. Three of these sources are close binaries, where the emissions mainly seem to be associated with the main source. These emissions then appear to interact and blend with the material surrounding the secondary source, as with IRAS32. In Ced110IRS4 and OphIRS43, the emission appears along the direction of the major axis of the dust disks and appears to trace the rotation of the disk instead of the outflow, similar to C^{18}O emission (see Figure 5.15). However, it also appears to trace the base of the outflow cavities along the minor axis of the continuum for both sources. In IRS7B,

although extended emission is seen surrounding the source, it does not seem to be directly associated with the protostar. As for IRS5N, although extended emissions from the large-scale surroundings are clearly present, there are some emissions that are most likely associated with the protostar. The most notable of these is the spiral feature seen towards the west of the source that is likely tracing infalling material (Sharma et al., 2023). Both IRS7B and IRS5N are part of the complex Coronet region, which harbors multiple highly energetic molecular hydrogen emission-line objects (MHOs) and dozens of Herbig–Haro (HH) objects that likely interact and conceal any emission from these sources (see Wang et al., 2004, and references therein). Furthermore, any low-velocity emissions close to the v_{sys} of these sources are difficult to distinguish due to line opacity effects and spatial filtering.

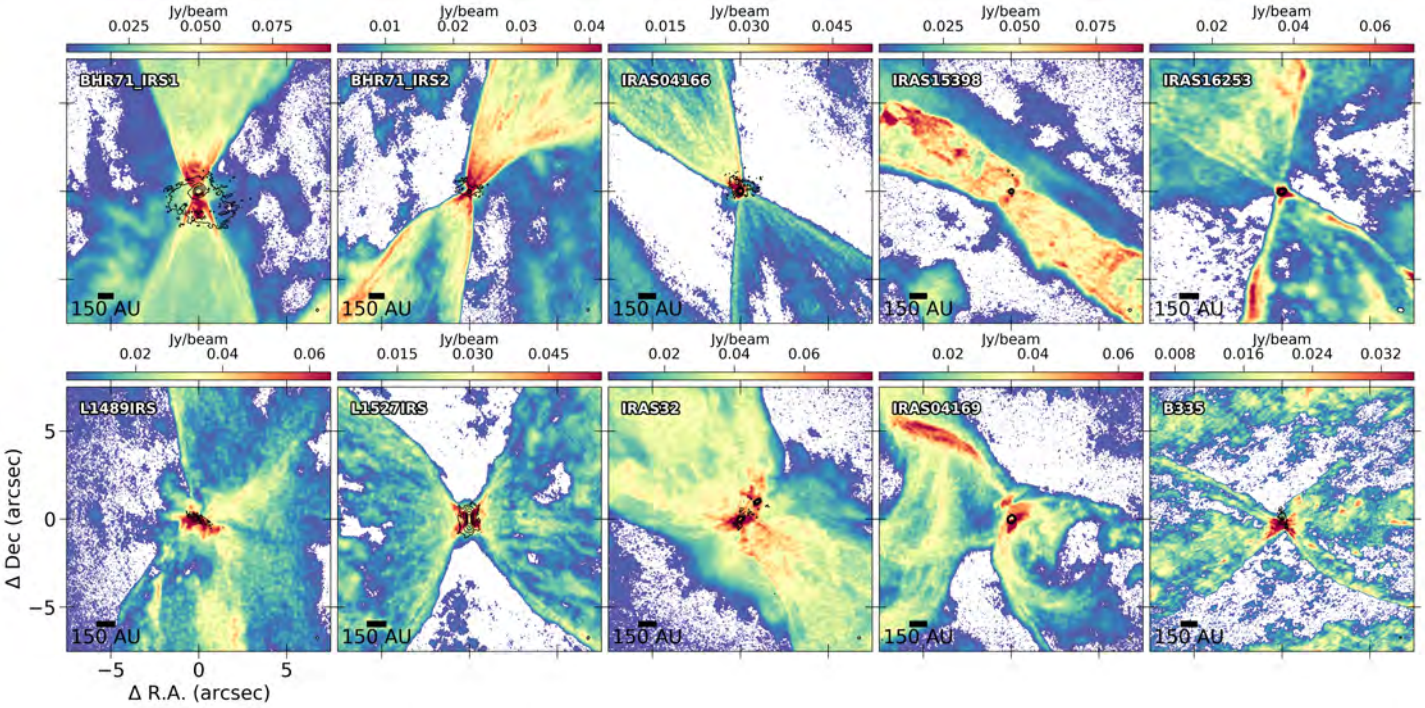

FIGURE 5.3 Moment 8 maps of ^{12}CO (J=2–1) created using $\geq 3\sigma$ emissions towards 10 representative eDisk sources. The contour lines display the continuum emission at thresholds of 5σ, 15σ, 45σ, 135σ, and 320σ for each source. The scale bar is located at the bottom left, and the synthesized beam is indicated in white at the bottom right corner of each image.

5.3.2 ^{13}CO

Emissions in ^{13}CO (2–1) are also observed toward all eDisk sources. Figure 5.4 displays the ^{13}CO moment 8 maps towards five eDisk sources. The emissions primarily trace the inner ∼3-4″area and peak in the disk and the warm inner envelope region near the protostar. Moment 9 maps show clear signs of rotation with the separation of blue- and red-shifted emissions along the major axis of the continuum (see Figure 5.29). The extended large-scale ^{13}CO emissions trace the outflows in a few sources (e.g., IRAS16544 and BHR71 IRS1; see Figure 5.4), and the sections of the outflow cavity walls in others (e.g., IRAS04166 and IRAS16253; see Figure 5.4). ^{13}CO is a well-known tracer of dense regions as it is sensitive to higher column densities

than ^{12}CO. The extended emissions are likely resulting from the outflows and the cavity walls. The cavity walls have higher densities than those of the surrounding envelope, and their temperatures are expected to be above 20 K, the sublimation temperature of CO. In addition, the materials in the cavity walls are exposed to passive heating from the UV radiation of the protostar, which can further elevate temperatures in this region, sublimating more CO from ices and facilitating the production of hydrocarbons (see Sect. 5.4.1 and also Lee et al. 2014, 2015).

The ^{13}CO emission towards IRS5N and IRS7B once again appears to be affected by the surrounding environment, although to a lesser extent compared to the ^{12}CO emission. The zoomed-in moment 9 map of IRS7B shows a distinct region coinciding with the continuum that exhibits a much different velocity profile compared to the surrounding emission (see Figure 5.29). This emission likely originates from the disk and inner envelope of IRS7B. Likewise, the ^{13}CO emission observed along the north-south direction of IRS5N is closer to the systemic velocity and slightly red-shifted, which is in contrast with the predominantly blue-shifted large-scale emission surrounding the source.

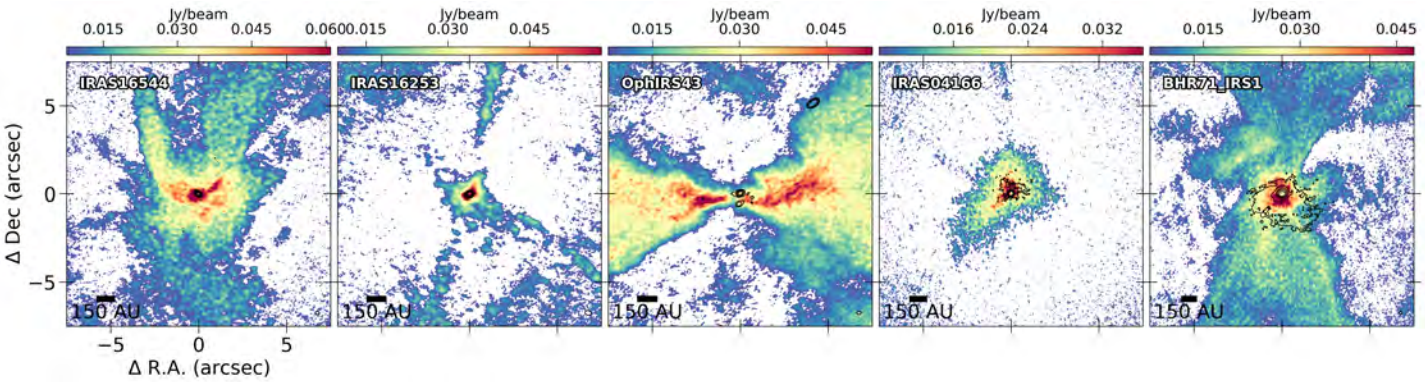

FIGURE 5.4 Moment 8 maps of ^{13}CO (J=2–1) created using $\geq 3\sigma$ emissions towards 5 representative eDisk sources. The contours display the continuum emission at the same levels as Figure 5.3. The scale bar is located at the bottom left, and the synthesized beam is indicated in white at the bottom right corner of each image.

5.3.3 $C^{18}O$

In line with the observations of other CO isotopologues, C^{18}O (2–1) emissions are detected in all sources within the eDisk sample. Figure 5.5 shows the zoomed-in moment 8 maps (top) and moment 9 maps (bottom) of the C^{18}O emissions towards five eDisk sources. The moment 8 maps show that the emissions are mostly concentrated in the inner envelope and the disk region, similar to that of the ^{13}CO emissions. For most sources, the C^{18}O emission appears to have an absorption profile at the protostar position. This feature likely results from the optically thick and cold foreground clouds absorbing the warmer continuum emissions at low velocities, causing the continuum oversubtraction. This absorption also occurs towards the emissions of ^{12}CO and ^{13}CO but due to their relatively high brightness, are less apparent and important in those molecules. Furthermore, bright and optically thick continuum emissions at small radii can block the relatively

weak $C^{18}O$ emissions resulting in continuum oversubtraction during data reduction. A distinct separation between the blue- and the red-shifted emission can be seen in the moment 9 maps along the major axis of the continuum. PV analyses of the $C^{18}O$ emission conducted as part of the first look results of eDisk sources show that Keplerian disks are prevalent in most eDisk sources (Flores et al., 2023; van't Hoff et al., 2023; Kido et al., 2023; Lin et al., 2023; Ohashi et al., 2023; Sai et al., 2023; Sharma et al., 2023; Thieme et al., 2023; Yamato et al., 2023).

Large-scale $C^{18}O$ emissions extending over 3–4″are also observed towards a couple of sources (see Figure 5.17). In IRAS15398, IRAS16253, and L1527, the large-scale emission faintly traces an outline of the outflow cavity walls. In IRAS16544 and IRAS04169, the extended $C^{18}O$ emission likely traces an accretion streamer that transports material from the outer envelope to the inner envelope and disk nonaxisymmetrically (see Section 5.4.1), whereas the arc-like structure seen towards the north of Ced110IRS4 is most likely tracing shocked shell caused by a large-scale outflow in the past (Sai et al., 2023). As with the ^{12}CO and ^{13}CO emission maps, the large-scale $C^{18}O$ emission seen towards IRS5N and IRS7B most likely originates from the complex environment of the Coronet region. However, they also exhibit compact emissions that overlap the continuum with a much different velocity profile than the surrounding emissions and likely trace the disk rotation, as shown in the bottom panels of Figure 5.5.

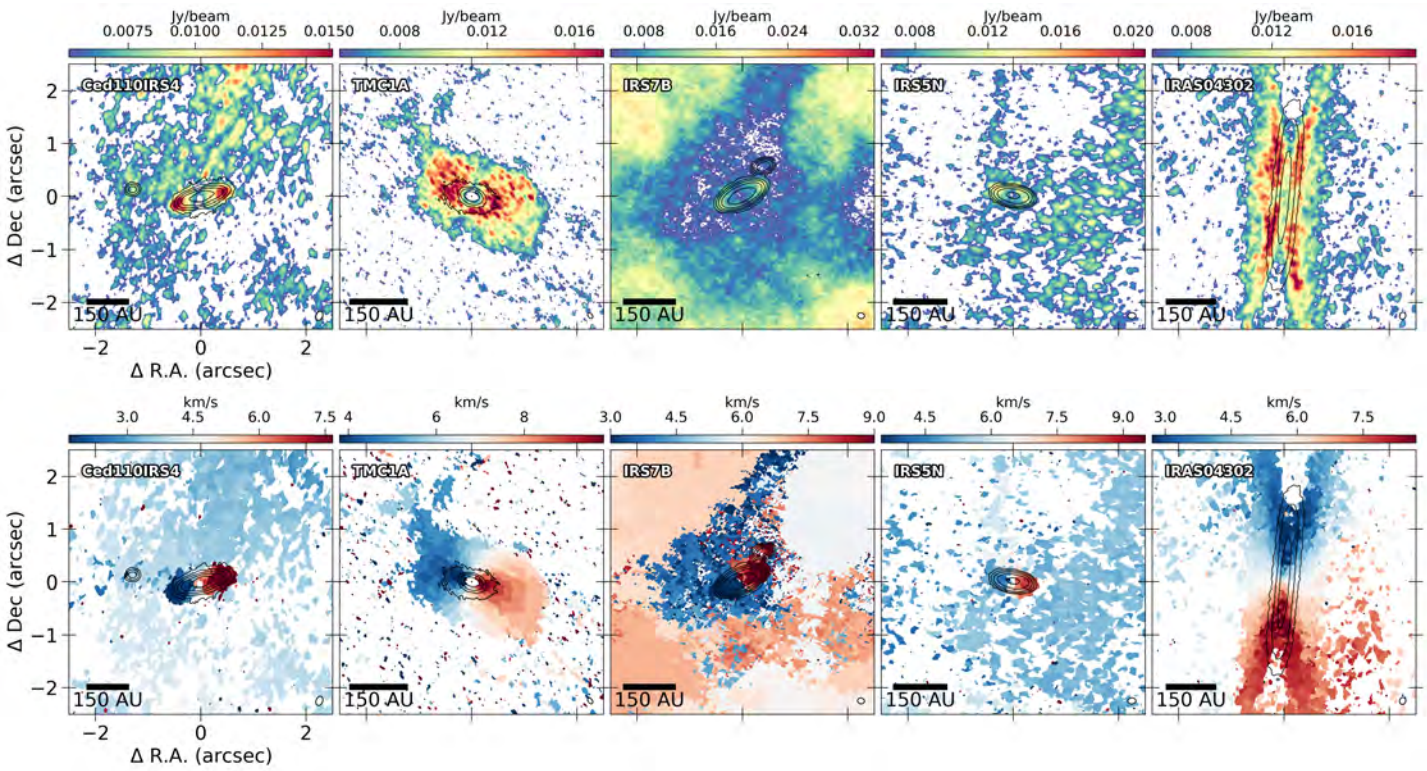

FIGURE 5.5 Zoomed-in moment 8 maps (*top*) and moment 9 maps (*bottom*) of $C^{18}O$ (J=2–1) created using $\geq 3\sigma$ emissions towards 5 representative eDisk sources. The contours display the continuum emission at the same levels as Figure 5.3. The scale bar is located at the bottom left, and the synthesized beam is indicated in white at the bottom right corner of each image.

5.3.4 *SiO*

SiO (5–4) emission is only clearly detected towards eight eDisk sources, namely BHR71 IRS1/2, IRAS16544, IRAS15398, IRAS04166, GSS30IRS3, L1527, and IRS7B. Figure 5.6 shows the moment 8 maps of the SiO emission towards four systems. SiO is a well-known tracer of protostellar jets, and, unlike other molecules, the emission from SiO has generally been observed to be much more compact and collimated, containing knots and clumps (Jhan et al., 2022; Takahashi et al., 2024). The moment 8 maps for BHR71 IRS2 and IRAS 04166 show multiple knots throughout the elongated SiO emission, closely aligned with their outflows. The emissions toward BHR71 IRS1, IRAS16544, and L1527, while much less prominent and only observed near the protostar, also appear in the same direction as the outflow. Isolated clumps of SiO emission are observed $\sim$4″away from the protostar position towards GSS30IRS3, IRAS15398, and IRS7B in the west, southwest, and southeast, respectively (see Figure 5.18). The clumps observed in GSS30IRS3 and IRS7B are observed along the direction of the major axis of the continuum, whereas the clump seen in IRAS15398 is oriented along the outflow direction. These clumps may be created by other shocks taking place in these regions. Nevertheless, it should be acknowledged that both sources are situated in complex regions, and some of the SiO emissions detected might be unrelated to the sources.

5.3.5 *SO*

Emissions from SO (6_5–5_4) are detected in all eDisk sources. However, in the case of IRS5N, all of the emission only appears towards the edges of the map and is most likely associated with the surrounding environment and not with the protostar itself. Figure 5.7 shows the zoomed-in moment 8 maps of SO (6_5–5_4) emission observed towards five systems. The emission generally peaks near the position of the protostar and, in most cases, appears to trace the inner envelope and disk region. In IRAS04169 and OphIRS63, the emissions reveal spiral structures that connect to the inner envelope and disk regions. These structures likely represent accretion streamers that funnel material non-axisymmetrically to the inner envelope and the disk regions (Flores et al., 2023; Lee et al., 2023, 2024; Phuong et al., 2024). The moment 9 maps of the SO emission towards most sources show that near the continuum, the emission shows clear signs of rotation (see Figure 5.19).

Large-scale emissions are also observed in a couple of sources. These extended emissions appear to trace different components among the different sources. In BHR71 IRS2 and L1527, the extended SO emissions faintly trace a section of the outflow cavity wall, whereas in IRAS32 and IRAS15398, extended emissions are seen perpendicular to the outflow direction. A clump of blue-shifted SO emission is also seen southwest of IRAS15398 at the same location as the SiO clump. In IRAS16544 and Ced110IRS4, extended emissions seen toward the north of the protostar weakly trace the streamer and the shocked shell due to outflow, respectively, as observed in $C^{18}O$ emission. The extended emissions observed towards GSS30IRS3 and IRS7B appear to be affected by the environment.

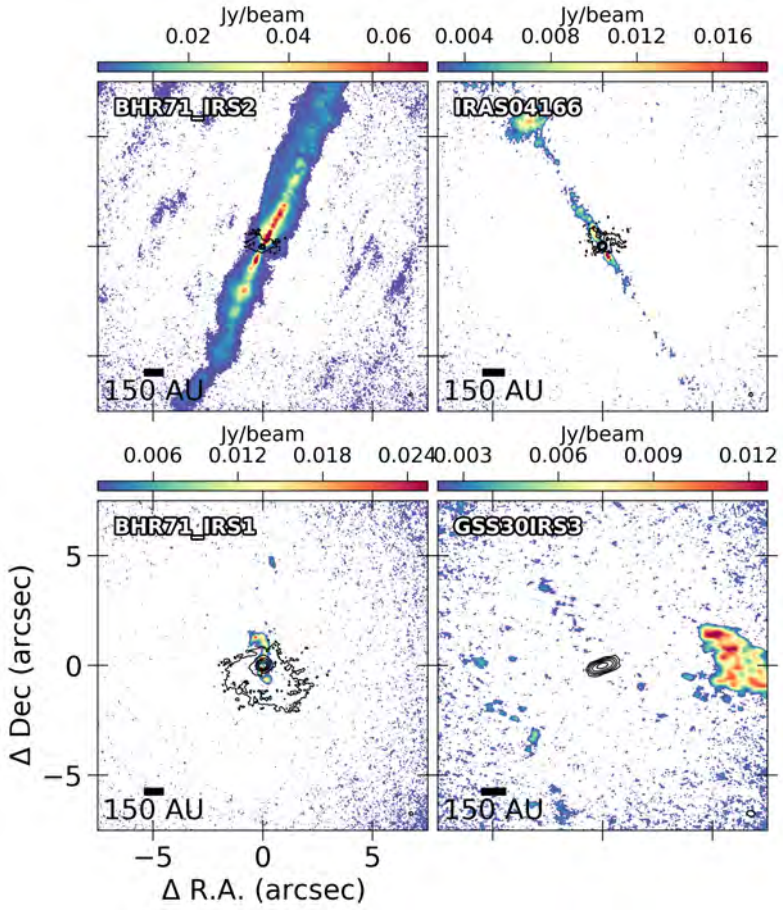

FIGURE 5.6 Moment 8 maps of SiO (J=5–4) created using $\geq 3\sigma$ emissions towards 4 representative eDisk sources. The contours display the continuum emission at the same levels as Figure 5.3. The scale bar is located at the bottom left, and the synthesized beam is indicated in white at the bottom right corner of each image.

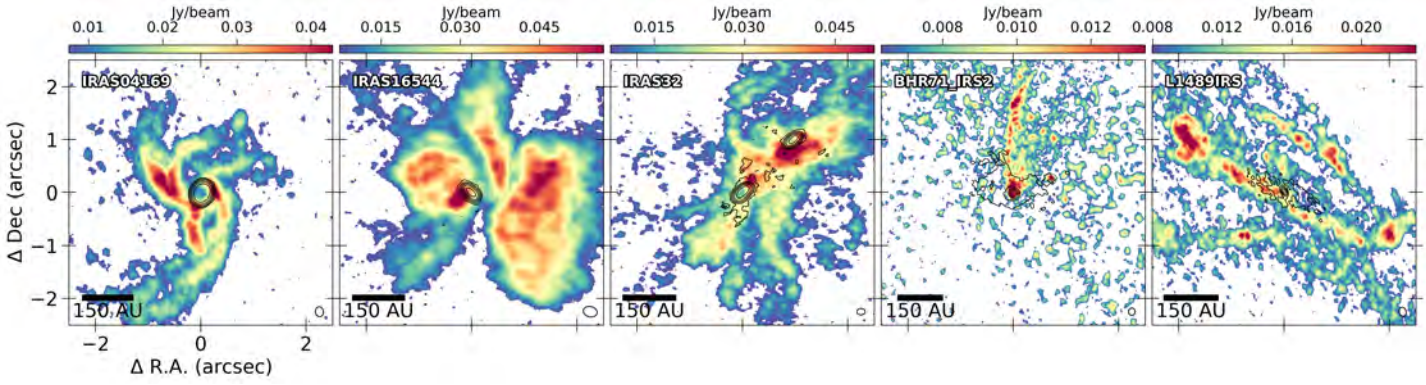

FIGURE 5.7 Moment 8 maps of SO (J=6_5–5_4) created using $\geq 3\sigma$ emissions towards 5 representative eDisk sources. The contours display the continuum emission at the same levels as Figure 5.3. The scale bar is located at the bottom left, and the synthesized beam is indicated in white at the bottom right corner of each image.

5.3.6 *DCN*

Emissions from DCN (3–2) are clearly detected in nine sources and generally seem to originate in the inner warm envelope and disk region of the protostar. Figure 5.8 shows the zoomed-in moment 8 maps of DCN emission observed

towards four eDisk sources. Emissions in BHR71 IRS1/2, IRAS16544, and L1489 are concentrated towards the disk region and show signs of rotation in the moment 9 maps (see Figure 5.33). Notably, the emissions in BHR71 IRS1 and L1489 show ring-shaped structures with an absorption profile in the middle, similar to the ones seen in $C^{18}O$. Emission towards IRAS15398 shows an elongated structure extending from the northeast to the southwest, along the direction of the outflow, and has a similar velocity structure as shown by the ^{13}CO emission.

DCN emission is also detected towards L1527, IRAS04166, IRAS32, and IRAS16253. However, these detections lack clear association with specific source structures. In IRAS32, knotty emission is detected in between the two continuum sources of the binary, accompanied by two sets of elongated emissions. One emission is slightly blue-shifted in the north-south direction, while the other one is slightly red-shifted in the northeast-southwest direction (see Figure 5.20). Patches of emission are seen towards the south and the northwest of the continuum in IRAS16253, while tentative and relatively weak emissions are also seen near the continuum positions of L1527 and IRAS04166. These sources are also affected by strong absorption at the position of their continuum. In addition to the nine sources mentioned above, DCN emission is also seen in IRS7B. Although the emissions towards IRS7B again appear to be affected by the surrounding environment, as seen in observations of other molecules, a distinct patch of highly blue-shifted emission is present towards the southeast, near the edge of the major axis of the continuum. This distinct velocity structure of this patch compared to surrounding emissions suggests a separate origin, likely associated with IRS7B itself, similar to the emissions in $C^{18}O$(see Figures 5.5,5.33).

5.3.7 CH_3OH

Emissions in CH_3OH (4_2–3_1) are clearly detected toward seven sources. Figure 5.9 shows the zoomed-in moment 8 maps illustrating CH_3OH emissions towards four eDisk sources. Towards BHR71 IRS 1/2, IRAS16544, and IRAS04166, these emissions are mostly compact and concentrated in the inner envelope and disk region, with its peak coinciding with the position of the corresponding protostar. In contrast, the emission towards IRAS15398 peaks near the position of the protostar, but additional patchy emissions are also seen in the direction of the outflow.

In addition, patches of CH_3OH emission can be seen in the large-scale maps of a few sources (see Figure 5.21). Toward IRAS15398 and GSS30IRS3, a knot-like feature can be seen in the northeast direction, which aligns with the direction of their respective outflow. IRAS04166 also exhibits a similar but slightly more elongated emission in the direction of its outflow. These knots might suggest previous outbursts in these sources (Kim et al., 2024; Lee et al., 2024). A compact, likely unresolved blue-shifted patch of emission is observed near the primary source of IRAS32, potentially indicating molecular jets that have recently emerged from the source (see Figure 5.34; but for a better view, consult the web application). The IRAS15398 map again reveals a clump of CH_3OH emission in the large-scale map at the same location as the SiO and SO emissions.

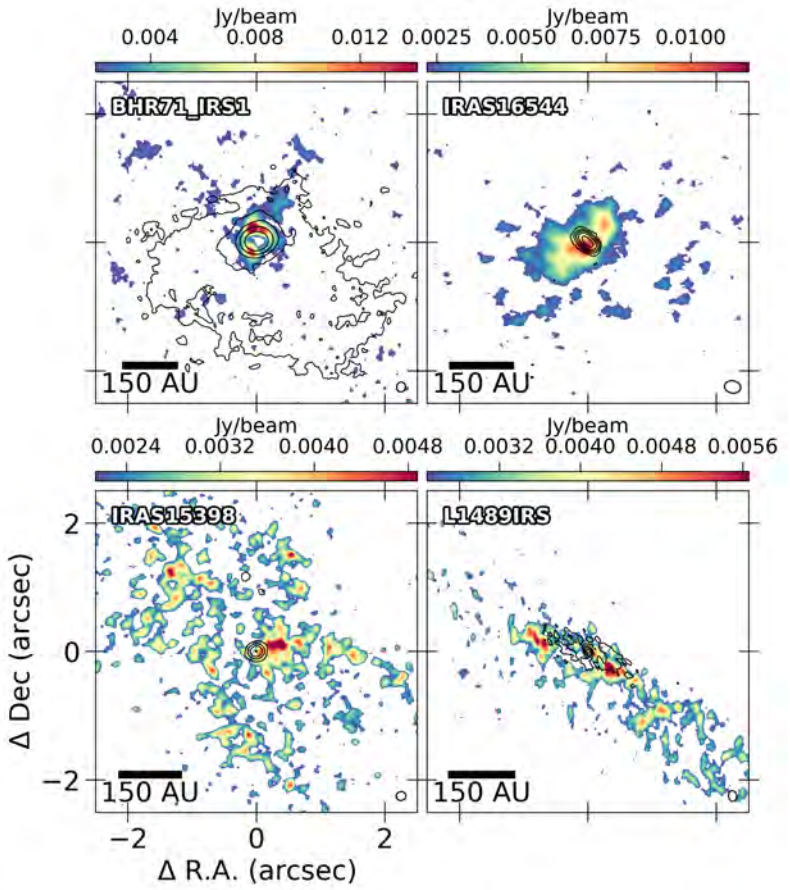

FIGURE 5.8 Zoomed-in moment 8 maps of DCN (J=3–2) created using $\geq 3\sigma$ emissions towards 4 representative eDisk sources. The contours display the continuum emission at the same levels as Figure 5.3. The scale bar is located at the bottom left, and the synthesized beam is indicated in white at the bottom right corner of each image.

5.3.8 H_2CO

The spectral windows of the eDisk observations also cover three transitions of H_2CO: $3_{0,3}$–$2_{0,2}$, $3_{2,1}$–$2_{2,0}$, and $3_{2,2}$–$2_{2,1}$. Figure 5.10 displays the zoomed-in moment 8 maps of the H_2CO emissions for the $3_{0,3}$–$2_{0,2}$ transition with E_{up} = 21 K and the $3_{2,2}$–$2_{2,1}$ transition E_{up} = 68 K towards five eDisk sources. The plots show that, in most cases, the different transitions exhibit similar morphologies for a given source, with stronger and more extended emissions seen in the lower-energy transition. Emissions in H_2CO are observed in all 19 eDisk sources for the lower-energy $3_{0,3}$–$2_{0,2}$ transition, with emissions mostly concentrating near the position of the protostar. These emissions likely trace the inner envelope and disk regions and, in some cases, also trace the base of the outflow cavity walls, forming a U-shaped morphology on either side of the minor axis of the continuum. In the large-scale map of a few sources such as BHR71 IRS2, IRAS15398, and IRAS04166, clumpy emissions are also seen in the direction of the outflow, which is suggestive of jets and can be released in shocks (Tychoniec et al., 2020).

Additionally, the moment maps of the H_2CO emission also trace the inner envelope and disks and accretion streamers towards some sources (see Figure 5.22). In L1489, L1527, IRAS16253, and OphIRS43, the emission is

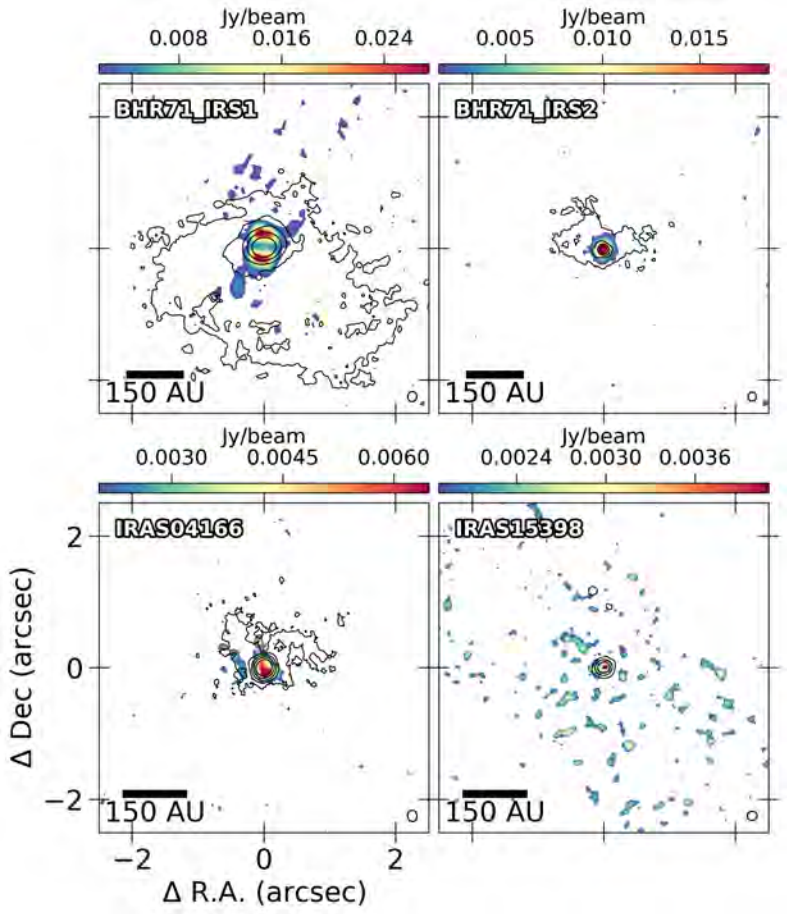

FIGURE 5.9 Zoomed-in moment 8 maps of CH_3OH (J=4_2–3_1) created using $\geq 3\sigma$ emissions towards 4 representative eDisk sources. The contours display the continuum emissions at the same levels as Figure 5.3. The scale bar is located at the bottom left, and the synthesized beam is indicated in white at the bottom right corner of each image.

elongated along the major axis of the continuum. In IRAS04169, the emission traces the spiral structure around the source, while in Ced110IRS4, the emission traces the extended structure seen towards the north of the source. These components have also been observed in $C^{18}O$ and SO molecules and are likely trace accretion streamers in IRAS04169 and outflow shocked shell in Ced110IRS4. In IRAS32, the H_2CO emission is observed mostly in the mutual envelope material between the two binary sources. The emission towards OphIRS43 peaks towards the west of the source and is extended in the east-west direction. In GSS30IRS3, an elongated band of H_2CO emission in the north-south direction is seen towards the northeast of the source. IRS7B once again has two small patches of H_2CO emission with vastly different velocity structures with respect to the surrounding emission (see Figure 5.35).

5.3.9 c–C_3H_2

The spectral windows of the eDisk observations also cover four transitions of c–C_3H_2 emissions: $6_{0,6}$–$5_{1,5}$, $6_{1,6}$–$5_{0,5}$, $5_{1,4}$–$4_{2,3}$, and $5_{2,4}$–$4_{1,3}$. Emissions in c–C_3H_2 are detected towards twelve eDisk sources. Figure 5.11 shows the moment 8 maps made with the blended $6_{0,6}$–$5_{1,5}$ and $6_{1,6}$–$5_{0,5}$ transitions

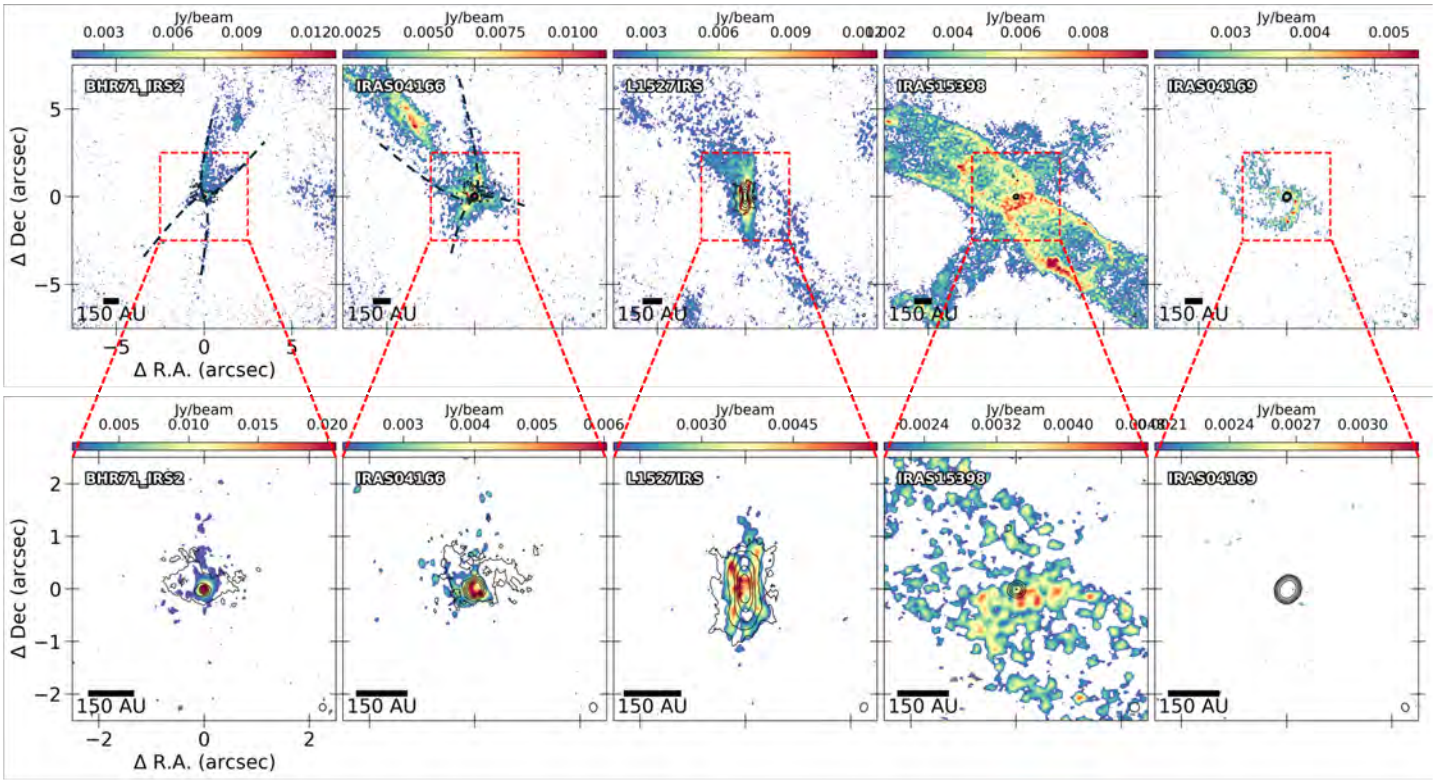

FIGURE 5.10 Moment 8 maps of H_2CO emissions in $3_{0,3}$–$2_{0,2}$ (*top*) and $3_{2,2}$–$2_{2,1}$ (*bottom*) created using $\geq 3\sigma$ emissions towards 5 of the eDisk sources. Dashed lines show the outflow cavity walls seen towards the $3_{0,3}$–$2_{0,2}$ emisions. The contours display the continuum emission at the same levels as Figure 5.3. The scale bar is located at the bottom left, and the synthesized beam is indicated in white at the bottom right corner of each image.

towards four eDisk sources. The emissions of c—C_3H_2 appear to primarily trace the outflow cavity walls near the position of the protostar in many sources, such as BHR71 IRS1/2, IRAS15398, IRAS04166, IRAS16253, and IRAS16544. Emissions are also seen towards the envelope in L1527, L1489, IRAS32, IRAS16253, and IRAS16544. These emissions generally have constant velocities that are close to the systemic velocity (v_{sys}) of the source (see Figure 5.38). Likewise, the emission towards Ced110IRS4 traces the outflow shocked shell that is also seen in other molecules, and IRS7B once again shows large-scale emissions from the surroundings.

The emissions from the remaining two transitions also trace similar structures as the two blended lines towards the different sources. One notable exception to this is the source BHR71 IRS2, where each transition displays a different feature. Emissions are seen tracing the cavity walls in the blended lines, no emission is seen in the $5_{1,4}$–$4_{2,3}$ transition, and a patch of highly red-shifted emission is seen right at the center in the $5_{2,4}$–$4_{1,3}$ line (see Figures 5.38, 5.39, and 5.40; but for a better view, consult the web application).

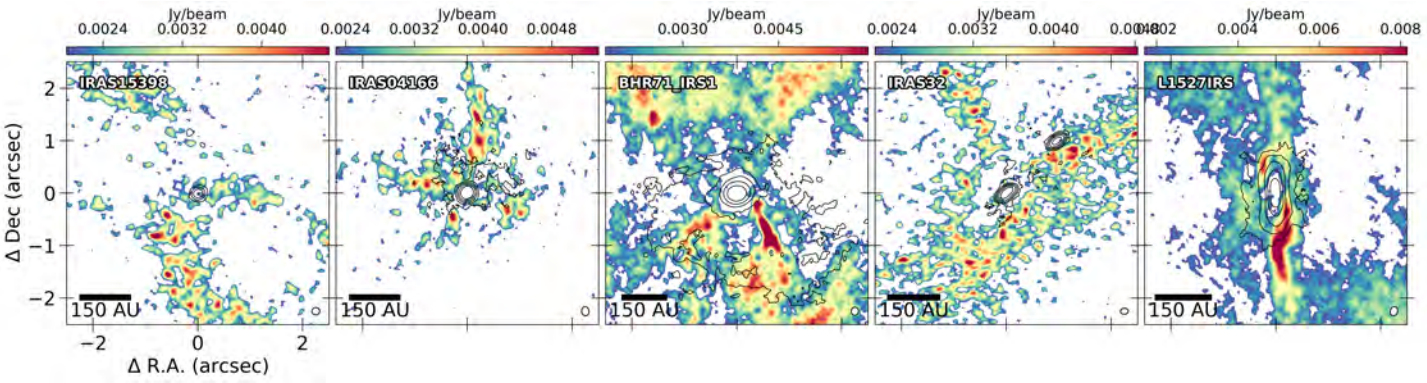

FIGURE 5.11 Zoomed-in moment 8 maps of blended c–C_3H_2 J=$6_{0,6}$–$5_{1,5}$ and J=$6_{1,6}$–$5_{0,5}$ transitions created using $\geq 3\sigma$ emissions towards 5 representative eDisk sources. The contours display the continuum emissions at the same levels as Figure 5.3. The scale bar is located at the bottom left, and the synthesized beam is indicated in white at the bottom right corner of each image.

5.4 DISCUSSION

5.4.1 *Chemical morphology of the embedded sources*

The high resolution and sensitivity of the eDisk observations provide a unique opportunity to study the spatial distribution of the molecules in the inner envelope and disk regions of embedded sources. Table 5.3 summarizes the primary molecular lines detected towards each source in this study. In this section, we only discuss these primary molecules targeted by the spectral window of the eDisk observations. For the sources, BHR71 IRS1/2, as well as IRAS16544, line emissions of several other complex organic molecules are seen beyond the CH_3OH emissions presented in Sect. 5.3.7. A more detailed analysis and discussion of these species toward the eDisk sources are presented in a separate paper (S. Lee et al. in prep.).

Outflowing material

Outflows and jets play a crucial role in transferring the excess angular momentum back to the molecular cloud and are essential feedback processes in protostellar systems (Offner & Arce, 2014). Outflows generally consist of low-velocity components, with gases moving at velocities up to 20 km s^{-1} relative to the v_{sys} of the source. In eDisk observations, they are commonly traced by low-velocity channels of ^{12}CO and ^{13}CO emissions. All eDisk sources display a certain extent of ^{12}CO emission in the direction of the outflow (perpendicular to the major axis of the continuum). Fifteen of the nineteen sources clearly trace large-scale bipolar outflows in ^{12}CO emission whereas the distinction is not as clear in the remaining sources (see Figure 5.15). The low-velocity ^{12}CO emission typically displays a parabolic shape with a wide-angle morphology. Our observations show that such outflows originate within the inner disk region, very close to the position of the protostar. Similar structures are also observed in the ^{13}CO emission towards some eDisk sources (see Figure 5.16). The ^{13}CO emission, however, is associated with denser regions of a protostar, as it is much less abundant than ^{12}CO with the abundance ratio of ^{12}CO/^{13}CO ~77 (Wilson & Rood,

TABLE 5.3 Summary of molecules observed towards eDisk sources

Source Name	^{12}CO	^{13}CO	C^{18}O	SiO	SO	DCN	CH_3OH	H_2CO	$c-C_3H_2$
BHR71 IRS1	✓	✓	✓	✓	✓	✓	✓	✓	✓
BHR71 IRS2	✓	✓	✓	✓	✓	✓	✓	✓	✓
Ced110IRS4	✓	✓	✓	✗	✓	✗	✗	✓	✓
GSS30IRS3	✓	✓	✓	✓	✓	✗	✓	✓	✓
IRAS04166	✓	✓	✓	✓	✓	✓	✓	✓	✓
IRAS15398	✓	✓	✓	✓	✓	✓	✓	✓	✓
IRAS16253	✓	✓	✓	✗	✓	✓	✗	✓	✓
IRAS16544	✓	✓	✓	✓	✓	✓	✓	✓	✓
L1527	✓	✓	✓	✓	✓	✓	✗	✓	✓
IRAS32	✓	✓	✓	✗	✓	✓	✓	✓	✓
IRS5N	✓	✓	✓	✗	⊘	✗	✗	✓	✗
IRAS04169	✓	✓	✓	✗	✓	✓	✗	✓	✗
IRAS04302	✓	✓	✓	✗	✓	✗	✗	✓	✗
L1489	✓	✓	✓	✗	✓	✓	✗	✓	✓
OphIRS43	✓	✓	✓	✗	✓	✗	✗	✓	✗
OphIRS63	✓	✓	✓	✗	✓	✗	✗	✓	✗
IRS7B	⊘	✓	✓	⊘	⊘	✓	⊘	✓	⊘
B335	✓	✓	✓	–	–	–	–	–	–
TMC1A	✓	✓	✓	–	–	–	–	–	–

✓ Emission is detected at $\geq 3\sigma$ level towards the source.
✗ No emission is detected at 3σ level.
⊘ Emission is detected at $\geq 3\sigma$ level, but is unlikely to be directly associated with the protostellar system.

TABLE 5.4 Summary of molecules observed towards the various components

Components	^{12}CO	^{13}CO	C^{18}O	SiO	SO	DCN	CH_3OH	H_2CO	$c-C_3H_2$
Outflows	✓	✓					✓	✓	
High velocity jets	✓			✓					
Outflow cavity walls	✓	✓						✓	✓
Inner envelope and disk		✓	✓		✓	✓	✓		✓
Accretion streamers			✓		✓			✓	

1994).

In contrast, protostellar jets consist of high-velocity components, with gases moving at speeds greater than 20 km s^{-1} relative to v_{sys} of the source. These jets are often seen in high-velocity channels of ^{12}CO and SiO emissions. Figure 5.12 shows the moment 8 maps of high-velocity ^{12}CO emission seen towards four eDisk sources. Compared to low-velocity outflows, these jets are much more collimated, have narrower opening angles, and originate much closer to the protostar. Furthermore, they typically show clumpy emission towards very young protostars, which is believed to be indicative of past episodic accretion (Plunkett et al., 2015; Vorobyov et al., 2018; Sharma et al., 2020). Except in GSS30IRS3, all other sources that display high-velocity ^{12}CO emission also display corresponding jets in SiO. These SiO emissions also exhibit similar structures to their high-velocity ^{12}CO counterparts. In

contrast, ^{12}CO emissions in L1527 do not show any high-velocity components, and the only indication of a jet is a patch of mostly unresolved high-velocity SiO emission close to the protostar (van't Hoff et al., 2023).

The absence of SiO emission in GSS30IRS3 as a complement to its high-velocity ^{12}CO emission could be attributed to the lack of sensitivity of the observation to detect the SiO present in the jets or to the jets themselves not being energetic enough to generate shocks to release SiO into gas, as SiO is a well-known shock tracer (Martin-Pintado et al., 1992; Bergin et al., 1998). Although SiO emissions in IRAS16544 align well with the outflow direction, their velocities are close to v_{sys} of the source, suggesting that these emissions may result from other shock processes, such as shock created by the interaction of the infalling streamer depositing material onto the disk (Garufi et al., 2022; Kido et al., 2023) rather than from shocks due to high-velocity jets. The general lack of SiO emission in the outflow towards most eDisk sources is in contrast to the findings of Tychoniec et al. (2021) where jets in SiO were seen towards six of the seven Class 0 sources observed. The Class 0 targets of Tychoniec et al. (2021) are much more luminous, averaging $\sim 19\ L_{\odot}$. This could reflect that these sources are potentially more actively accreting and driving more energetic outflows than those targeted as part of eDisk. However, both samples are still relatively small for any more conclusive statements about this.

As mentioned in Sect.5.3, sporadic emissions of other molecules such as CH_3OH and H_2CO are also seen towards the outflow direction in some sources. These emissions likely trace the regions that are shock-heated by the outflows and jets, which can raise the temperatures in these regions to sublimate the frozen molecules off the dust grains. We discuss these molecules in more detail in Sect.5.4.1 and Sect.5.4.2.

Outflows cavity walls

The boundary where the infalling envelope meets the cavity opened up by the outflows and jets is referred to as the outflow cavity wall. These walls typically exhibit increased chemical complexity due to the interaction between the infalling envelope and the outflows and also due to their exposure to UV radiation from the protostar (Arce & Sargent, 2006; Visser et al., 2012; Murillo et al., 2018; Tychoniec et al., 2021). Emissions of ^{12}CO, ^{13}CO, and $c-C_3H_2$ are commonly seen towards the outflow cavity walls in the eDisk sources. A few sources also show emissions in H_2CO and SO in the cavity walls. We discuss these two molecules separately in Sect. 5.4.2.

In addition to tracing the outflows, both ^{12}CO and ^{13}CO emissions delineate the parabolic shape of the outflow cavity walls. The emissions seen towards the cavity walls generally have velocities close to the v_{sys} of the source and likely originate from the sublimation of these molecules from the dust grains caused by the heating of the material by UV radiation and high-velocity jets interacting with the infalling envelope. For the protostars IRAS04166, IRAS15398, IRAS16253, and B335, most of the ^{13}CO emission in the direction of the outflow is concentrated primarily in the cavity walls. This indicates that the cavity walls are typically denser compared to both the outflow and the surrounding envelope.

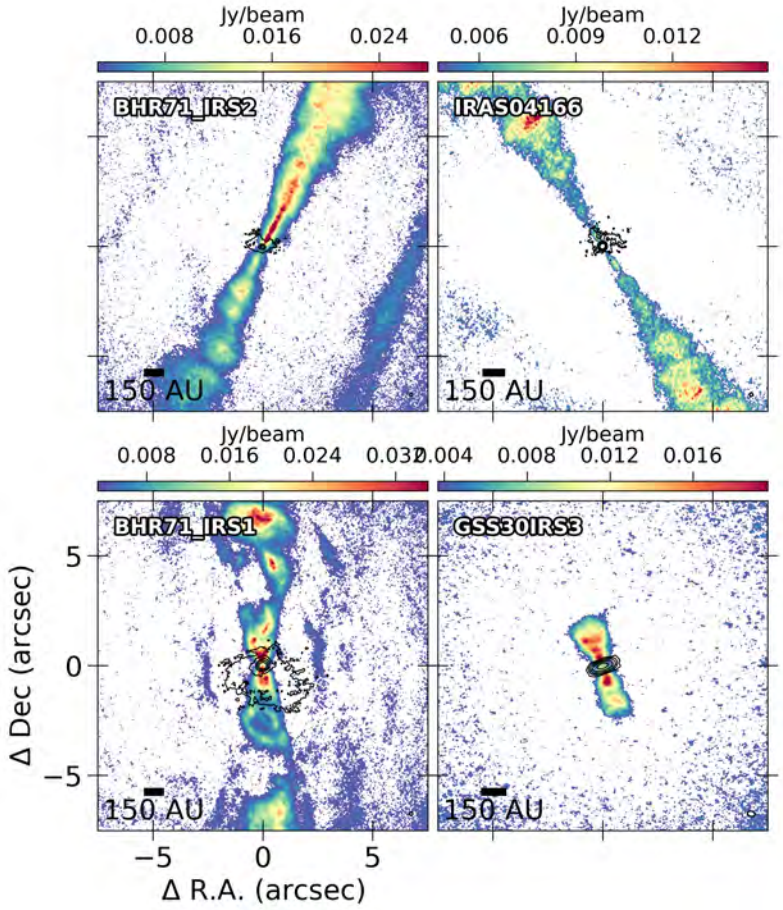

FIGURE 5.12 Moment 8 maps of high-velocity jets seen in ^{12}CO emission towards 4 of the eDisk sources. The maps are created using the velocity channels where $|v_{sys} - v_{chan}| > 20$ km s^{-1}. These are the same sources used for the SiO images in Figure 5.6, allowing for a comparison with the SiO emissions. The contours display the continuum emission at the same levels as Figure 5.3. The scale bar is located at the bottom left, and the synthesized beam is indicated in white at the bottom right corner of each image.

Hydrocarbons such as c−C_3H_2 are well-known tracers of photo-dissociation regions (PDRs), which are dominated by UV radiation (e.g., van der Wiel et al., 2009; Guzmán et al., 2015). Exposure of the cavity walls to UV radiation from the source creates the PDR-like environment necessary for the release of atomic carbon, enabling the production of c−C_3H_2. The emission in c−C_3H_2 is concentrated in the cavity walls close to the protostar in many sources (see Figures 5.38,5.39,5.40). This is anticipated as the walls nearest to the protostar are exposed to more intense UV radiation from the protostar. Over time, this concentration of c−C_3H_2 in the outflow cavity shifts towards the inner envelope and disk as more of the envelope is accreted, allowing UV radiation to penetrate further (Drozdovskaya et al., 2015). This can likely explain some of the c−C_3H_2 emissions observed towards the envelope regions of some of the protostars.

Inner envelope and disk

The inner envelope consists of regions within several hundred au of the protostar and is characterized by higher temperatures and densities compared

to the outer envelope. This leads to a rich chemistry in this region, including the formation of COMs (see reviews by Jørgensen et al., 2020; Öberg et al., 2023). Infalling material from the inner envelope to the protostar funnels onto the circumstellar disk, which not only regulates the material accreted onto the protostar but also serves as a site for planet formation. Among the molecules targeted in the eDisk observations, emissions of ^{13}CO, C^{18}O, DCN, and CH_3OH are commonly seen towards the inner envelope and disk regions of the sources.

The CO isotopologues ^{13}CO and C^{18}O are well-known tracers of the gas distribution and kinematics in the inner envelope and disk region of protostars. This is because CO is ubiquitous in regions where temperatures rise above 20 K and does not require chemistry to be observed at high enough column densities. Moment 9 maps from both these molecules at small and intermediate scales display a velocity gradient along the major axis of the continuum, consistent with the rotation of disk or infalling envelope (see Figures 5.29, 5.30). van 't Hoff et al. (2018) found that emissions from ^{13}CO and C^{18}O in the inner envelope and disk regions of embedded sources are mostly optically thick. This suggests that temperatures in these regions are at least high enough to cause the CO molecules to sublimate ($T \geq 20$ K).

Unlike ^{13}CO and C^{18}O, the DCN emissions observed towards the eDisk sources are much more compact and generally peak near the central protostar (see Figure 5.33). DCN is produced by two main reaction pathways that are active in protostellar disks. At temperatures below 30 K, it forms via D-atom transfer with H_2D^+ and at temperatures above 30 K, it forms through reactions with deuterated hydrocarbons such as C_2HD^+ (Millar et al., 1989; Turner, 2001; Willacy, 2007; Aikawa et al., 2018). The low-temperature pathway is primarily active in the outer disk midplane, just inside the CO snowline, while the warmer formation pathway is prevalent at disk surface layers where the temperatures are elevated. The observation of DCN emissions in the inner disk region, very close to the protostar towards BHR71 IRS1/2, IRAS16544, IRAS04166, and IRAS15398, suggests that the warmer temperature pathway predominantly drives DCN production in these sources. Alternatively, these emissions could also arise from DCN molecules that sublimate off dust grains in envelope regions that are close to the protostar, where temperatures are high. The extended emissions seen towards some sources likely trace the DCN produced through the lower temperature route.

An interesting result obtained in our observations is that, except for L1489, DCN emissions are observed only towards the Class 0 sources. This non-detection towards Class I sources can simply be attributed to the lack of sensitivity in our observations to the less abundant DCN emissions towards the Class I sources. This result would be a natural consequence of the alternative pathway for the DCN emission mentioned above. It is likely that DCN shares similar chemistry in the envelopes of both Class 0 and Class I sources; however, since the masses of the envelopes of the Class I sources are smaller, detecting them becomes more challenging. Alternatively, as accretion proceeds, DCN gets broken down readily by reactions with H^+ and H_3^+ (Albertsson et al., 2013), leading to a reduction in the amount of DCN detectable at the provided sensitivity. In either case, DCN might be a more

reliable tracer of the earlier, younger stages of protostellar evolution.

Similar to DCN, emissions from CH_3OH are also very compact and generally peak near the position of the central protostar, likely tracing the hot core region. The emitting regions of CH_3OH are contained within the emitting regions of DCN, suggesting that they trace higher temperature regions than the DCN emissions (see Figure 5.34). CH_3OH primarily forms on grain surfaces through successive hydrogenation of CO-rich ices (Hiraoka et al., 1994; Watanabe & Kouchi, 2002; Fuchs et al., 2009; Simons et al., 2020) or surface chain reaction in H_2O-rich ices (Bergner et al., 2017; Qasim et al., 2018) and sublimate at high temperatures (∼100 K; Brown & Bolina, 2007; Kristensen et al., 2010; Penteado et al., 2017). The presence of CH_3OH in the inner envelope and disk regions of BHR71 IRS1/2, IRAS16544, and likely IRAS04166 indicates that these sources are "hot corinos", where the temperatures exceed 100 K in the innermost ($\leq$ 100 au) dense regions around protostars (Ceccarelli, 2004; Ceccarelli et al., 2007). These hot corinos are regions rich in COMs, suggesting that the production of complex molecules is well underway in the early stages of star formation.

Accretion streamers

The recent increase in the detection of streamers toward YSOs suggests that these structures likely play a crucial role in the star and planet formation process (see Pineda et al., 2023, for an overview). Accretion streamers channel material from the broader surrounding environment, such as filaments and fibers, directly onto the protostar's inner disk-forming region (e.g. Pineda et al., 2020; Valdivia-Mena et al., 2024). They serve as a critical means to replenish the mass of the system, often having infall rates that exceed the accretion rates of protostars (Hsieh et al., 2019; Kido et al., 2023; Lee et al., 2023; Flores et al., 2023). This influx of material can change the temperatures and densities of the system and can also generate shocks and instabilities at regions where material is deposited (Lee et al., 2024). This can lead to the formation of dust traps, the development of substructures, the initiation of outbursts, and changes in the chemical makeup of the system (Pineda et al., 2023).

Streamers are identified toward IRAS16544, IRAS04169, IRAS16253, OphIRS63, and L1489, observed in emissions of $C^{18}O$, SO, and H_2CO. Figure 5.13 presents the moment 8 maps of $C^{18}O$, SO, and H_2CO $3_{0,3}$–$2_{0,2}$ emissions, with the streamers marked by dashed lines. For IRAS16544, IRAS04169, and L1489, all three molecules evidently trace the same streamer structures, whereas the distinction is less clear in IRAS16253 and OphIRS63. The $C^{18}O$ emissions reveal large-scale arc-like streamers in IRAS16544 and L1489, and spiral streamers in IRAS04169. These structures might extend beyond the MRS of our observations and likely trace regions of elevated column densities where temperatures exceed 20 K, causing the CO to be released from the ice. In contrast, the SO and H_2CO emissions trace the same structures but are confined within the inner 3″– 5″region of the protostar, with enhanced emissions at the landing point of where the streamer meets the inner disk-envelope region. This enhancement is likely due to the shock resulting from the streamer interacting with the disk-envelope region. In

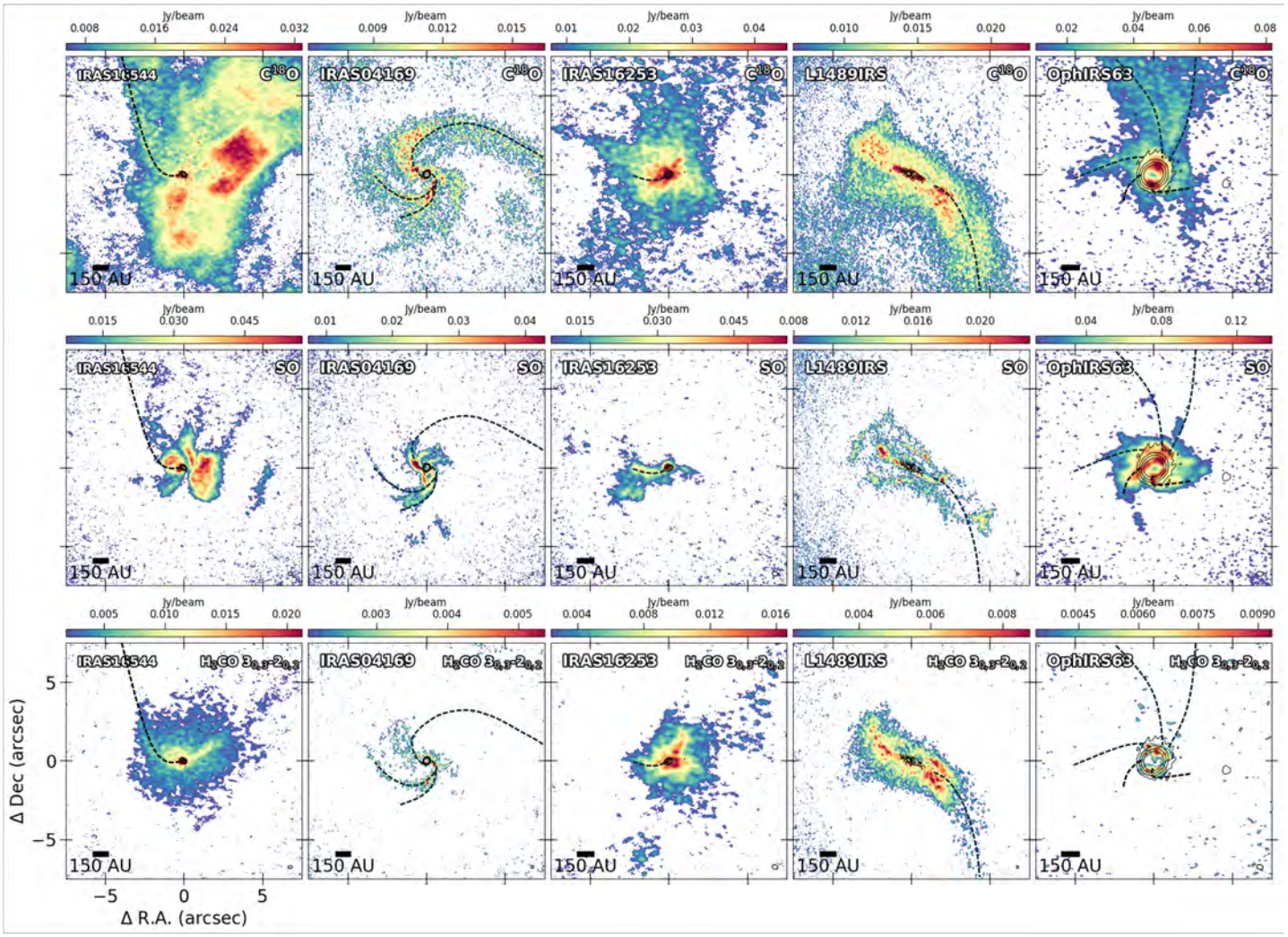

FIGURE 5.13 Moment 8 maps depicting the streamers observed towards the eDisk sources. The streamers seen towards each source are traced by the dashed lines. The contours display the continuum emission at the same levels as Figure 5.3. The scale bar is located at the bottom left, and the synthesized beam is indicated in white at the bottom right corner of each image.

IRAS16253, a small streamer is detected towards the east of the source in SO but appears to be obscured by emissions from the envelope in $C^{18}O$ and H_2CO.

For OphIRS63, the $C^{18}O$ emission shows a long arc-like streamer to the north of the protostar and a shorter spiral streamer towards the east. The SO emission does not show the extended streamer towards the north but shows three short spiral streamers arriving from the east, south, and west. The spiral arriving from the east likely traces the same streamer seen towards the east in the $C^{18}O$ emission. The H_2CO emissions from eDisk observations do not appear to trace any of the streamers observed in $C^{18}O$ and SO. However, a more sensitive observation conducted by the ALMA Large Program Fifty AU STudy of the chemistry in the disk/envelope system of solar-like protostars (FAUST) detected a streamer to the north of the source, likely tracing the same streamer seen towards the north in our $C^{18}O$ emissions (Podio et al., 2024).

A systematic survey of the NGC 1333 star-forming region conducted by

Valdivia-Mena et al. (2024) found that streamers were present in nearly 60% of the embedded sources. In the eDisk survey, streamers are detected in ∼30% of the sources (5 out of 19). However, the eDisk observations did not specifically target streamers and had considerably smaller spatial scales than the scales at which most streamers are detected. Consequently, streamers may have been missed in other sources, especially if they originate from much larger scales. Notably, streamers are present in both OphIRS63 and L1489, the only two sources in our sample that also show clear signs of substructures, suggesting a possible link between the presence of streamers and the development of these substructures.

5.4.2 *SO and H_2CO*

The emissions of SO and H_2CO exhibit complex morphology and trace disparate spatial distributions within the eDisk sources. These apparent variations suggest multiple concurrent physical processes at play in protostars, the understanding of which can provide valuable insights into the star formation process.

Morphology of SO emission

The SO emissions exhibit peaks near the outer edge of the continuum position in several eDisk sources (see Figure 5.32). SO is considered to be a reliable tracer of shocked regions in protostellar systems (e.g., Wakelam et al., 2005; Tafalla et al., 2010; Podio et al., 2015). In the cases of IRAS04169, IRAS16544, L1489, and OphIRS63, this enhancement is probably due to accretion shocks triggered by material from streamers landing onto the inner-disk envelope region (Flores et al., 2023; Kido et al., 2023; Yamato et al., 2023; Han et al., 2024). Likewise, the SO emissions show ring-like structures in L1527, OphIRS63, IRAS16253 (only visible in the robust = 0.5 image, see Aso & Sai 2023), and possibly in BHR71 IRS1. The emission in L1527 was found to be likely originating from the disk surface layer and outflow cavity walls (van't Hoff et al., 2023) and this might be the case for the other sources as well. Additionally, such ring-like morphology is also believed to result from accretion shocks at the centrifugal barrier, where the infalling material from the envelope or streamers interacts with the rotating disk (Ohashi et al., 2014; Sakai et al., 2014, 2017; Aso & Sai, 2023).

In the innermost regions ($\lesssim 0\farcs4$) of BHR71 IRS2, IRAS04166, IRAS15398, IRAS32, OphIRS43, and B335, the SO emissions peak on or close to the peak of the continuum and, in most cases, are asymmetric. The emissions at these distances might be associated with the hot core region (Drozdovskaya et al., 2018), where SO can sublimate off the disk surface, as temperatures can reach higher than its sublimation temperature of ∼50 K. Indeed, moment 9 maps show a velocity gradient along the major axis in most sources, which suggests that the emission close to the protostar likely originates from the innermost envelope and disk region. Similar findings have been noted in the outbursting protostar V883 Ori, where the central sublimated component of the SO emissions displays similar size and kinematic properties to those of the COMs (Lee et al., 2024). However, this scenario does not account for the asymmetry observed towards many sources. The asymmetrical peaks in

these sources are oriented in the direction of the outflow, which suggests that they probably result from localized enhancement of SO caused by disk winds or bow shocks from outflows and jets (Tabone et al., 2017). This enhancement likely complements the SO emissions from the inner envelope and disk surface. Additionally, the large-scale SO emissions seen in a few sources likely also trace shocked regions caused by the outflows (see Figure 5.19). A large arc-like structure is seen in the northeast of Ced110IRS4, and a small blob of emission is seen in the southwest of IRAS15398. Both structures are seen in the direction of the outflow and probably result from SO emissions from gas-phase reactions due to slow-moving outflows ($\sim$3 km s^{-1}) or sublimation of SO from ices due to fast-moving outflows ($\gtrsim$ 4 km s^{-1}; van Gelder et al. 2021). In BHR71 IRS2 and L1527, large-scale emissions are seen toward the outflow cavities and likely also originate from the sublimation of SO from the ices due to increased temperatures in these regions.

Tychoniec et al. (2021) discovered that SO and SiO emissions exhibit similar morphologies in most sources in their study. However, we only observe the similarity between the two molecules in IRAS16544, where both molecules peak near the protostar towards the southeast, and in IRAS15398, where a clumpy emission is seen $\sim$1000 au southwest in the direction of the outflow. Corresponding moment 9 maps of both molecules show that the emissions show velocity structures that are close to the v_{sys} of the corresponding source. This suggests that only the shocks produced by the low-velocity outflows with velocities $\lesssim$20 km s^{-1} are able to induce SO emissions either chemically or due to excitation. Likewise, Tychoniec et al. (2021) observed a clear decrease in emissions in SO from Class 0 sources to Class I sources. However, we do not see a discernible difference between the sources. It is crucial to note that Tychoniec et al. (2021) detected SO emissions in only five of the sixteen sources observed, with only one being a Class I source. Because of this small sample size, caution must be exercised in generalizing this as a trend. Nevertheless, this apparent decrease likely results from the observations lacking the sensitivity needed to detect the lower column densities of the SO emissions in Class I sources due to their thinner envelopes.

Morphology of H_2CO emission

H_2CO was the first organic molecule identified in the ISM that includes elements other than carbon and hydrogen (Snyder et al., 1969). It has multiple reaction pathways and can form both in warm regions through gas-phase reactions (e.g., Fockenberg & Preses, 2002; Atkinson et al., 2006; van der Marel et al., 2014; Loomis et al., 2015) and cold regions on grain surfaces through the hydrogenation of CO ices (e.g., Watanabe & Kouchi, 2002; Cuppen et al., 2009; Fuchs et al., 2009). Its importance goes beyond being a simple organic molecule, as it is considered a key intermediate molecule in the synthesis pathways of numerous COMs and is often detected in protostellar systems (e.g., Maret et al., 2004; Jørgensen et al., 2005; Öberg et al., 2017). The multiple H_2CO transitions covered by the eDisk observations provide a valuable opportunity to probe the physical conditions

of the protostellar environments where these emissions are observed.

The zoomed-in $3_{0,3}$–$2_{0,2}$ maps reveal that emissions in the inner envelope and disk regions are observed toward all eDisk sources (see Figure 5.35). Emissions from higher energy transitions are also concentrated in these regions toward BHR71 IRS1/2, IRAS16544, IRAS04166, IRAS15398, IRAS16253, IRAS32, and L1527 (see Figures 5.36, 5.37). These emissions likely trace the disk surface and inner envelope regions where temperatures exceed the excitation temperatures required to populate the high-energy states. The detection of emissions in high-energy lines and the fact that CO cannot remain frozen in dust grains in these areas suggest that gas-phase reactions are dominant in these regions (Loomis et al., 2015; Öberg et al., 2017). Similarly, clusters of H_2CO emissions are detected across all transitions toward GSS30IRS3, IRAS04169, and IRAS15398 at larger distances in the outflow direction. These emissions are also probably dominated by gas-phase reactions, with shock-induced heating from outflows raising the temperatures in these regions.

Although the H_2CO emissions from both the low- and high-energy transitions trace similar morphologies in the overall moment 8 maps, some differences are observed between these transitions, especially within the individual channel maps. For instance, for the source L1527, emissions in the $3_{2,2}$–$2_{2,1}$ transition were found to originate mostly from the disk surface layer, while significant contributions from the envelope are seen in $3_{0,3}$–$2_{0,2}$ transition (see van't Hoff et al. 2023 for further details). Such discrepancies indicate that emissions from different physical layers can contribute to different transitions.

Aside from BHR71 IRS1, IRAS15398, and OphIRS43, extended H_2CO emissions are detected only in the $3_{0,3}$–$2_{0,2}$ transition. This absence of extended emissions in the higher energy transitions indicates that these emissions primarily trace the relatively colder, outer regions of the protostellar envelope, where the temperatures are not quite warm enough to excite H_2CO molecules to higher energy states. Another possibility is that the quantity of molecules excited to the higher energy states in these outer regions is insufficient to produce emissions that exceed the brightness temperature thresholds sensitive to the eDisk observations. In either case, the emissions in these regions are likely dominated by the grain surface hydrogenation pathway, with H_2CO remaining frozen out until temperatures rise above the H_2CO sublimation temperatures of ∼40 – 70 K (Aikawa et al., 1997; Noble et al., 2012; Fedoseev et al., 2015). A more comprehensive analysis using chemical models incorporating both formation pathways is necessary to fully untangle the chemistry of H_2CO emissions in protostellar sources.

The ratios of different K_a ladders of H_2CO transitions such as $J_{K_aK_c} = 3_{0,3}$–$2_{0,2}$, and $J_{K_aK_c} = 3_{2,2}$–$2_{2,1}$ are often considered to be good tracers of the kinetic temperatures of dense regions (e.g., Mangum & Wootten, 1993; Tang et al., 2017; Artur de la Villarmois et al., 2019; van't Hoff et al., 2023). As mentioned in sections 5.3.8 and 5.4.2, the eDisk observations feature several sources where emissions are detected in both H_2CO ($3_{0,3}$–$2_{0,2}$) and ($3_{2,2}$–$2_{2,1}$) transitions. However, on the scales of the eDisk sources, the temperatures increase above 70 K and extinctions are $\gtrsim$100 mag corresponding to H_2 column densities of $\gtrsim 10^{23}$ cm^{-2}. A simple non-local thermal

equilibrium (non-LTE) calculation using RADEX (van der Tak et al., 2007) demonstrates that the $3_{0,3}$–$2_{0,2}$ transition becomes optically thick under these conditions even for a conservative H_2CO abundance of 10^{-9} which is why this method is not applicable on these scales. Additional molecular tracers that are optically thin and sensitive to higher temperatures, as well as more sophisticated radiative transfer modeling, are necessary to accurately determine the temperature structures on these scales of protostellar systems.

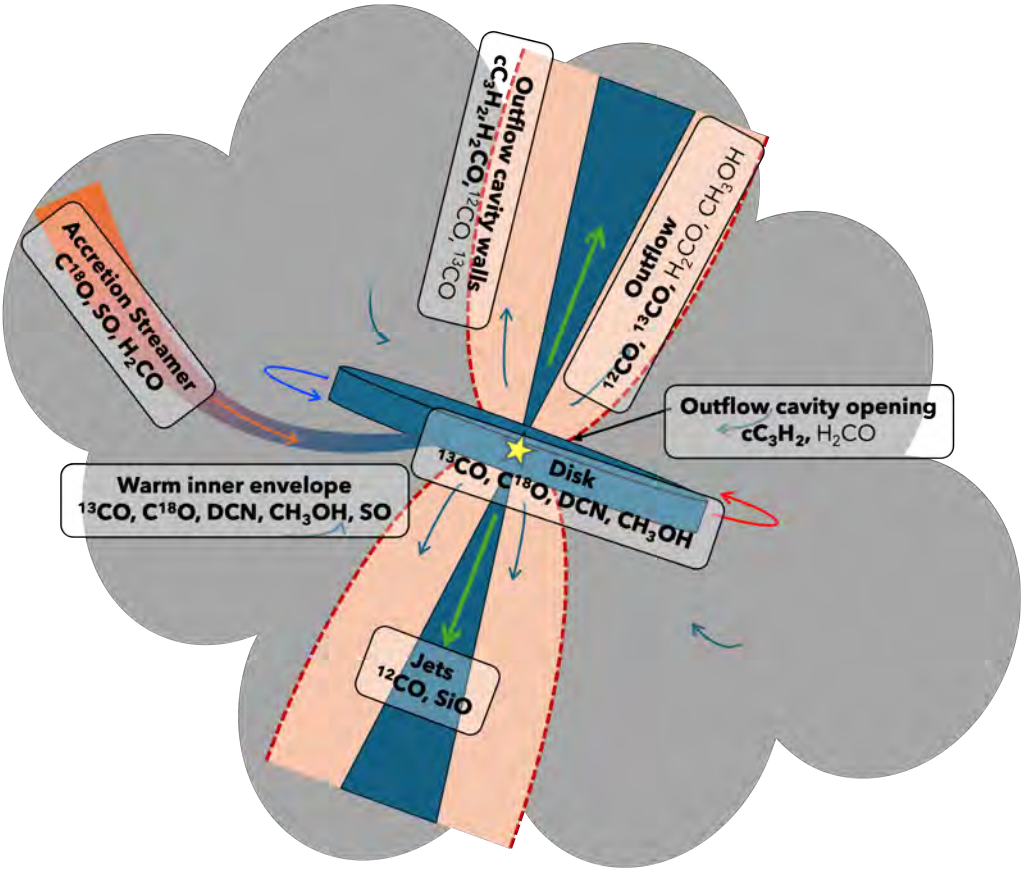

FIGURE 5.14 Cartoon image depicting the various molecules identified in different components of this study. Molecules highlighted in bold are tracers typically found in these components, whereas those in regular font indicate tracers that are occasionally identified in some sources.

5.5 CONCLUSIONS

We present high-angular resolution ($\sim 0\farcs1$ or $\sim$15 au) spectral line emissions detected toward 19 nearby Class 0/I protostars in an attempt to describe the various morphologies traced by different molecules and their physical and chemical implications. Figure 5.14 provides a summary of our results by showing the molecules detected in each section shown in Figure 5.1. Our main findings are as follows:

1. Protostellar outflows are observed in fifteen of the nineteen sources and are primarily traced by large-scale emissions in ^{12}CO and ^{13}CO. Additionally, several sources exhibit high-velocity molecular jets, traced by high-velocity emissions in ^{12}CO and SiO.

2. The walls of the outflow cavities have high densities and are delineated by large-scale ^{13}CO emissions. Exposure to UV radiation and outflow shocks leads to increased temperatures in the walls, and emissions in c−C_3H_2 and H_2CO are also frequently observed.
3. The rotation of the inner envelope and disk regions is traced by emissions in ^{13}CO and C^{18}O, with most sources showing Keplerian rotation. Emissions in DCN and CH_3OH are commonly confined to the innermost regions, likely tracing the hot cores.
4. Accretion streamers are identified in emissions of C^{18}O, SO, and H_2CO towards five sources and appear as spirals or elongated arc-like features.
5. Emissions in SO and H_2CO display complex morphologies and trace disparate structures across the different sources. Both molecules have multiple reaction pathways that likely contribute to the overall emissions observed towards the eDisk sources.

ACKNOWLEDGMENTS

This paper makes use of the following ALMA data: ADS/ JAO.ALMA#2019.1.00261.L, ADS/ JAO.ALMA#2019.A.00034.S. ALMA is a partnership of ESO (representing its member states), NSF (USA), and NINS (Japan), together with NRC (Canada), MOST and ASIAA (Taiwan), and KASI (Republic of Korea), in cooperation with the Republic of Chile. The Joint ALMA Observatory is operated by ESO, AUI/NRAO, and NAOJ. The National Radio Astronomy Observatory is a facility of the National Science Foundation operated under cooperative agreement by Associated Universities, Inc. R.S, J.K.J, and S.G. acknowledge support from the Independent Research Fund Denmark (grant No. 0135-00123B). J.J.T. acknowledges support from NASA XRP 80NSSC 22K1159. L.W.L. acknowledges support from NSF AST-2108794. Y.-L.Y. acknowledges support from Grant-in-Aid from the Ministry of Education, Culture, Sports, Science, and Technology of Japan (20H05845, 20H05844, 22K20389), and a pioneering project in RIKEN (Evolution of Matter in the Universe). J.-E.L. was supported by the National Research Foundation of Korea (NRF) grant funded by the Korea government (MSIT) (grant numbers 2021R1A2C1011718 and RS-2024-00416859).

5.a LARGE-SCALE MOMENT 8 AND MOMENT 9 MAPS

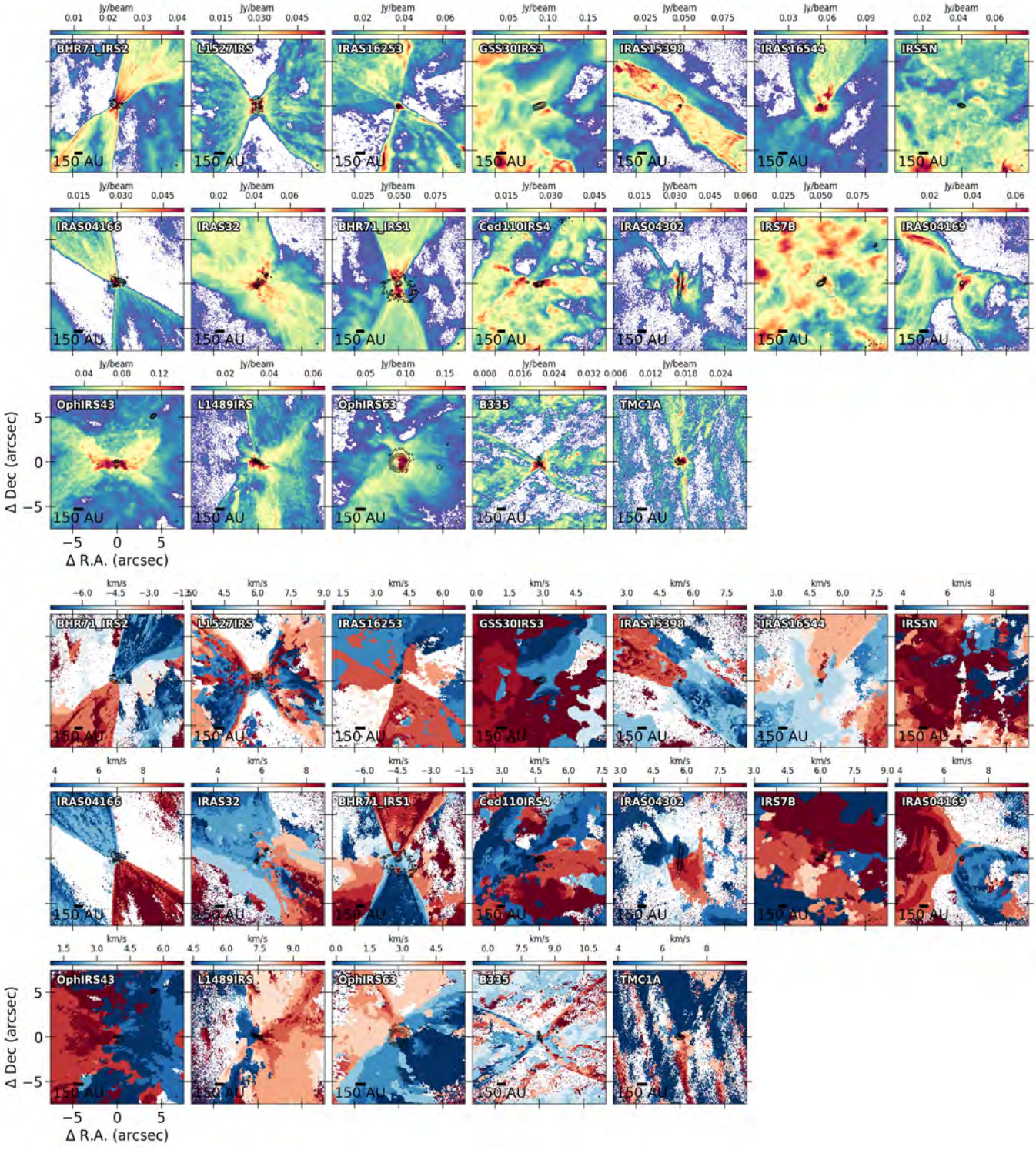

FIGURE 5.15 Moment 8 (*top*) and moment 9 (*bottom*) maps depicting the ^{12}CO (2–1) emission in the inner 15region of the nineteen eDisk sources. Moment maps were generated by integrating the regions where $I_\nu > 3\sigma$, where σ is the rms per channel. The sources are arranged in ascending order of L_{bol} except for B335 and TMC1A, the two sources taken from the archive. The contour lines display the continuum emission at thresholds of 5σ, 20σ, 80σ, and 320σ for each source. The scale bar located at the bottom left shows the 150 au scale in each source, and the synthesized beam is indicated in white at the bottom right corner of each image.

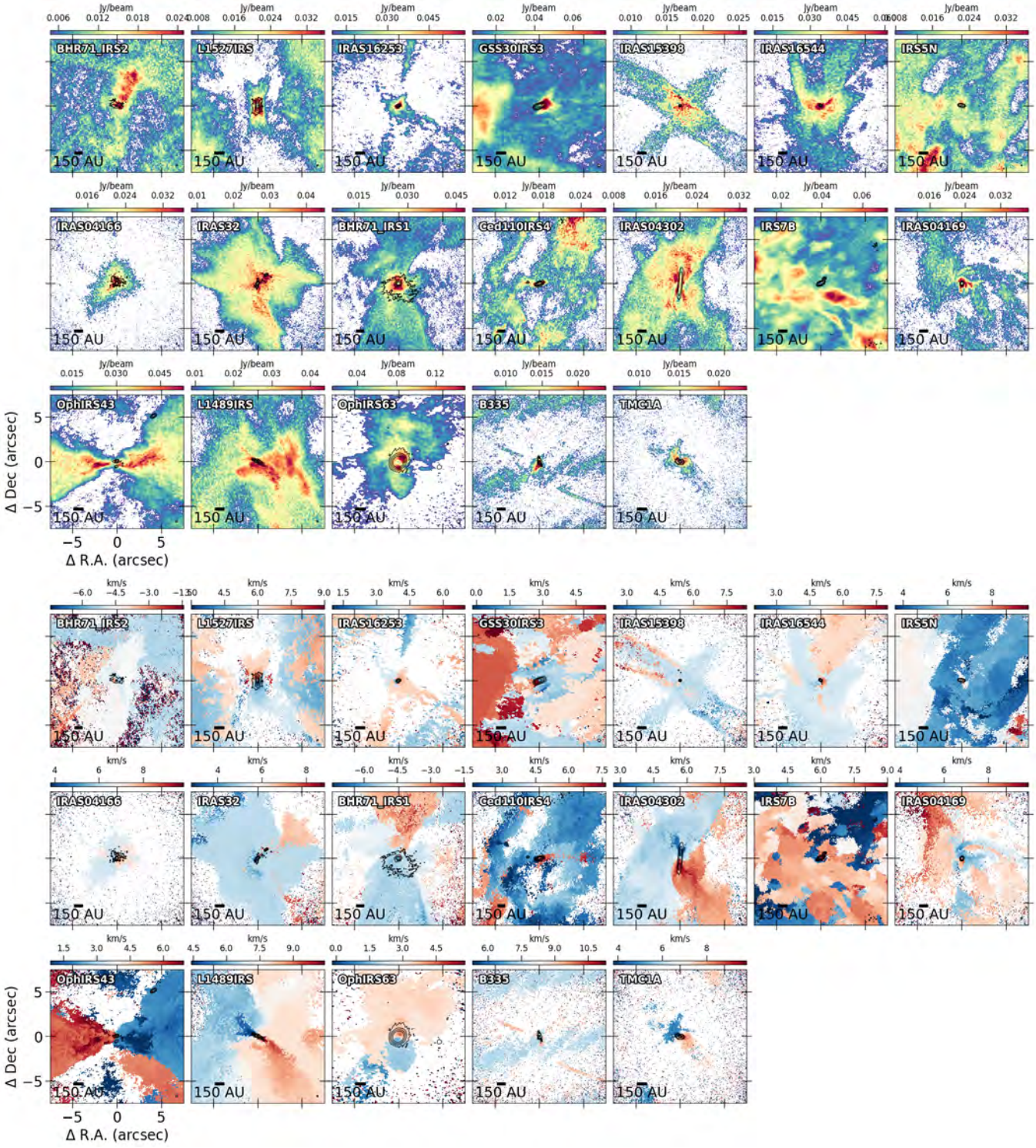

FIGURE 5.16 Same as Figure 5.15 but for ^{13}CO (2–1) instead.

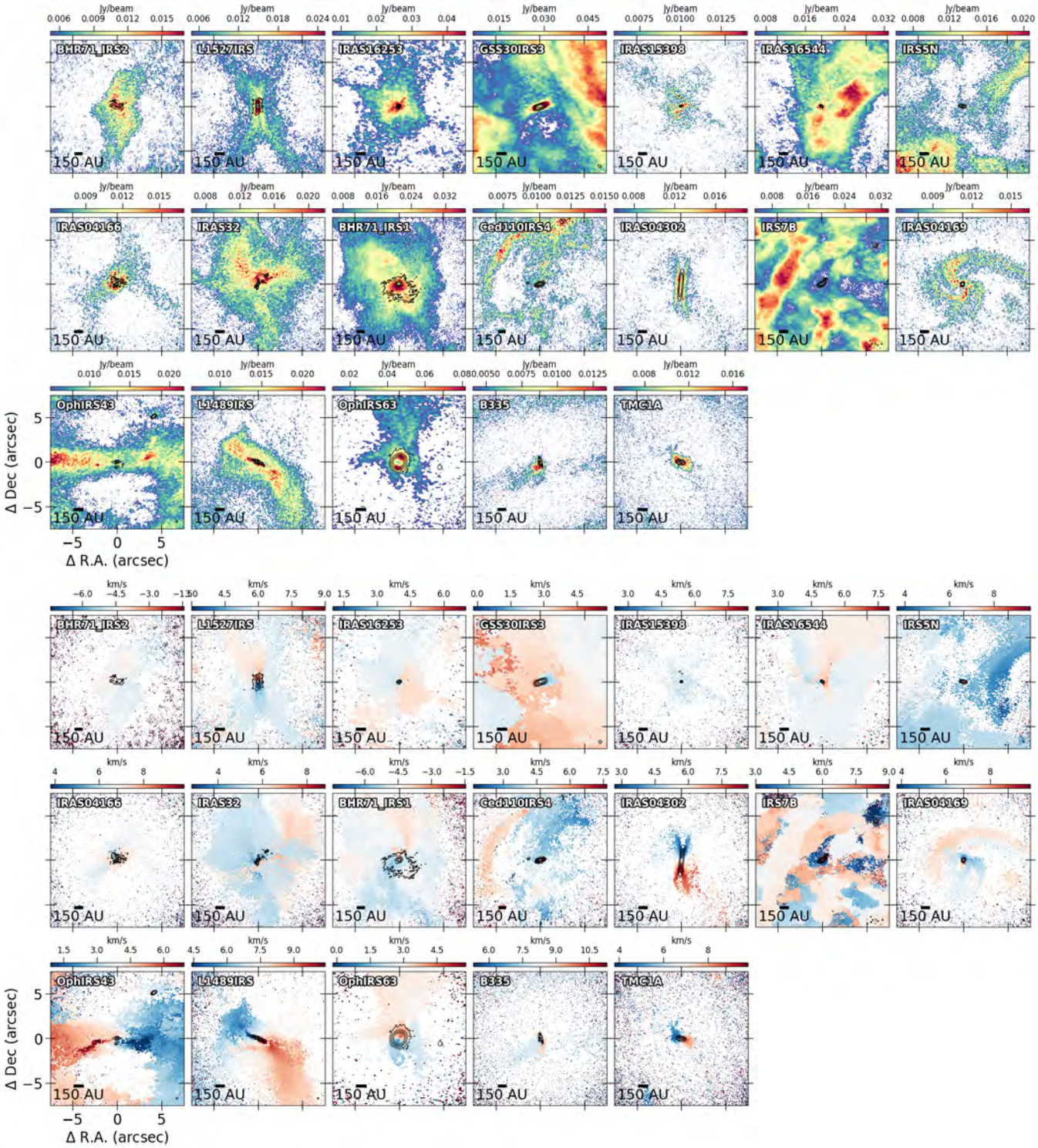

FIGURE 5.17 Same as Figure 5.15 but for $C^{18}O$ (2–1) instead.

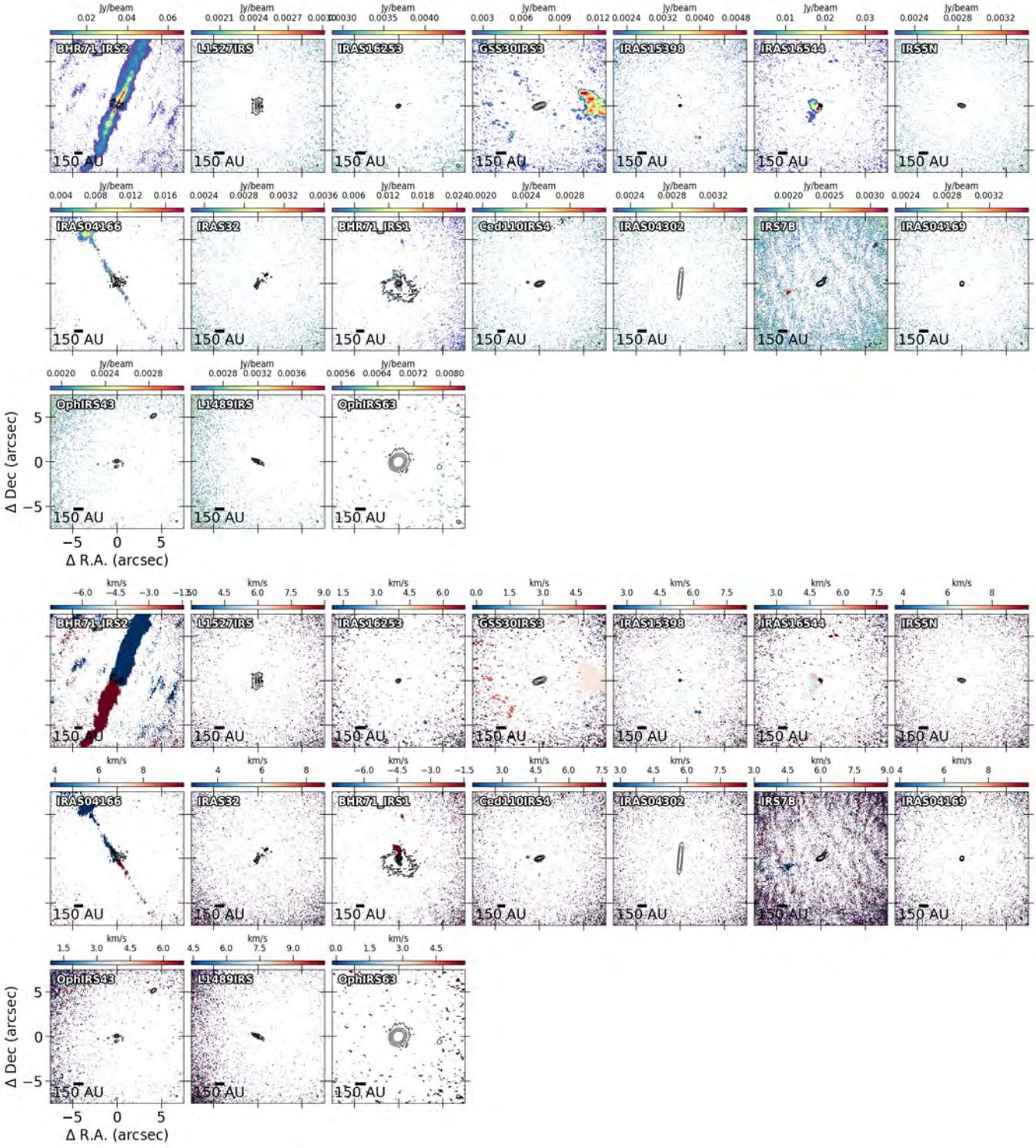

FIGURE 5.18 Same as Figure 5.15 but for SiO (5–4) instead.

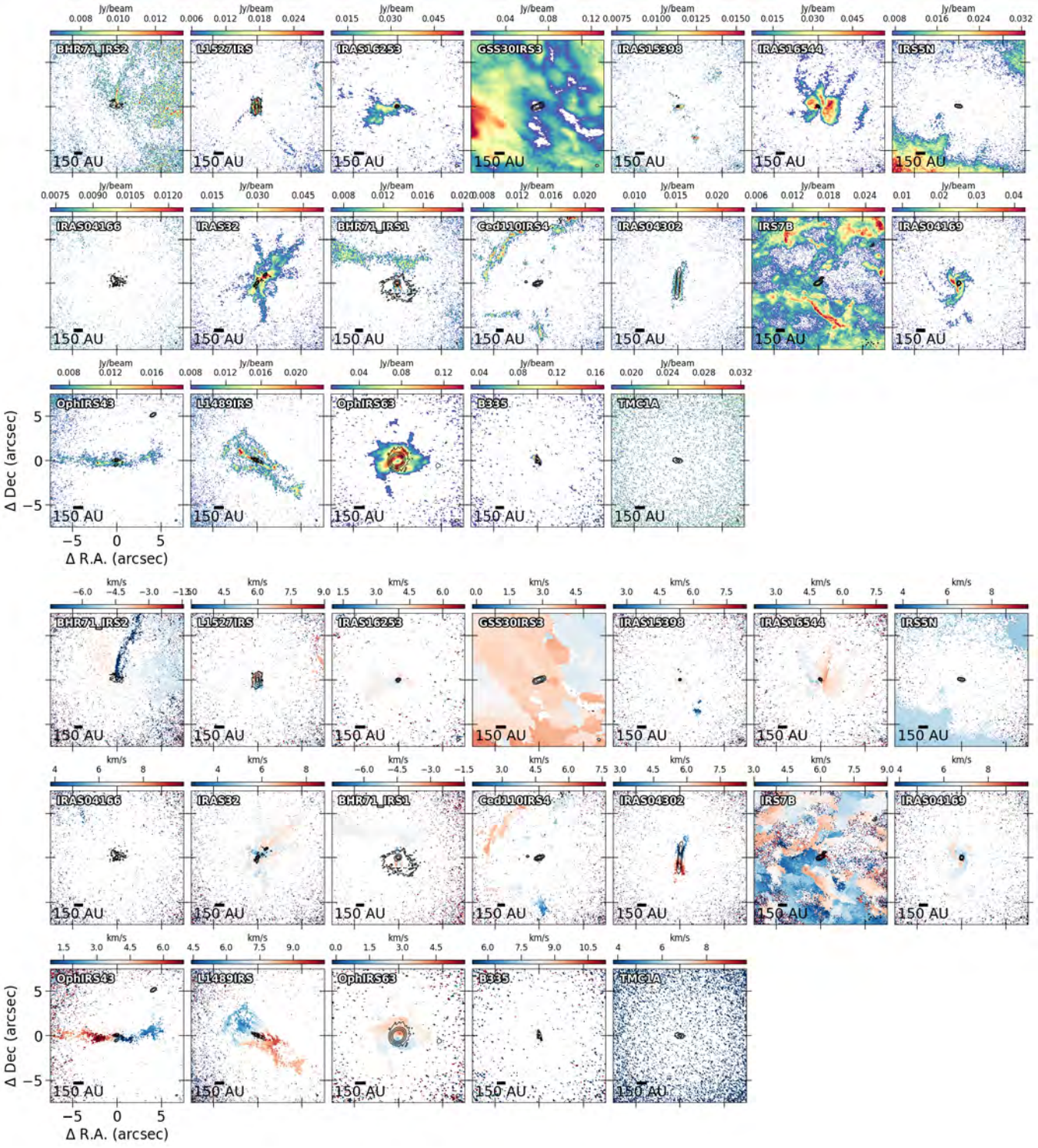

FIGURE 5.19 Same as Figure 5.15 but for SO (6_5–5_4) instead.

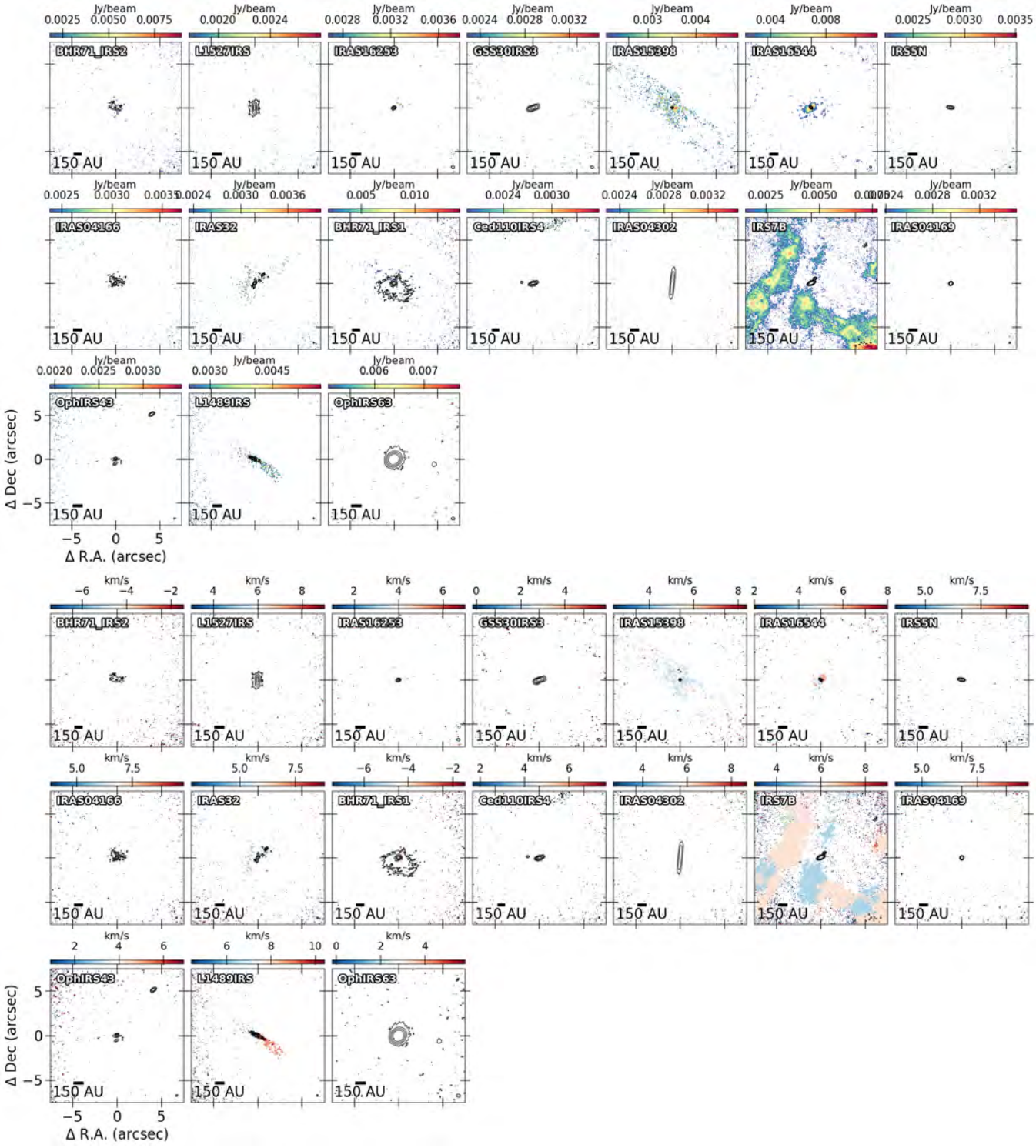

FIGURE 5.20 Same as Figure 5.15 but for DCN (3–2) instead.

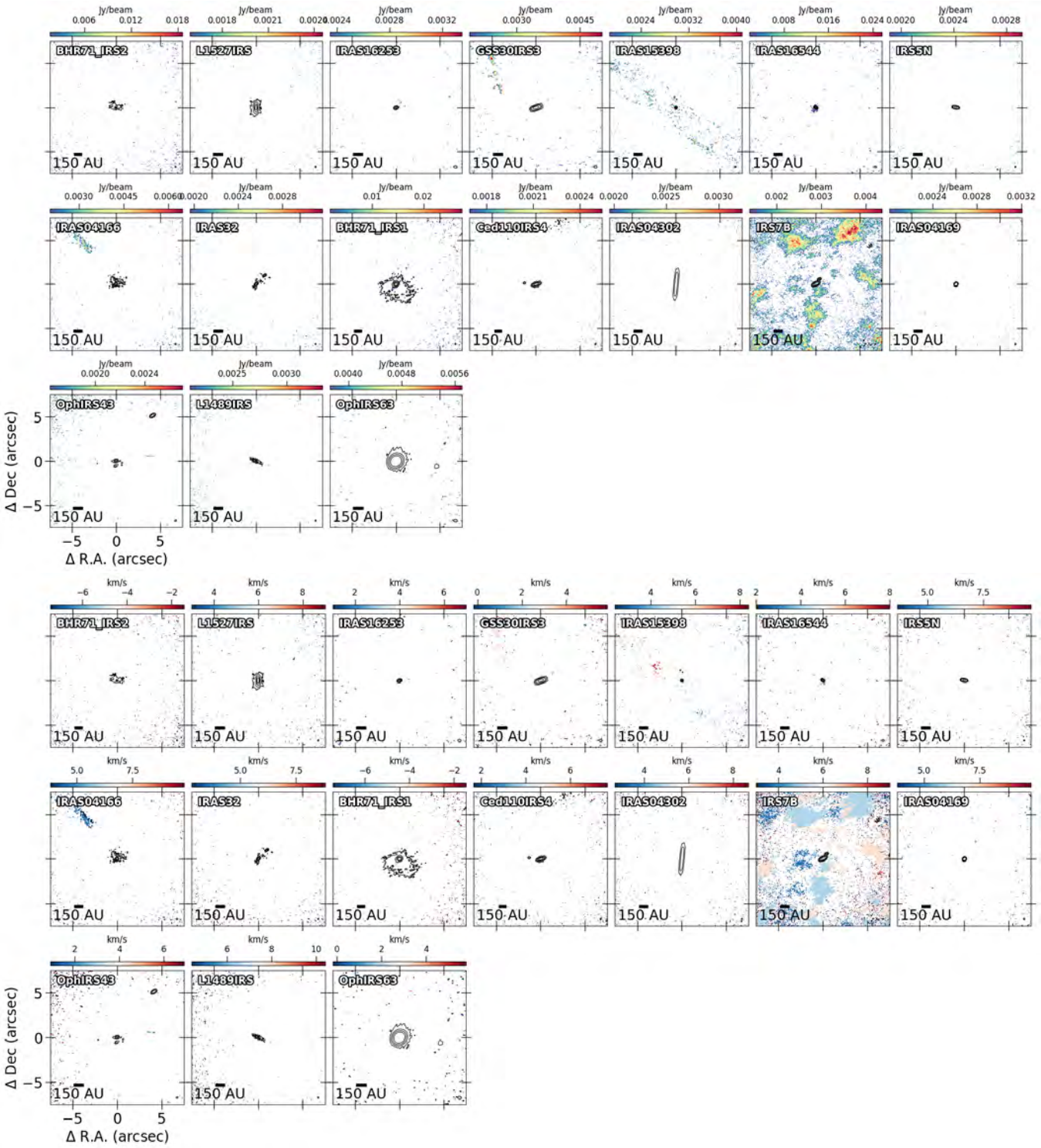

FIGURE 5.21 Same as Figure 5.15 but for CH_3OH (4_2–3_1) instead.

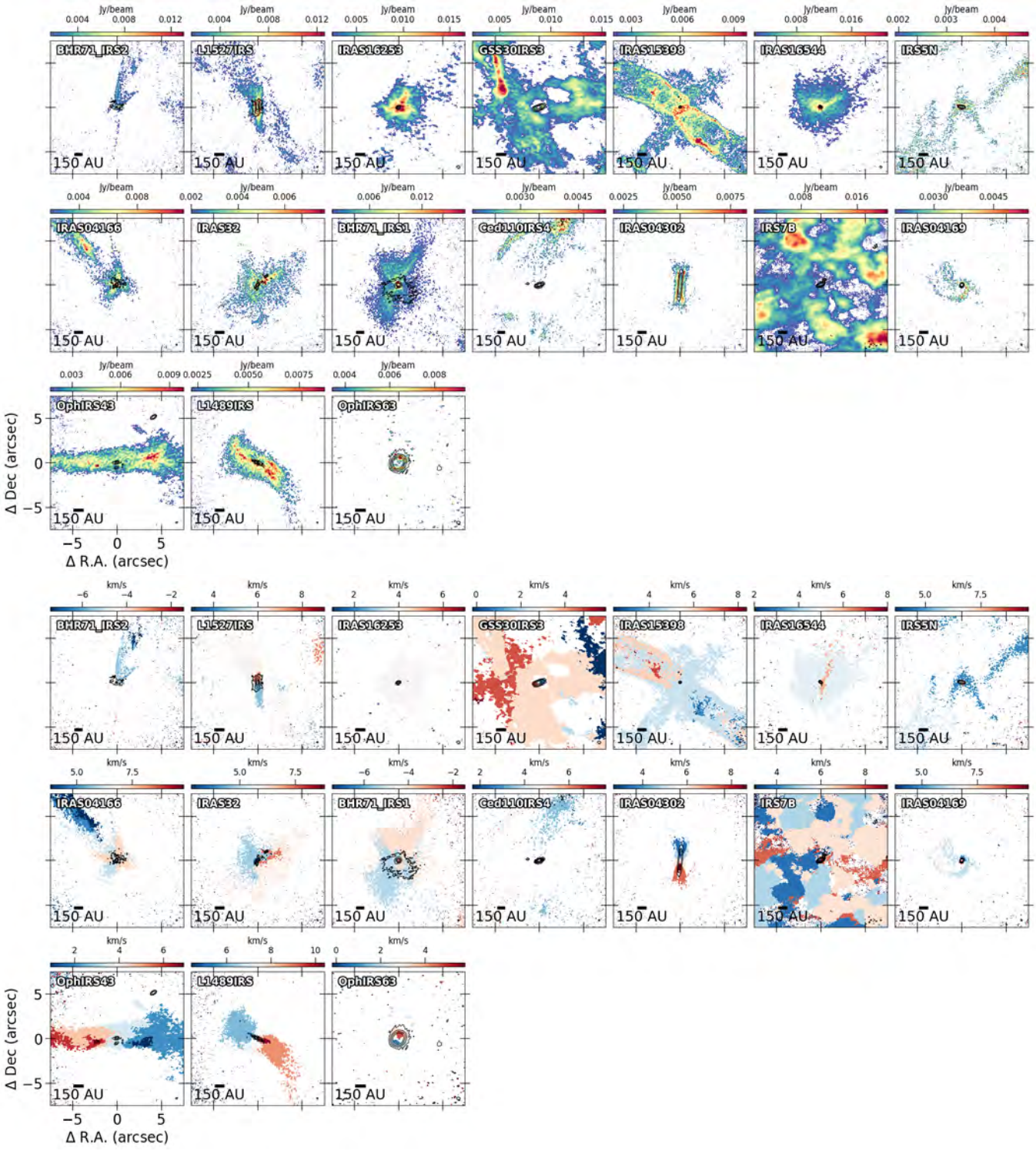

FIGURE 5.22 Same as Figure 5.15 but for H_2CO ($3_{0,3}$–$2_{0,2}$) instead.

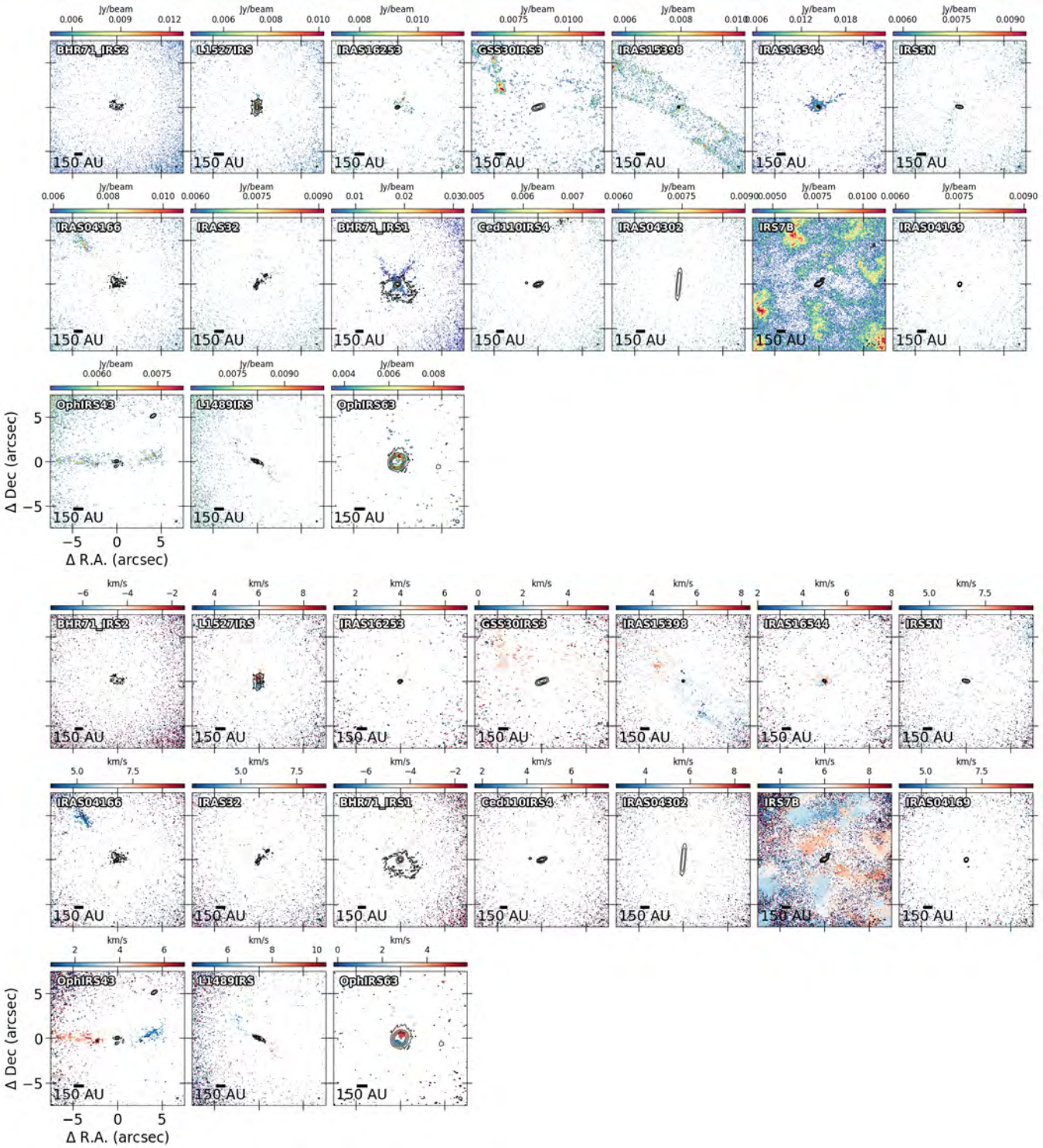

FIGURE 5.23 Same as Figure 5.15 but for H_2CO ($3_{2,1}$–$2_{2,0}$) instead.

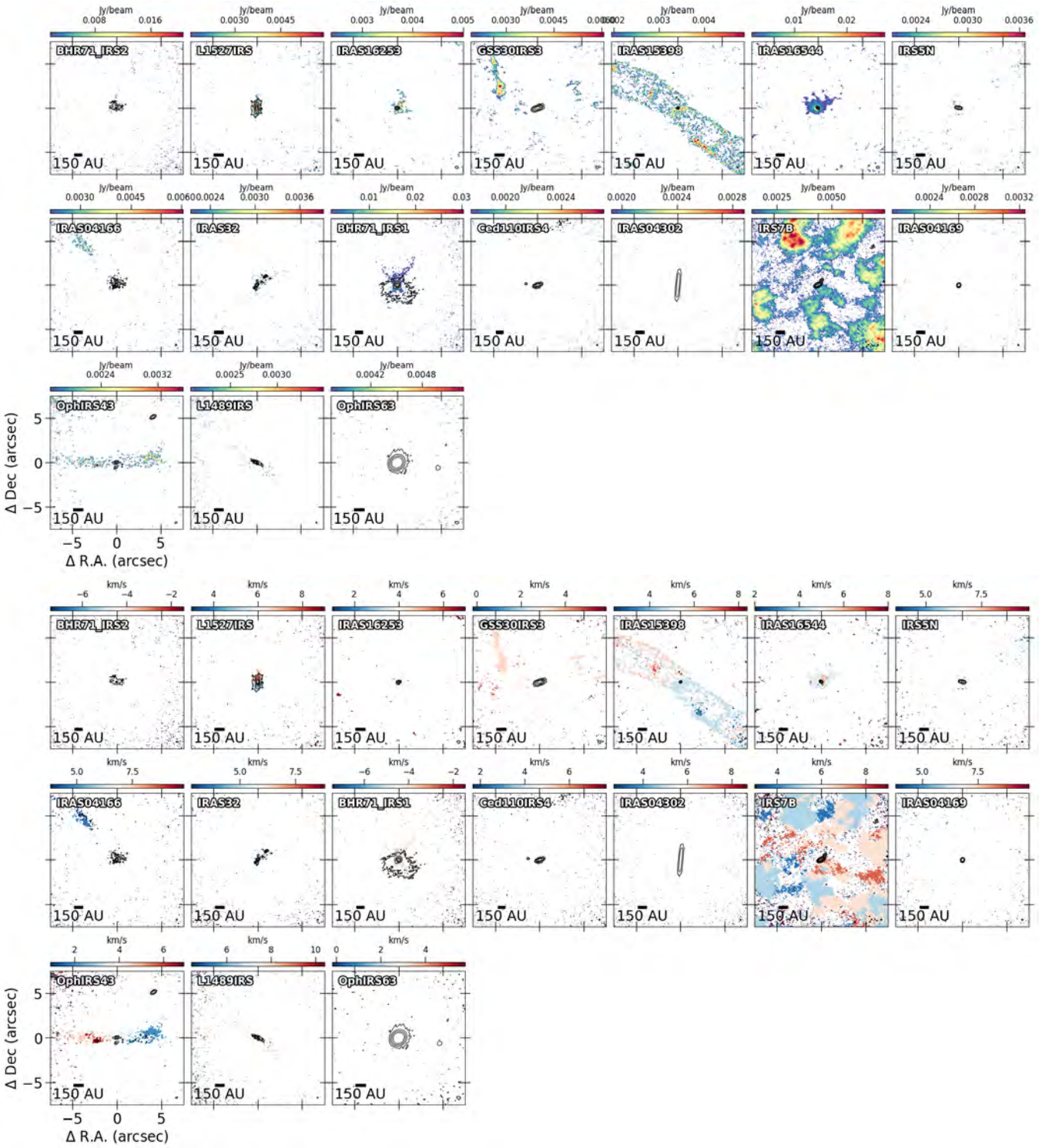

FIGURE 5.24 Same as Figure 5.15 but for H_2CO ($3_{2,2}$–$2_{2,1}$) instead.

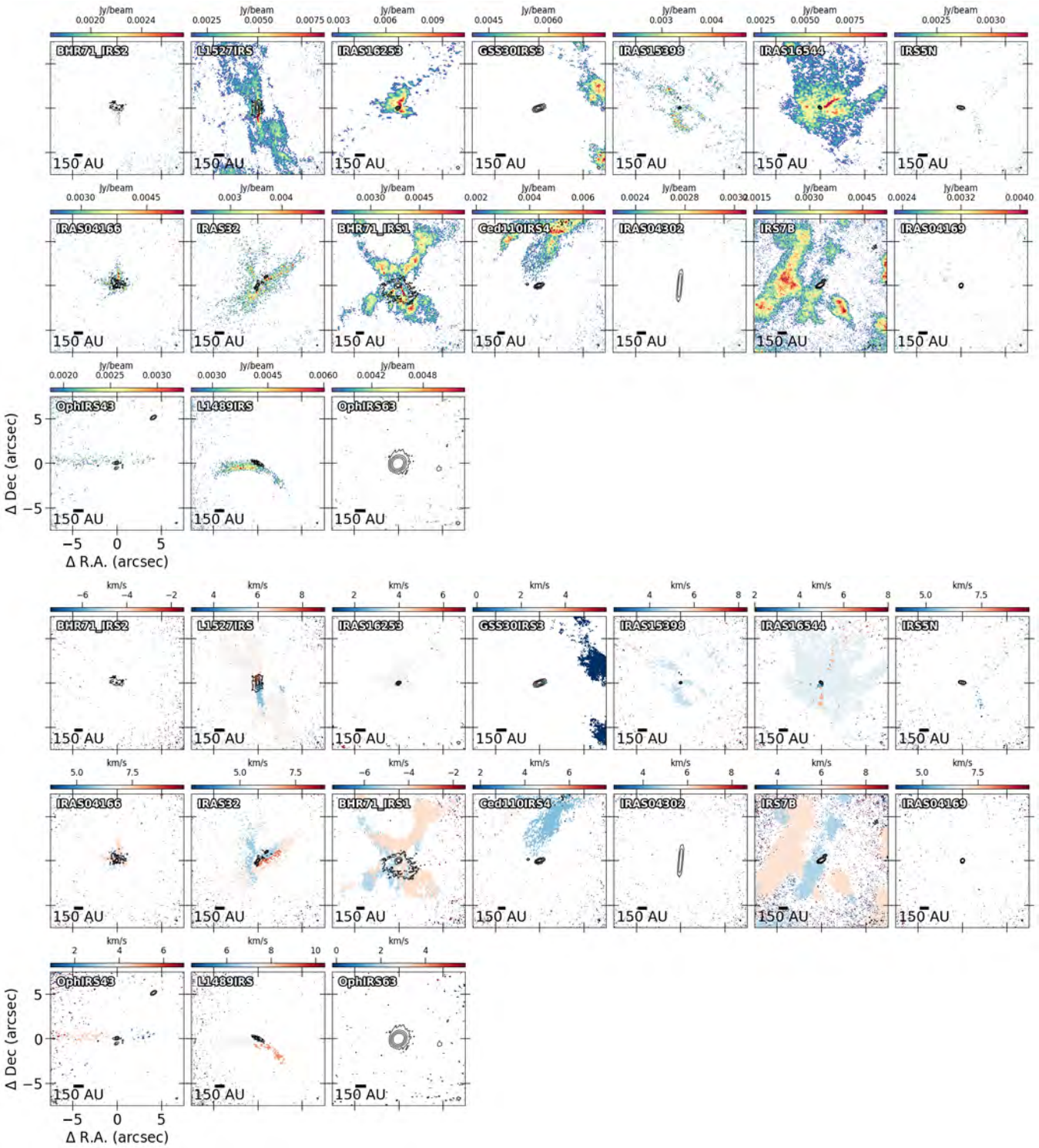

FIGURE 5.25 Same as Figure 5.15 but for the blended c–C_3H_2 ($6_{0,6}$–$5_{1,5}$) and ($6_{1,6}$–$5_{0,5}$) instead.

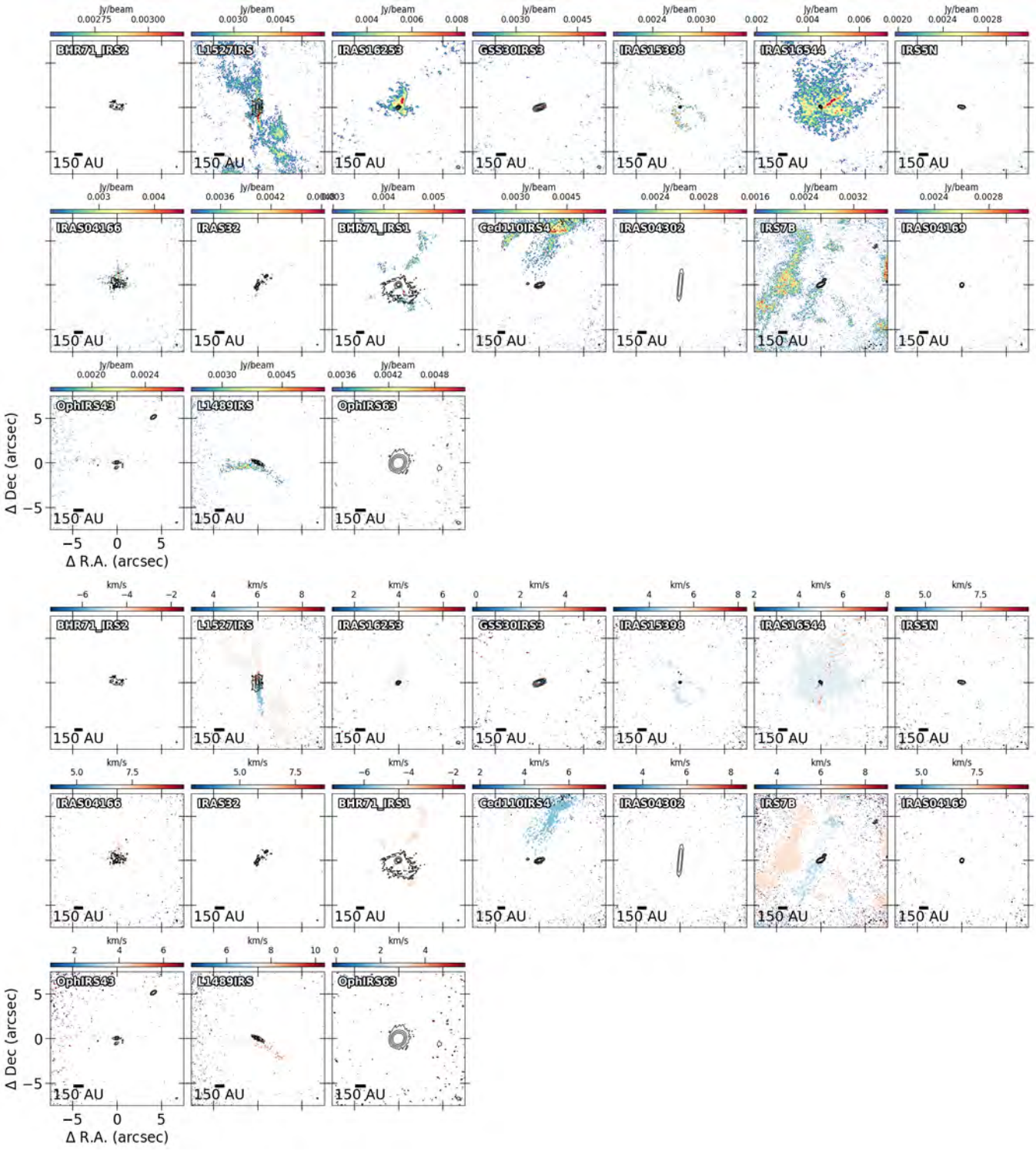

FIGURE 5.26 Same as Figure 5.15 but for c–C_3H_2 ($5_{1,4}$–$4_{2,3}$) instead.

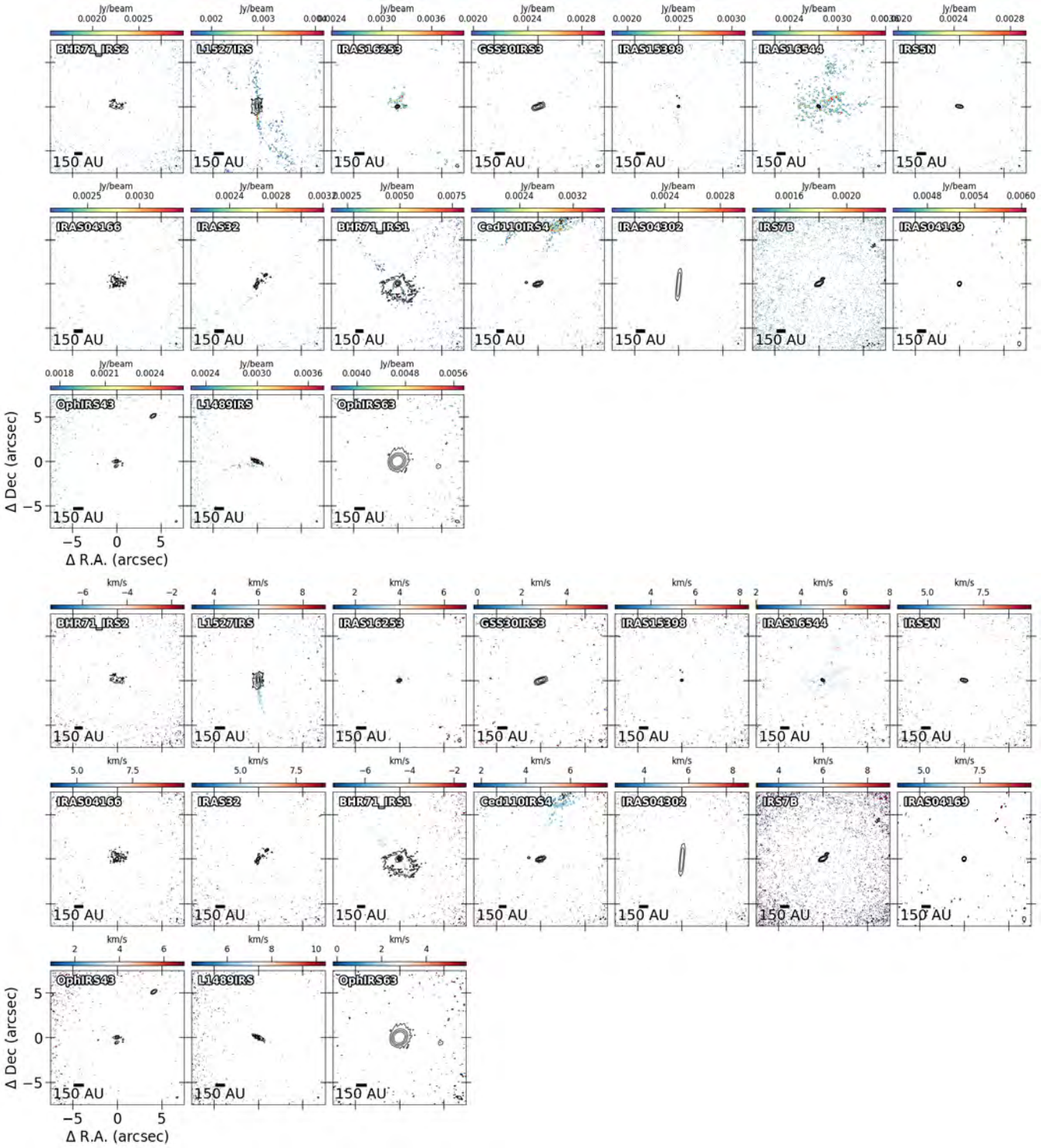

FIGURE 5.27 Same as Figure 5.15 but for c–C_3H_2 ($5_{2,4}$–$4_{1,3}$) instead.

5.b ZOOMED-IN SMALL-SCALE MOMENT 8 AND MOMENT 9 MAPS

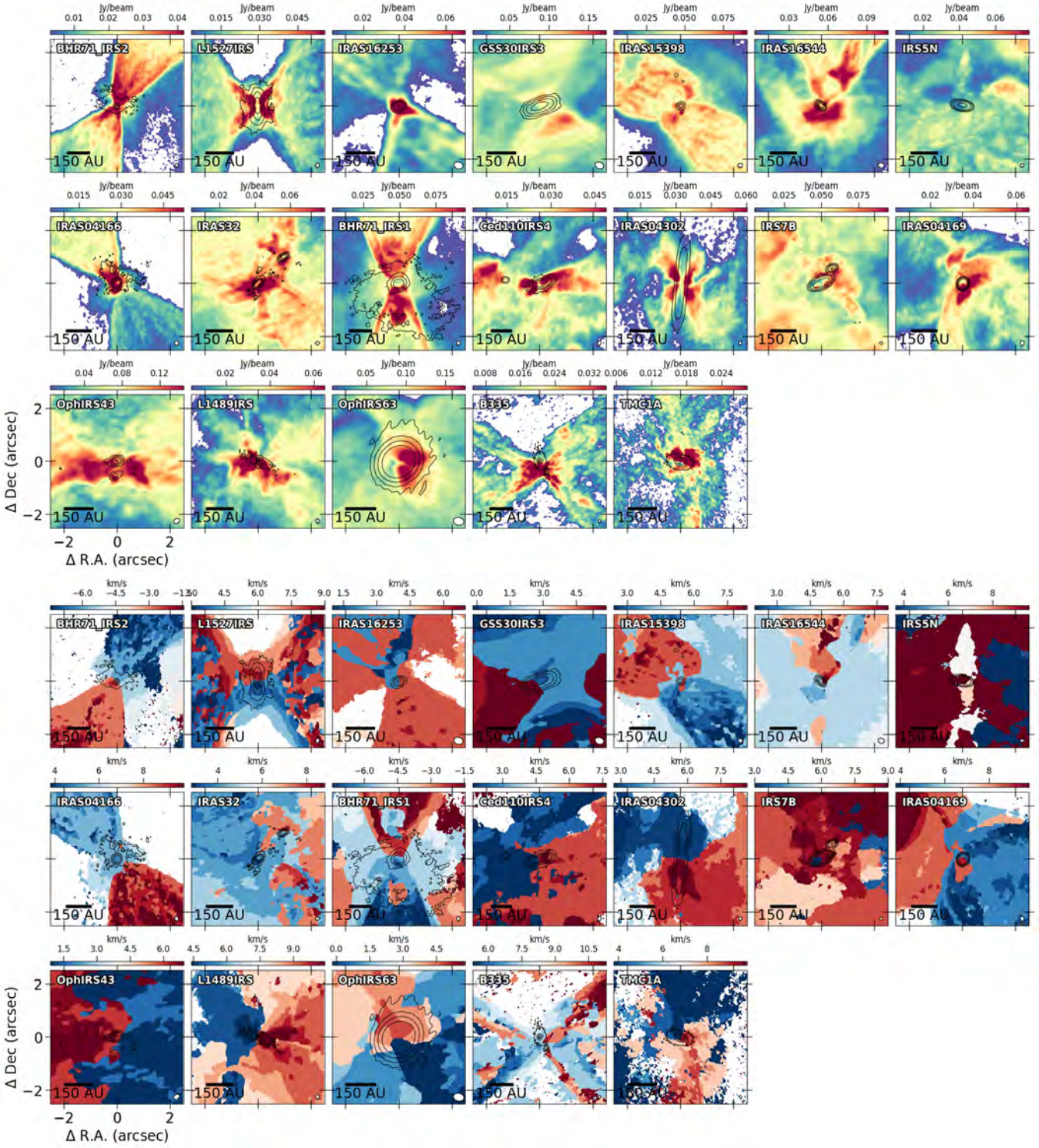

FIGURE 5.28 Moment 8 (*top*) and moment 9 (*bottom*) maps depicting the ^{12}CO (2–1) emission in the inner 5region of the nineteen eDisk sources. The moment maps were generated by integrating the regions where $I_\nu > 3\sigma$, where σ is the rms per channel. The contour lines display the continuum emission at thresholds of 5σ, 20σ, 80σ, and 320σ for each source. The scale bar is located at the bottom left, and the synthesized beam is indicated in white at the bottom right corner of each image.

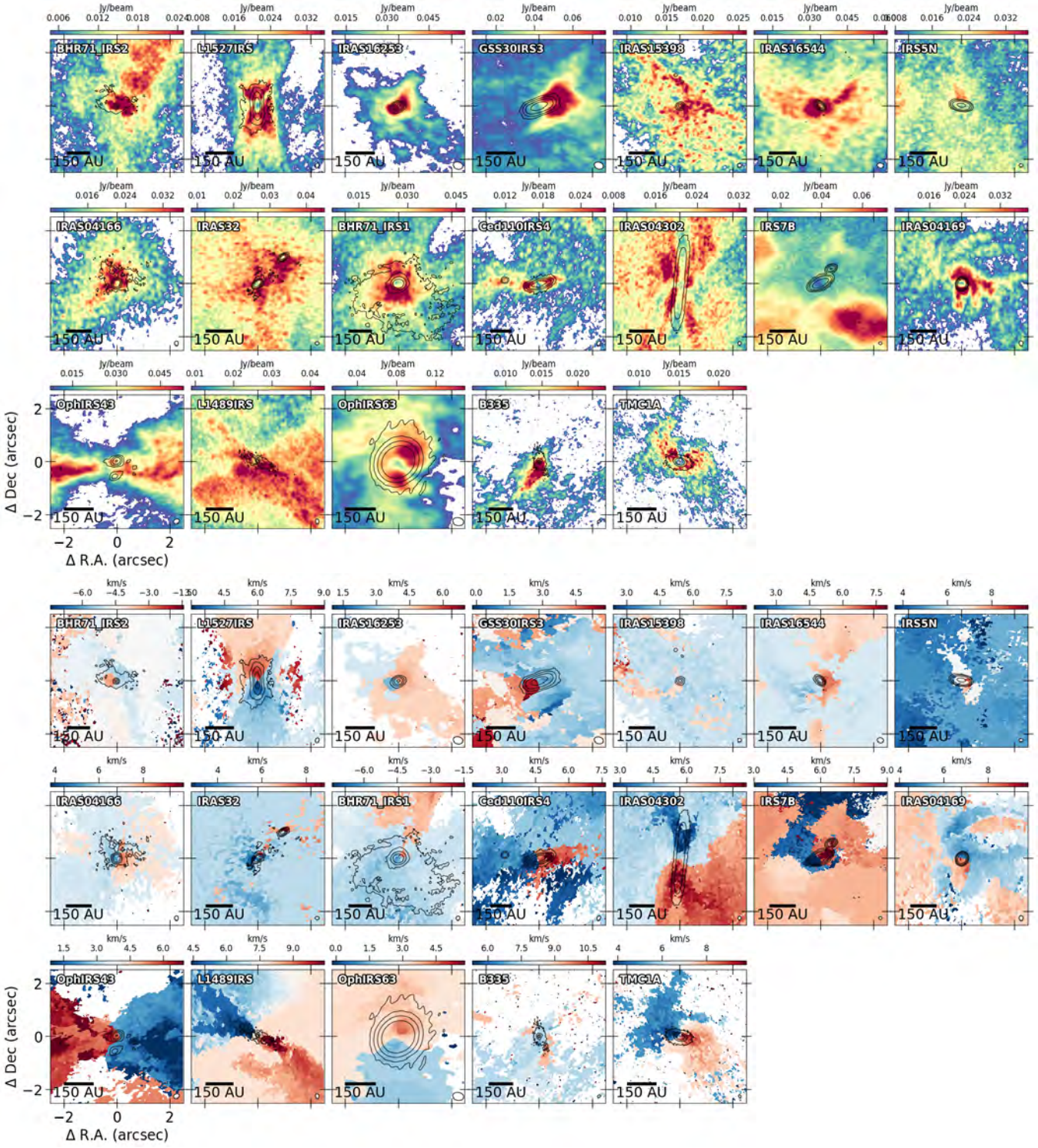

FIGURE 5.29 Same as Figure 5.28 but for ^{13}CO (2–1) instead.

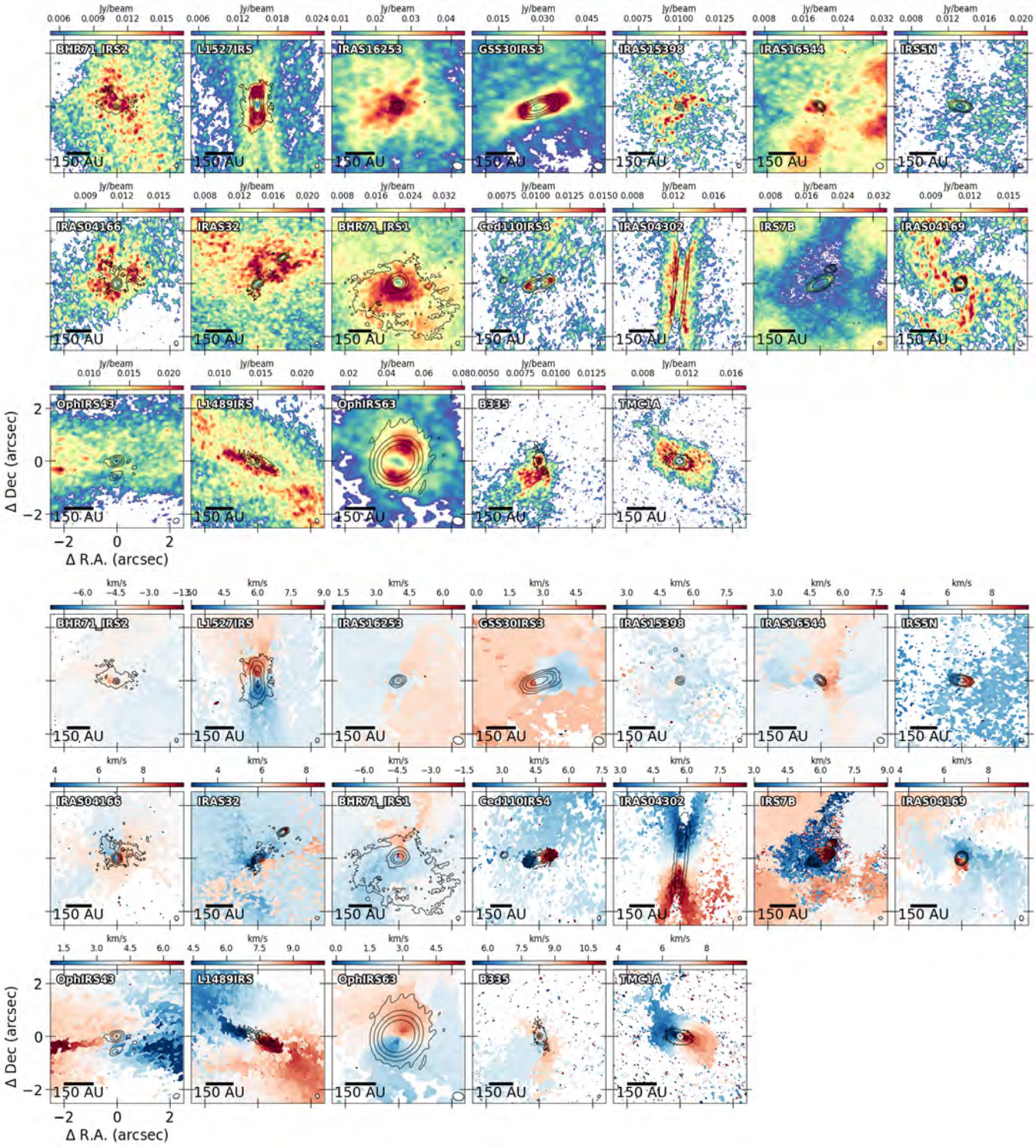

FIGURE 5.30 Same as Figure 5.28 but for $C^{18}O$ (2–1) instead.

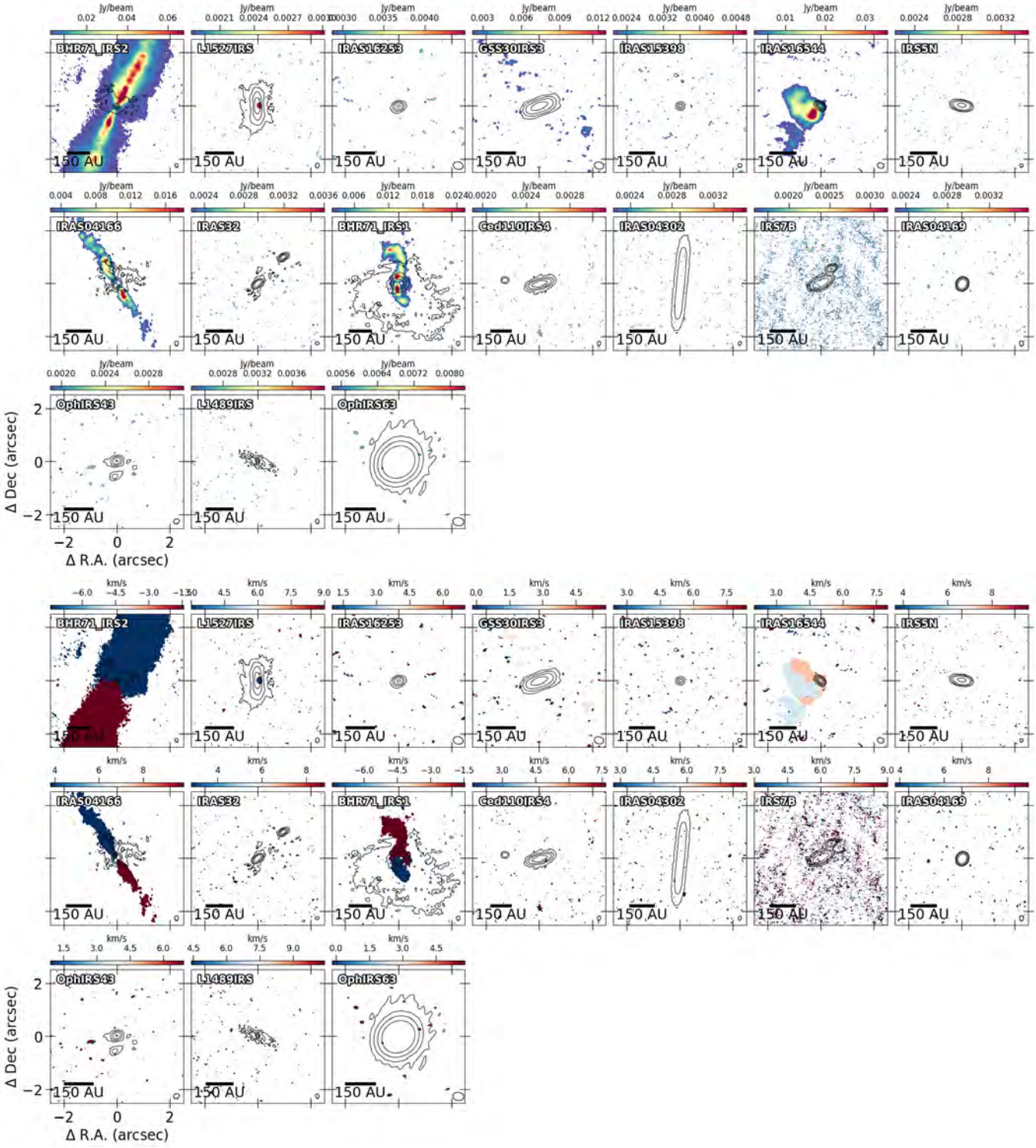

FIGURE 5.31 Same as Figure 5.28 but for SiO (5–4) instead.

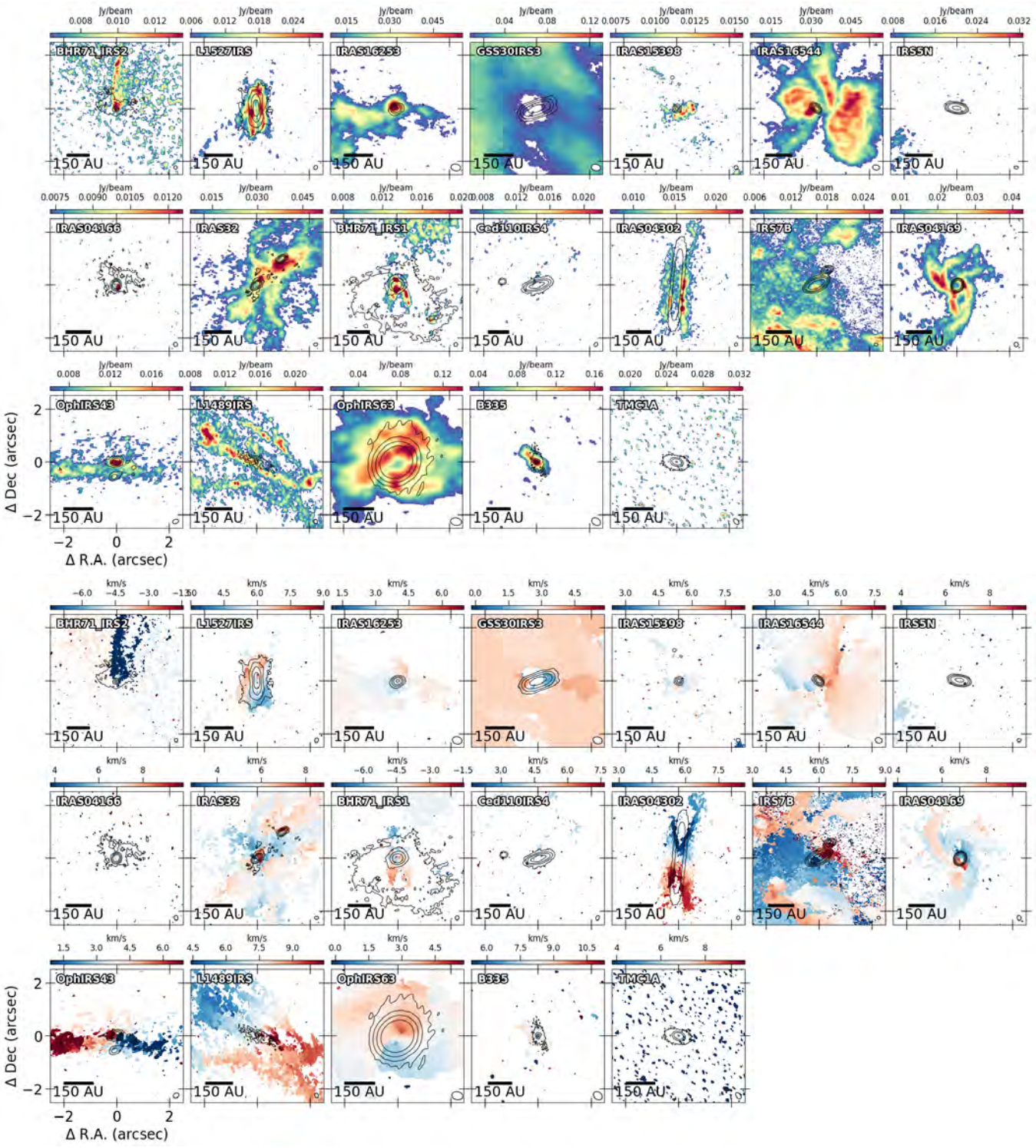

FIGURE 5.32 Same as Figure 5.28 but for SO (6_5–5_4) instead.

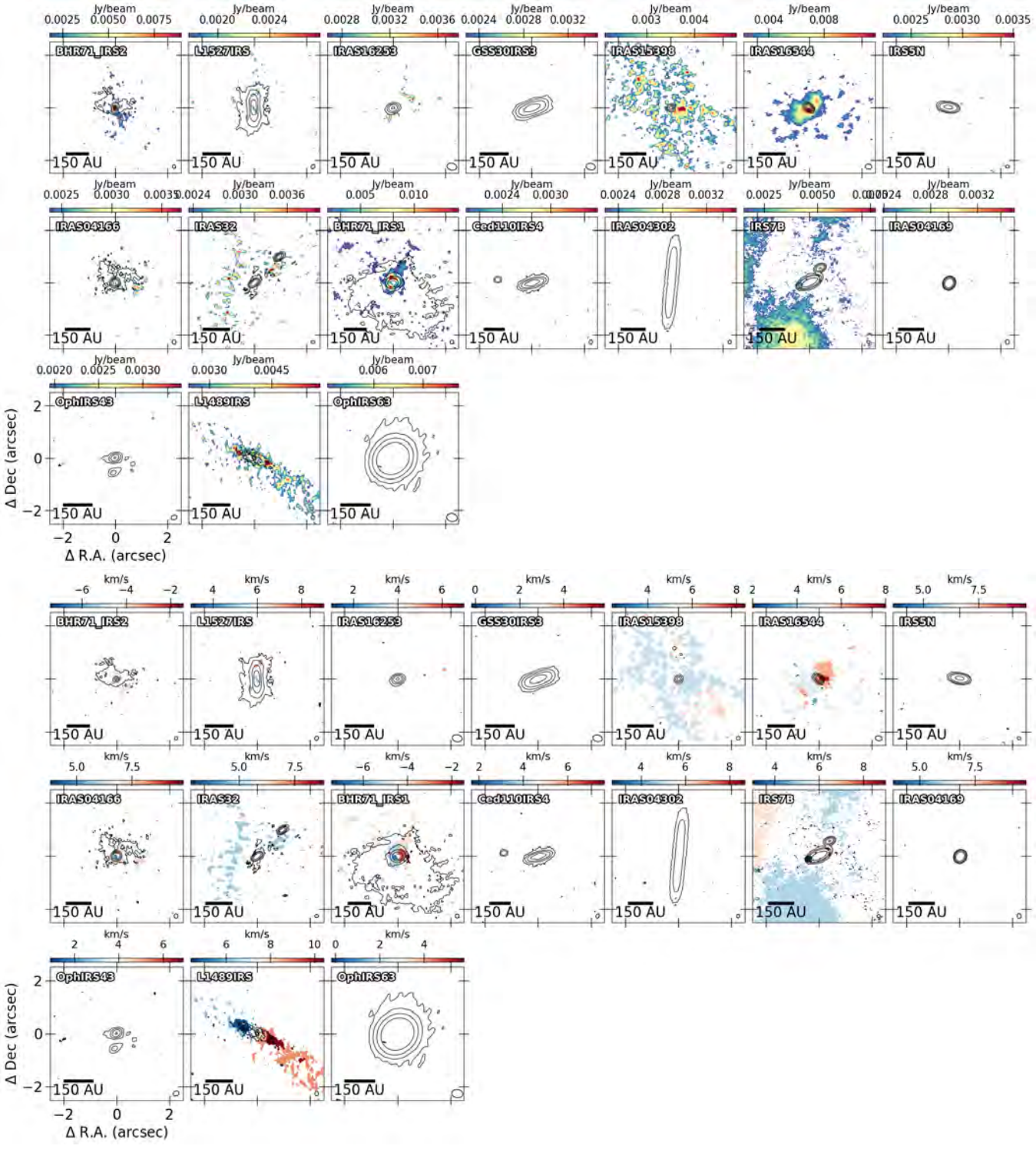

FIGURE 5.33 Same as Figure 5.28 but for DCN (3–2) instead.

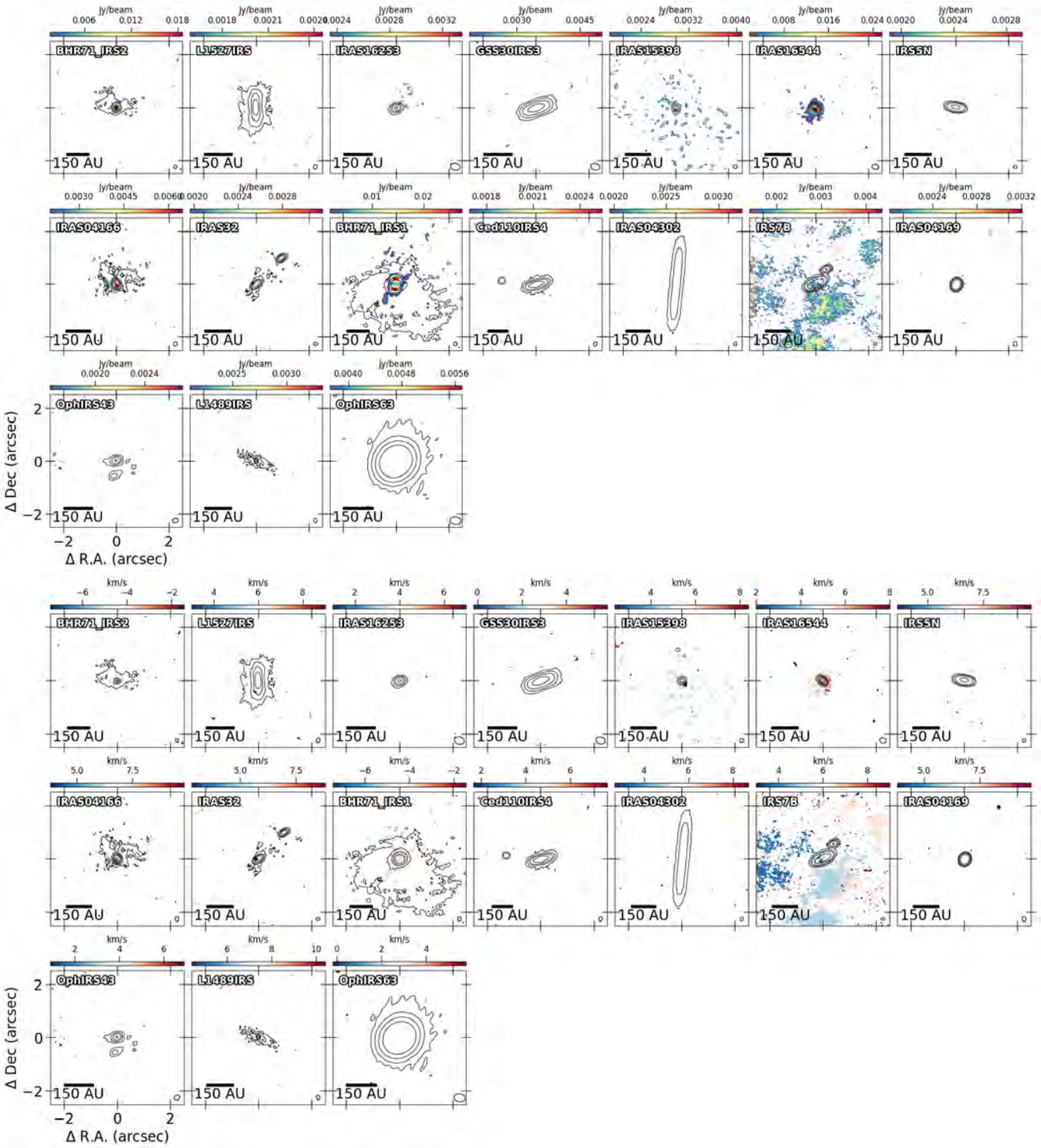

FIGURE 5.34 Same as Figure 5.28 but for CH_3OH (4_2–3_1) instead.

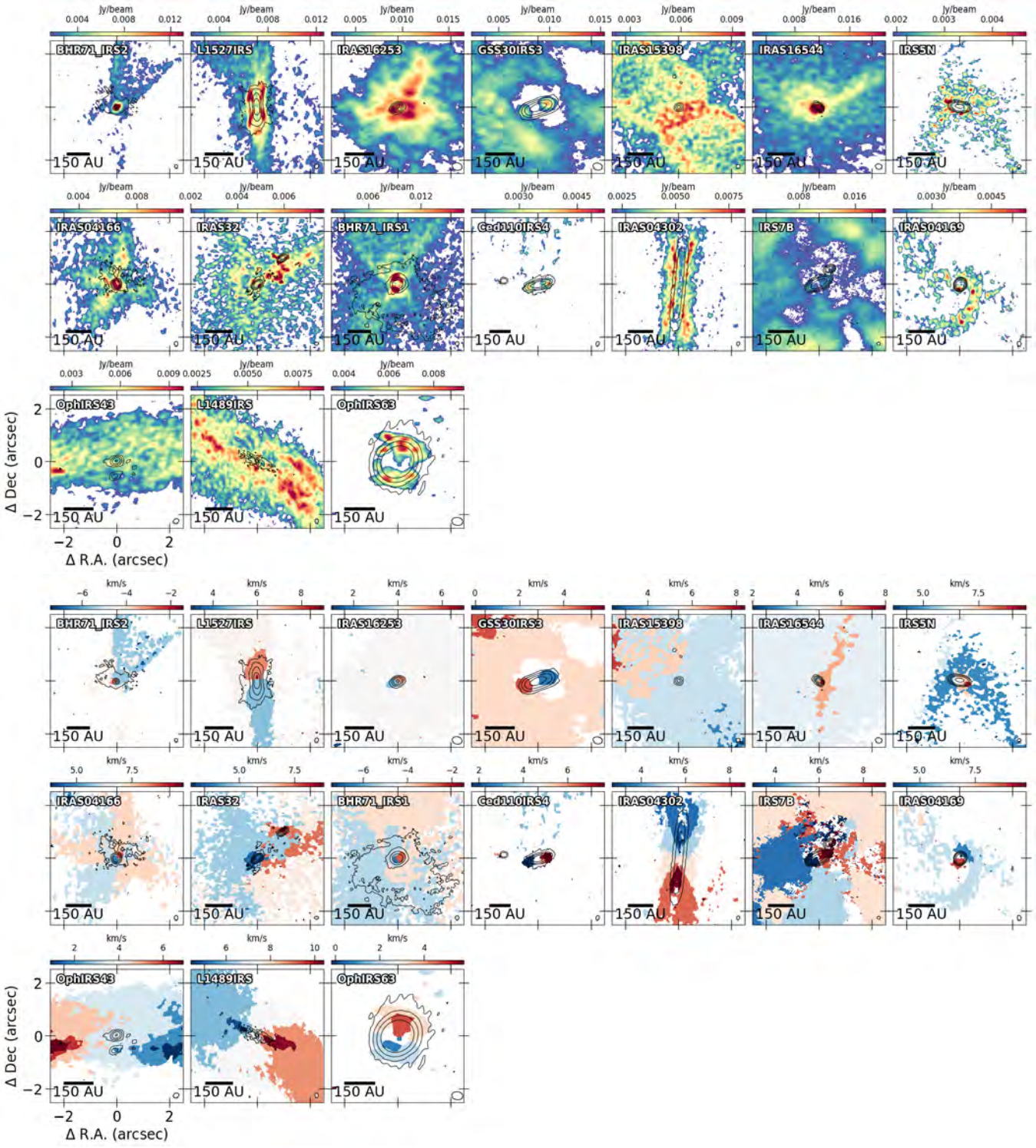

FIGURE 5.35 Same as Figure 5.28 but for H_2CO ($3_{0,3}$–$2_{0,2}$) instead.

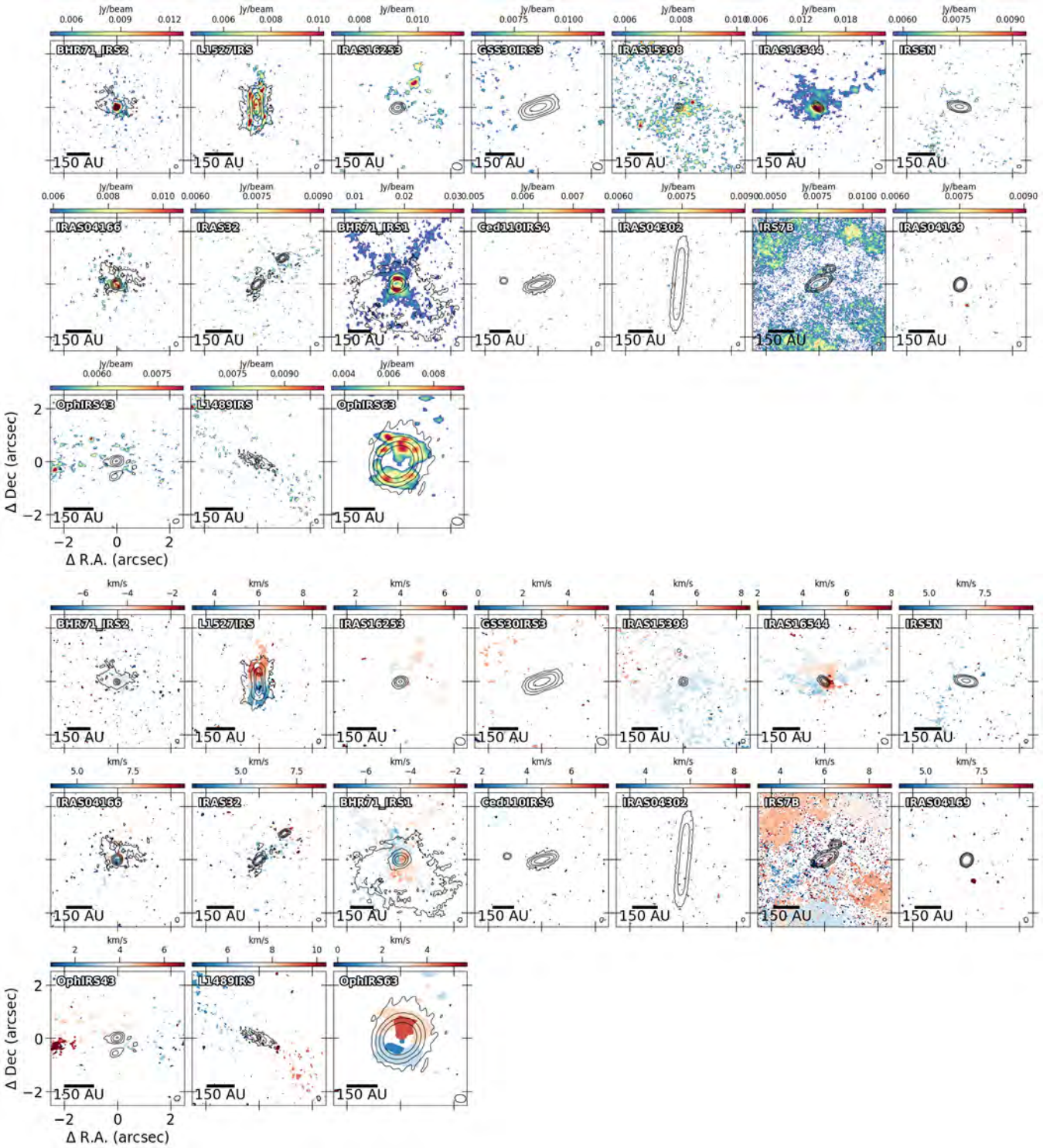

FIGURE 5.36 Same as Figure 5.28 but for H_2CO ($3_{2,1}$–$2_{2,0}$) instead.

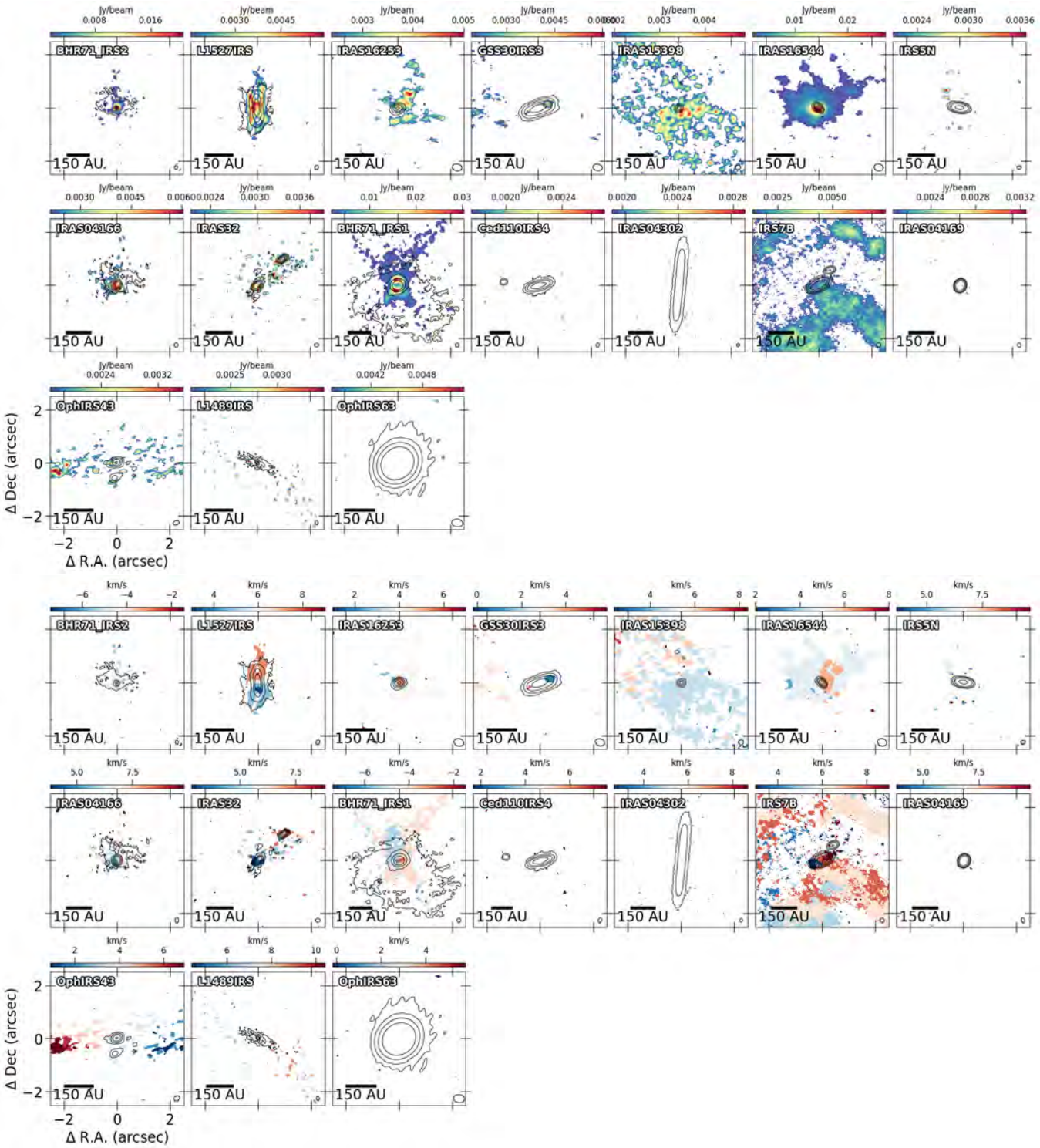

FIGURE 5.37 Same as Figure 5.28 but for H_2CO ($3_{2,2}$–$2_{2,1}$) instead.

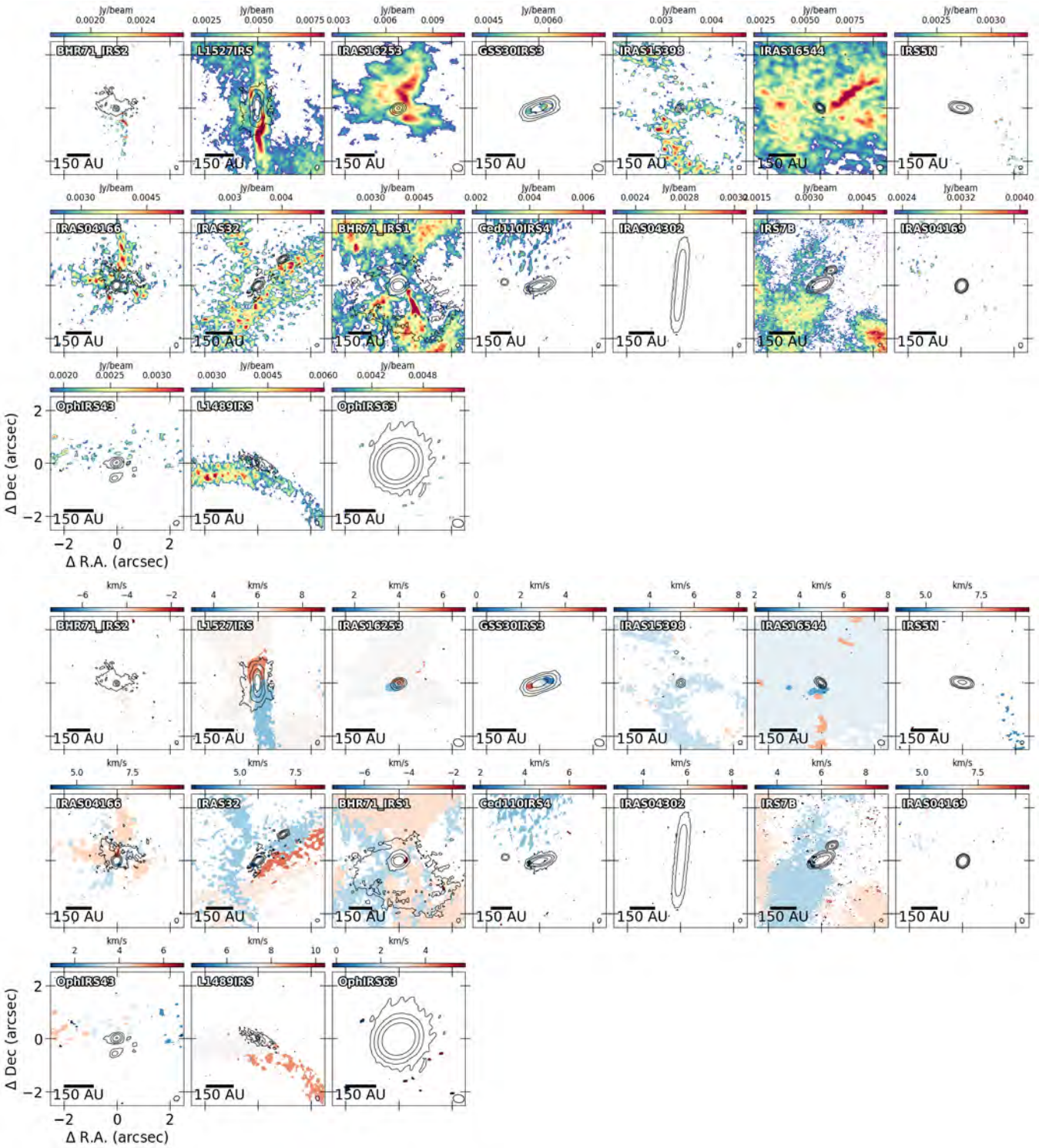

FIGURE 5.38 Same as Figure 5.28 but for the blended c–C_3H_2 ($6_{0,6}$–$5_{1,5}$) and ($6_{1,6}$–$5_{0,5}$) transitions instead.

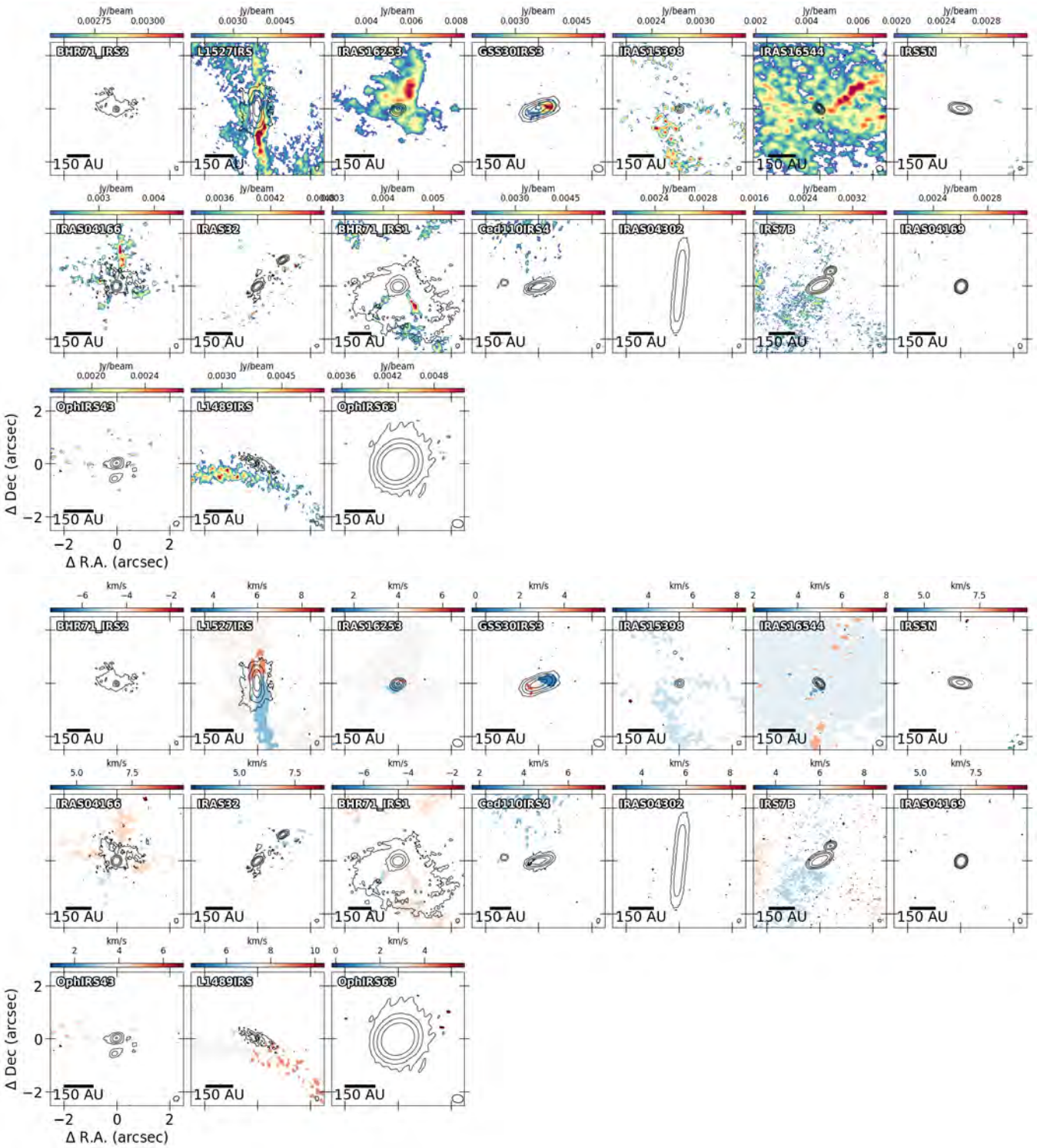

FIGURE 5.39 Same as Figure 5.28 but for c–C_3H_2 ($5_{1,4}$–$4_{2,3}$) instead.

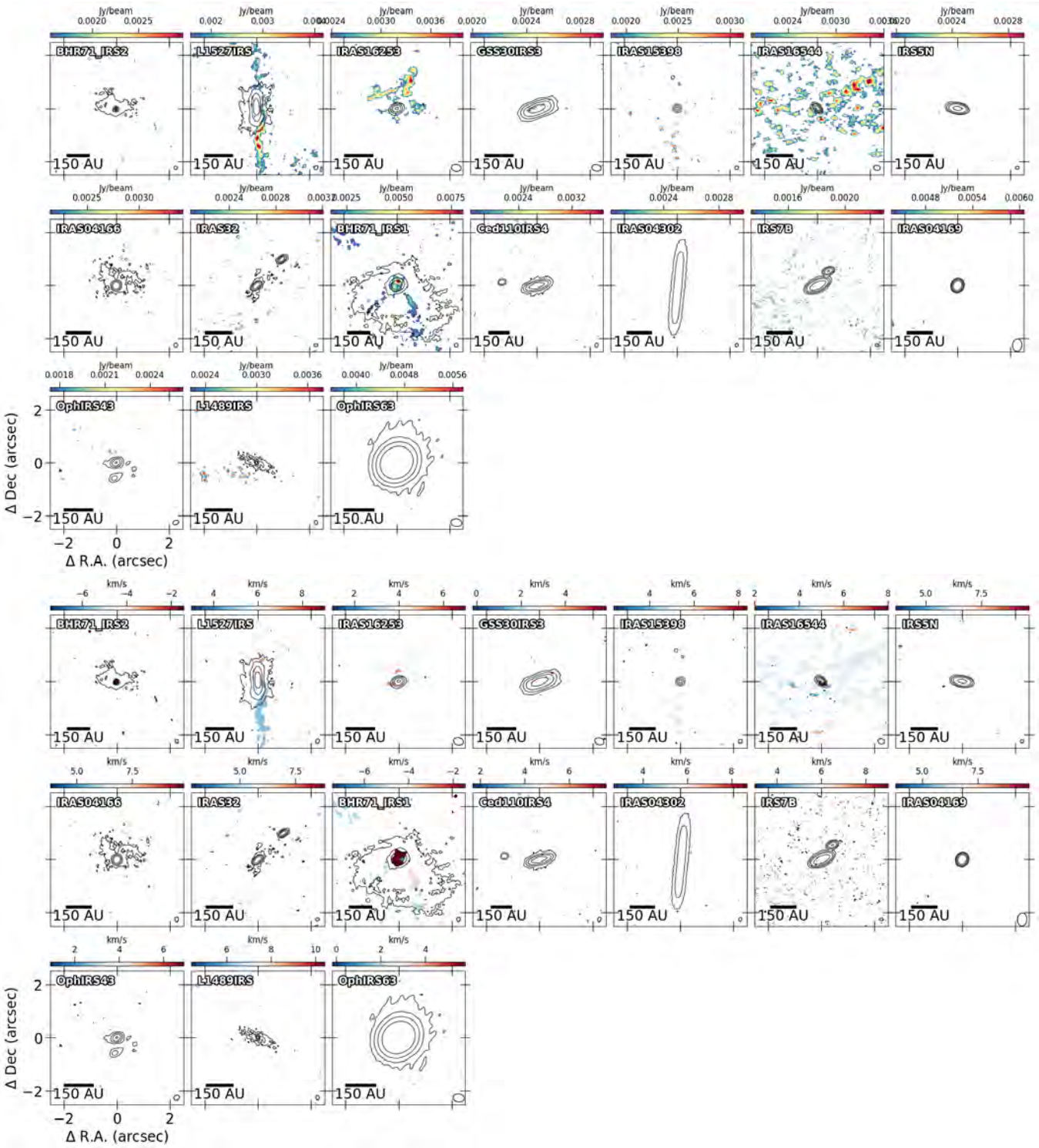

FIGURE 5.40 Same as Figure 5.28 but for c–C_3H_2 ($5_{2,4}$–$4_{1,3}$) instead.

6

High—J CO Observations with SOFIA FIFI-LS: Characterizing Warm Gas in the SVS13 region

Rajeeb Sharma[1], John J. Tobin[2], Jes K. Jørgensen[1]

[1] Niels Bohr Institute, University of Copenhagen, Jagtvej 155A, 2200 Copenhagen N., Denmark
[2] National Radio Astronomy Observatory, 520 Edgemont Rd., Charlottesville, VA 22903 USA

In preparation

Abstract

We present far-infrared (76 – 187 μm) spectroscopic observations conducted with SOFIA FIFI-LS towards the protostars SVS13-A and SVS13-C, as well as the Herbig-Haro object HH-7. These observations targeted high—J CO rotational transitions spanning $14 \leq J_u \leq 34$, allowing for a characterization of the molecular gas excitation in the SVS13 region. Emissions from CO $J = 14$–13 and 17–16 transitions are detected in all three sources, suggesting the global presence of warm molecular gas. On the other hand, emissions from higher—J transitions are detected only in some sources, which indicates the presence of localized processes such as spot shocks or disk winds that contribute to the higher—J transitions. Rotational diagrams show that emissions from $J = 14$–13 to 25–24 can be fit by a "warm" component with rotational temperatures of ∼200 K for SVS13-A and ∼250 K for HH-7 and SVS13-C. The higher-J transitions show deviations from the warm component, suggestive of a positive curvature, which indicates the presence of a separate "hot" component in SVS13-A and HH-7 with a temperature of ∼500 K towards SVS13-A.

6.1 INTRODUCTION

Stars form by dense envelopes of molecular gas and dust that collapse under the influence of gravity. The accretion of mass from the envelope to the central protostar is a dynamic and energetic process that heats up the surrounding gas to several 100 K to 1000 K (e.g., van Gelder et al., 2021). The material from the envelope is regulated by the protostellar disk before it gets accreted by the central star (e.g., Shu et al. 1987; Hartmann et al. 2016). Simultaneously, magnetohydrodynamic (MHD) processes in the protostellar system also drive powerful, bipolar jets called "molecular outflows" to release the angular momentum from the system. These outflows heat up the envelope materials at relatively large distances ($\geq$ 1000 AU) from the protostar and are the principal sources of feedback on the molecular clouds during star formation, especially in low-mass star-forming regions (see Offner & Arce, 2014, and references therein).

Molecular tracers are needed to disentangle the energetic processes in the molecular outflows since they are embedded in dense envelopes. One of the most widely used tracers of molecular outflow from protostars is low-J ($J \leq 6, E_u/k_B \leq 116$ K) CO lines in the millimeter (e.g., Plunkett et al., 2015; Kang et al., 2021). However, these low transitions are only sensitive to cold gas ($\lesssim$ 100 K). High—J ($J > 10$) CO lines are better diagnostics of warm and hot molecular gas and can in principle be used to characterize the density, temperature, molecular abundance, and spatial extent of the emitting region (e.g., Watson et al., 1980; van Kempen et al., 2010; Karska et al., 2013; Manoj et al., 2013; Yıldız et al., 2013; Matuszak et al., 2015). These high—J CO transitions are located in the submillimeter and the far-infrared (FIR) region, and from line cooling studies of dense cores, it is predicted that most of the released energy is produced in the spectral region where these high—J CO emissions are present (e.g., Doty & Neufeld, 1997; Karska et al., 2014, 2018; van Dishoeck et al., 2021). Hence, it is important to observe molecular line emission in the $\sim$ 50-200 μm range.

The high—J line emission can be disentangled into two components: a "warm" component ($\sim$ 300 K) and a "hot" component ($\sim$ 700 K). These transitions probe the outflow conditions on scales very near to the protostar and the jet driving the source (e.g., van Kempen et al. 2010; Green et al. 2013; Karska et al. 2013; Manoj et al. 2013). With the help of these lines, we can perform a rotational diagram analysis of the CO emission and also estimate the total FIR CO luminosity, enabling us to characterize the shock conditions and total cooling from the CO lines. This reflects the amount of energy injection into the molecular cloud and is thus essential to regulate the star formation efficiency of the cloud.

In this paper, we present observations of high—J CO lines in the far-infrared (FIR; 76-187 μm) of the Class I protostar SVS13-A, its companion SVS13-C, and the HH-7 outflow shock produced by the outflow from SVS13-A. The SVS13 system is located in the NGC 1333 cluster in the Perseus molecular cloud at a distance of 299 $\pm$ 14 pc (Zucker et al., 2020). SVS13-A propels the most powerful protostellar outflow in NGC 1333; however, the FIR CO emission spectrum of this system was never observed with *Herschel*. The observations of the sources are described in Section 6.2. The results

and their discussion are presented in Section 6.3 and our conclusions are presented in Section 6.4.

6.2 OBSERVATIONS AND DATA REDUCTION

We observed the SVS13 region using the Far Infrared Field-Imaging Line Spectrometer (FIFI-LS) instrument (Colditz et al., 2012; Fischer et al., 2018) onboard the Stratospheric Observatory for Infrared Astronomy telescope (SOFIA; Young et al., 2012). The observations were conducted in multiple flights during Cycle 6 and Cycle 7 (Project ID: 06_0121 and 07_0185, PI: John Tobin) between 2018 November 06 and 2020 February 26 with aircraft altitudes ranging from 38000 to 43000 feet. FIFI-LS is a dual-channel spectrograph that splits incoming light into two wavelength channels: a blue side (50–125 μm) and a red side (115–203 μm). Our observations target several CO transitions, including $J = 14$–13, 17–16, and 21–20 transitions on the red side and $J = 22$–21, 25–24, 30–29, and 34–33 transitions on the blue side. The observations have spectral resolutions ranging from ∼570 towards $J = 34$–33 at the shorter wavelengths to ∼1570 towards $J = 14$–13 at the longer wavelengths (Colditz et al., 2018; Fadda et al., 2023).

The raw FIFI-LS data were reduced using the standard FIFI-LS reduction pipeline, which results in a FITS cube with a number of extensions, including the telluric corrected flux and error, uncorrected flux and error, exposure map, and the atmospheric transmission (Vacca et al., 2020). The spectra are extracted by integrating the observed intensities over a chosen number of pixels corresponding to the diffraction limit of the telescope at the observed wavelength from each side of the source position. A low-order polynomial ($n \leq 4$) is fitted to the continuum and then subtracted from the extracted spectra to obtain continuum-free spectra for each transition. The line fluxes for each transition are measured by integrating over the FWHM range of the Gaussian fitted to the continuum-subtracted spectrum. In a few cases where detections are evident but the Gaussian fitting failed, the integration range for the line flux was determined by eye. For non-detections and tentative detections, we calculate the upper limits of the emissions instead.

6.3 RESULTS AND DISCUSSION

6.3.1 *Line Detections*

Figure 6.1 shows the continuum subtracted high−J CO spectrum obtained toward SVS13-A, HH-7, and SVS13-C, respectively. The $J = 14$–13 and 17–16 lines are detected towards all three regions and generally are the two strongest lines across the spectra. At higher−J transitions, however, the emission patterns become more complicated and vary between the sources.

For instance, the $J = 21$–20 emission is clearly detected towards HH-7 but is not observed towards SVS13-A or SVS13-C. Likewise, SOFIA observations only targeted the $J = 22$–21 transitions toward SVS13-A and SVS13-C. Emission is clearly detected towards SVS13-C, but for the case of SVS13-A, the observed emission appears to be shifted, peaking near λ ∼118.64 μm instead. The $J = 25$–24 transition is detected towards HH-7 and SVS13-C,

with the emission peak for HH-7 shifted slightly to a lower wavelength at $\lambda \sim$104.0 μm. The transitions J = 30–29 and 34–33 were only targeted towards SVS13-A and HH-7. The 30–29 transition is clearly detected in SVS13-A but appears to be blended with the emission of another species, which peaks at $\lambda \sim$87.10 μm. On the other hand, emission is not detected towards HH-7. Finally, emission from the J = 34–33 transition is detected toward both SVS13-A and HH-7. Table 6.1 provides the total line flux or the upper limits observed towards each transition. Some of the transitions were observed multiple times during the different observation sessions. For those transitions, the average flux observed is given.

The high J CO lines generally arise from UV-heated cavity walls, shocks by outflows, or the heated molecular envelope. Several studies in the past have shown that the emission from UV-heated cavity walls alone is unable to explain the observed emission in protostars (e.g., Manoj et al., 2013; Kristensen et al., 2017). The J = 14–13 and 17–16 lines in our observations are also likely dominated by the presence of warm molecular gas in these regions. This is supported by the fact that there is no significant drop in emission towards HH-7, which is ∼18000 au away from SVS13-A and does not receive much UV-radiation from SVS13-A. This suggests that UV-heating from the protostar cannot be the dominant process for these transitions. The emissions are likely dominated by warm gases that are being heated in shocks from the interaction with the outflow, similar to those found for H_2O emissions in protostellar sources observed with *Herschel* PACS and HIFI (e.g., Santangelo et al., 2012; Tafalla et al., 2013; Mottram et al., 2014).

The variations observed in the CO line profiles across the sources for transitions $J_u > 21$ indicate that these emissions probably result from local physical processes that are only present in select regions of the sources. For instance, the detection of J = 21–20 and 25–24 transitions in HH-7 but not in SVS13-A indicates that these emissions likely arise from small-scale localized shocks called spot shocks (Kristensen et al., 2012, 2013; Mottram et al., 2014). HH-7 is located along the outflow axis and is thus a prime location for such shocks due to bow interaction with the molecules entrained by the jet-driven outflow. Spot shocks also result in an offset in the observed peak, as seen in Figure 6.1. Likewise, the 30–29 transition observed towards SVS13-A and not in HH-7 most likely indicates small-scale C-type and spot shocks in the cavity walls of SVS13-A. The line profile of the 30–29 transition also has a slight offset to a higher wavelength, which further corroborates the shock origin of the emission. and also appears to be blended with another feature at a lower wavelength. The highest CO transitions $J_u \geq 30$ are usually associated with highly excited and dense regions. In protostars, these are usually thought to arise from the hot-core region ($\lesssim$100 au) near the protostar where the disk wind and outflow collide with the neutral and ionized gas to form CO and OH (Neufeld & Dalgarno, 1989; Kristensen et al., 2017). Towards HH-7, it most likely traces the region where the material that gets pushed by the jet gets concentrated and heated, creating a region of hot and dense molecular gas.

Table 6.1. CO line fluxes observed towards the SVS13 system.

CO Transition	Wavelength	E_{up}	A_{ul}	Flux		
				SVS13A	HH7	SVS13C
	(μm)	(K)	(s^{-1})	(Jy)	(Jy)	(Jy)
J=14–13	186.9992	580.4901	2.739e-04	441 ± 29	472 ± 32	584 ± 26
J=17–16	153.2667	845.5984	4.829e-04	164 ± 11	161 ± 11	142 ± 22
J=21–20	124.1934	1276.0535	8.833e-04	< 249	80 ± 31	< 57
J=22–21	118.5806	1397.3866	1.006e-03	22 ± 5	–	32 ± 2
J=25–24	104.4449	1794.2384	1.432e-03	< 65	15 ± 3	16 ± 4
J=30–29	87.1904	2564.8512	2.321e-03	87 ± 10	< 11	–
J=34–33	77.0585	3279.1871	3.175e-03	32 ± 8	61 ± 12	–

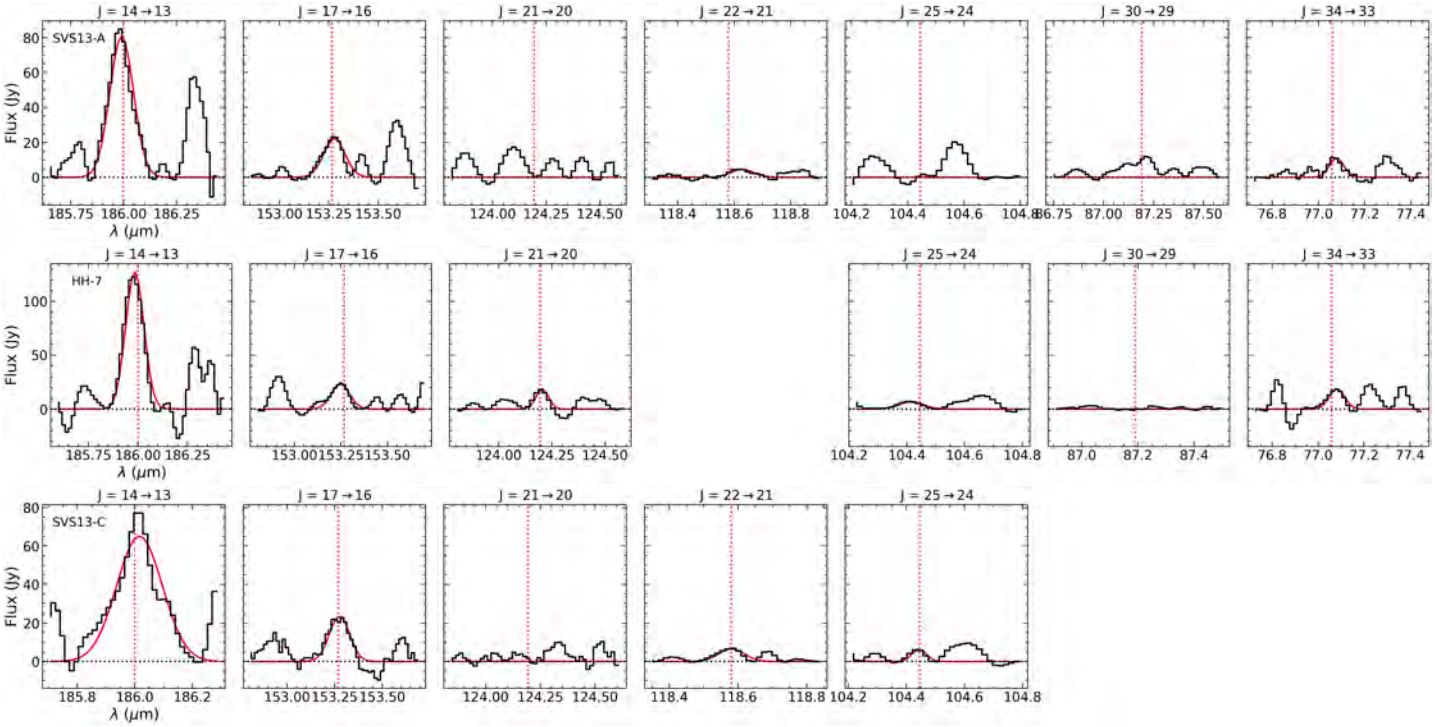

FIGURE 6.1 Continuum-subtracted spectral line profiles of the various CO transitions observed towards the targeted sources. Each row represents a separate source which is identified on the top-left of the first plot. The individual transitions are identified at the top of each plot. The dashed vertical line marks the wavelength of the emission line, while the solid red curve represents the Gaussian fit to the observed spectra.

6.3.2 *Rotation Diagrams*

The CO emissions obtained for the multiple rotational transitions can be analyzed by plotting the fluxes in a rotational diagram. The rotational diagram shows the relative population of the rotational states of a molecule derived from its observed flux. This population diagram can be obtained from the Boltzmann relation:

$$\frac{\mathcal{N}_u}{g_u} = \frac{\mathcal{N}}{Q} exp\left(\frac{-E_{\rm up}}{T_{\rm rot}}\right) \tag{6.1}$$

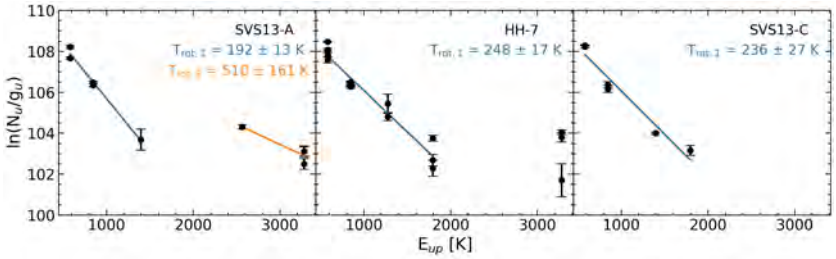

FIGURE 6.2 CO rotational diagrams for SVS13-A (*left*), HH-7 (*middle*) and SVS13-C (*right*). The solid blue lines represent the linear fit to the CO populations for $14 \leq J_u \leq 25$, representing the "warm" gas component and the solid orange line represents the linear fit to the higher-J_u populations, indicative of the additional "hot" component.

where $\mathcal{N}_u$ is the number of molecules in the upper state, g_u is the degeneracy of the upper state, Q is the partition function, $E_{\rm up}$ is the excitation energy of the upper state, and $T_{\rm rot}$ is the rotational temperature. $\mathcal{N}_u$ can be found using:

$$\mathcal{N}_u = \frac{4\pi D^2 F_\nu}{h\nu A_{ul}} \tag{6.2}$$

where D is the distance to the target, F_ν is the observed flux of the CO transition at frequency ν, h is the Planck's constant, and A_{ul} is the Einstein A coefficient for the transition.

By plotting the logarithm of $\mathcal{N}_u/g_u$ against $E_{\rm up}$, the result can be fitted by a straight line, whose slope gives us the value of $T_{\rm rot}$, assuming the gas is in local thermodynamic equilibrium (LTE). A detailed description is provided in Goldsmith & Langer (1999).

Figure 6.2 displays the rotational diagram obtained for SVS13-A, HH-7, and SVS13-C, and Table 6.2 summarizes the results of the fitting. In all three cases, the CO transition population up to $J_u = 25$ can be fitted with a single temperature profile. These transitions are generally associated with the "warm" component with rotational temperatures of ∼300 K. From our analysis, we find rotational temperatures of ∼200 K toward SVS13-A and ∼250 K toward HH-7 and SVS13-C. The temperatures for HH-7 and SVS13-C fall within the range of temperatures reported for other sources in previous studies (e.g., Manoj et al., 2013; Green et al., 2013; Karska et al., 2013). Although the temperature derived for SVS13-A is slightly lower, it still falls on the tail end of the derived temperatures for low-mass protostars. Additionally, from our observations, we only obtained clear emission in 3 CO transitions, which significantly limits the fitting. Additional observations from more transitions will help in obtaining a more robust temperature for SVS13-A.

The higher transitions observed towards SVS13-A and HH-7 appear to deviate from the straight line, showing signs of positive curvature. Such positive profiles in CO transitions have been observed with *Herschel* towards multiple sources (e.g., van Kempen et al., 2010; Manoj et al., 2013; Green et al., 2013; Karska et al., 2018; Yang et al., 2018). This behavior suggests that the observed CO gas likely has an additional "hot" component that accounts for these higher CO transitions. For SVS13-A, where we observe both $J = 30$–29 and 34–33 lines, the linear fit gives us a rotational temperature of ∼500, which is slightly lower than the theoretical value for "hot" components

Table 6.2. Temperatures and number of molecules derived from the rotational diagram.

Source	$T_{\rm rot}$		log(N)	
	T_1 (K)	T_1 (K)	log($\mathcal{N}_1$)	log($\mathcal{N}_2$)
SVS13-A	195 ± 13	510 ± 161	$115.2^{+0.41}_{-0.40}$	$114.5^{+2.11}_{-2.02}$
HH-7	248 ± 17	–	$114.6^{+0.40}_{-0.39}$	–
SVS13-C	236 ± 27	–	$114.7^{+0.66}_{-0.65}$	–

at ∼700 K. However, since we only observe two transitions for SVS13-A and only one for HH-7, we lack enough data points to conclusively confirm its existence. Nevertheless, this result provides a preliminary estimate of the temperatures of these sources. Future, more sensitive observations of additional J—transitions of CO as well as other molecules such as H_2O and OH combined with shock radiative transfer modeling can help constrain these values.

6.4 SUMMARY

We have conducted spectral line observations of several high—J CO rotational transitions using SOFIA FIFI-LS towards SVS13-A, HH-7, and SVS13-C located in the NGC 1333 cluster. Emissions from 14–13 and 17–16 transitions are detected in all three sources and display similar profiles and intensities, suggesting they likely arise from emissions of warm molecular gas that have been heated throughout the region and are not dominated by UV-heated cavity walls alone. The higher—J transitions are only observed towards some of the sources, suggesting variations in localized processes such as spot shocks. Rotational diagrams reveal that the CO population for $J_u \leq 25$ is well-represented by rotational temperatures of ∼200 K for SVS13-A and ∼250 K for HH-7 and SVS13-C. Higher-J transitions towards SVS13-A and HH-7 show deviations from this temperature, which suggests the presence of an additional "hot" component in the CO molecular gas. The fit to the 30–29 and 34–33 transitions towards SVS13-A gives a temperature of ∼500 K. This temperature, while slightly lower than the theoretical value of ∼700 K, indicates the presence of highly hot and energized CO molecules near the protostar in the hot core region formed by localized shock processes. Additional, higher-sensitivity observations of these transitions as well as more high—J transitions are needed to better characterize temperatures in these regions. Unfortunately, no FIR observatories are currently operational to carry out these studies. The launch of new FIR instruments, such as the upcoming PRobe Far Infrared Mission for Astrophysics (PRIMA) telescope, can achieve the desired resolution and sensitivity to eventually conduct these observations and constrain the cooling budget in each source. Until then, observational and theoretical efforts can be made to shed light on the different heating processes, such as the various types of shocks, that contribute to the creation of these high-temperature components.

ACKNOWLEDGMENTS

This work is based on observations made with the NASA/DLR Stratospheric Observatory for Infrared Astronomy (SOFIA). SOFIA is jointly operated by the Universities Space Research Association, Inc. (USRA), under NASA contract NNA17BF53C, and the Deutsches SOFIA Institut (DSI) under DLR contract 50 OK 2002 to the University of Stuttgart.

Bibliography

Adams, W. S. 1941, ApJ, 93, 11, doi: 10.1086/144237

Aikawa, Y., Furuya, K., Hincelin, U., & Herbst, E. 2018, ApJ, 855, 119, doi: 10.3847/1538-4357/aaad6c

Aikawa, Y., Umebayashi, T., Nakano, T., & Miyama, S. M. 1997, ApJ, 486, L51, doi: 10.1086/310837

Albertsson, T., Semenov, D. A., Vasyunin, A. I., Henning, T., & Herbst, E. 2013, ApJS, 207, 27, doi: 10.1088/0067-0049/207/2/27

ALMA Partnership, Brogan, C. L., Pérez, L. M., et al. 2015, ApJ, 808, L3, doi: 10.1088/2041-8205/808/1/L3

Andersen, B. C., Stephens, I. W., Dunham, M. M., et al. 2019, ApJ, 873, 54, doi: 10.3847/1538-4357/ab05c7

André, P., Di Francesco, J., Ward-Thompson, D., et al. 2014, in Protostars and Planets VI, ed. H. Beuther, R. S. Klessen, C. P. Dullemond, & T. Henning, 27–51, doi: 10.2458/azu_uapress_9780816531240-ch002

André, P., Ward-Thompson, D., & Barsony, M. 1993, ApJ, 406, 122, doi: 10.1086/172425

André, P., Ward-Thompson, D., & Barsony, M. 2000, in Protostars and Planets IV, ed. V. Mannings, A. P. Boss, & S. S. Russell, 59, doi: 10.48550/arXiv.astro-ph/9903284

André, P., Men'shchikov, A., Bontemps, S., et al. 2010, A&A, 518, L102, doi: 10.1051/0004-6361/201014666

Andrews, S. M., & Williams, J. P. 2005, ApJ, 631, 1134, doi: 10.1086/432712

Andrews, S. M., Huang, J., Pérez, L. M., et al. 2018, The Astrophysical Journal Letters, 869, L41, doi: 10.3847/2041-8213/aaf741

Ansdell, M., Williams, J. P., van der Marel, N., et al. 2016, ApJ, 828, 46, doi: 10.3847/0004-637X/828/1/46

Arce, H. G., & Sargent, A. I. 2006, ApJ, 646, 1070, doi: 10.1086/505104

Arce, H. G., Shepherd, D., Gueth, F., et al. 2007, in Protostars and Planets V, ed. B. Reipurth, D. Jewitt, & K. Keil, 245, doi: 10.48550/arXiv.astro-ph/0603071

Artur de la Villarmois, E., Kristensen, L. E., & Jørgensen, J. K. 2019, A&A, 627, A37, doi: 10.1051/0004-6361/201935575

Aso, Y., & Sai, J. 2023, jinshisai/SLAM: First Release of SLAM, v1.0.0, Zenodo, doi: 10.5281/zenodo.7783868

Atkinson, R., Baulch, D. L., Cox, R. A., et al. 2006, Atmospheric Chemistry & Physics, 6, 3625, doi: 10.5194/acp-6-3625-200610.5194/acpd-5-6295-2005

Balucani, N., Ceccarelli, C., & Taquet, V. 2015, MNRAS, 449, L16, doi: 10.1093/mnrasl/slv009

Barsony, M. 1994, in Astronomical Society of the Pacific Conference Series, Vol. 65, Clouds, Cores, and Low Mass Stars, ed. D. P. Clemens & R. Barvainis, 197

Bate, M. R. 2018, MNRAS, 475, 5618, doi: 10.1093/mnras/sty169

Beckwith, S. V. W., Sargent, A. I., Chini, R. S., & Guesten, R. 1990, AJ, 99, 924, doi: 10.1086/115385

Benisty, M., Bae, J., Facchini, S., et al. 2021, ApJ, 916, L2, doi: 10.3847/2041-8213/ac0f83

Bergin, E. A., Melnick, G. J., & Neufeld, D. A. 1998, ApJ, 499, 777, doi: 10.1086/305656

Bergin, E. A., & Tafalla, M. 2007, ARA&A, 45, 339, doi: 10.1146/annurev.astro.45.071206.100404

Bergner, J. B., Öberg, K. I., & Rajappan, M. 2017, ApJ, 845, 29, doi: 10.3847/1538-4357/aa7d09

Beuther, H., van Dishoeck, E. F., Tychoniec, L., et al. 2023, A&A, 673, A121, doi: 10.1051/0004-6361/202346167

Bjerkeli, P., van der Wiel, M. H. D., Harsono, D., Ramsey, J. P., & Jørgensen, J. K. 2016, Nature, 540, 406, doi: 10.1038/nature20600

Bjerkeli, P., Ramsey, J. P., Harsono, D., et al. 2019, A&A, 631, A64, doi: 10.1051/0004-6361/201935948

Blandford, R. D., & Payne, D. G. 1982, MNRAS, 199, 883, doi: 10.1093/mnras/199.4.883

Boogert, A. C. A., Gerakines, P. A., & Whittet, D. C. B. 2015, ARA&A, 53, 541, doi: 10.1146/annurev-astro-082214-122348

Briggs, D. S. 1995, in American Astronomical Society Meeting Abstracts, Vol. 187, American Astronomical Society Meeting Abstracts, 112.02

Brinch, C., & Hogerheijde, M. R. 2010, A&A, 523, A25, doi: 10.1051/0004-6361/201015333

Brinch, C., & Jørgensen, J. K. 2013, A&A, 559, A82, doi: 10.1051/0004-6361/201322463

Brown, W. A., & Bolina, A. S. 2007, MNRAS, 374, 1006, doi: 10.1111/j.1365-2966.2006.11216.x

Busch, L. A., Belloche, A., Cabrit, S., Hennebelle, P., & Commerçon, B. 2020, A&A, 633, A126, doi: 10.1051/0004-6361/201936432

Carlhoff, P., Nguyen Luong, Q., Schilke, P., et al. 2013, A&A, 560, A24, doi: 10.1051/0004-6361/201321592

Ceccarelli, C. 2004, in Astronomical Society of the Pacific Conference Series, Vol. 323, Star Formation in the Interstellar Medium: In Honor of David Hollenbach, ed. D. Johnstone, F. C. Adams, D. N. C. Lin, D. A. Neufeeld, & E. C. Ostriker, 195

Ceccarelli, C., Caselli, P., Herbst, E., Tielens, A. G. G. M., & Caux, E. 2007, in Protostars and Planets V, ed. B. Reipurth, D. Jewitt, & K. Keil, 47, doi: 10.48550/arXiv.astro-ph/0603018

Chen, H., Myers, P. C., Ladd, E. F., & Wood, D. O. S. 1995, ApJ, 445, 377, doi: 10.1086/175703

Chen, W. P., & Graham, J. A. 1993, ApJ, 409, 319, doi: 10.1086/172665

Chevance, M., Krumholz, M. R., McLeod, A. F., et al. 2023, in Astronomical Society of the Pacific Conference Series, Vol. 534, Protostars and Planets VII, ed. S. Inutsuka, Y. Aikawa, T. Muto, K. Tomida, & M. Tamura, 1, doi: 10.48550/arXiv.2203.09570

Chiang, E. I., & Goldreich, P. 1997, ApJ, 490, 368, doi: 10.1086/304869

Chini, R., Kämpgen, K., Reipurth, B., et al. 2003, A&A, 409, 235, doi: 10.1051/0004-6361:20031115

Cieza, L. A., González-Ruilova, C., Hales, A. S., et al. 2021, MNRAS, 501, 2934, doi: 10.1093/mnras/staa3787

Colditz, S., Fumi, F., Geis, N., et al. 2012, in Society of Photo-Optical Instrumentation Engineers (SPIE) Conference Series, Vol. 8446, Ground-based and Airborne Instrumentation for Astronomy IV, ed. I. S. McLean, S. K. Ramsay, & H. Takami, 844617, doi: 10.1117/12.924510

Colditz, S., Beckmann, S., Bryant, A., et al. 2018, Journal of Astronomical Instrumentation, 7, 1840004, doi: 10.1142/S2251171718400044

Commerçon, B., Launhardt, R., Dullemond, C., & Henning, T. 2012, A&A, 545, A98, doi: 10.1051/0004-6361/201118706

Cornwell, T. J. 2008, IEEE Journal of Selected Topics in Signal Processing, 2, 793, doi: 10.1109/JSTSP.2008.2006388

Cuppen, H. M., van Dishoeck, E. F., Herbst, E., & Tielens, A. G. G. M. 2009, A&A, 508, 275, doi: 10.1051/0004-6361/200913119

Dong, R., Zhu, Z., & Whitney, B. 2015, ApJ, 809, 93, doi: 10.1088/0004-637X/809/1/93

Doty, S. D., & Neufeld, D. A. 1997, ApJ, 489, 122, doi: 10.1086/304764

Draine, B. T. 2003, ARA&A, 41, 241, doi: 10.1146/annurev.astro.41.011802.094840

—. 2011, Physics of the Interstellar and Intergalactic Medium

Drozdovskaya, M. N., Walsh, C., Visser, R., Harsono, D., & van Dishoeck, E. F. 2015, MNRAS, 451, 3836, doi: 10.1093/mnras/stv1177

Drozdovskaya, M. N., van Dishoeck, E. F., Jørgensen, J. K., et al. 2018, MNRAS, 476, 4949, doi: 10.1093/mnras/sty462

Dunham, M. M., Stutz, A. M., Allen, L. E., et al. 2014, in Protostars and Planets VI, ed. H. Beuther, R. S. Klessen, C. P. Dullemond, & T. Henning, 195–218, doi: 10.2458/azu_uapress_9780816531240-ch009

Dutta, S., Lee, C.-F., Hirano, N., et al. 2022, ApJ, 931, 130, doi: 10.3847/1538-4357/ac67a1

Eley, D. D., & Rideal, E. K. 1940, Nature, 146, 401, doi: 10.1038/146401d0

Encalada, F. J., Looney, L. W., Takakuwa, S., et al. 2024, ApJ, 966, 32, doi: 10.3847/1538-4357/ad3442

Evans, Neal J., I., Dunham, M. M., Jørgensen, J. K., et al. 2009, ApJS, 181, 321, doi: 10.1088/0067-0049/181/2/321

Fadda, D., Colditz, S., Fischer, C., et al. 2023, AJ, 166, 237, doi: 10.3847/1538-3881/acffb4

Fedoseev, G., Cuppen, H. M., Ioppolo, S., Lamberts, T., & Linnartz, H. 2015, MNRAS, 448, 1288, doi: 10.1093/mnras/stu2603

Fiorellino, E., Tychoniec, Ł., Cruz-Sáenz de Miera, F., et al. 2023, ApJ, 944, 135, doi: 10.3847/1538-4357/aca320

Fischer, C., Beckmann, S., Bryant, A., et al. 2018, Journal of Astronomical Instrumentation, 7, 1840003, doi: 10.1142/S2251171718400032

Fischer, W. J., Hillenbrand, L. A., Herczeg, G. J., et al. 2023, in Astronomical Society of the Pacific Conference Series, Vol. 534, Protostars and Planets VII, ed. S. Inutsuka, Y. Aikawa, T. Muto, K. Tomida, & M. Tamura, 355, doi: 10.48550/arXiv.2203.11257

Fischer, W. J., Safron, E., & Megeath, S. T. 2019, ApJ, 872, 183, doi: 10.3847/1538-4357/ab01dc

Fischer, W. J., Megeath, S. T., Tobin, J. J., et al. 2012, ApJ, 756, 99, doi: 10.1088/0004-637X/756/1/99

Flores, C., Ohashi, N., Tobin, J. J., et al. 2023, ApJ, 958, 98, doi: 10.3847/1538-4357/acf7c1

Fockenberg, C., & Preses, J. M. 2002, Journal of Physical Chemistry A, 106, 2924, doi: 10.1021/jp0141880

Frank, A., Ray, T. P., Cabrit, S., et al. 2014, in Protostars and Planets VI, ed. H. Beuther, R. S. Klessen, C. P. Dullemond, & T. Henning, 451–474, doi: 10.2458/azu_uapress_9780816531240-ch020

Friesen, R. K., Pon, A., Bourke, T. L., et al. 2018, ApJ, 869, 158, doi: 10.3847/1538-4357/aaeff5

Fuchs, G. W., Cuppen, H. M., Ioppolo, S., et al. 2009, A&A, 505, 629, doi: 10.1051/0004-6361/200810784

Galli, P. A. B., Bouy, H., Olivares, J., et al. 2020, A&A, 643, A148, doi: 10.1051/0004-6361/202038717

Garufi, A., Podio, L., Codella, C., et al. 2022, A&A, 658, A104, doi: 10.1051/0004-6361/202141264

Gavino, S., Jørgensen, J. K., Sharma, R., et al. 2024, ApJ, submitted

Gerin, M., Pety, J., Fuente, A., et al. 2015, A&A, 577, L2, doi: 10.1051/0004-6361/201525777

Goldsmith, P. F., & Langer, W. D. 1999, ApJ, 517, 209, doi: 10.1086/307195

Gonzalez, J. F., Laibe, G., & Maddison, S. T. 2017, MNRAS, 467, 1984, doi: 10.1093/mnras/stx016

Gould, R. J., & Salpeter, E. E. 1963, ApJ, 138, 393, doi: 10.1086/147654

Gredel, R., Lepp, S., Dalgarno, A., & Herbst, E. 1989, ApJ, 347, 289, doi: 10.1086/168117

Green, J. D., Evans, Neal J., I., Jørgensen, J. K., et al. 2013, ApJ, 770, 123, doi: 10.1088/0004-637X/770/2/123

Greene, T. P., Wilking, B. A., Andre, P., Young, E. T., & Lada, C. J. 1994, ApJ, 434, 614, doi: 10.1086/174763

Guzmán, V. V., Pety, J., Goicoechea, J. R., et al. 2015, ApJ, 800, L33, doi: 10.1088/2041-8205/800/2/L33

Han, I., Kwon, W., Ohashi, N., et al. 2024, ApJ, in prep.

Harilal, S. S., Brumfield, B. E., LaHaye, N. L., Hartig, K. C., & Phillips, M. C. 2018, Applied Physics Reviews, 5, 021301, doi: 10.1063/1.5016053

Harju, J., Haikala, L. K., Mattila, K., et al. 1993, A&A, 278, 569

Harris, J., & Kasemo, B. 1981, Surface Science, 105, L281, doi: 10.1016/0039-6028(81)90004-2

Harsono, D., Bjerkeli, P., van der Wiel, M. H. D., et al. 2018, Nature Astronomy, 2, 646, doi: 10.1038/s41550-018-0497-x

Hartmann, L., Herczeg, G., & Calvet, N. 2016, ARA&A, 54, 135, doi: 10.1146/annurev-astro-081915-023347

Haugbølle, T., Padoan, P., & Nordlund, Å. 2018, ApJ, 854, 35, doi: 10.3847/1538-4357/aaa432

Herbst, E. 2001, Chem. Soc. Rev., 30, 168, doi: 10.1039/A909040A

Herbst, E., & Klemperer, W. 1973, ApJ, 185, 505, doi: 10.1086/152436

Herbst, E., Lee, H. H., Howe, D. A., & Millar, T. J. 1994, MNRAS, 268, 335, doi: 10.1093/mnras/268.2.335

Herbst, E., & van Dishoeck, E. F. 2009, ARA&A, 47, 427, doi: 10.1146/annurev-astro-082708-101654

Hinshelwood, C. N. 1940 (Oxford University Press), 36–39

Hiraoka, K., Ohashi, N., Kihara, Y., et al. 1994, Chemical Physics Letters, 229, 408, doi: 10.1016/0009-2614(94)01066-8

Högbom, J. A. 1974, A&AS, 15, 417

Hollenbach, D., & Salpeter, E. E. 1971, ApJ, 163, 155, doi: 10.1086/150754

Hsieh, T.-H., Murillo, N. M., Belloche, A., et al. 2019, ApJ, 884, 149, doi: 10.3847/1538-4357/ab425a

Huang, B., Girart, J. M., Stephens, I. W., et al. 2024, ApJ, 963, L31, doi: 10.3847/2041-8213/ad27d4

Huang, J., Andrews, S. M., Dullemond, C. P., et al. 2018, ApJ, 869, L42, doi: 10.3847/2041-8213/aaf740

Hull, C. L. H., Girart, J. M., Tychoniec, Ł., et al. 2017, ApJ, 847, 92, doi: 10.3847/1538-4357/aa7fe9

Iqbal, W., & Wakelam, V. 2018, A&A, 615, A20, doi: 10.1051/0004-6361/201732486

Isella, A., Benisty, M., Teague, R., et al. 2019, ApJ, 879, L25, doi: 10.3847/2041-8213/ab2a12

Jansky, K. G. 1933, Nature, 132, 66, doi: 10.1038/132066a0

Jeans, J. H. 1902, Philosophical Transactions of the Royal Society of London Series A, 199, 1, doi: 10.1098/rsta.1902.0012

Jhan, K.-S., Lee, C.-F., Johnstone, D., et al. 2022, ApJ, 931, L5, doi: 10.3847/2041-8213/ac6a53

Jørgensen, J. K., Belloche, A., & Garrod, R. T. 2020, ARA&A, 58, 727, doi: 10.1146/annurev-astro-032620-021927

Jørgensen, J. K., Hogerheijde, M. R., Blake, G. A., et al. 2004, A&A, 415, 1021, doi: 10.1051/0004-6361:20034216

Jørgensen, J. K., Johnstone, D., Kirk, H., & Myers, P. C. 2007, ApJ, 656, 293, doi: 10.1086/510150

Jørgensen, J. K., Kuruwita, R. L., Harsono, D., et al. 2022, Nature, 606, 272, doi: 10.1038/s41586-022-04659-4

Jørgensen, J. K., Schöier, F. L., & van Dishoeck, E. F. 2002, A&A, 389, 908, doi: 10.1051/0004-6361:20020681

—. 2005, A&A, 437, 501, doi: 10.1051/0004-6361:20042060

Jørgensen, J. K., van Dishoeck, E. F., Visser, R., et al. 2009, A&A, 507, 861, doi: 10.1051/0004-6361/200912325

Jørgensen, J. K., Visser, R., Williams, J. P., & Bergin, E. A. 2015, A&A, 579, A23, doi: 10.1051/0004-6361/201425317

Jørgensen, J. K., Harvey, P. M., Evans, Neal J., I., et al. 2006, ApJ, 645, 1246, doi: 10.1086/504373

Jørgensen, J. K., van der Wiel, M. H. D., Coutens, A., et al. 2016, A&A, 595, A117, doi: 10.1051/0004-6361/201628648

Kang, M., Choi, M., Wyrowski, F., et al. 2021, ApJS, 255, 2, doi: 10.3847/1538-4365/abfd35

Karska, A., Herczeg, G. J., van Dishoeck, E. F., et al. 2013, A&A, 552, A141, doi: 10.1051/0004-6361/201220028

Karska, A., Herpin, F., Bruderer, S., et al. 2014, A&A, 562, A45, doi: 10.1051/0004-6361/201321954

Karska, A., Kaufman, M. J., Kristensen, L. E., et al. 2018, ApJS, 235, 30, doi: 10.3847/1538-4365/aaaec5

Keppler, M., Benisty, M., Müller, A., et al. 2018, A&A, 617, A44, doi: 10.1051/0004-6361/201832957

Kessler, M. F., Steinz, J. A., Anderegg, M. E., et al. 1996, A&A, 315, L27

Kido, M., Takakuwa, S., Saigo, K., et al. 2023, ApJ, 953, 190, doi: 10.3847/1538-4357/acdd7a

Kim, C.-H., Lee, J.-E., Peña, C. C., et al. 2024, ApJ, 961, 108, doi: 10.3847/1538-4357/ad1400

Kratter, K., & Lodato, G. 2016, ARA&A, 54, 271, doi: 10.1146/annurev-astro-081915-023307

Kristensen, L. E., & Dunham, M. M. 2018, A&A, 618, A158, doi: 10.1051/0004-6361/201731584

Kristensen, L. E., van Dishoeck, E. F., Benz, A. O., et al. 2013, A&A, 557, A23, doi: 10.1051/0004-6361/201321619

Kristensen, L. E., van Dishoeck, E. F., van Kempen, T. A., et al. 2010, A&A, 516, A57, doi: 10.1051/0004-6361/201014182

Kristensen, L. E., van Dishoeck, E. F., Bergin, E. A., et al. 2012, A&A, 542, A8, doi: 10.1051/0004-6361/201118146

Kristensen, L. E., van Dishoeck, E. F., Mottram, J. C., et al. 2017, A&A, 605, A93, doi: 10.1051/0004-6361/201630127

Kuffmeier, M., Calcutt, H., & Kristensen, L. E. 2019, A&A, 628, A112, doi: 10.1051/0004-6361/201935504

Kuffmeier, M., Haugbølle, T., & Nordlund, Å. 2017, ApJ, 846, 7, doi: 10.3847/1538-4357/aa7c64

Kusaka, T., Nakano, T., & Hayashi, C. 1970, Progress of Theoretical Physics, 44, 1580, doi: 10.1143/PTP.44.1580

Kwon, W., Looney, L. W., Mundy, L. G., Chiang, H.-F., & Kemball, A. J. 2009, ApJ, 696, 841, doi: 10.1088/0004-637X/696/1/841

Lada, C. J. 1987, in IAU Symposium, Vol. 115, Star Forming Regions, ed. M. Peimbert & J. Jugaku, 1

Lada, C. J., & Wilking, B. A. 1984, ApJ, 287, 610, doi: 10.1086/162719

Langmuir, I. 1922, Trans. Faraday Soc., 17, 607, doi: 10.1039/TF9221700607

Larson, R. B. 1969, MNRAS, 145, 271, doi: 10.1093/mnras/145.3.271

—. 1981, MNRAS, 194, 809, doi: 10.1093/mnras/194.4.809

Lee, J.-E., Matsumoto, T., Kim, H.-J., et al. 2023, ApJ, 953, 82, doi: 10.3847/1538-4357/acdd5b

Lee, J.-E., Kim, C.-H., Lee, S., et al. 2024, ApJ, 966, 119, doi: 10.3847/1538-4357/ad3106

Lee, S., Lee, J.-E., & Bergin, E. A. 2015, ApJS, 217, 30, doi: 10.1088/0067-0049/217/2/30

Lee, S., Lee, J.-E., Bergin, E. A., & Park, Y.-S. 2014, ApJS, 213, 33, doi: 10.1088/0067-0049/213/2/33

Lee, S., Lee, J.-E., Aikawa, Y., et al. in prep., ApJ, in prep.

Li, Z. Y., Banerjee, R., Pudritz, R. E., et al. 2014, in Protostars and Planets VI, ed. H. Beuther, R. S. Klessen, C. P. Dullemond, & T. Henning, 173–194, doi: 10.2458/azu_uapress_9780816531240-ch008

Lin, Y., Liu, H. B., Dale, J. E., et al. 2017, ApJ, 840, 22, doi: 10.3847/1538-4357/aa6c67

Lin, Z.-Y. D., Li, Z.-Y., Tobin, J. J., et al. 2023, ApJ, 951, 9, doi: 10.3847/1538-4357/acd5c9

Lindberg, J. E., Jørgensen, J. K., Green, J. D., et al. 2014, A&A, 565, A29, doi: 10.1051/0004-6361/201322184

Loomis, R. A., Cleeves, L. I., Öberg, K. I., Guzman, V. V., & Andrews, S. M. 2015, ApJ, 809, L25, doi: 10.1088/2041-8205/809/2/L25

Mangum, J. G., & Wootten, A. 1993, ApJS, 89, 123, doi: 10.1086/191841

Manoj, P., Watson, D. M., Neufeld, D. A., et al. 2013, ApJ, 763, 83, doi: 10.1088/0004-637X/763/2/83

Maret, S., Ceccarelli, C., Caux, E., et al. 2004, A&A, 416, 577, doi: 10.1051/0004-6361:20034157

Maret, S., Maury, A. J., Belloche, A., et al. 2020, A&A, 635, A15, doi: 10.1051/0004-6361/201936798

Martin-Pintado, J., Bachiller, R., & Fuente, A. 1992, A&A, 254, 315

Matuszak, M., Karska, A., Kristensen, L. E., et al. 2015, A&A, 578, A20, doi: 10.1051/0004-6361/201526021

Maureira, M. J., Arce, H. G., Dunham, M. M., et al. 2020, MNRAS, 499, 4394, doi: 10.1093/mnras/staa2894

Maury, A. J., Girart, J. M., Zhang, Q., et al. 2018, MNRAS, 477, 2760, doi: 10.1093/mnras/sty574

Maury, A. J., André, P., Testi, L., et al. 2019, A&A, 621, A76, doi: 10.1051/0004-6361/201833537

Maxwell, J. C. 1865, Philosophical Transactions of the Royal Society of London Series I, 155, 459

McGuire, B. A. 2022, ApJS, 259, 30, doi: 10.3847/1538-4365/ac2a48

McKee, C. F., & Ostriker, E. C. 2007, ARA&A, 45, 565, doi: 10.1146/annurev.astro.45.051806.110602

McKellar, A. 1940, PASP, 52, 187, doi: 10.1086/125159

McMullin, J. P., Waters, B., Schiebel, D., Young, W., & Golap, K. 2007, in Astronomical Society of the Pacific Conference Series, Vol. 376, Astronomical Data Analysis Software and Systems XVI, ed. R. A. Shaw, F. Hill, & D. J. Bell, 127

Millar, T. J., Bennett, A., & Herbst, E. 1989, ApJ, 340, 906, doi: 10.1086/167444

Millar, T. J., Walsh, C., Cordiner, M. A., Ní Chuimín, R., & Herbst, E. 2007, ApJ, 662, L87, doi: 10.1086/519376

Mottram, J. C., Kristensen, L. E., van Dishoeck, E. F., et al. 2014, A&A, 572, A21, doi: 10.1051/0004-6361/201424267

Murillo, N. M., van Dishoeck, E. F., van der Wiel, M. H. D., et al. 2018, A&A, 617, A120, doi: 10.1051/0004-6361/201731724

Myers, P. C. 2009, ApJ, 700, 1609, doi: 10.1088/0004-637X/700/2/1609

Myers, P. C., & Ladd, E. F. 1993, ApJ, 413, L47, doi: 10.1086/186956

Nakamura, F., & Li, Z.-Y. 2014, ApJ, 783, 115, doi: 10.1088/0004-637X/783/2/115

Narayanan, S., Williams, J. P., Tobin, J. J., et al. 2023, ApJ, 958, 20, doi: 10.3847/1538-4357/acfd24

Neufeld, D. A., & Dalgarno, A. 1989, ApJ, 340, 869, doi: 10.1086/167441

Neugebauer, G., Habing, H. J., van Duinen, R., et al. 1984, ApJ, 278, L1, doi: 10.1086/184209

Neuhäuser, R., & Forbrich, J. 2008, in Handbook of Star Forming Regions, Volume II, ed. B. Reipurth, Vol. 5, 735

Nisini, B., Antoniucci, S., Giannini, T., & Lorenzetti, D. 2005, A&A, 429, 543, doi: 10.1051/0004-6361:20041409

Noble, J. A., Theule, P., Mispelaer, F., et al. 2012, A&A, 543, A5, doi: 10.1051/0004-6361/201219437

Nutter, D. J., Ward-Thompson, D., & André, P. 2005, MNRAS, 357, 975, doi: 10.1111/j.1365-2966.2005.08711.x

Öberg, K. I., Facchini, S., & Anderson, D. E. 2023, ARA&A, 61, 287, doi: 10.1146/annurev-astro-022823-040820

Öberg, K. I., Guzmán, V. V., Merchantz, C. J., et al. 2017, ApJ, 839, 43, doi: 10.3847/1538-4357/aa689a

Offner, S. S. R., & Arce, H. G. 2014, ApJ, 784, 61, doi: 10.1088/0004-637X/784/1/61

Ohashi, N., Saigo, K., Aso, Y., et al. 2014, ApJ, 796, 131, doi: 10.1088/0004-637X/796/2/131

Ohashi, N., Tobin, J. J., Jørgensen, J. K., et al. 2023, ApJ, 951, 8, doi: 10.3847/1538-4357/acd384

Penteado, E. M., Walsh, C., & Cuppen, H. M. 2017, ApJ, 844, 71, doi: 10.3847/1538-4357/aa78f9

Persson, M. V. 2014, doi: 10.6084/m9.figshare.1121574.v2

Peterson, D. E., Caratti o Garatti, A., Bourke, T. L., et al. 2011, ApJS, 194, 43, doi: 10.1088/0067-0049/194/2/43

Phuong, N. T., Lee, C. W., Ohashi, N., et al. 2024, ApJ, in prep.

Pilbratt, G. L., Riedinger, J. R., Passvogel, T., et al. 2010, A&A, 518, L1, doi: 10.1051/0004-6361/201014759

Pineda, J. E., Segura-Cox, D., Caselli, P., et al. 2020, Nature Astronomy, 4, 1158, doi: 10.1038/s41550-020-1150-z

Pineda, J. E., Arzoumanian, D., Andre, P., et al. 2023, in Astronomical Society of the Pacific Conference Series, Vol. 534, Protostars and Planets VII, ed. S. Inutsuka, Y. Aikawa, T. Muto, K. Tomida, & M. Tamura, 233, doi: 10.48550/arXiv.2205.03935

Plunkett, A. L., Arce, H. G., Mardones, D., et al. 2015, Nature, 527, 70, doi: 10.1038/nature15702

Podio, L., Codella, C., Gueth, F., et al. 2015, A&A, 581, A85, doi: 10.1051/0004-6361/201525778

Podio, L., Ceccarelli, C., Codella, C., et al. 2024, arXiv e-prints, arXiv:2407.04813, doi: 10.48550/arXiv.2407.04813

Pontoppidan, K. M., Salyk, C., Bergin, E. A., et al. 2014, in Protostars and Planets VI, ed. H. Beuther, R. S. Klessen, C. P. Dullemond, & T. Henning, 363–385, doi: 10.2458/azu_uapress_9780816531240-ch016

Prasad, S. S., & Tarafdar, S. P. 1983, ApJ, 267, 603, doi: 10.1086/160896

Qasim, D., Chuang, K. J., Fedoseev, G., et al. 2018, A&A, 612, A83, doi: 10.1051/0004-6361/201732355

Rayleigh. 1879, The London, Edinburgh, and Dublin Philosophical Magazine and Journal of Science, 8, 261, doi: 10.1080/14786447908639684

Sadavoy, S. I., Myers, P. C., Stephens, I. W., et al. 2018, ApJ, 869, 115, doi: 10.3847/1538-4357/aaef81

Safron, E. J., Fischer, W. J., Megeath, S. T., et al. 2015, ApJ, 800, L5, doi: 10.1088/2041-8205/800/1/L5

Sai, J., Yen, H.-W., Ohashi, N., et al. 2023, ApJ, 954, 67, doi: 10.3847/1538-4357/ace52d

Sakai, N., Sakai, T., Hirota, T., et al. 2014, Nature, 507, 78, doi: 10.1038/nature13000

Sakai, N., Oya, Y., Higuchi, A. E., et al. 2017, MNRAS, 467, L76, doi: 10.1093/mnrasl/slx002

Sandell, G., Reipurth, B., Vacca, W. D., & Bajaj, N. S. 2021, ApJ, 920, 7, doi: 10.3847/1538-4357/ac133d

Santamaría-Miranda, A., de Gregorio-Monsalvo, I., Ohashi, N., et al. 2024, ApJ, in prep.

Santangelo, G., Nisini, B., Giannini, T., et al. 2012, A&A, 538, A45, doi: 10.1051/0004-6361/201118113

Schilke, P., Walmsley, C. M., Pineau des Forets, G., & Flower, D. R. 1997, A&A, 321, 293

Schnee, S., Di Francesco, J., Enoch, M., et al. 2012, ApJ, 745, 18, doi: 10.1088/0004-637X/745/1/18

Segura-Cox, D. M., Schmiedeke, A., Pineda, J. E., et al. 2020, Nature, 586, 228, doi: 10.1038/s41586-020-2779-6

Sharma, R., Tobin, J. J., Sheehan, P. D., et al. 2020, ApJ, 904, 78, doi: 10.3847/1538-4357/abbdf4

Sharma, R., Jørgensen, J. K., Gavino, S., et al. 2023, ApJ, 954, 69, doi: 10.3847/1538-4357/ace35c

Sheehan, P. D., & Eisner, J. A. 2017, ApJ, 851, 45, doi: 10.3847/1538-4357/aa9990

Sheehan, P. D., Tobin, J. J., Federman, S., Megeath, S. T., & Looney, L. W. 2020, ApJ, 902, 141, doi: 10.3847/1538-4357/abbad5

Shimonishi, T., Nakatani, N., Furuya, K., & Hama, T. 2018, ApJ, 855, 27, doi: 10.3847/1538-4357/aaaa6a

Shu, F. H. 1977, ApJ, 214, 488, doi: 10.1086/155274

Shu, F. H., Adams, F. C., & Lizano, S. 1987, ARA&A, 25, 23, doi: 10.1146/annurev.aa.25.090187.000323

Simon, M., Dutrey, A., & Guilloteau, S. 2000, ApJ, 545, 1034, doi: 10.1086/317838

Simons, M. A. J., Lamberts, T., & Cuppen, H. M. 2020, A&A, 634, A52, doi: 10.1051/0004-6361/201936522

Snow, T. P., & McCall, B. J. 2006, ARA&A, 44, 367, doi: 10.1146/annurev.astro.43.072103.150624

Snyder, L. E., Buhl, D., Zuckerman, B., & Palmer, P. 1969, Phys. Rev. Lett., 22, 679, doi: 10.1103/PhysRevLett.22.679

Solomon, P. M., Rivolo, A. R., Barrett, J., & Yahil, A. 1987, ApJ, 319, 730, doi: 10.1086/165493

Stahler, S. W., & Palla, F. 2004, The Formation of Stars

Stutz, A. M., Tobin, J. J., Stanke, T., et al. 2013, ApJ, 767, 36, doi: 10.1088/0004-637X/767/1/36

Sweatman, M. B. 2024, Time and Mind, 0, 1, doi: 10.1080/1751696X.2024.2373876

Swings, P., & Rosenfeld, L. 1937, ApJ, 86, 483, doi: 10.1086/143880

Tabone, B., Cabrit, S., Bianchi, E., et al. 2017, A&A, 607, L6, doi: 10.1051/0004-6361/201731691

Tafalla, M., Santiago-García, J., Hacar, A., & Bachiller, R. 2010, A&A, 522, A91, doi: 10.1051/0004-6361/201015158

Tafalla, M., Liseau, R., Nisini, B., et al. 2013, A&A, 551, A116, doi: 10.1051/0004-6361/201220422

Takahashi, S., Machida, M. N., Omura, M., et al. 2024, ApJ, 964, 48, doi: 10.3847/1538-4357/ad2268

Takakuwa, S., Ohashi, N., Jørgensen, J. K., Tobin, J. J., & eDisk Team. in prep., ApJ

Takakuwa, S., Saigo, K., Kido, M., et al. 2024, ApJ, 964, 24, doi: 10.3847/1538-4357/ad1f57

Tang, X. D., Henkel, C., Chen, C. H. R., et al. 2017, A&A, 600, A16, doi: 10.1051/0004-6361/201630183

Taylor, K. N. R., & Storey, J. W. V. 1984, MNRAS, 209, 5P, doi: 10.1093/mnras/209.1.5P

Terebey, S., Shu, F. H., & Cassen, P. 1984, ApJ, 286, 529, doi: 10.1086/162628

Testi, L., Birnstiel, T., Ricci, L., et al. 2014, in Protostars and Planets VI, ed. H. Beuther, R. S. Klessen, C. P. Dullemond, & T. Henning, 339, doi: 10.2458/azu_uapress_9780816531240-ch015

Teyssier, R. 2002, A&A, 385, 337, doi: 10.1051/0004-6361:20011817

Thieme, T. J., Lai, S.-P., Lin, S.-J., et al. 2022, ApJ, 925, 32, doi: 10.3847/1538-4357/ac382b

Thieme, T. J., Lai, S.-P., Ohashi, N., et al. 2023, ApJ, 958, 60, doi: 10.3847/1538-4357/ad003a

Tobin, J. 2023, eDisk data reduction scripts, 1.0.0, Zenodo, doi: 10.5281/zenodo.7986682

Tobin, J. J., Hartmann, L., Chiang, H.-F., et al. 2012, Nature, 492, 83, doi: 10.1038/nature11610

Tobin, J. J., Hartmann, L., Looney, L. W., & Chiang, H.-F. 2010, ApJ, 712, 1010, doi: 10.1088/0004-637X/712/2/1010

Tobin, J. J., Looney, L. W., Mundy, L. G., Kwon, W., & Hamidouche, M. 2007, ApJ, 659, 1404, doi: 10.1086/512720

Tobin, J. J., Stutz, A. M., Megeath, S. T., et al. 2015, ApJ, 798, 128, doi: 10.1088/0004-637X/798/2/128

Tobin, J. J., Kratter, K. M., Persson, M. V., et al. 2016, Nature, 538, 483, doi: 10.1038/nature20094

Tobin, J. J., Sheehan, P. D., Megeath, S. T., et al. 2020, ApJ, 890, 130, doi: 10.3847/1538-4357/ab6f64

Tomida, K., Okuzumi, S., & Machida, M. N. 2015, ApJ, 801, 117, doi: 10.1088/0004-637X/801/2/117

Tsukamoto, Y., Maury, A., Commercon, B., et al. 2023, in Astronomical Society of the Pacific Conference Series, Vol. 534, Protostars and Planets VII, ed. S. Inutsuka, Y. Aikawa, T. Muto, K. Tomida, & M. Tamura, 317, doi: 10.48550/arXiv.2209.13765

Turner, B. E. 2001, ApJS, 136, 579, doi: 10.1086/322536

Tychoniec, Ł., Manara, C. F., Rosotti, G. P., et al. 2020, A&A, 640, A19, doi: 10.1051/0004-6361/202037851

Tychoniec, Ł., van Dishoeck, E. F., van't Hoff, M. L. R., et al. 2021, A&A, 655, A65, doi: 10.1051/0004-6361/202140692

Vacca, W., Clarke, M., Perera, D., Fadda, D., & Holt, J. 2020, in Astronomical Society of the Pacific Conference Series, Vol. 527, Astronomical Data Analysis Software and Systems XXIX, ed. R. Pizzo, E. R. Deul, J. D. Mol, J. de Plaa, & H. Verkouter, 547

Valdivia-Mena, M. T., Pineda, J. E., Segura-Cox, D. M., et al. 2022, A&A, 667, A12, doi: 10.1051/0004-6361/202243310

Valdivia-Mena, M. T., Pineda, J. E., Caselli, P., et al. 2024, A&A, 687, A71, doi: 10.1051/0004-6361/202449395

van Cittert, P. 1934, Physica, 1, 201, doi: https://doi.org/10.1016/S0031-8914(34)90026-4

van der Marel, N., van Dishoeck, E. F., Bruderer, S., & van Kempen, T. A. 2014, A&A, 563, A113, doi: 10.1051/0004-6361/201322960

van der Tak, F. F. S., Black, J. H., Schöier, F. L., Jansen, D. J., & van Dishoeck, E. F. 2007, A&A, 468, 627, doi: 10.1051/0004-6361:20066820

van der Wiel, M. H. D., van der Tak, F. F. S., Ossenkopf, V., et al. 2009, A&A, 498, 161, doi: 10.1051/0004-6361/200811391

van der Wiel, M. H. D., Jacobsen, S. K., Jørgensen, J. K., et al. 2019, A&A, 626, A93, doi: 10.1051/0004-6361/201833695

Van Dishoeck, E., Millar, T., & Williams, D. 1988, TJ

van Dishoeck, E. F., & Black, J. H. 1986, ApJS, 62, 109, doi: 10.1086/191135

van Dishoeck, E. F., Kristensen, L. E., Mottram, J. C., et al. 2021, A&A, 648, A24, doi: 10.1051/0004-6361/202039084

van Gelder, M. L., Tabone, B., van Dishoeck, E. F., & Godard, B. 2021, A&A, 653, A159, doi: 10.1051/0004-6361/202141591

van Kempen, T. A., Green, J. D., Evans, N. J., et al. 2010, A&A, 518, L128, doi: 10.1051/0004-6361/201014686

van 't Hoff, M. L. R., Tobin, J. J., Harsono, D., & van Dishoeck, E. F. 2018, A&A, 615, A83, doi: 10.1051/0004-6361/201732313

van't Hoff, M. L. R., Harsono, D., Tobin, J. J., et al. 2020, ApJ, 901, 166, doi: 10.3847/1538-4357/abb1a2

van't Hoff, M. L. R., Tobin, J. J., Li, Z.-Y., et al. 2023, ApJ, 951, 10, doi: 10.3847/1538-4357/accf87

Villenave, M., Ménard, F., Dent, W. R. F., et al. 2020, A&A, 642, A164, doi: 10.1051/0004-6361/202038087

Visser, R., Kristensen, L. E., Bruderer, S., et al. 2012, A&A, 537, A55, doi: 10.1051/0004-6361/201117109

Vorobyov, E. I., Elbakyan, V. G., Plunkett, A. L., et al. 2018, A&A, 613, A18, doi: 10.1051/0004-6361/201732253

Wagner, K., Leisenring, J., Cugno, G., et al. 2024, AJ, 167, 181, doi: 10.3847/1538-3881/ad11d5

Wakelam, V., Ceccarelli, C., Castets, A., et al. 2005, A&A, 437, 149, doi: 10.1051/0004-6361:20042566

Wakelam, V., Bron, E., Cazaux, S., et al. 2017, Molecular Astrophysics, 9, 1, doi: 10.1016/j.molap.2017.11.001

Wakker, B. P., & Schwarz, U. J. 1988, A&A, 200, 312

Wang, H., Mundt, R., Henning, T., & Apai, D. 2004, ApJ, 617, 1191, doi: 10.1086/425493

Watanabe, N., & Kouchi, A. 2002, ApJ, 571, L173, doi: 10.1086/341412

Watson, D. M., Storey, J. W. V., Townes, C. H., Haller, E. E., & Hansen, W. L. 1980, ApJ, 239, L129, doi: 10.1086/183308

Watson, W. D. 1974, ApJ, 188, 35, doi: 10.1086/152681

Wernecke, & D'Addario. 1977, IEEE Transactions on Computers, C-26, 351, doi: 10.1109/TC.1977.1674845

Werner, M. W., Roellig, T. L., Low, F. J., et al. 2004, ApJS, 154, 1, doi: 10.1086/422992

Willacy, K. 2007, ApJ, 660, 441, doi: 10.1086/512796

Williams, J. P., & Cieza, L. A. 2011, ARA&A, 49, 67, doi: 10.1146/annurev-astro-081710-102548

Williams, J. P., & McKee, C. F. 1997, ApJ, 476, 166, doi: 10.1086/303588

Wilson, T. L., & Rood, R. 1994, ARA&A, 32, 191, doi: 10.1146/annurev.aa.32.090194.001203

Woods, R. C., Dixon, T. A., Saykally, R. J., & Szanto, P. G. 1975, Phys. Rev. Lett., 35, 1269, doi: 10.1103/PhysRevLett.35.1269

Yamamoto, S. 2017, Introduction to Astrochemistry: Chemical Evolution from Interstellar Clouds to Star and Planet Formation, doi: 10.1007/978-4-431-54171-4

Yamato, Y., Aikawa, Y., Ohashi, N., et al. 2023, ApJ, 951, 11, doi: 10.3847/1538-4357/accd71

Yang, Y.-L., Green, J. D., Evans, Neal J., I., et al. 2018, ApJ, 860, 174, doi: 10.3847/1538-4357/aac2c6

Yang, Y.-L., Sakai, N., Zhang, Y., et al. 2021, ApJ, 910, 20, doi: 10.3847/1538-4357/abdfd6

Yen, H.-W., Takakuwa, S., Koch, P. M., et al. 2015, ApJ, 812, 129, doi: 10.1088/0004-637X/812/2/129

Yıldız, U. A., Kristensen, L. E., van Dishoeck, E. F., et al. 2013, A&A, 556, A89, doi: 10.1051/0004-6361/201220849

Young, A. K., Bate, M. R., Mowat, C. F., Hatchell, J., & Harries, T. J. 2018, MNRAS, 474, 800, doi: 10.1093/mnras/stx2669

Young, E. T., Becklin, E. E., Marcum, P. M., et al. 2012, ApJ, 749, L17, doi: 10.1088/2041-8205/749/2/L17

Zernike, F. 1938, Physica, 5, 785, doi: 10.1016/S0031-8914(38)80203-2

Zhang, C., Ren, Z., Wu, J., et al. 2020, MNRAS, 497, 793, doi: 10.1093/mnras/staa1958

Zhang, K., Blake, G. A., & Bergin, E. A. 2015, The Astrophysical Journal Letters, 806, L7, doi: 10.1088/2041-8205/806/1/L7

Zhang, S., Zhu, Z., Huang, J., et al. 2018, The Astrophysical Journal Letters, 869, L47, doi: 10.3847/2041-8213/aaf744

Zucker, C., Speagle, Joshua S., Schlafly, Edward F., et al. 2020, A&A, 633, A51, doi: 10.1051/0004-6361/201936145

Öberg, K. I., Guzmán, V. V., Walsh, C., et al. 2021, The Astrophysical Journal Supplement Series, 257, 1, doi: 10.3847/1538-4365/ac1432